UNIVERSITY OF QUEBEC IN MONTREAL

CLOUD SUBGRID-SCALE VARIABILITY PARAMETERIZATIONS IN THE GEMCLIM MODEL WITH THE MCICA METHODOLOGY

THESIS SUBMITTED

IN PARTIAL FULFILLMENT OF THE REQUIREMENTS

FOR THE DEGREE OF

PH.D IN EARTH AND ATMOSPHERIC SCIENCES

BY

DANAHÉ PAQUIN-RICARD

DECEMBER 2014

UNIVERSITÉ DU QUÉBEC À MONTRÉAL

PARAMÉTRAGES DE LA VARIABILITÉ SOUS-MAILLE DES NUAGES À L'AIDE DE LA MÉTHODE MCICA DANS LE MODÈLE GEMCLIM

THÈSE

PRÉSENTÉE

COMME EXIGENCE PARTIELLE

DU DOCTORAT EN SCIENCES DE LA TERRE ET DE L'ATMOSPHÈRE

PAR

DANAHÉ PAQUIN-RICARD

DÉCEMBRE 2014

Remerciements

Même si le doctorat semble un travail personnel et parfois solitaire, son accomplissement ne peut se faire seul. Dans mon cas, je ne serais tout simplement pas là sans l'aide, l'appui et les encouragements de plusieurs personnes...

Tout d'abord, je remercie chaleureusement mon directeur Paul Vaillancourt. C'est grâce à ses conseils, ses encouragements et ses questions, que j'ai pu entreprendre, poursuivre et terminer cette thèse. Il a su me laisser l'indépendance pour que j'apprenne, que je travaille et que je me trompe sans toutefois me laisser tourner en rond trop longtemps! Son sens critique et sa vision globale des questions scientifiques sont une source d'inspiration et j'espère pourvoir encore en profiter dans les prochaines années! De son côté, mon co-directeur René Laprise a su m'écouter et me conseiller lors de moments cruciaux, tout au long de ma thèse. Par sa grande expérience et ses bons mots, il a su me rassurer à plusieurs moments. Ma formation à l'UQAM m'a apportée beaucoup et c'est en grande partie grâce à son enseignement.

Also, Howard Barker and Jason Cole have been available to give me their insights on many McICA and other scientific aspects of my research, even when I was not giving news for many months at the time. It was always a pleasure to discuss with you and to come back in Montreal filled with new ideas, I hope these occasional exchanges will continue.

Sans Katja, toutes les ressources qui sont à notre disposition ne seraient pas exploitées comme elles le sont et les mystères informatiques ne seraient pas percés! Évidemment, elle n'est pas la seule personne ressource à m'avoir aidé: je remercie aussi chaleureusement Nadjet, Delphine, Georges et Adelina.

Je remercie le Centre ESCER et le CRSNG pour mon financement durant ma thèse et pour les nombreuses conférences auxquelles j'ai eu la chance de participer. Ces participations sont très formatrices et m'ont permis de sortir de ma petite "bulle" de recherche!

Sans les collègues et amis, le quotidien ne serait pas le même. Les échanges, scientifiques ou non, donnent un sens au travail quotidien. Un merci particulier à Fred avec qui j'ai pu échanger plus spécifiquement sur mon sujet, alors que je me sentais bien seule à parler "nuages et radiation". Les amis et la famille en général ont aussi été une source de soutien, alors qu'ils n'abandonne pas à tenter de comprendre ce que je fais de mes journées!

Je tiens à remercier particulièrement mes parents qui ont toujours été là pour moi, qui n'ont jamais douté de mes choix d'éducation, et qui les ont financés! Si j'ai choisi la physique en entrant à l'université, c'est parce j'ai toujours senti que tous les choix étaient possibles, et c'est grâce à vous! Et un gros merci maman pour toutes les petites attentions du quotidien.

Yani, sans toi je n'en serais tout simplement pas là. On a fait un choix, un peu inconscient, de se lancer dans cette aventure ensemble il y a de cela quelques années. Depuis le début, tu me soutiens, m'encourages, m'endures et même, tu m'écoutes parler de mes problèmes de code! Dans la dernière année particulièrement, tu as pris le relais pour tout ce qui a trait à notre famille pour nous permettre de vivre de bons moments ensemble, tous les trois, quand je suis là, aux dépens de tes projets! Ce soutien est inestimable et plus précieux que tout.

Finalement, Isis, qui est née au milieu de tout ça, m' a apporté un équilibre vital dans ma vie et même dans mon doctorat. Un enfant et un doctorat en même temps peuvent sembler incompatible... Mais quand on se demande ce qu'on fait là et pourquoi on le fait, un enfant nous ramène dans le moment présent, dans les joies du quotidien et, pour moi, ce fut bien souvent l'échappatoire qui m'a redonné le goût de continuer et de terminer! Tu m'as donné un équilibre entre l'abstrait du travail et le concret d'être avec toi!

À tous, merci.

À Yani

TABLE OF CONTENT

LIST OF FIGURES

LIST OF TABLES

LIST OF ACRONYMS

AMIP	Atmospheric Model Intercomparison Project
CALIPSO	Cloud-aerosol lidar and infrared pathfinder satellite observation
CAM	Community atmosphere model
CERES	Clouds and the Earth's Radiant Energy System
CF	Cloud fraction
CKD	Correlated-k distribution
CLDS	Cloud McICA version
CPS	Cumulative probability space
CRCM5	Canadian regional climate model version 5
CRE	Cloud radiative effect
CWC	Cloud water content
CWP	Cloud water path
DJF	December-January-February
EBAF	Energy Balanced and Filled data set
ECMWF	European Centre for Medium-Range Weather Forecasts
ESCER	Centre pour l'étude et la simulation du climat à l'échelle régionale
GCM	General circulation model
GEM	Global environmental multi-scale model
GEMCLIM	Global environmental multi-scale model in climate mode
HU	Absolute humidity
ICA	Independent column approximation
IWC	Ice water content
IWP	Ice water path

IWV	Integrated water vapor
JJA	June-July-August
LW	Longwave
LWC	Liquid water content
LWD	Downwelling longwave
LW-GD	Longwave gamma distribution
LWU	Upwelling longwave
LWP	Liquid water path
McICA	Monte Carlo independent column approximation
MODIS	Moderate Resolution Imaging Spectroradiometer
MRO	Maximum-random cloud vertical overlap
NWP	Numerical weather prediction
PPH	Plane-parallel homogeneous
REF	Reference McICA version
RMSE	Root mean square error
RT	Radiative transfer
SCG	Stochastic cloud generator
SFC	Surface
SSM/I	Special Sensor Microwave Imager
SPEC	Spectral McICA version
SST	Sea surface temperature
SW	Shortwave
SW-ACOD	Shortwave adjusted cloud optical depth
SWD	Downwelling shortwave
SWU	Upwelling shortwave
T	Temperature

TKE	Turbulent kinetic energy
TOA	Top of atmosphere
TOTWC	Total water content
TOTWP	Total water path
f_w	relative standard deviation of cloud water content
L_{cf}	Decorrelation length for cloud fraction
L_{cw}	Decorrelation length for cloud water content
r_{eff}	effective radius
ν	Cloud horizontal variability parameter
τ	Cloud optical depth

RÉSUMÉ

La représentation des processus sous-maille reliés aux nuages demeure une source importante d'incertitudes dans les modèles climatiques. Plus particulièrement, l'interaction nuage-rayonnement dépend fortement de la manière dont est représentée la variabilité sous-maille des nuages dans les modèles. La méthode McICA a été proposée par Barker *et al.* (2002) et Pincus *et al.* (2003) afin de remplacer les hypothèses fixes des nuages implémentées dans les schémas de transfert radiatif par une représentation stochastique de la variabilité sous-maille des nuages. Cette méthode permet de relier beaucoup plus aisément les paramètres sous-mailles des nuages aux observations ou aux variables du modèle. Par contre, puisque les modèles sont souvent ajustés afin d'obtenir un bon budget radiatif au sommet de l'atmosphère, enlever les corrections constantes des nuages pourrait révéler d'autres biais, auparavant cachés.

Cette thèse présente l'implémentation de la méthode McICA dans le modèle GEM-CLIM ainsi qu'une analyse détaillée de ses impacts sur les différentes composantes du budget radiatif et sur la structure de l'atmosphère simulée. Les dépendances fondamentales des effets radiatifs de la variabilité sous-maille sont aussi analysées en parallèle avec les possibilités de paramétrages, basées sur les observations ou les variables du modèle, qui s'offrent avec cette méthode.

Le cadre général de cette thèse est composé de simulations globales dont les mailles de la grille horizontale sont de 0.5° afin d'échantillonner le plus d'états possibles de nuages. Les simulations varient de 48 h à trois ans, limitées par le grand nombre de simulations requises pour tester les différents paramétrages. Seulement quelques simulations ont été étendues jusqu'à trois ans afin d'observer la réponse du modèle à plus long terme à la méthode McICA. Les effets radiatifs des différentes composantes la méthode McICA et des différents paramètres, sont étudiés sous plusieurs angles: des moyennes globales et zonales au sommet de l'atmosphère et à la surface, des profils verticaux moyens zonaux et des cartes de 0.5° de résolution horizontale. Les données satellites de CERES-EBAF, CERES-SYN1deg et SSM/I sont utilisées pour fin de comparaison et de validation des différentes simulations.

Les résultats montrent que la méthode McICA, par l'introduction de l'inhomogénéité horizontale, réduit généralement l'albédo des nuages et leur émissivité, en

comparaison au traitement homogène des nuages. Quant au changement d'hypothèse de recouvrement vertical, il produit des effets radiatifs opposés mais de second ordre, avec comme résultats, une tendance générale d'atténuation des effets radiatifs de l'inhomogénéité horizontale.

Puisqu'un biais important dans le contenu en eau liquide des nuages simulés a été établi, l'implémentation de la méthode McICA dans le modèle GEMCLIM dégrade les performances du modèle en comparaison aux flux observés par CERES, autant à la surface qu'au sommet de l'atmosphère, puisque cette méthode n'est pas conçue pour corriger les biais des nuages simulés. Lorsqu'on compare aux corrections d'inhomogénéité existantes, l'introduction d'inhomogénéité horizontale par McICA est bien plus faible quant à sa réduction de l'albédo et de l'émissivité des nuages. La surestimation du contenu en eau liquide amplifie ces résultats puisque les effets McICA sont plus faibles pour des valeurs élevées de contenu en eau, alors que les effets des corrections existantes sont plus importants. Une fois la méthode implémentée dans le modèle, de petites modifications quant aux nuages bas sont visibles dans la structure atmosphérique simulée et ce, pour toutes les échelles de temps. Une fraction nuageuse et un contenu en eau réduits sont discernables, ce qui atténue les effets radiatifs totaux de McICA, excepté pour les flux de longues longueurs d'onde au sommet de l'atmosphère qui sont moins sensibles aux variations des nuages bas.

D'un point de vue plus général, il est démontré que l'inhomogénéité horizontale de McICA varie en fonction de l'épaisseur optique des nuages, produisant plus d'effets à de faibles valeurs, comme la théorie le suggérait. De plus, les nuages de glace montrent un effet opposé pour les courtes longueurs d'ondes avec une augmentation de leur albédo, ce qui était aussi expliqué par la théorie. Les effets sont plus importants pour les courtes longueurs d'ondes que les longues longueurs d'ondes. Ceci s'explique par la relation de l'émissivité des nuages en fonction du contenu en eau qui sature plus rapidement que la relation de l'albédo des nuages en fonction du contenu en eau. Finalement, les effets McICA augmentent avec la fraction nuageuse puisque plus de nuages peuvent alors contribuer aux flux modifiés.

Cette thèse porte aussi sur la comparaison de paramétrages de différentes complexités, autant pour l'inhomogénéité horizontale que pour le recouvrement vertical des nuages. Il est démontré que, pour le modèle GEMCLIM, l'inhomogénéité horizontale a plus de potentiel radiatif que le recouvrement vertical. De plus, dans la plupart des cas, les différentes combinaisons de paramètres produisent les effets attendus, exceptés quelques cas où des interactions non-linéaires sont révélées. Les paramétrages qui dépendent de la phase des nuages ou de leur type (e.g. en fonction du déclenchement de la convection) sont prometteurs puisqu'ils sont plus physiquement réalistes (ils peuvent être basés sur des observations ou reliés aux processus nuageux simulés) et qu'ils produisent des effets radiatifs significatifs. Enfin, ces paramétrages permettront de relier les différents schémas de nuages d'un modèle de manière plus cohérente autant par les échelles sous-mailles que résolues.

ABSTRACT

Subgrid scale cloud process representation is still a dominant source of uncertainty in climate models. Cloud-radiation interactions are highly dependent on how the cloud subgrid-scale variability is represented in models. The McICA methodology has been proposed by Barker *et al.* (2002) and Pincus *et al.* (2003) to replace fixed hypotheses on unresolved cloud structure from the radiative transfer scheme by a stochastic representation of cloud subgrid-scale variability. This methodology offers a new flexibility to link subgrid-scale cloud parameters to observed cloud properties or to model variables. However, since models are often tuned to have the right top of atmosphere radiative budget, removing fixed cloud corrections may reveal hidden biases.

This work presents the McICA implementation in the GEMCLIM model with a detailed analysis of its modifications to the different radiative components and its consequences on the model atmospheric state. The fundamental dependencies of the subgrid scale cloud variability radiative effects are also addressed in parallel with possible parameterizations that can be used to link these processes with observational data or model variables.

The general framework is composed of global simulations with an horizontal grid mesh of 0.5° in order to sample all possible cloud states. The simulation timescales vary from 48 h to three years, mainly limited by the many simulations needed to study the different parameterizations. A few simulations are done up to three years to assess the model longer timescale responses to McICA. The radiative sensitivities of the McICA components and its different parameters are studied through a range of perspectives: from global and zonal mean sensitivities at surface and top of atmosphere, to zonal mean vertical profiles, to 0.5° by 0.5° maps. CERES-EBAF, CERES-SYN1deg and SSM/I satellite data sets are used to compare and validate the different simulations.

Results show that, compared to the homogeneous cloud treatment, the McICA methodology generally reduces the cloud albedo and emissivity due to its dominant effect of horizontal inhomogeneity. The change in vertical overlap generally produces opposite radiative effects but is far less important, hence it generally only attenuates the horizontal inhomogeneity radiative effects.

Given that a significant overestimation in liquid water path is established com-

pared to observations, the McICA implementation in the GEMCLIM model degrades the model performance in comparison to the CERES fluxes, both at surface and top of atmosphere, since this methodology is not conceived to compensate for simulated cloud biases. When compared to the GEMCLIM existing inhomogeneity corrections, the McICA horizontal inhomogeneity introduction is far less effective at reducing the cloud albedo and emissivity. The liquid water path overestimate is amplifying these results since the McICA effects are smaller at larger values while the existing corrections are greater. Experiments with McICA show small low cloud adjustments, visible on all timescales. The reduced cloud fraction and cloud water path are attenuating McICA radiative total signals, except for the LWU at TOA which are less sensitive to low clouds.

From a general point of view, the McICA horizontal inhomogeneity is shown to be cloud optical depth dependent with more effects at low values as suggested by the theory. Moreover, ice clouds exhibit opposite shortwave radiative effects with increased cloud albedo, a feature that was also explained by theory. The shortwave fluxes exhibit greater McICA sensitivities compared to the longwave fluxes. These differences can be explained by the more rapid saturation of cloud emissivity as a function of cloud water path compared to the variation of cloud albedo as a function of cloud water path. As a last point, the McICA effects are increasing with cloud fraction since more clouds can contribute to these modified fluxes.

This work has compared many parameterizations of different complexity, both for the horizontal inhomogeneity and the vertical overlap parameters. It shows that, in this model context, the horizontal inhomogeneity parameter has more potential radiative sensitivities than the vertical overlap parameter. Moreover, it shows that in most of the cases, the combined parameters are producing what is theoretically expected but a few cases produce unexpected non-linear results. Parameterizations that are function of cloud phases or cloud types (e.g. when convection is triggered) are promising since, on one side, they are more physically based (either linked to observations or modeled processes), and on the other side, they can produce significant radiative effects. These parameterizations will allow to link the different cloud schemes more coherently both by the sudgrid and the resolved scales.

INTRODUCTION

0.1 Clouds, climate and subgrid-scale variability

Currently, general circulation model (GCM) horizontal resolutions vary from ten to hundreds km, still far from the cloud resolving model resolutions. This includes climate models (global and regional) and numerical weather prediction models (NWP) of various complexities. Even though computational resources are increasing, the model spatiotemporal resolution growth is in part limited by growing demand for ensemble simulations to quantify uncertainty in model projection (e.g. with perturbed physics ensembles, Meehl *et al.*, 2007), to distinguish internal variability from climate change signal (Randall *et al.*, 2007) or to obtain climate features that are generally improved with multi-model ensembles compared to a single model simulation (Randall *et al.*, 2007; Hegerl *et al.*, 2007). Thus, parameterizations for subgrid-scale processes will still be needed for the foreseeable future.

An important part of the subgrid-scale parameterizations concerns clouds and their feedbacks on the climate system. Clouds are a great example of how processes of different scales are interacting. Figure 0.1 illustrates well how the cloud-controlling processes span from the microphysics scale to the planetary scale. Moreover, clouds are the link between the radiative balance of the earth and its hydrological cycle. It relates a part of the atmospheric chemistry to the formation of precipitation to the development and evolution of storm systems to the large-scale dynamics. Therefore, the simulation of clouds and their feedbacks implies

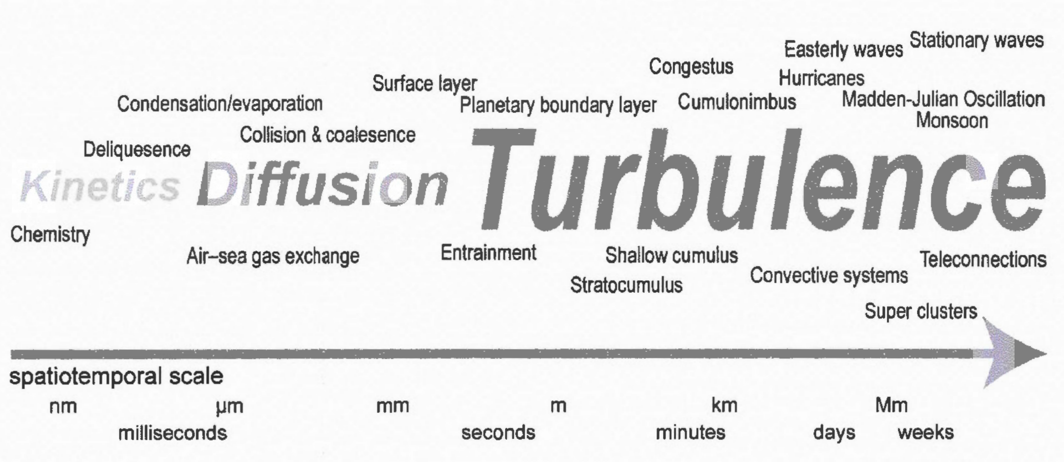

Figure 0.1 Schematic diagram of the cloud-related processes as a function of the spatiotemporal scale. The grey text indicates the categories of atmospheric dynamics from which processes emerge. From Siebesma *et al.* (2008), figure 12.1.

the simulation or the parameterization of the microphysical processes (e.g. condensation, evaporation, auto-conversion, Bergeron-Findeisen effect) jointly with the clouds macro-characteristics (e.g. cloud top temperature, vertical overlap) and the cloud radiative properties (albedo, emissivity, transmissivity).

Cloud process representation has been recognized as a dominant source of uncertainty in climate models since the 1970's (e.g. Arakawa, 1975; Charney *et al.*, 1979; Cess *et al.*, 1989; Randall *et al.*, 2003; Arakawa, 2004; Bony *et al.*, 2006; Randall *et al.*, 2007) and is still a primary source of spread in climate projections in the last Intergovernmental Panel on Climate Change assessment report (Boucher *et al.*, 2013).

As highlighted by Siebesma *et al.* (2008), cloud uncertainty in GCMs has different origins. For example, there is a lack of observations or knowledge of some fundamental cloud processes (particularly for ice- and mixed-phase clouds), as well as a deficiency of knowledge about how to represent sub-grid processes (that can be well understood at their native scale) at grid-box scale. This misrepresentation can affect not only the cloud itself but also the circulation and precipitation patterns, for example.

0.2 Cloud parameterizations in climate models

Cloud representation in climate models implies many parameterizations: from turbulence and microphysics to convection and radiative transfer. All these parameterizations are connected through different cloud processes and ideally, they should be as physically realistic as possible and work coherently, while they also need to be computationally efficient and numerically stable. However, in GCMs, these cloud processes and interactions were, and sometimes are still, over-simplified within the microphysics, convective and radiative transfer schemes (Randall *et al.*, 2003).

Parameters in these schemes are derived from observations or from physical or statistical relationships, both introducing their own weaknesses, as the former are usually limited to specific cases and include observational uncertainty (Isaac and Schmidt, 2008), the latter are mostly educated guesses since physical processes are not always well understood (Lopez, 2006). Moreover, GCMs are often tuned to balance the global energy budget at the top of the atmosphere and while achieving this goal, they cannot easily reproduce the observed clouds or precipitation (Pincus *et al.*, 2008). This underlines the fact that the radiative budget can be right for wrong reasons or from compensating biases (Tjernström *et al.*, 2008; Markovic *et al.*, 2008). Even with the recent advances in cloud parameterizations, the CMIP5 models are still presenting the 'too few, too bright' low-cloud problem (Nam *et al.*, 2012) where the cloud optical depth overestimation is compensating the cloud cover underestimation. In a changing climate, we cannot assume that these compensating errors will still hold and result in realistic projections.

0.3 The representation of cloud-radiation subgrid-scale variability in the GEMCLIM model

Since observations show that variability exists at all scales when considering clouds, the challenge of modeling boils down to taking into account this variability in all model schemes that are cloud related: in microphysical schemes, in convective schemes, in planetary boundary layer schemes as well as in radiative transfer schemes. In this work, the Monte Carlo Independent Column Approximation (McICA) methodology is used to relax fixed hypotheses on unresolved cloud structures from the radiative transfer solution and to replace them with a flexible stochastic representation of cloud subgrid-scale variability. On the bright side, such an approach gives much more flexibility to test observed cloud properties (e.g. vertical overlap, cloud water content distributions) and allows, for example, to potentially use different properties for different cloud types. On the down side, models are often tuned to give the right mean top of atmosphere radiative budget, which hides compensating biases. Correcting a specific bias could degrade the general model performance.

This thesis is based on the McICA implementation in the GEMCLIM model (Global Environmental Multi-scale Climate model, Hernández-Díaz *et al.*, 2013; Martynov *et al.*, 2013; Zadra *et al.*, 2008). The goal is to provide a detailed analysis of McICA impacts and possibilities that is beyond the model specificity. It is also to explain how the subgrid scale cloud variability radiative effects vary and on what conditions they are dependent. Furthermore, since the cloud subgrid scale variability representation in the radiative transfer boils down to two distinct components, the horizontal distribution of cloud water content and the vertical overlap, it is to understand how their radiative effects compare and interact, and how they can be more physically connected to model variables or processes.

The first chapter of this thesis presents the cloud-radiation known biases in GCMs and proposed solutions to account for the unresolved cloud variability. Chapter two details the McICA methodology theory, its applications and results in different models.

The following three chapters present the thesis main results. First, a detailed evaluation of the McICA implementation in the GEMCLIM model is performed using online and offline radiative transfer calculations. This analysis focuses on top of the atmosphere and surface fluxes as a function of cloud fraction and cloud water path to analyze the different cloud component contributions. Secondly, the model results are compared to satellite observations to put in perspective the McICA modifications to the radiative fluxes. Vertical profiles are also used to connect and understand top of atmosphere and surface effects. Finally, since McICA offers a new flexibility in cloud subgrid-scale parameterizations, the free parameters are tested and compared. Tests are also performed with different cloud optical depth scalings to put in perspective the different radiative sensitivities and to analyze the McICA methodology in different regimes.

CHAPTER I

HOW TO PARAMETERIZE SUBGRID-SCALE VARIABILITY FOR THE CLOUD-RADIATION INTERACTIONS

1.1 Common assumptions and known biases

Up until recently, the plane-parallel homogeneous clouds (PPH, Fouquart and Bonnell, 1980; Stephens, 1984) and the maximum-random cloud vertical overlap (MRO, Geleyn and Hollingsworth, 1979; Morcrette and Fouquart, 1986) were the most common assumptions used in the radiative transfer schemes of GCMs. The former assumes that within each model grid cell, cloud are homogeneous and occupy a fractional volume, whereas the later assumes a maximal vertical overlap between contiguous cloud fraction within each model column and a vertical random overlap otherwise.

From a theoretical point of view, one can refer to the cloud albedo relationship to cloud water path to understand how an homogeneous cloud representation would generally lead to an overestimation of its albedo. Figure 1.1 shows examples of this relationship. First the top panel, from Stephens and Webster (1981), shows how the cloud albedo and effective emittance increase with liquid water path (LWP) for a given zenith angle of 30°, based on a simple parameterization for water clouds. Secondly, the bottom panels, from Liou (2002), show a computed broadband solar albedo (0.2-5 μm) as a function of liquid or ice water path (LWP or IWP) and as a function of different effective radius or diameter. In this case, the albedo is obtained by a multiple scattering program for spherical droplets for water clouds and hexagonal ice crystals for ice clouds.

Both examples exhibit a fast increasing albedo at low LWP followed by a saturation at higher LWP values. As the relationship is non-linear, a mean value of LWP, for example 60 g/m^2 would be associated with an albedo value of ≈ 0.45 (for a 16 μm effective radius, represented by the full blue line in figure 1.1), but a constant distribution of liquid water paths with the same mean value and ranging from 20 to 100 g/m^2 would lead to a distribution of corresponding albedos (represented by the dashed blue arrows) with a different and generally lower mean albedo, in this case around 0.4. The former case represents the homogeneous cloud assumption, since the cloud albedo is calculated with the mean LWP value, while the later case represents the inhomogeneous assumption, since the mean cloud albedo is calculated from the distribution of LWP corresponding albedos.

This misfit between homogeneous and inhomogeneous assumptions should be increasing as the relationship is steeper. In this regard, at higher LWP values where the slope is lower, the difference between an homogeneous and inhomogeneous cloud albedo should be smaller (represented by the orange arrows). Similarly, the cloud emissivity varying slower than cloud albedo as a function of LWP, the underestimation due to homogeneous assumption should be reduced. Furthermore, since the ice cloud solar albedo relationship at low IWP values is concave rather than convex compared to the liquid clouds relationship at high LWP values, the inhomogeneous cloud albedo should be larger than the homogeneous cloud albedo (represented by the red arrows). In summary, from these simple theoretical considerations, it is expected that neglecting inhomogeneity results in overestimating albedo of liquid clouds while it underestimates albedo of ice clouds.

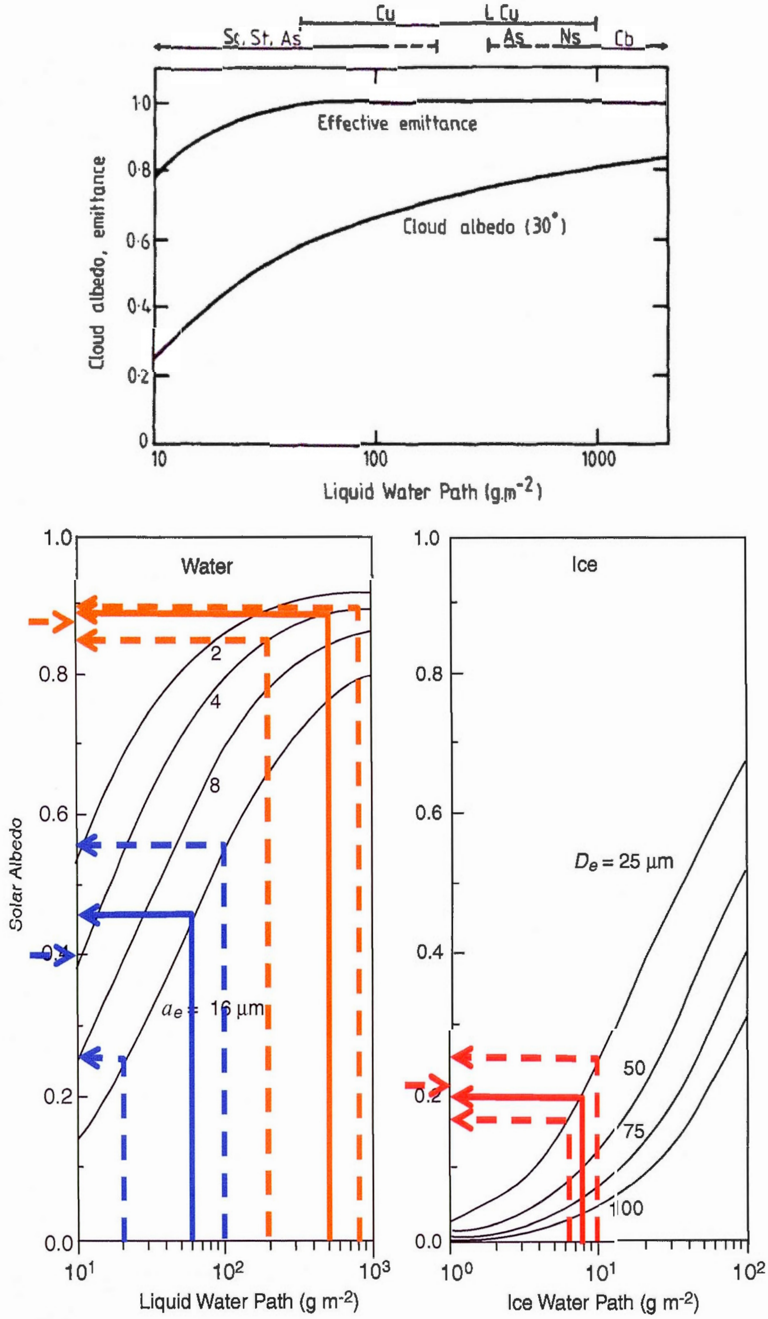

Figure 1.1 Top panel: cloud albedo and cloud effective emittance as a function of LWP for a zenith angle of 30°, from Stephens and Webster (1981), figure 1a. Bottom panel: Solar albedo of water and ice clouds as a function of liquid or ice water path for different mean effective radius or diameter, from Liou (2002), figure 8.16.

As the previous explanation is based on many assumptions, such as cloud droplet distributions or zenith angles, more complete simulations have been performed to verify these preliminary conclusions. Barker *et al.* (1998), using a 3D Monte Carlo photon transport algorithm, have shown that PPH clouds generally transmit less and reflect more radiation compared to 3D clouds. However, for low sun, the opposite is seen since PPH clouds intercept less photons than 3D clouds (as there is no cloud side effects). It was also shown that MRO systematically underestimates vertically projected cloud fraction (Räisänen and Barker (2004)) and therefore, it relies on homogeneous clouds to balance the reflectivity underestimate (Barker *et al.* (1998), Barker *et al.* (2003)).

To compensate for these known biases, simple tuning parameters were used as correcting factors with these assumptions in GCMs. For example, in the radiative transfer scheme operational in GEM (Global Environmental Multi-scale model, Zadra *et al.*, 2008; Côté *et al.*, 1998) up until June 2009, the cloud optical thickness was tuned by multiplying it by a factor of 0.3, whereas for the NWP model of the European Centre for Medium-Range Weather Forecasts (ECMWF), it was multiplied by 0.7 until version 32R2 (Tiedtke, 1996; Morcrette *et al.*, 2008).

1.2 Proposed solutions to account for unresolved clouds variability

Common cloud radiation parameterizations, such as PPH clouds and MRO, often combined with tuning parameters are generally embedded in the radiative transfer equations. This makes it quite complex and time consuming to test different assumptions and parameters. Furthermore, it is not clear to which extent these parameters are adaptable to increasing resolution, or to which extent they can be relaxed or adapted to GCMs that are growing in complexity.

To remedy this situation, different solutions were proposed around the same period. To name only a few, Li and Barker (2002) and Li *et al.* (2005) proposed an optical-depth adjustment algorithm to implement in GCM radiative transfer scheme to account for horizontal inhomogeneous clouds both for the infrared and solar spectra. On the other hand, Barker *et al.* (2002) and Pincus *et al.* (2003) proposed a radical alternative to calculate mean-column radiative fluxes: the Monte Carlo independent column approximation (McICA) based on a stochastic version of the independent column approximation (ICA, Stephens *et al.*, 1991) to be used with a subgrid-scale stochastic cloud generator (SCG).

From another perspective, Grabowski and Smolarkiewicz (1999) introduced the super-parameterized GCM, where a cloud resolving model is embedded in each GCM grid cell. As the super-parameterized GCM is 10^2 to 10^3 times more expensive and cannot be widely used to this day, this approach won't be presented further in this work. As the first solution is used in our control model for this study, a brief description will follow before the main subject of McICA methodology is presented.

The work of Li and Barker (2002) demonstrated that infrared radiative impacts of cloud subgrid-scale variability can be well accounted when cloud optical depth horizontal variability is approximated by a gamma distribution that respects the model grid mean value ($\bar{\tau}$). The complexity of this calculation is based on the fact that radiative interactions between two model levels depend on the horizontal cloud subgrid-scale variability integrated over the two levels. This variability, defined as $\nu = (\bar{\tau}/\sigma)^2$ (Barker *et al.*, 1996), where σ is the standard deviation of τ, has to be determined as an integrated value for continuous cloud layers. In this study, ν for individual cloud layers generated by a cloud resolving model, was varying between 0.8 and 1.2, whereas for whole cloud blocks (defined by consecutive vertical cloud layers in a GCM column), ν was always found to be lower than for individual layer due to vertical overlap conditions. Therefore, the authors have chosen to set ν to the minimum value found in the cloud block and have tested specific values like 0.5, 1 and 2.

Previous results from Barker *et al.* (1996), which derived ν values from different Landsat scenes, showed values ranging from 0.1 for scattered cumuli to as high as 22.5 for overcast stratocumuli with reduced values when clear-sky contributions were included. Furthermore, Oreopoulos and Barker (1999), based on 3D generated cloud and Monte Carlo photon transport algorithm, proposed a first order parameterization for ν as a function of cloud fraction (CF): $\nu \approx 4$ when CF=1 decreasing to $\nu \approx 1$ when CF=0.9 and hold constant to 1 for CF <0.9.

As the use of a gamma distribution is not as simple for the solar radiative transfer due to scattering, Li *et al.* (2005) put forward an optical-depth adjustment algorithm that can be incorporated within the cloud overlap assumption. When using a gamma-function-weighted transmission (as proposed by Li and Barker, 2002, for the infrared radiation) for the solar spectrum, the scattering is neglected and the mean optical depth for inhomogeneous cloud leads to an underestimation of transmission. Consequently, for a given cloud block, the cloud optical depth is reduced following an empirical scheme. For a layer k in a cloud block, the adjusted cloud optical depth τ_k^* becomes

$$\begin{aligned} \tau_k^* &= \frac{\tau_k}{1 + 0.185(2 - \mu_0)^{0.4} f_\nu f_\tau} \\ f_\nu &= \frac{1}{1 + 5.68\nu^{1.4}} \\ f_\tau &= \tau_k + 9.2\sqrt{\sum_{j=i}^{k} \tau_j} \end{aligned} \tag{1.1}$$

where ν is also set to the minimum value for every layer within the cloud block and μ_0 is the cosine of the solar zenith angle. The summation is done from the cloud top to the bottom and the layer optical depth is reduced increasingly going down since the error in direct transmission is increasing with the mean optical depth. Figure 1.2 presents an example of the adjusted cloud optical depth behavior as a function of cloud optical depth. As can be seen, the adjusted cloud optical depth is reduced increasingly with lower ν (since inhomogeneity is greater at lower ν), but also with higher τ or more cloud layers.

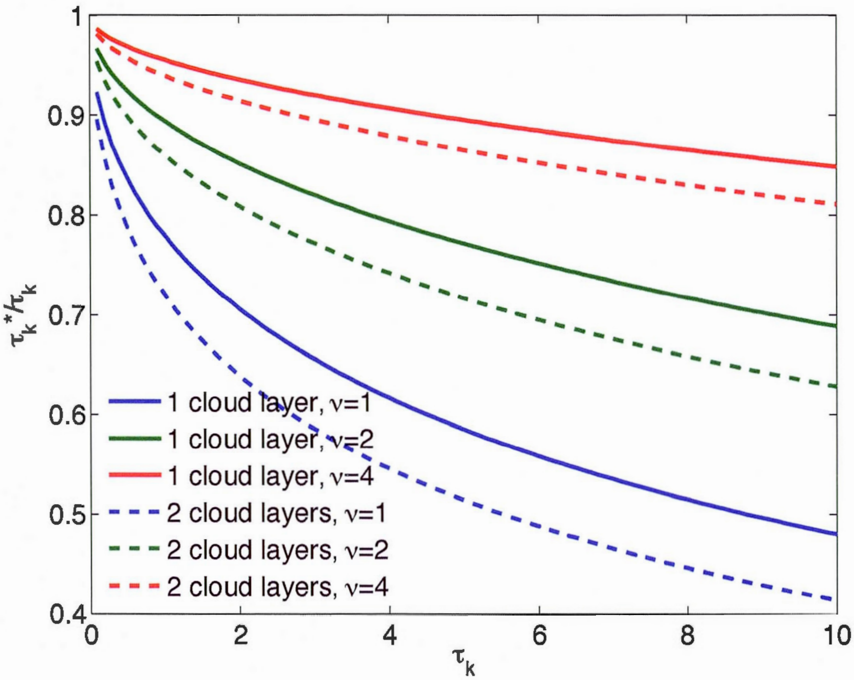

Figure 1.2 Example of the ratio of adjusted cloud optical depth (τ_k^*/τ_k) as a function of cloud optical depth (τ_k) for different ν values and for one or two cloud layers, with the 2 layers having the same cloud optical depth. μ_0 is set to 1.

CHAPTER II

A STOCHASTIC TREATMENT FOR CLOUD SUBGRID-SCALE VARIABILITY: THE MCICA METHODOLOGY

The basic principle of the McICA methodology is to generate and treat the subgrid-scale cloud structure stochastically separately from the radiative transfer (RT) calculations. This implies that the description of the subgrid-scale cloud structure (both the horizontal cloud water distribution and the vertical overlap) must be extracted from the core radiation calculation. Within McICA, a stochastic cloud generator randomly generates cloudy subcolumns of the possible cloud fields respecting the grid mean fields provided by the model cloud schemes (Räisänen and Barker, 2004). The subcolumns are then randomly selected for the RT calculations. These steps are performed without further cloud correction since the subgrid-scale information has already been taken into account. Hence, by its nature, McICA provides unbiased radiative fluxes and heating rates (with respect to ICA) at the cost of random errors. However, the cloud information (both at the model scale and the subgrid-scale) can be biased, depending on the multiple cloud schemes and parameterizations used in a model. These possible biases will be transferred to the McICA methodology and the RT calculations. This methodology further allows a simplification of the RT scheme and a highly flexible description of the subgrid-scale cloud structure within the cloud generator

(Pincus *et al.*, 2003).

This section reviews the basic assumptions behind the McICA methodology, the methodology in itself, the stochastic cloud generator and a few alternatives to reduce noise sampling. An overview of evaluations done with different GCMs for different spatiotemporal resolutions and different versions of the McICA methodology is presented with the latest developments of cloud parameterizations. It concludes with what is left to evaluate in our model and in general for the McICA community.

2.1 The background hypotheses in the radiative transfer scheme

At scales resolved by GCMs, 3D horizontal transport of photons across column boundaries is generally ignored. This greatly simplifies the radiative calculations for a minimal cost in accuracy. This method is the independent column approximation (ICA) and is defined as:

$$\langle F\rangle \approx \langle F^{ICA}\rangle = \int S(\lambda)\left\{\iint F_{1D}(x,y,\lambda)dxdy\right\}d\lambda \qquad (2.1)$$

where F_{1D} is flux for a wavelength λ at a point (x, y) computed by a 1D radiative transfer algorithm and $S(\lambda)$ is a spectral weighting function for each spectral interval $d\lambda$ that depends on the incoming spectral flux.

ICA has been shown to perform well for different cloud regimes (Chambers *et al.*, 1997; Fu *et al.*, 2000; Barker *et al.*, 1999) and for resolutions as high as those used in cloud resolving models (CRMs, O'Hirok and Gautier, 2005). Barker *et al.* (1998) have shown that even for towering 3D clouds, the ICA approximation produced similar solar heating than 3D calculations.

To numerically solve this radiative transfer equation, the spectral intervals need to be transformed in discrete sums with weights $w(\lambda_k)$ (that could be unequal) as follow:

$$\langle F^{ICA} \rangle = \sum_{k=1}^{K} w(\lambda_k) S(\lambda_k) F_{1D}(\lambda_k) \tag{2.2}$$

The discrete summation can be done over the the quasi-monochromatic intervals k as defined by the correlated-k distribution (CKD, Lacis and Oinas, 1991; Fu and Liou, 1992) which is based on the absorption coefficients (k). This method is commonly used in climate models since it has been demonstrated to be efficient and accurate (Li and Barker, 2005) and it will be used in this study. Moreover, this equation can be separated between clear-sky and cloudy-sky areas with CF representing the vertically projected cloud fraction and $p(s)$ the possible cloud states:

$$\begin{aligned} \langle F^{ICA} \rangle &= (1 - CF) \sum_{k=1}^{K} w(\lambda_k) S(\lambda_k) F_{1D}^{clr}(\lambda_k) \\ &+ CF \sum_{k=1}^{K} w(\lambda_k) S(\lambda_k) \sum_{j=1}^{J} p(s_j) F_{1D}^{cld}(s_j, \lambda_k) \end{aligned} \tag{2.3}$$

2.2 The stochastic cloud generator

Barker *et al.* (2002) and Pincus *et al.* (2003) introduced the McICA methodology to produce unbiased radiative budgets within GCMs and to extricate the subgrid-scale cloud structure description from the RT scheme. The motivation is that with limited and imprecise information available to work with (on cloud subgrid-scale structure), there is an infinite number of compatible underlying 3D fields and corresponding domain-averaged radiative flux profiles. Consequently, an algorithm is needed to generate possible cloud states from the GCM variables.

The stochastic cloud generator (SCG) introduced by Räisänen and Barker (2004) (hereafter RB2004) creates subcolumn cloud fields based on the model layer cloud fraction and cloud condensates, and probability distributions that describe the horizontal variation of cloud water. The first assumption behind the generator is that horizontal correlations in unresolved cloud structure are unimportant for computation of radiative fluxes in GCMs. This implies that subcolumns are independent and that the ICA holds.

The SCG uses variables from the GCM: the number of vertical layers (Z) with their cloud fraction (C_z) and total water content (w_z). It generates J subcolumns in which each vertical layer k is either clear or filled with cloud (c_{jz} =0 or 1):

$$c_{jz} = \begin{cases} 0 & x_{jz} \leq 1 - C_z \\ 1 & x_{jz} > 1 - C_z \end{cases} \qquad \forall z : C_z > 0 \tag{2.4}$$

For cloudy cells (c_{jz} =1), the condensate amount w_{jz} is distributed following y_{jz}, the cumulative frequency distribution of w:

$$\begin{aligned} y_{jz} &= \textstyle\sum_{i=1}^{j} p_z(w)dw \\ w_{jz} &= y_{jz} w_z \end{aligned} \qquad \forall z : c_{jz} = 1 \tag{2.5}$$

The form of the normalized probability density function $p_z(w)$ can be prescribed following different distributions.

Based on Hogan and Illingworth (2000) and Bergman and Rasch (2002), the authors introduce a generalized vertical overlap in the SCG as it reproduces better vertically integrated cloud fraction compared to MRO, and since the MRO was used to partly compensate for homogeneous clouds. Hence, the SCG vertically distributes the cloud with a linear combination of maximum and random overlap that is a function of decorrelation lengths L_{cf} and L_{cw} for cloud fraction and cloud water content respectively following:

$$\begin{aligned} C_{z1,z2} &= \alpha * max(C_{z1}, C_{z2}) + (1-\alpha)(C_{z1} + C_{z2} - C_{z1}C_{z2}) \\ \alpha &= exp\Big(- \int_{z1}^{z2} \frac{dz}{L_{cf}(z)} \Big) \end{aligned} \tag{2.6}$$

where $C_{z1,z2}$ is the vertically projected cloud fraction for two layers ($z1$ and $z2$), L is the decorrelation length for cloud fraction or cloud water and α is the cloud overlap parameter. These equations imply some assumptions. First, the linear combination of maximum and random overlap (equation 2.6) implies no anti-correlation: $\alpha = [0:1]$. Second, non-overlapping and overlapping portions of cloud have the same $p_z(w)$ distribution; any potential conditionality between cloud geometry and distributions of w are neglected. Third, the ratio of liquid to solid condensate amounts is horizontally invariant.

RB2004 conclude that with these three assumptions, when reproducing cloud profiles from a cloud-resolving model, the SCG has a smaller underestimate of cloud fraction combined with a smaller overestimate of cloud water path compared to the MRO assumption. RMSEs for radiative fluxes and heating rates are also reduced by $\approx 60\%$ compared to MRO.

2.3 The McICA methodology

Computing equation 2.2 in a GCM is nearly impossible, as it would require enormous computational resources (typical numbers of k intervals in GCMs are of the order of 50-100 and with only 10 possible cloud states, it would require 500-1000 radiative calculations per model column). As an alternative to a deterministic solution, the Monte Carlo methodology randomly samples possible inputs and calculates a deterministic solution of these inputs. As the number of samples ($M = k * J$) is growing, the methodology error converges in $1/\sqrt{M}$.

The Monte Carlo methodology applied to ICA consists of randomly selecting a cloud state (a subcolumn generated by the SCG) for each interval k (as defined in equation 2.2) used in the radiative transfer scheme to calculate the mean-column radiative fluxes $\langle F^{McICA}\rangle$. As the clear-sky radiation is generally calculated separately in models for diagnostic purposes, the random selection is concentrated on cloudy subcolumns j as shown by the following equation:

$$\langle F^{McICA} \rangle = (1 - CF) \sum_{k=1}^{K} F_k^{clr} + CF \sum_{k=1}^{K} F_{j_k,k}^{cld} \tag{2.7}$$

If a single cloud state exists in the column, then the McICA is equivalent to ICA. The methodology requires the same integration time as a broadband calculation but introduces a sampling error that is random, unbiased and uncorrelated (e. g. correlation of 1 to the spatiotemporal resolution of the radiative transfer scheme and correlation of 0 for longer/larger resolutions).

The authors suggest that this inner-scale unbiased error may not be a problem for a GCM as it is incapable of generating organized structures that can significantly affect the simulation. Furthermore, Pincus *et al.* (2003) suggest that, because of the relatively long time scale impact of radiation on atmosphere and ocean, it is better to solve the right problem approximately with the McICA methodology than the wrong problem exactly.

2.4 McICA: proof of concept

McICA usefulness depends on its sampling errors having no statistically significant impact on a simulation and being considered beneath or close to the system's intrinsic noise horizon. Moreover, its intrinsic goal is to allow the implementation of different flexible cloud parameterizations that could improve radiative transfer simulations and remove systematic biases deriving from the vertical overlap assumptions or fixed inhomogeneous corrections. Most studies have focused on the former aspect of the noise impact and few have looked at the direct improvement of the methodology in simulated cloud and radiation biases. These results are summarized in the next two sections followed by a section on the parameterization sensitivity studies.

McICA has been tested in at least five global climate models: the Finnish Meteorological Institute ECHAM5 model (Räisänen *et al.*, 2007, 2008), the National Center for Atmospheric Research's Community Atmosphere Model (CAM Räisänen *et al.*, 2005; Zhang *et al.*, 2014), the Geophysical Fluid Dynamics Laboratory's Atmosphere Model version 2 (Pincus *et al.*, 2006), the Environment Canada–Canadian Centre for Climate Modelling and Analysis model (Barker *et al.*, 2008), the GEOS-5 Atmospheric General Circulation Model (Oreopoulos *et al.*, 2012a). It has been also tested in three NWP models: the European Centre for Medium-Range Weather Forecasts model (ECMWF, Morcrette *et al.*, 2008), the UK Met Office Unified Model (MetUM Hill *et al.*, 2011b) and the GEM model (Barker *et al.*, 2008)). For the ECMWF model, McICA has been used operationally since 2007. Different time periods (10 to 14 day forecasts, 12 to 36 months, 10, 17 and 70 years) were tested with atmospheric models and one study was done with an interactive mixed-layer ocean model (Räisänen *et al.*, 2008).

McICA can be implemented in many different ways, based on how many subcolumns are produced in the cloud generator and how many are selected randomly for the radiative transfer calculations. The simplest version is called the 1COL, which maximizes the noise level by selecting only one subcolumn from the cloud generator for all spectral interval calculations at every timestep. The CLDS version is the original version shown in equation 2.7 where the random selection is done only with cloudy subcolumns and clear-sky fluxes are computed separately. At the opposite, the most complete version (and expensive in computer time) is the REF, which minimizes the random noise by generating many more (over 1000) subcolumns in the generator and using almost all these in the radiative calculations.

Räisänen and Barker (2004) suggest that at some level of significance, overly large random errors would be undesirable in a GCM simulation. Therefore, they introduced techniques to reduce the magnitude of these errors in McICA. One of these techniques is the optimal spectral sampling (hereafter SPEC), which consists in repeated sampling and averaging for the CKD terms with large cloud radiative effects (CREs) to maximize the reduction of the noise introduced and minimize the additional cost of cloudy-sky radiation calculations (as for CLDS, clear-sky fluxes are computed separately). Therefore, additional sampling (the summation over j) is done for the k points in the cumulative probability space (CPS), with the largest CREs:

$$\langle F^{ICA} \rangle = (1 - CF) \sum_{k=1}^{K} F_{j,k}^{clr} + CF \sum_{k=1}^{K} \left(\frac{1}{J_k} \sum_{j=1}^{J_k} F_{j_k,k}^{cld} \right) \tag{2.8}$$

where J_k represents the number of subcolumns used for the calculation for each k intervals. It will be 1 for the less-contributing intervals and could be as high as 10 for the most-contributing intervals. To determine the different J_k, fractional contributions from each point k to SW and LW CREs are determined for net fluxes at surface and for heating rates. This evaluation can be done once for a specific GCM.

The most utilized and logically designed methods for climate modeling (best ratio between minimum random noise and computational time) are CLDS and SPEC. SPEC uses generally 50% more cloudy subcolumns in its calculation than CLDS specifically for spectral intervals that contribute more to the CREs (equation 2.8). As an example, the ECMWF model uses the CLDS version.

Different studies show that the impact of McICA noise introduction is model dependent. The CLDS version shows a small but statistically significant impact principally on global-mean low cloud fraction at the 95 to 99 % confidence level. These differences from the reference simulation tend to cluster over tropical oceans (CAM and ECHAM5, Räisänen *et al.*, 2005, 2007). On the other hand, SPEC shows no statistically significant difference at the 95 % confidence level for most models (Räisänen *et al.*, 2005; Barker *et al.*, 2008) for global mean values of many variables such as precipitation, cloud radiative forcing, 2 m temperature, as well as for their annual mean horizontal variability. For the CAM model, Räisänen *et al.* (2005) estimated that the model noise horizon was between the noise levels introduced by the CLDS and the SPEC version of McICA. Hill *et al.* (2011b) showed that for a low resolution NWP simulation, the CLDS version produced worse forecast of near-surface temperature than the PPH-MRO assumptions while the SPEC version they proposed, produced better results.

2.5 Results in climate and NWP models

When looking at the improvements on clouds and radiative variables with the McICA implementation, results varied but all authors agree on the positive simplification and new flexibility that the methodology brings to the radiative transfer scheme.

At one end of the spectra, Morcrette *et al.* (2008) implemented the McICA methodology in parallel with a new radiative transfer scheme, new cloud and surface properties in the ECWMF model. This new package was shown to benefit most variables and particularly the cloud-radiation interactions in the Tropics. The authors further specify that these improvements are only visible when all modifications are applied together but are mainly due to the McICA methodology. However, other studies have shown that McICA alone has not led to direct improvement in simulated climate (e.g. Pincus *et al.*, 2006).

At the other end of the spectra, for the ECHAM5 and CAM models, McICA-CLDS version have shown a small reduction in low cloud fraction, especially over tropical oceans (Räisänen *et al.*, 2005, 2007). Further investigations by Räisänen *et al.* (2008) have shown that, for the ECHAM5 model, this bias is originating from a non-linear response of the autoconversion rate to McICA noise in heating rates and is further amplified by radiative feedbacks. When coupled to an interactive mixed-layer ocean, the model drifts to a warmer climate. The authors suggest putting emphasis on radiative-heating rates with a noise reduction technique such as the SPEC version (see equation 2.8).

Räisänen and Järvinen (2010) tested the introduction of the Tompkins cloud scheme in the ECHAM5 model as well as the transmission of the subgrid-scale information of that scheme into the McICA calculations (again with the CLDS version). As the model was using a cloud optical depth scaling before the McICA implementation, tuning parameters were modified to counteract the shift produced by McICA and the cloud scheme, as they increased the SWU at TOA. The authors highlight that the use of McICA strengthen the negative short-wave cloud radiative effect without noticeable change in cloud cover. An important conclusion was that even if, for current climate, all model versions were performing similarly, for a climate change projections, the McICA version showed a response in global warming 1.5 time stronger (in global mean 2 m temperature) than the control model, mainly due to cloud feedbacks.

2.6 Specifying the free parameters in the SCG

With the use of the McICA method, parameterization paradigm switches from cloud overlap or homogeneous plane parallel cloud assumptions embedded in previous radiative schemes to the cloud stochastic generator decorrelation lengths (L_{cf} and L_{cw}) and horizontal variability of cloud condensate ($f_w = \sigma_w/\bar{w}$, where f_w is the relative standard deviation of cloud water content). Since the McICA and SCG introduction, some studies have, first, derived the SCG parameters from observations and second, assessed model sensitivities to these parameters. Following is a brief recapitulation of these studies in which this thesis is embedded.

Zhang *et al.* (2013) provided a good overview of this modeling problematic using the Cloud-Aerosol-Radiation ensemble modeling system to evaluate the individual contribution of cloud optical properties, cloud horizontal inhomogeneity, cloud vertical overlap, and gas absorptions to the spread among the major radiation schemes in terms of cloud radiative effects (CREs). They demonstrated that cloud subgrid-scale structures (overlap and horizontal inhomogeneity) were responsible for 40-75% of model spread. More specifically, different cloud vertical overlap assumptions were critical for SW components and TOA LW CREs while the horizontal inhomogeneity assumptions were key factors for SFC LW components.

Also from a modeling perspective, Barker and Räisänen (2005) presented a sensitivity study on the three SCG parameters. As a diagnostic tool, they used the stochastic cloud generator initialized by a CRM's data together with the McICA methodology. Estimates of radiative sensitivities and uncertainties with respect to one of the three studied variables were computed diagnostically by varying the variables ($\delta L_{cf} = \pm\, 0.5$ km, $\delta L_{cw} = \pm\, 0.25$ km and $\delta f_w = \pm\, 0.1$, where $f = 1/\sqrt{\nu}$) and using the two others directly from the CRM dataset. The results showed that global-mean radiative sensitivities in TOA and surface SW flux for L_{cf} and f_w were of similar amplitude whereas for L_{cw} they were generally five times smaller. Generally, the radiative sensitivities were much larger in the SW than in the LW. The authors also compared these parameter sensitivities to parameterizations of effective radius (r_{eff}) with a $\pm 10\%$ variation and found that sensitivities from f_w and r_{eff} were well correlated as they both operate on horizontal layers. r_{eff} sensitivities were larger than f_w for high latitudes but of the same order of magnitude in the Tropics. The authors emphasized that cloud overlap and horizontal variability parameterizations should be studied as much as cloud microphysical structures.

From the observations point of view, Barker (2008b) used two months of the cloud-mask product derived from CloudSat and Cloud-Aerosol Lidar and Infrared Pathfinder Satellite Observation (CALIPSO, Stephens *et al.*, 2002; Winker *et al.*, 2003) data to derive an effective L_{cf} to be used in GCMs with the SCG as the majority of previous studies used decorrelation lengths L_{cf} and L_{cw} of 2 km and 1 km respectively (based on Räisänen *et al.*, 2005). The median values of L_{cf} were shown to be weakly dependent on the satellite cross-section length. On the global scale (for satellite cross section between 100 and 1000 km), the median values of L_{cf} tended to 0 km for very small CF (vertically projected cloud fraction), increased linearly to 2-3 km for CF around 0.7 and decreased to 1.5 km when CF tended to 1. Looking at the spatial and temporal variability of L_{cf}, maxima appeared in polar regions during their respective winters and in the northern tropics during summer. As precipitation was present in the cloud-mask satellite data, the author applied a rough precipitation screening and global median values of L_{cf} were reduced from $\approx$ 2 km to $\approx$ 1.5 km.

In a second article, Barker (2008a) estimated the impact of a constant L_{cf} value of 2 km with off-line radiation calculations. Tests were done for homogeneous and inhomogeneous clouds. Compared to L_{cf} derived from observations in the previous article, the use of a constant L_{cf} showed that zonal-mean biases and random errors for TOA SW and LW CRE increase only slightly and sometimes even decrease (due to random error cancellations). However, the largest errors ($\approx$ 15 %) are in the tropics for the SW heating rates at altitude between 10 and 15 km because of an overestimate of CF, corresponding to too much cloud top exposed to direct solar radiation.

In a two part article, Shonk *et al.* (2010) and Shonk and Hogan (2010) derived and evaluated a relative standard deviation of water content ($f_w = \sigma_w/\bar{w} = 1/\sqrt{\nu}$) and a decorrelation length L_{cf} to be used in the Tripleclouds scheme of Shonk and Hogan (2008). For the f_w values, it was derived from a number of studies (based both on optical depth and water content observations) and the authors did not find any consensus on how it varied with cloud type or grid size, for example. They found a general value of 0.75 ± 0.17 (for a corresponding ν of 1.8 with a range between 1.2 and 3.0). For the decorrelation length, they derived a linear fit as a function of latitude based on the studies of Hogan and Illingworth (2000) and Mace and Benson-Troth (2002) to be used in an exponential-random overlap parameterization (as the one in the SCG). The L_{cf} values vary from 0.4 km at the poles to 2.9 km at the Equator. When these parameters were tested in radiative transfer calculations, the largest radiative effects were noted in marine stratocumulus areas for the f_w parameters and in deep tropical convection areas for the L_{cf} parameters for individual contributions of SW and LW effects. The sensitivity was assessed with values of f_w of 0.57 and 0.93 and L_{cf} ranges of $[0.46 - 2.5]$km and $[0.77 - 3.5]$km. The uncertainty on top of atmosphere radiative budget was found to be of the order of $\pm 60\%$ for the f_w while for the L_{cf}, it was much smaller.

Hill *et al.* (2011a) derived a relative standard deviation (f_w) parameterization for ice clouds based on CloudSat and MODIS data, function of horizontal scale, thickness layer and cloud fraction. Results showed that f_w is generally between 0.2 to 0.8 (wich corresponds to a range of 1.6 to 25 for ν). It increases with the horizontal scale, the thickness layer, and with small cloud fraction but becomes smaller for overcast conditions.

Boutle *et al.* (2013) derived a similar parameterization to that of Hill *et al.* (2011a), although for liquid clouds. It is based on aircraft in situ measurements, land-based radars and lidars, and CloudSat data. It is function only of horizontal scale and cloud fraction. As for the ice, f_w increases with the horizontal scale and cloud fraction, but drops for overcast conditions. This parameterization produces f_w values around 0.75 for grid box sizes in the range 50-150 km, as it was suggested by Shonk and Hogan (2008).

Oreopoulos *et al.* (2012a) introduced a spatiotemporal fit for the decorrelation lengths based on CloudSat and CALIPSO measurements. The parameterization is a Gaussian fit with values ranging from 1.5 km at the poles to 3.5 km around the Equator (for the L_{cf}, while L_{cw} vary from 0.75 km to 1.5 km) with the maximum following the intertropical convergence zone during the year. Furthermore, for two model versions (with different convective assumptions and different stratiform cloud parameterizations), the authors tested the effects of cloud overlap and horizontal inhomogeneity. They found that the overlap parameterizations was cloud-scheme dependent, whereas the horizontal inhomogeneity effects were more consistent across cloud schemes.

Finally, Zhang *et al.* (2014) introduced two distinct L_{cf}, one for the deep convective clouds (set to 10 km) and one for the other clouds (set to 1 km). These decorrelation lengths are weighted by their respective cloud fraction and the sum is applied on the model grid point. It produces a global mean L_{cf} of 1.7 km, with zonal mean maximum between 3 and 3.5 km in the Tropics depending on the season, similarly to Oreopoulos *et al.* (2012a). Compared to constant L_{cf}, they found local differences >20 W/m^2 for the SW CRE and >10 W/m^2 for the LW CRE in regions of frequent convection. However, the horizontal inhomogeneity introduction produced the most striking effects, both globally and zonally, with maximum of 1 K differences for near-surface temperature at the mid-latitudes over 10 years of simulations.

These studies show that the SCG parameters and their related radiative sensitivities are still being assessed. On one hand, parameter radiative sensitivities are not well understood and seem to be model dependent and even cloud scheme dependent. One the other hand, results from observations show that variability can come from physical processes that can be linked to cloud phase or cloud regime, or from the model representation in itself, such as horizontal and vertical resolutions. To this day, it is still not clear to which extent complex physical parameterizations would improve model radiative results as these parameters are intimately associated with cloud representation through convective, microphysics and stratiform cloud schemes. However, the SCG offers a framework to test extensively these open questions.

2.7 McICA in the GEMCLIM model: a detailed analysis and beyond

As the McICA methodology has shown to be model or even cloud scheme dependent, a detailed evaluation of its implementation in the GEMCLIM model needs to be done. Since the McICA implementation implies the removal of inhomogeneity corrections that were implemented in the RT scheme, four components must be analyzed and disentangled in their radiative effects, if possible: the inhomogeneity corrections removal, the McICA horizontal inhomogeneity introduction, the McICA vertical overlap assumption and the model adjustment or response to this new methodology.

Once the McICA methodology implementation in the GEMCLIM model is understood, validation against global observation data sets becomes important to understand how the model reproduces the cloud-radiation interactions. From there, radiative biases can be explained, put in context, and it will show how the McICA methodology affects these results.

Finally, to provide a more complete overview of the McICA methodology radiative sensitivities, the SCG parameters must be assessed with all the flexibility it offers, in a variety of conditions, and moreover, they must be compared to other radiative parameterizations like the effective radius. Furthermore, one cannot ignore the possible non-linear effects when combining changes in different parameters, these effects must at least be studied, if not completely understood.

CHAPTER III

COMPARING TWO APPROACHES TO ACCOUNT FOR CLOUD SUBGRID-SCALE VARIABILITY IN THE GEMCLIM MODEL

3.1 Introduction

The first part of this thesis is an analysis of the replacement of fixed inhomogeneity corrections and maximum-random overlap by the McICA methodology in the GEMCLIM model, in global mode. As explained in the previous section, the McICA implementation effects have four different contributions: the inhomogeneity correction removal, the McICA horizontal inhomogeneity introduction, the McICA vertical overlap assumption and the model adjustment or response to this new methodology. To analyze separately these contributions, different simulations, in which the first three components are implemented one at the time, are presented. Furthermore, offline (or diagnostic) McICA fluxes are compared with online McICA fluxes to isolate McICA direct radiative effects from the general model signals, which include possible atmospheric adjustments to McICA methodology as well as model internal variability.

The present analysis is concentrated over different axes to try to detail the McICA radiative effects. The analysis is performed as a function of cloud variables to illustrate the intrinsic relationships between McICA subgrid-scale parameterizations and their radiative effects. Besides, the time scale evolution of the different signals is presented to see how instantaneous signals contribute to the mean seasonal signals. Finally, analysis is also performed as a function of cloud phases as liquid and ice clouds interact differently with radiation.

3.2 Methodology

3.2.1 Model description and configuration

The GEM model (Global Environmental Multiscale model) used in this study was developed for NWP applications (Côté *et al.*, 1998) at Environment Canada and is now used at ESCER Centre for regional climate studies under the name CRCM5 (Canadian Regional Climate Model version 5, Hernández-Díaz *et al.*, 2013; Martynov *et al.*, 2013). It can be used in global uniform or stretched grid as well as limited area mode. The particular setup of GEM used in this work, which is similar but not identical to the operational NWP versions, is referred to as GEMCLIM in this thesis.

GEM employs a two-time-level semi-Langragian, semi-implicit advection scheme. Surface fluxes of heat, moisture and momentum are calculated over four surface sub-types following the ISBA scheme (in this version, Bélair *et al.*, 2003b,a). Subgrid scale turbulent fluxes are calculated using an implicit vertical diffusion scheme with prognostic turbulent kinetic energy (TKE) and a mixing length based on Bougeault and Lacarrère (1989) (Bélair *et al.*, 1999).

GEM uses a prognostic total cloud water variable with a bulk-microphysics scheme for non-convective clouds. Fractional cloudiness is based on a diagnostic relative humidity threshold approach (Sundqvist, 1988). The deep convection scheme is that of Kain and Fritsch (Kain and Fritsch, 1990, 1993), whereas a Kuo Transient scheme is used for shallow convection (Kuo, 1965; Bélair *et al.*, 2005).

The radiation scheme is that of Li and Barker (2005). It employs a correlated k-distribution (CKD) method for gaseous transmission, with nine frequency intervals for longwave and four for shortwave radiation. While the longwave spectrum and the near-infrared portion of the shortwave spectrum are treated using the CKD method, the rest of the shortwave spectrum is dealt with in frequency space with UVC, UVB, UVA and photosynthetically active radiation is separately considered. The scheme treats the following gases interactively, H_2O, CO_2, O_3, N_2O, CH_4, $CFC11$, $CFC12$, $CFC13$ and $CFC14$. Background aerosols are included based on the climatology of Toon and Pollack (1976). This simple climatology specifies maximum aerosol loading at the equator and a decrease towards the poles, with different values for continents and oceans.

The total water content is transferred without tuning to the radiative transfer (RT) scheme. The separation of total cloud water into liquid and solid is based on the local air temperature and total water content ranging from all ice at $-40°$C to all liquid at 0°C (Boudala *et al.*, 2004). The liquid effective radius is a function of LWC and CCN (Lohman and Roeckner, 1996) and has a range of $[4 - 17]\mu m$ whereas the ice effective radius is set to a constant value of $15\mu m$. The integrated cloud fraction (CF) is calculated with the maximum-random overlap assumption. In the RT scheme, a gamma distribution correction is used following Li and Barker (2002) to account for fluctuations in cloud absorption in the infrared (hereafter, LW-GD correction) and an adjusted cloud optical depth is used to take into account the overestimation of homogeneous clouds albedo for the shortwave fluxes (hereafter, SW-ACOD correction) following Li *et al.* (2005), as explained in section 1.2.

In Oreopoulos *et al.* (2012b), an intercomparison of various radiative transfer codes is presented with respect to reference line-by-line calculations for seven particular cases with two including overcast liquid clouds. The Li and Barker (2005) radiative transfer code is evaluated in this article and identified as the number 4 model. The results show that for the overcast homogeneous liquid cloud cases, the code produces a small overestimation of SWU at TOA with more important underestimation in SWD at SFC, reaching 10 %. However, the LW biases are quite small, below 1 %.

In our study, when McICA methodology is used, the intermediate noise reduction version is used with 100 subcolumns generated, with 45 sampled for the SW radiative calculations and 71 for the LW. The SCG parameters are set to standard values from the literature: the decorrelation lengths for CF and cloud water content (CWC) are 2 km and 1 km respectively, the horizontal water content distribution (p_γ) is a gamma distribution and its normalized standard deviation ($f = 1/\sqrt{\nu}$) is kept to the model definition ($\nu = [1; 2; 4]$ as a function of CF $= [< 0.9; \geq 0.9\& < 1; 1]$):

$$p_\gamma(CWC|\langle CWC\rangle, \nu) = \frac{1}{\Gamma(\nu)}\Big(\frac{\nu}{\langle CWC\rangle}\Big)^{\nu} CWC^{\nu-1} e^{-\nu CWC/\langle CWC\rangle} \tag{3.1}$$

The model is run with an horizontal grid mesh of 0.5° and 56 vertical levels, extending up to 10 hPa on a global grid. The global evaluation is required in order to sample all cloudy conditions (from polar clouds to deep convection, over land as well as over ocean) since the McICA methodology can respond very differently. The model time step is 1200 s whereas the radiative time step is 3600 s. In between the radiative time steps, the LW fluxes and heating rates are constant, whereas the SW fluxes and heating rates are corrected for the change in solar angle. Different simulations are made for the period 2006/11 to 2009/12 both employing observed sea surface temperatures (SSTs) and sea-ice as the lower boundary conditions

Table 3.1 Simulation descriptions

name	description	offline McICA
CTL	reference model	yes
HOMOG*	reference model without the inhomog. corrections	yes, with MRO
HOMOG	reference model without the inhomog. corrections	yes
McICA	online McICA (without the inhomog. corrections)	no

from the Atmospheric Model Intercomparison Project dataset (Hurrell *et al.*, 2008, AMIP). The first month of simulation is excluded from seasonal analysis.

3.2.2 Experiments: offline vs. online McICA calculations

As both the LW-GD and the SW-ACOD corrections are implemented in the control model to account for cloud subgrid scale inhomogeneity (see section 1.2), these corrections are removed when using the McICA methodology, because of the explicit inhomogeneity treatment through the SCG. To have a measure of these removal effects, the HOMOG simulation was performed by removing these corrections from the control model, therefore treating the cloud homogeneously in the RT scheme. In order to better understand all the impacts of the McICA methodology, four simulations were conducted as listed in table 3.1: one with the control model (CTL), two with the SW-ACOD and LW-GD inhomogeneity corrections removed (HOMOG) and one with the McICA calculations (McICA).

For the CTL and the two HOMOG simulations, the model is run with two calls to the RT scheme: first with the classic RT calculations and second, with the SCG and McICA methodology applied. The second call to the RT with the McICA methodology is an offline calculation (sometimes called diagnostic calculation in the literature, e.g. Oreopoulos *et al.*, 2012a) as the resulting fluxes are not fed back into the model simulations. These offline calculations allow a direct comparison between the RT classic calculations and the McICA RT calculations for the exact same atmospheric profiles, over the whole domain and period of integration. The HOMOG* simulation is different from the second one (HOMOG) only in its offline McICA application since the MRO assumption (see section 1.1) is kept contrarily to the the other McICA applications where decorrelation lengths are applied.

As listed in table 3.2, the differences seen in radiative fluxes with the offline calculations allow to, first, understand the McICA direct effects of only introducing horizontal inhomogeneity ($\text{HOMOG}^*_{\text{McICA,MRO}}$ - HOMOG*). Secondly, to understand the McICA direct effects of introducing horizontal inhomogeneity and changing the vertical overlap assumption ($\text{HOMOG}_{\text{McICA}}$ - HOMOG). Finally, it allows to understand the effects of replacing the SW-ACOD and LW-GD corrections by the McICA methodology ($\text{CTL}_{\text{McICA}}$ - CTL) without any change to the cloud and atmospheric variables. On the other hand, the McICA - CTL differences will include internal variability of the model simulations and to an extent, possible drift to new atmospheric states. These two sets of comparisons (with offline/online calculations and with different simulations) allow to distinguish first, what is coming from the McICA methodology directly and second, how this signal is modified when the modeled atmosphere is allowed to respond to the new flux calculations.

3.2.3 Surface and top of atmosphere fluxes

This chapter focuses on four flux components: the downwelling shortwave and longwave fluxes at surface (SWD and LWD at SFC respectively), and the up-

Table 3.2 Comparison list

Δ simulations	effects
$\mathrm{HOMOG}^{*}_{\mathrm{McICA,MRO}}$ - HOMOG*	offline horizontal inhomog. McICA effects
$\mathrm{HOMOG}_{\mathrm{McICA}}$ - HOMOG	offline McICA effects
$\mathrm{CTL}_{\mathrm{McICA}}$ - CTL	offline McICA - inhomog. correction effects
McICA - CTL	online McICA - inhomog. correction effects

welling shortwave and longwave fluxes at top of atmosphere (SWU and LWU at TOA). The SFC downwelling fluxes present how clouds modify, on one part, the incoming solar radiation as a primary reflective and scattering component of the atmosphere, and on the other part, how clouds, together with water vapor, absorb and radiate back the SFC and atmospheric thermal heat. Whereas at TOA, the upwelling fluxes integrate both the SFC, cloud and other atmospheric components signatures.

For the SW fluxes, regions of high incoming solar radiation can produce significantly more flux differences and therefore contribute more to the global mean differences. For this reason, SW fluxes are presented divided by the incoming solar radiation at TOA creating a "SWD ratio" at SFC (SWD at SFC divided by SWD at TOA) and the TOA albedo (SWU at TOA divided by SWD at TOA).

3.2.4 Co-variability diagrams

Co-variability diagrams of radiative fluxes as a function of cloud variables such as cloud fraction (CF) or cloud water path (CWP) are the main tool used in this chapter for the analysis of the results. Since the radiative response of the model to radiative modifications can be non-linear depending on the various cloud variables, these diagrams allow to extricate those relationships and to better understand the underlying contributions to the total response.

Building co-variability diagrams when looking at differences between offline and online fluxes of a specific simulation is simple. The cloud variables being identical by definition, it becomes easy to simply subtract the two flux variables, McICA offline fluxes (f_{ij}^{off}) and classic online fluxes (f_{ij}^{on}), for each grid point (i,j). These flux differences (Δf_{ij}) can be distributed as a function of CF or CWP (c_{ij}), creating a 2D relative frequency distribution of flux differences (D_{off-on}):

$$\begin{aligned}\Delta f_{ij} &= f_{ij}^{off} - f_{ij}^{on}\\ D_{off-on}(\Delta f, c) &= \frac{dist[\Delta f_{ij}(c_{ij})]}{\sum_i \sum_j f_{ij}} * 100\%\end{aligned} \tag{3.2}$$

However, when comparing independent simulations, the model freely evolves creating different cloud variable distributions. As the flux differences between two simulations cannot be taken at a single grid point, since the atmosphere conditions are possibly different, 2D frequency distributions of fluxes as a function of CF or CWP are first created for each simulation (n_x) over an identical co-variability space (with identical intervals for the X and Y-coordinates). Then a relative difference of distributions (d_{y-x}) is calculated:

$$\begin{aligned}n_x(f,c) &= dist[f_{ij}^{x}(c_{ij})]\\ n_y(f,c) &= dist[f_{ij}^{y}(c_{ij})]\\ d_{y-x}(f,c) &= \frac{n_y - n_x}{\sum_i \sum_j n_x} * 100\%\end{aligned} \tag{3.3}$$

Figure 3.1 presents an example of the two treatments for the downwelling longwave fluxes (LWD) at surface as a function of CF. The first row is the relative frequency distribution of the flux differences (D_{off-on}) between $\mathrm{CTL_{McICA}}$ offline fluxes and fluxes for the CTL simulation. Whereas the second row presents, in order, the frequency distributions of LWD as a function of CF for the CTL (n_{CTL})

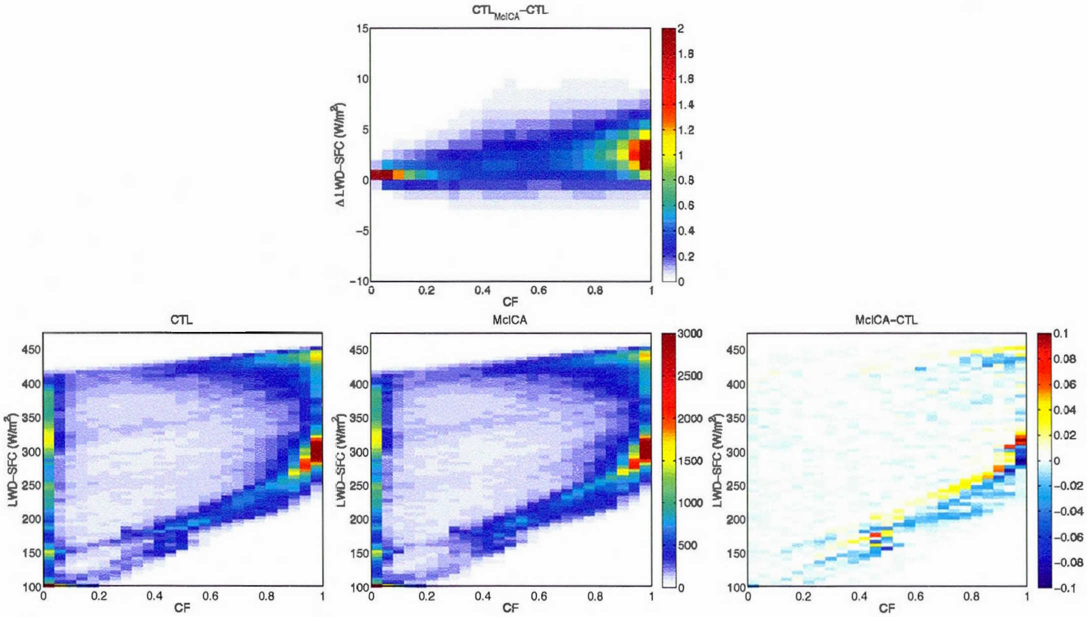

Figure 3.1 First row: example of D_{off-on} (in %) for LWD as a function of CF for the CTL simulation. Second row: example of n_{CTL} and n_{McICA} for the same variables for the CTL and McICA simulation (left and middle panel, in number of occurrences) with their relative difference of distributions $d_{McICA-CTL}$ (right panel, in %).

and McICA (n_{McICA}) simulations, followed by the relative differences of these distributions ($d_{McICA-CTL}$).

3.3 Results and interpretation

Results are presented in four parts. First, an idealized case is used to demonstrate simply the McICA horizontal inhomogeneity effects on fluxes. The second part presents the offline results with instantaneous flux difference distributions at two time steps together, January 1^{st} 2007 at 00 UTC and 12 UTC. This analysis helps to understand all the components of the McICA application and to illustrate the effects of its stochastic nature. January 1^{st} is chosen as a middle day of the winter season and the two time steps are chosen 12 hours apart to sample the whole globe with the sun up. Next, the offline flux difference distributions are presented for a seasonal mean boreal winter (DJF 2006-2007) to understand how the instantaneous conclusions are preserved or not over a seasonal mean. Finally, the online results are presented over a 3 year DJF seasonal mean (2006-2009) with relative differences of distributions. As a reference, the offline results are presented in parallel to the online results in the same manner.

Co-variability diagrams of flux variables as a function of CWP are filtered such that CF$>$ 0.9 for instantaneous data, and for CF$>$ 0.7 for seasonal mean data. This is necessary to isolate the relationship between fluxes and CWP without the influence of varying CF. The SW fluxes are also filtered for daytime only. The global mean flux (or ratio) or global mean difference in flux (or ratio) is shown in all diagrams. For the SW ratios, the global mean flux or global mean flux difference is also indicated in parenthesis to illustrate the differences due to the two calculations.

To isolate effects from liquid, mixed or ice cloud phases, a filtering is applied on liquid and ice water content (LWC and IWC). The limit was set to 0.01 g/kg for LWC and IWC to detect a liquid, an ice or a mixed cloud at a specific vertical level for each model grid point. To isolate the phase related signal, a second filtering is applied to consider only model columns with a single cloud phase. This limit has been tested with lower and higher threshold values to find a compromize between enough occurrences of each cloud type (a lower limit is more restrictive and reduces the number of model columns containing only one cloud phase) and not too many mixed signals (i.e. a higher limit allows, for example, small values of LWC in model columns identified as containing only ice clouds).

Note that the analysis is presented for the boreal winter season (DJF) only but the boreal summer (JJA) was also analyzed and yielded similar conclusions. A few JJA results are presented for comparison in the last result section.

3.3.1 McICA horizontal inhomogeneity effects: a simple idealized case

As an introduction to the McICA horizontal inhomogeneity effects on SW and LW fluxes for different water content values, a simple idealized case is presented. This case includes only one cloud layer with a CF of 1, with three different specified LWP values: 1.0, 0.5 and 0.1 kg/m^2. The specific humidity and temperature vertical profiles are presented in figure 3.2 left column. The McICA REF version is used (see definition in section 2.4) in order to remove any stochastic noise contributions.

To illustrate the basic McICA effects of introducing horizontal inhomogeneity against an homogeneous cloud treatment, vertical flux differences are shown in figure 3.2 between the offline McICA methodology and the homogeneous cloud radiative transfer. The middle and right top panels show that McICA horizontal inhomogeneity effect is to reduce the cloud reflectivity by increasing the SWD and reducing the SWU. The different colors show that differences in SW fluxes are increasing for decreasing LWP values. The middle and right bottom panels show that for the LW, a reduced emissivity (which decreases the LWD and increases the LWU) is seen with McICA only at the lowest LWP values. For the other cases, the emissivity is even slightly increased. These results confirm that the homogeneous assumption produces greater biases (or greater cloud albedo overestimations) at low LWP values as explained theoretically in section 1.1. Moreover, this effect disappears rapidly with increasing LWP for the LW fluxes, since the cloud emissivity relationship as a function of LWP reaches its maximum value rapidly and therefore, the McICA methodology has almost no impact.

3.3.2 Offline results for instantaneous fluxes

Figure 3.3 shows the SWD ratio differences at SFC and TOA albedo differences between the offline McICA calculations and the classic RT calculations for the HOMOG*, HOMOG and CTL simulations as a function of total water path (TOTWP) and cloud fraction (CF).

The first column presents the horizontal inhomogeneity McICA effects compared to homogeneous cloud treatment ($\mathrm{HOMOG}^{*}_{\mathrm{McICA,MRO}}$ - HOMOG*). The signal shows a stochastic noise ($\pm$ differences in fluxes due to the Monte Carlo sampling of cloudy sub-columns) with a positive or negative skewness (a positive or negative signal) due to the horizontal inhomogeneity introduction which decreases the cloud reflectivity (as explained in section 1.1), hence increases the SWD ratio at SFC and decreases the TOA albedo. This signal is clearly decreasing with increasing CWP (1^{st} and 3^{rd} rows); a feature that is directly derived from the cloud albedo and CWP relationship, the slope being steeper (hence more sensitive) at lower CWP as explained in section 1.1. On the other hand, as a function of CF (2^{nd} and 4^{th} rows) the signal is growing with CF as it is expected with more clouds of reduced reflectivity that contribute to modify the SW fluxes.

The second column presents both McICA effects: the horizontal inhomogeneity introduction and the decorrelation length vertical overlap assumption ($\mathrm{HOMOG}_{\mathrm{McICA}}$ - HOMOG). The overall signal is similar to the HOMOG* differences except for a general decrease in amplitude and mean signal. This is the effect of switching from MRO to decorrelation lengths, which generally leads to a small increase in integrated CF (Räisänen and Barker, 2004), which decreases SWD ratio at SFC

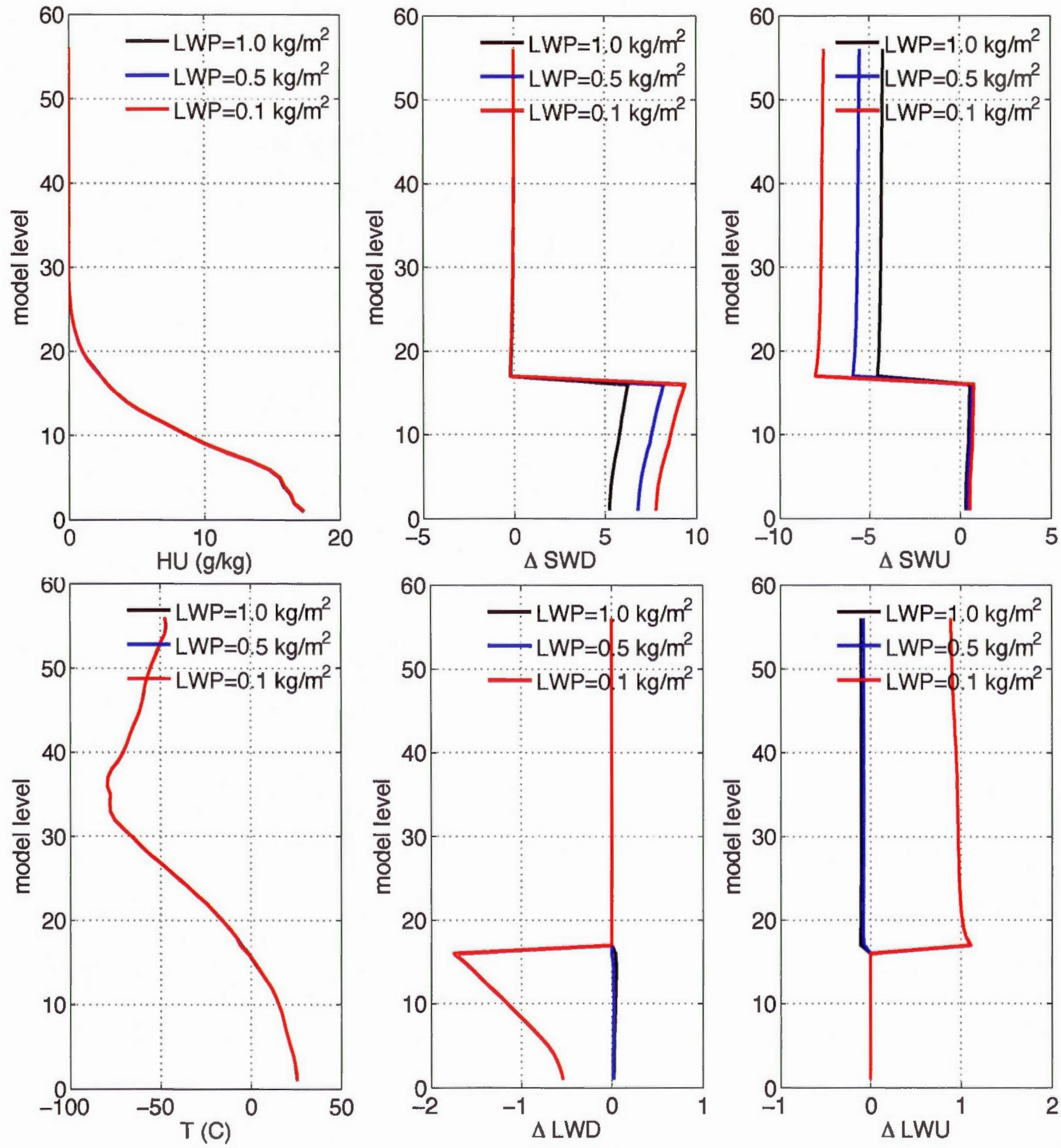

Figure 3.2 Vertical profiles of: specific humidity and temperature profiles (left column), downwelling flux differences (middle column) and upwelling flux differences (right column) between offline McICA methodology and homogeneous cloud radiative transfer ($\mathrm{HOMOG_{McICA}}$ - HOMOG) for three different LWP values.

and increases TOA albedo. However, this signal cannot be identified directly in this figure as the inhomogeneity effect is dominant and of opposite direction. Occurrences of negative signal at SFC and positive signal at TOA can be either attributed to the stochastic noise or the secondary effect of changing the overlap assumption. A particular case is seen for TOA albedo as a function of TOTWP with a mean TOA albedo increased signal of 0.002 but a mean SWU at TOA of -2.9 W/m^2. This can come from the regional distribution of positive and negative flux differences that are divided by the SWD at TOA. The TOA albedo ratio will give more weight on regions with less incoming solar radiation and thus, the global mean values can switch sign. In this case, the global mean TOA albedo shows a small increased signal, meaning that the overlap assumption slightly overrides the horizontal inhomogeneity introduction. Since the global mean SWU at TOA is negative, it suggests that the positive signal comes from regions of lower incoming solar radiation, or higher latitudes.

When replacing the SW-ACOD corrections by the McICA methodology (CTL_{McICA} - CTL, 3^{rd} column), the signal is completely reversed with an important decrease in SWD ratio at SFC and increase in TOA albedo, result of an increased cloud reflectivity. This can be attributed to the SW-ACOD removal effects (see section 1.2) that now dominate over the McICA effects. In other words, the treatment of cloud inhomogeneity by the SW-ACOD is much stronger in terms of reducing cloud reflectivity than the treatment of cloud inhomogeneity through the present McICA methodology. Moreover, the signal is now increasing with TOTWP, at least up to 0.5 kg/m^2 and then fades out as occurrences of high TOTWP are also decreasing. This can be explained by the fact that the SW-ACOD corrections are increasing with cloud optical depth, or TOTWP. However, the McICA signature may be visible at low TOTWP (where its effects are stronger and the SW-ACOD effects are weaker) with few occurrences of small positive flux differences at SFC and negative flux differences at TOA. Stochastic noise may also be responsible for these occurrences.

For all simulations, the TOA signal is similar to the SFC signal with opposite signs. However, a reduction both in the maximum amplitude and in the mean signal is visible. This signal attenuation can be understood for cases over high reflective surface, where the modified cloud reflectivity is compensated by the surface reflection, resulting in smaller flux differences at TOA compared to SFC. To confirm this hypothesis, figure 3.4 shows that over land for all cases, where surface albedo is higher relative to ocean (particularly for winter season), the McICA response is particularly damped for SWU at TOA (right) compared to SWD at SFC (left).

Flux differences as a function of cloud phase are not shown (see annex 5.4 for the detailed diagrams) but their global mean values are presented in table 3.3. For all simulations, the liquid and mixed clouds are contributing the most to the signal since SW flux are mainly modified by larger cloud optical depth values that are representative of liquid and mixed clouds. On the other hand, the ice clouds exhibit almost a null global mean signal for the $\mathrm{HOMOG}^*_{\mathrm{McICA,MRO}}$ - HOMOG* differences. This can be understood by looking at figure 1.1 where the cloud albedo relationship to IWP exhibits regions where the homogeneous assumption will overestimate the cloud reflectivity and regions where it will underestimate it. Moreover, ice clouds exhibit opposite signals for SWD ratio at SFC (-0.006) and TOA albedo (0.003) for the $\mathrm{HOMOG}_{\mathrm{McICA}}$ - HOMOG differences. This opposite signal is now the visible effect of changing the overlap assumption since the horizontal inhomogeneity effect is almost not affecting the ice clouds (0.0 global mean difference for the SWD ratio at SFC and -0.002 for the TOA albedo for the $\mathrm{HOMOG}^*_{\mathrm{McICA,MRO}}$ - HOMOG* differences). As a function of CWP, both the liquid and ice clouds exhibit a positive TOA albedo signal of 0.004 responsible for the positive signal seen in figure 3.3.

Figure 3.5 presents the offline LWD flux differences at SFC and LWU flux differences at TOA between the offline McICA calculations and the classic RT calculations for the HOMOG*, HOMOG and CTL simulations as a function of total water path (TOTWP) and cloud fraction (CF).

The horizontal inhomogeneity McICA effects (HOMOG$^{*}_{\mathrm{McICA,MRO}}$ - HOMOG*, first column) produces decreased LWD at SFC and increased LWU at TOA due to a reduced cloud emissivity as expected (see section 1.1). This is analog to the SW signal due to reduced reflectivity but with smaller signal since the emissivity relationship to CWP has a lower slope than cloud albedo and it reaches saturation more rapidly (at lower CWP). This means that the McICA treatment generally decreases the cloud greenhouse effect.

Opposite occurrences to the mean signal are also visible and can be due to the stochastic noise. Similarly to the SW, the signal decreases with TOTWP but its amplitude is maximum at CF around 0.6 for the LWD at SFC and towards CF=1 for LWU at TOA. Unlike the SW signals, the LW signals are not as symmetrical between SFC and TOA: a broader signal as a function of TOTWP and higher global mean signals are seen for LWU at TOA. These discrepancies will be discussed in more detail as a function of cloud phase.

When the overlap assumption is also modified with the McICA methodology, (HOMOG$_{\mathrm{McICA}}$ - HOMOG, second column), the global mean signal is attenuated compared to the first column and opposite occurrences (positive occurrences for LWD at SFC and negative occurrences for LWU at TOA) are more visible. As explained for the SW, this is the effect of switching from MRO to decorrelation lengths, which generally leads to a small increase in integrated CF (Räisänen and Barker, 2004), which increases LWD at SFC and decreases LWU at TOA. The

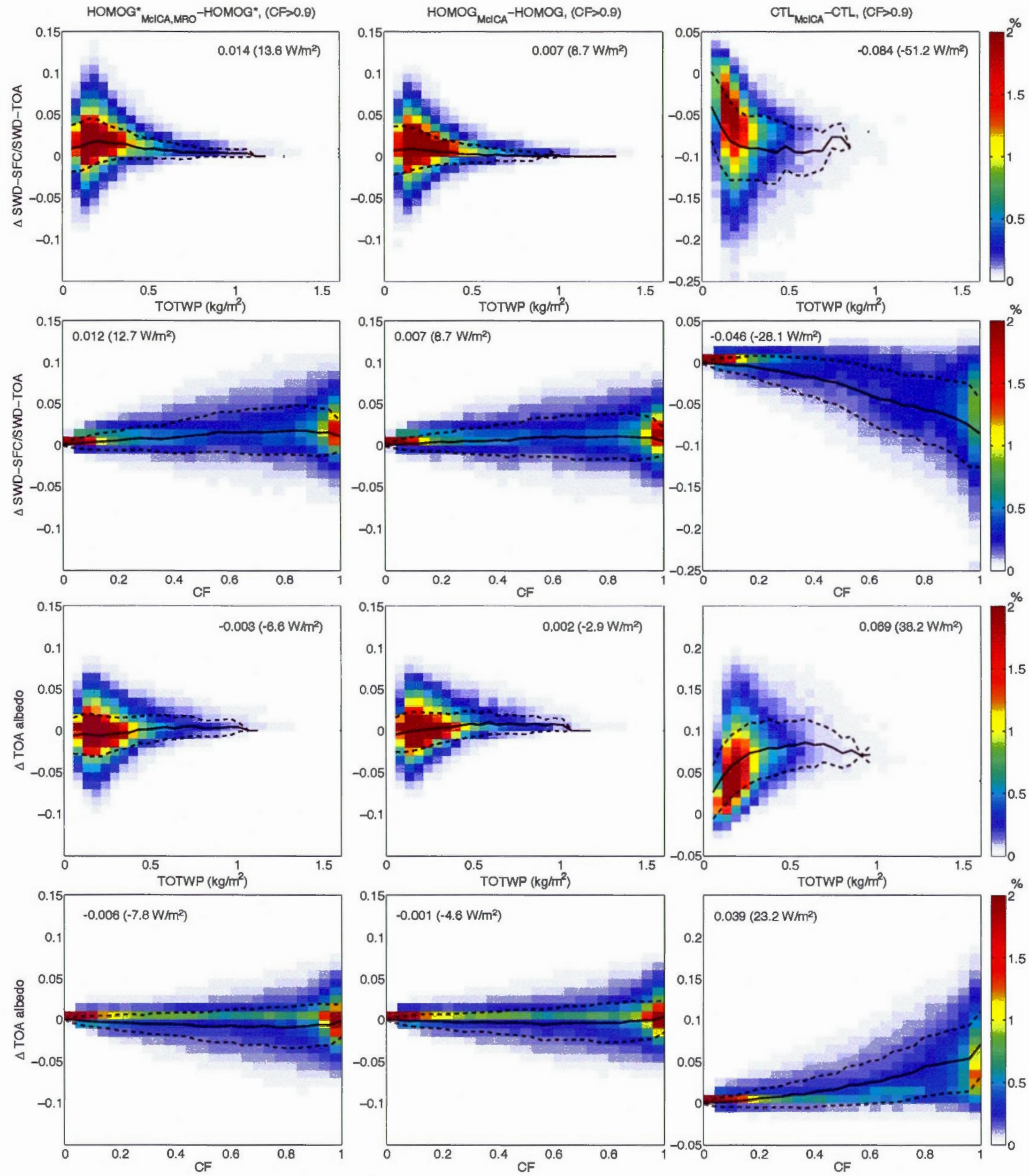

Figure 3.3 SW ratio differences for January 1^{st} for the HOMOG* (1^{st} column), the HOMOG (2^{nd} column) and the CTL simulations (3^{rd} column). First and second rows are for SWD at SFC divided by SWD at TOA as a function of TOTWP and CF respectively, while 3^{rd} and 4^{th} rows are for TOA albedo differences. The global mean ratio differences (or the global mean flux differences, i.e. without the normalization by the SWD at TOA) are indicated in each panel. The distribution mean and standard deviation are represented with the full and dashed lines.

Table 3.3 Global mean offline SW flux differences as a function of cloud type. All conditions is equivalent to co-variability diagrams (as a function of CF) inset information. Values in parenthesis correspond to co-variability diagrams as a function of CWP (for CF >0.9).

cloud type	SWD ratio	SWD at SFC	TOA albedo	SWU at TOA
$\mathrm{HOMOG}^{*}_{\mathrm{McICA,MRO}}$ - HOMOG*				
all	0.012 (0.014)	12.7 (13.6)	-0.006 (-0.003)	-7.8 (-6.6)
liquid	0.016 (0.011)	16.8 (12.3)	-0.008 (0.001)	-10.0 (-4.1)
ice	0.000 (0.012)	6.1 (13.8)	-0.002 (-0.005)	-4.7 (-8.7)
mixed	0.018 (0.016)	17.2 (14.4)	-0.009 (-0.005)	-10.3 (-7.8)
$\mathrm{HOMOG}_{\mathrm{McICA}}$ - HOMOG				
all	0.007 (0.007)	8.7 (8.7)	-0.001 (0.002)	-4.6 (-2.9)
liquid	0.012 (0.007)	12.8 (9.2)	-0.004 (0.004)	-6.9 (-2.0)
ice	-0.006 (0.0)	2.7 (5.9)	0.003 (0.004)	-2.1 (-3.5)
mixed	0.010 (0.008)	10.7 (8.8)	-0.002 (0.0)	-5.3 (-3.6)
$\mathrm{CTL}_{\mathrm{McICA}}$ - CTL				
all	-0.046 (-0.084)	-28.1 (-51.2)	0.039 (0.069)	23.2 (38.2)
liquid	-0.055 (-0.099)	-34.9 (-56.2)	0.049 (0.061)	29.3 (42.2)
ice	-0.038 (-0.071)	-14.6 (-36.0)	0.024 (0.051)	10.3 (26.2)
mixed	-0.061(-0.071)	-37.4 (-44.5)	0.048 (0.056)	27.9 (32.060)

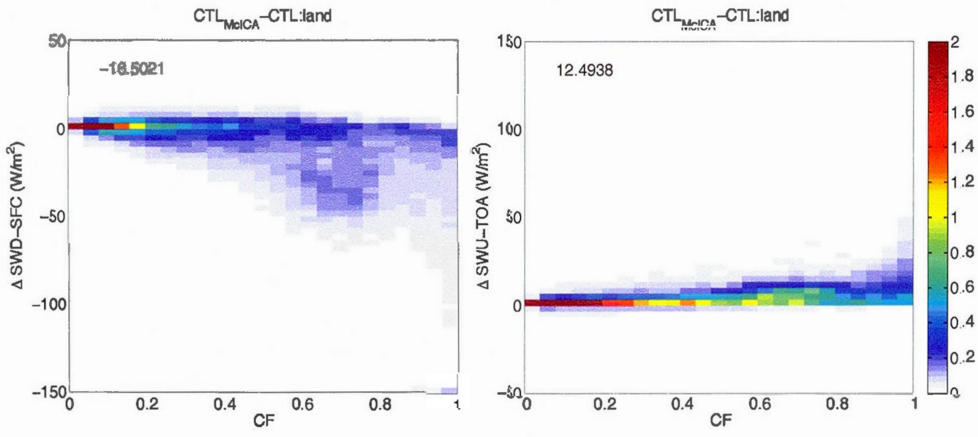

Figure 3.4 SWD differences at SFC (left) and SWU differences at TOA (right) as a function of CF for CTL over land only.

signal attenuation is more important at TOA compared to SFC.

The third column presents the effects of replacing the LW-GD corrections by McICA (CTL_{McICA} - CTL). As for the SW, the LW-GD corrections are stronger than what McICA can produce and therefore, their removal results in an increased LWD at SFC and decreased LWU at TOA. This signal also decreases rapidly with TOTWP and increases with CF. This behavior as a function of TOTWP is not expected (as it was for the SW), since the LW-GD corrections are highly non-linear as a function of cloud optical depth. Similarly to the SW, the McICA signal may be visible at low TOTWP values, where its effects are more pronounced but stochastic noise contribution cannot be excluded.

Table 3.4 presents global mean LW flux differences as a function of cloud phase. Contrarily to the SW counterpart, the ice clouds exhibit the largest McICA signals ($HOMOG^*_{McICA,MRO}$ - HOMOG* and $HOMOG_{McICA}$ - HOMOG), both in global mean signals and amplitude (see annex 5.4 for diagrams). Moreover, the ice cloud signals as a function of CF are also maximum at CF around 0.6, where the ice cloud occurrences are maximum. Since the ice clouds are the major contributors to the LW signals, it can explain the maximum seen around CF=0.6 for LWD at SFC. For the LWU at TOA, mixed clouds are also contributing to the signals towards CF=1, removing the decreasing trend in amplitude between CF=0.6 and CF=1.

On the other hand, liquid clouds exhibit the smallest McICA signals. This can be explained by the liquid clouds reaching rapidly the emissivity saturation (of 1) since their LWP is generally greater than the ice cloud IWP. Moreover, the ice clouds are presenting more occurrences at very low IWP. When the cloud emissivity is reaching saturation, the McICA horizontal inhomogeneity introduction will have little effect on the model column emissivity whereas the overlap effect can produce opposite signals: an increased LWD at SFC or decreased LWU at TOA. The LWU signal at TOA is effectively negative only for the liquid clouds for the $\mathrm{HOMOG_{McICA}}$ - HOMOG difference.

For the $\mathrm{CTL_{McICA}}$ - CTL differences, the mixed clouds are presenting the greater global mean signal probably due to the LW-GD corrections that are non-linear as a function of cloud optical depth.

This first section has shown that:

- The main McICA effect is a decreased cloud reflectivity and emissivity due to WC horizontal inhomogeneity introduction, which increases the SWD ratio at SFC and reduces the TOA albedo, while decreases LWD at SFC and increases LWU at TOA;

  - The LW differences are much less than the SW differences;

  - This effect strongly decreases as a function of CWP, and increases with CF;

- The McICA overlap assumption, which results in a small increasing CF, offsets the horizontal inhomogeneity effect;

  - This secondary effect is mainly seen for ice clouds where the mean horizontal inhomogeneity effect is almost zero for the SW, and for liquid clouds for the LW;

- Replacing the SW-ACOD and LW-GD corrections by the present McICA methodology results in an increased cloud reflectivity and emissivity, which decreases the SWD ratio at SFC and increases the TOA albedo, while increases the LWD at SFC and decreases the LWU at TOA;

  - This means that the SW-ACOD and LW-GD corrections are much stronger (in decreasing the cloud reflectivity and emissivity) than the present McICA inhomogeneity introduction;

  - This effect increases with TOTWP up to $0.5 kg/m^2$ for the SW and decreases for the LW, while it increases with CF for both SW and LW;

  - For low TOTWP values, the McICA effects may be visible but the stochastic noise contribution cannot be excluded;

- All SW signals are damped at TOA since the surface reflection partly compensates the modified cloud reflectivity, whereas for LW signals, amplitude is similar but different patterns are seen (such as different decreasing rates and different maximum localizations);

- For all SW signals, the liquid and mixed clouds are contributing the most since the SW flux are mainly modified by larger cloud optical depth values which correspond generally to the liquid and mixed clouds; while for LW McICA signals, the ice clouds exhibit the greater signals both at SFC and TOA.

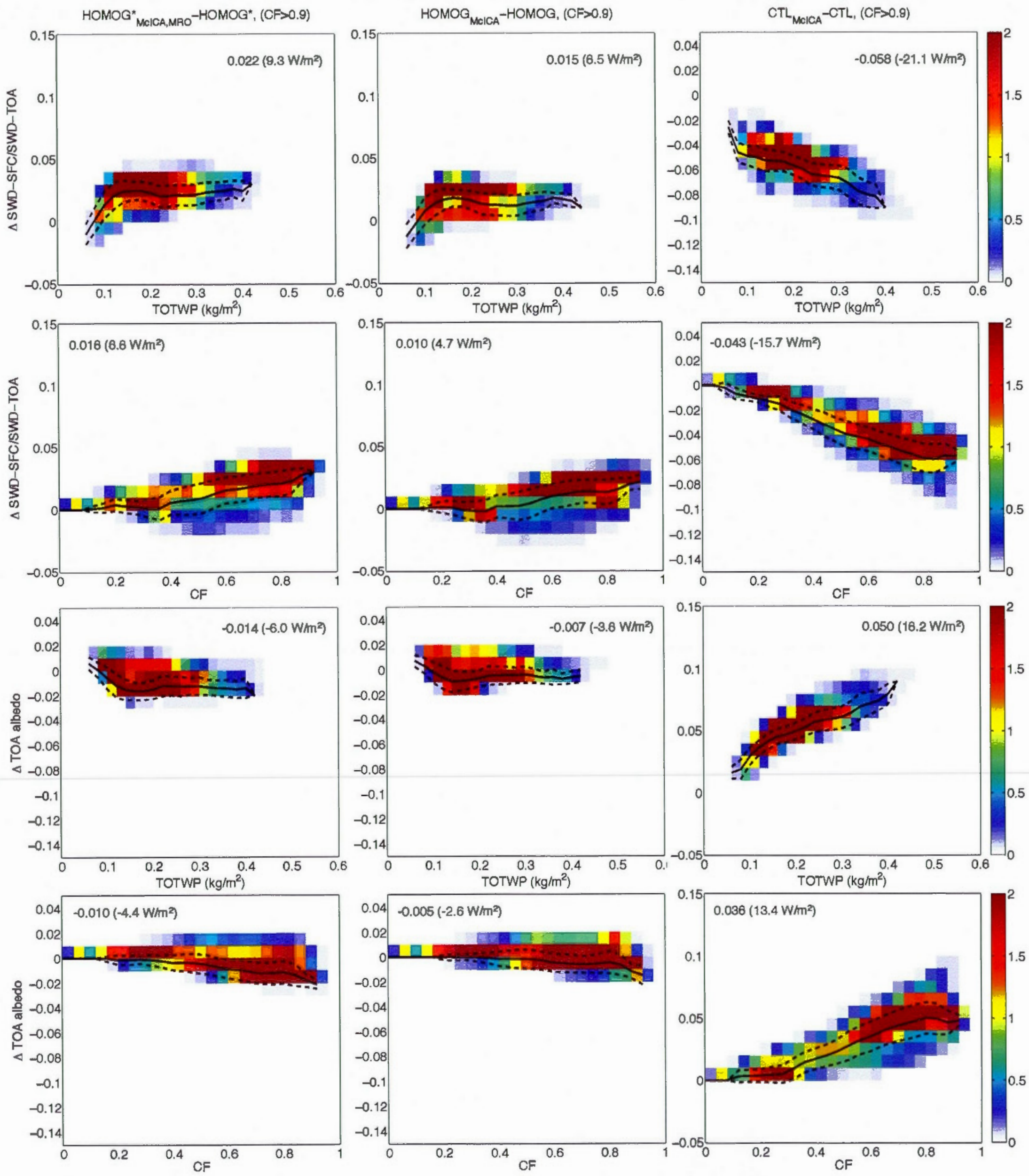

Figure 3.5 LW differences for January 1^{st} for the HOMOG* (1^{st} column), the HOMOG (2^{nd} column) and the CTL simulations (3^{rd} column). First and second rows are for LWD at SFC as a function of TOTWP and CF respectively, while third and fourth rows are for LWU differences at TOA. The global mean flux differences are indicated in each panel. The distribution mean and standard deviation are represented with the full and dashed lines.

Table 3.4 As table 3.3 but for LW flux differences.

cloud type	LWD at SFC	LWU at TOA
$HOMOG^*_{McICA,MRO}$ - HOMOG*		
all	-1.2 (-0.7)	1.6 (1.9)
liquid	-0.9 (-0.3)	0.1 (-0.2)
ice	-3.3 (-2.0)	3.1(2.8)
mixed	-1.4 (-0.8)	1.6(1.7)
$HOMOG_{McICA}$ - HOMOG		
all	-0.8 (-0.5)	0.8 (0.9)
liquid	-0.5 (-0.3)	-0.1 (-0.4)
ice	-2.3 (-1.4)	2.0 (1.6)
mixed	-0.9 (-0.6)	0.7 (0.8)
CTL_{McICA} - CTL		
all	1.3 (1.8)	-1.6 (-2.5)
liquid	1.6 (2.1)	-1.2 (-1.5)
ice	1.6 (1.8)	-1.9 (-3.3)
mixed	2.0 (1.9)	-2.1 (-2.4)

3.3.3 Offline results for seasonal mean fluxes

This section presents the offline SW ratio and LW flux differences similarly to the previous section but for one winter (DJF 2006-2007) seasonal mean to see how instantaneous signals are modified over a season average.

Figure 3.6 presents the seasonal mean SW ratio differences as a function of TOTWP and CF. The first column presents the horizontal inhomogeneity McICA effects. Similar results to the previous section are found: a decreased cloud reflectivity which increases the SWD ratio at SFC and decreases the TOA albedo. Since the difference are now taken over a seasonal mean period, the stochastic noise should disappear. However, occurrences of opposite sign to the mean signal are still visible and they are mainly coming from the ice and mixed clouds. The ice clouds even exhibits a negative global mean effect as a function of CF (see table 3.5) with a maximum in amplitude around CF=0.5 (not shown, see annex 5.4 for detailed diagrams). This feature was not seen at the instantaneous time scale. It means that, at the seasonal scale, the McICA horizontal inhomogeneity introduction increases the ice clouds reflectivity. Finally, the decreasing McICA inhomogeneity effect with increasing TOTWP is no more visible in the seasonal mean signal and its increasing tendency with CF is reduced, particularly for TOA albedo.

The second column presents the combination of horizontal inhomogeneity and decorrelation length effects. Similarly to the instantaneous results, the global mean signal is reduced (compared to the horizontal inhomogeneity effects only) and more opposite occurrences are visible since the vertical overlap assumption is producing opposite effects to the inhomogeneity introduction. Again, occurrences of opposite sign to the mean signal are mainly coming from the ice and mixed clouds (not shown). The ice clouds exhibit a global mean signal of -0.006 for SWD ratio at SFC and 0.004 for TOA albedo since the horizontal inhomogeneity and the vertical overlap are producing effects of same sign.

For both experiments (first and second column), global mean signals are greater at the seasonal scale compared to the instantaneous values. This may be due to the stochastic noise cancellation or to a time sampling effect: January 1^{st} may not be representative of the season.

The third column presents the SW-ACOD and LW-GD removal effects combined to the McICA inhomogeneity and vertical overlap effects. As for the instantaneous results, the SW-ACOD removal effects are dominant and no more opposite occurrences are visible. However, the global mean signals are reduced compared to the instantaneous values, maybe due to the increased McICA signals over the seasonal scale. As seen in the previous section, the liquid and mixed clouds are contributing more importantly since the SW-ACOD correction is proportional to cloud optical depth.

The LW seasonal mean effects are presented in figure 3.7. Looking at the horizontal inhomogeneity McICA effects on the first column, the results are similar to the instantaneous results for the LWD at SFC, even keeping the decreasing tendency as a function of TOTWP. The ice clouds are still the main contributors for the signal, particularly for the maximum signal seen at CF=0.5. However, for the LWU at TOA, the signal is changed as a function of TOTWP due to contributions of liquid clouds to the higher LWU differences occurrences. Looking at table 3.5, for the LWU at TOA, the three cloud phases are exhibiting a similar global mean signal.

The second column, which presents the horizontal inhomogeneity and vertical overlap McICA effects, is similar to the first column. The signals are similar to the instantaneous results for the LWD at SFC with the ice clouds being the main contributors while it is different for the LWU at TOA with the liquid and mixed clouds contributing to the higher LWU difference occurrences.

For both experiments (first and second column), contrarily to the SW signals, the LWD global mean signals remain approximately the same at the seasonal scale compared to the instantaneous time scale. However, the maximum amplitude is reduced as expected from stochastic noise cancellation at the seasonal scale.

Finally, the third column presents similar results to the instantaneous results for the combined McICA effects and SW-ACOD and LW-GD removal effects. Opposite occurrences to the mean signal have almost disappeared while global mean signals remain the same. Tendency of increasing effects as a function of TOTWP and CF are still visible.

This section has presented how the instantaneous offline signals are changed or maintained over a one year seasonal mean. In summary, the main results are:

- The same McICA horizontal inhomogeneity effect is seen at the seasonal mean: a general increased SWD ratio at SFC and LWU at TOA, while a reduced TOA albedo and LWD at SFC, due to decreased cloud reflectivity and emissivity ;

  - Its decreasing effect as a function of TOTWP is no longer visible for the SW and only at SFC for the LW;

  - TOA signals are still reduced compared to SFC signals for the SW only;

  - Without the stochastic noise, the ice clouds exhibits more clearly their opposite response with an increased cloud reflectivity while their emissivity is still decreasing with McICA;

  - For the LW, the ice clouds are still the main contributors at SFC while at TOA, liquid clouds are more contributing, particularly to higher LWU difference occurrences;

- As before, the McICA effect due to vertical overlap assumption counteracts partly the horizontal inhomogeneity effect;

  - For the ice clouds, both effects are increasing the reflectivity;

- Compared to instantaneous results for the McICA effects only, the maximum amplitude is reduced in all cases, but the global mean signal is increased for the SW and remains generally the same for the LW;

- Similarly to the instantaneous time scale, the SW-ACOD and LW-GD correction removal effects are dominant over the McICA effects;

  - Almost no more opposite occurrences (that were attributed to either stochastic noise or McICA inhomogeneity signals) are visible at the seasonal scale;

  - The liquid and mixed clouds are still the most contributing clouds to this effect;

  - As for the McICA effects only, the maximum amplitude is reduced compared to instantaneous results. However, the global mean signal is reduced for the SW and maintained for the LW.

3.3.4 Online results for seasonal mean fluxes

This section presents online seasonal average results as it is the goal of this study to show and explain the McICA replacement effects at the seasonal scale. Since the flux differences between two simulations cannot be illustrated with the co-variability diagrams of flux differences for each grid point (as the cloud variables

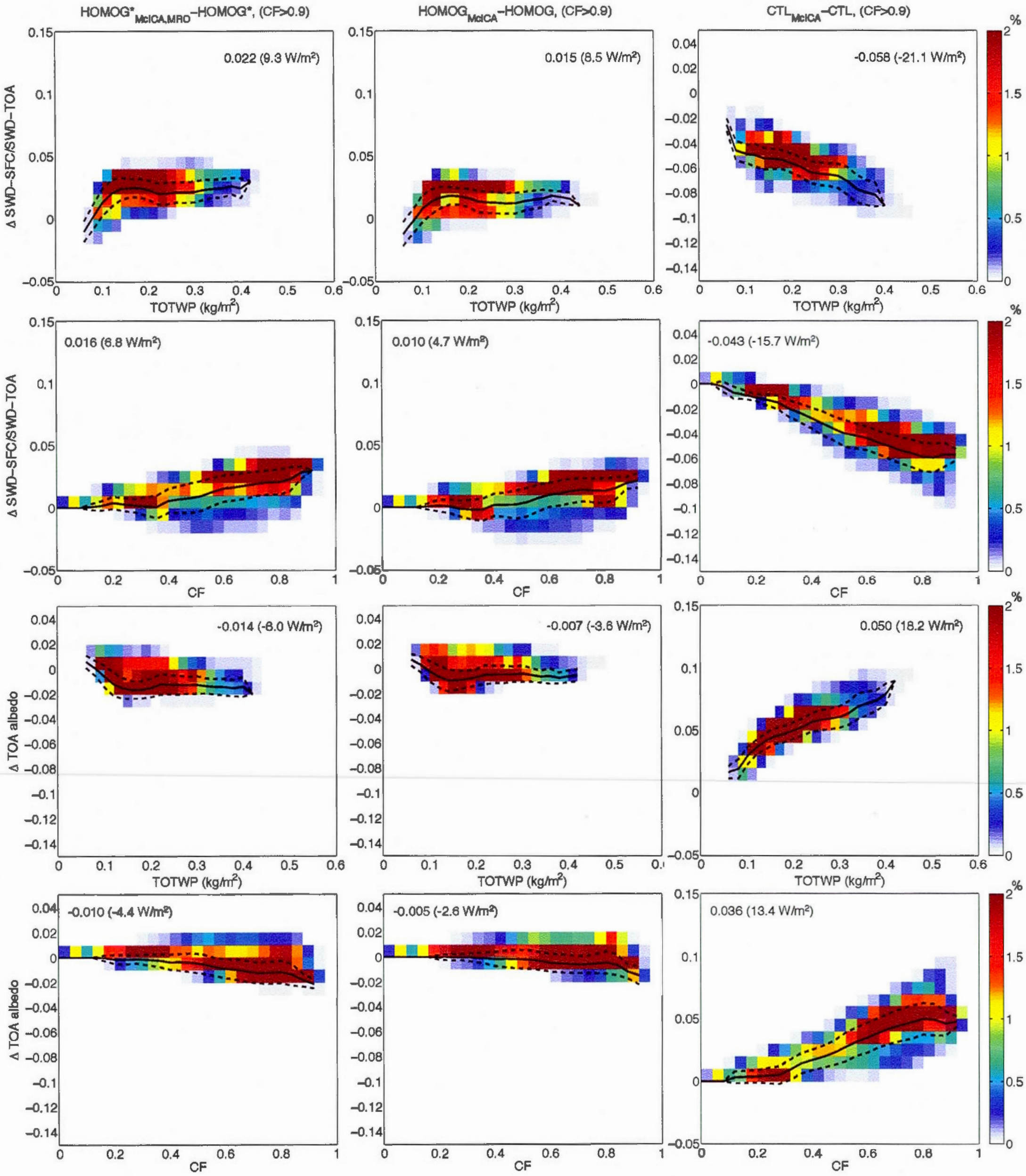

Figure 3.6 SW ratio differences for DJF2007 for the HOMOG-MRO (1st column), the HOMOG (2nd column) and the CTL simulations (3rd column). First and 2nd rows are for SWD at SFC divided by SWD at TOA as a function of TOTWP and CF respectively, while 3rd and 4th rows are for TOA albedo differences. The global mean ratio differences (or the global mean flux differences, i.e. without the normalization by the SWD at TOA) are indicated in each panel. The distribution mean and standard deviation are represented with the full and dashed lines.

Table 3.5 Global mean offline SW ratio and LW flux differences as a function of cloud type for DJF 2007. All conditions is equivalent to co-variability diagrams (as a function of CF) inset information. Values in parenthesis correspond to co-variability diagrams as a function of CWP (for CF>0.7).

cloud type	SWD ratio	TOA albedo	LWD at SFC	LWU at TOA
$HOMOG^{*}_{McICA,MRO}$ - HOMOG*				
all	0.016 (0.022)	-0.010 (-0.014)	-1.2 (-1.2)	1.5 (1.9)
liquid	0.019 (0.025)	-0.012 (-0.016)	-0.8 (-0.8)	1.2 (1.4)
ice	-0.001 (0.001)	0.002 (0.001)	-2.6 (-2.4)	1.5 (1.9)
mixed	0.018 (0.021)	-0.011 (-0.013)	-1.3 (-1.4)	1.7 (1.8)
$HOMOG_{McICA}$ - HOMOG				
all	0.010 (0.015)	-0.005 (-0.007)	-0.8 (-0.8)	0.8 (1.0)
liquid	0.014 (0.019)	-0.008 (-0.011)	-0.4 (-0.5)	0.6 (0.7)
ice	-0.006 (-0.005)	0.004 (0.005)	-2.0 (-1.9)	0.8 (1.1)
mixed	0.011(0.013)	-0.005 (-0.006)	-0.8 (-0.9)	0.9 (0.9)
CTL_{McICA} - CTL				
all	-0.043 (-0.058)	0.036 (0.050)	1.3 (1.7)	-1.6 (-2.0)
liquid	-0.043 (-0.057)	0.039 (0.051)	1.2 (1.7)	-1.5 (-1.8)
ice	-0.038 (-0.043)	0.018 (0.029)	1.7 (2.3)	-1.2 (-1.8)
mixed	-0.049 (-0.050)	0.041 (0.047)	1.7 (1.9)	-1.9 (-2.0)

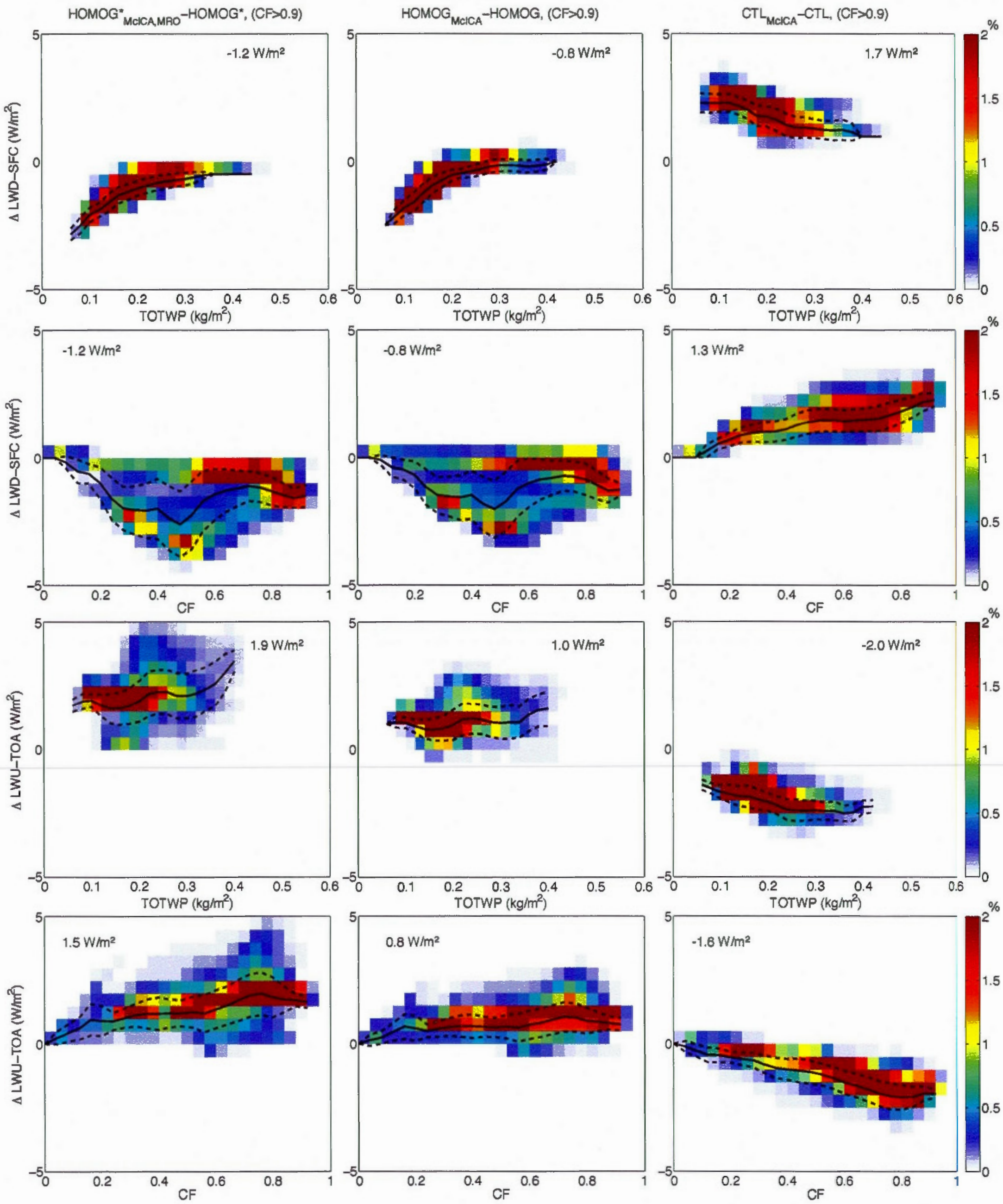

Figure 3.7 LW differences for DJF2007 for the HOMOG-MRO (1^{st} column), the HOMOG (2^{nd} column) and the CTL simulations (3^{rd} column). First and 2^{nd} rows are for LWD at SFC as a function of TOTWP and CF respectively, while 3^{rd} and 4^{th} rows are for LWU differences at TOA. The global mean flux differences are indicated in each panel. The distribution mean and standard deviation are represented with the full and dashed lines.

can freely evolve in each simulation), the co-variability diagrams now present the differences of distributions. To disentangle the offline "direct" results (where only fluxes are calculated differently) from the online results (where the atmospheric conditions can also differ), the offline results (CTL_{McICA} - CTL) are presented in parallel to the online results (McICA-CTL) for the same co-variability diagrams.

Figure 3.8 presents the SW ratio at SFC and TOA albedo relative frequency distributions as a function of CWP and CF, and their offline and online relative distribution differences. The 2^{nd} column presents the same offline signal (CTL_{McICA} - CTL) as figure 3.6 but for a 3 year seasonal mean DJF (from December 2006 to February 2009) instead of one year. The red and blue dipole indicates the same decrease in SWD ratio at SFC with less occurrences (in blue) at higher values and more occurrences (in red) at lower values. The inverse is seen for the TOA albedo with a general decrease. With these co-variability diagrams, no clear tendency emerges as a function of CF or TOTWP. The global mean signals are almost the same as the one year seasonal mean of figure 3.6.

The 3^{rd} column presents the online results (McICA - CTL), where the atmosphere can evolve freely and respond to the modified McICA fluxes. The patterns are very similar to the offline results but the global mean signals are reduced in all cases. This suggests that the cloud variables may be different in the McICA simulation.

Figure 3.9 presents the LWD at SFC and LWU at TOA relative frequency distributions as a function of CWP and CF, and their offline and online relative distribution differences. Similarly to the SW, the global mean offline signals (CTL_{McICA} - CTL) are almost identical to the previous section (see figure 3.7). Since LW signals are much weaker than the SW signals, the LWD increase at SFC and the LWU decrease at TOA are barely visible on these diagrams. For the online signals (McICA-CTL, 3^{rd} column), the relative distribution of differences exhibit different patterns compared to the offline distributions but without any clear tendency. However, the global mean signals are reduced at SFC and approximately the same at TOA.

This reduction in LW signal at SFC, together with the reduction in SW signals, suggest that the differences in cloud variables may be more important in the lower clouds since the LWU at TOA are almost unchanged. However, this may also be a result of canceling signals at TOA. In table 3.6, the ice clouds exhibit the smallest changes in SW global mean signal between offline and online signals, while the mixed clouds exhibits the largest changes. Moreover, table 3.7 shows that the CF, IWV and LWP are slightly reduced in the McICA simulation while the IWP remained almost constant. These atmospheric adjustments and their radiative consequences will be discussed in more detail in the next chapter.

To conclude with the online seasonal mean analysis, it has been shown that:

- The online McICA effects (which include the SW-ACOD and LW-GD corrections removal, the horizontal inhomogeneity introduction and the change of vertical overlap assumption) are diminished for all flux variables except LWU at TOA compared to the offline McICA effects;

  - The results are still a decrease in SWD ratio at SFC and LWU at TOA, and an increase in TOA albedo and LWD at SFC, due to an increased cloud albedo and emissivity;

  - The tendencies (or patterns) as a function of TOTWP or CF remain the same, particularly for the SW signals;

  - The reduction in global mean signal suggests some atmospheric modifications for the McICA simulation, particularly in the low clouds.

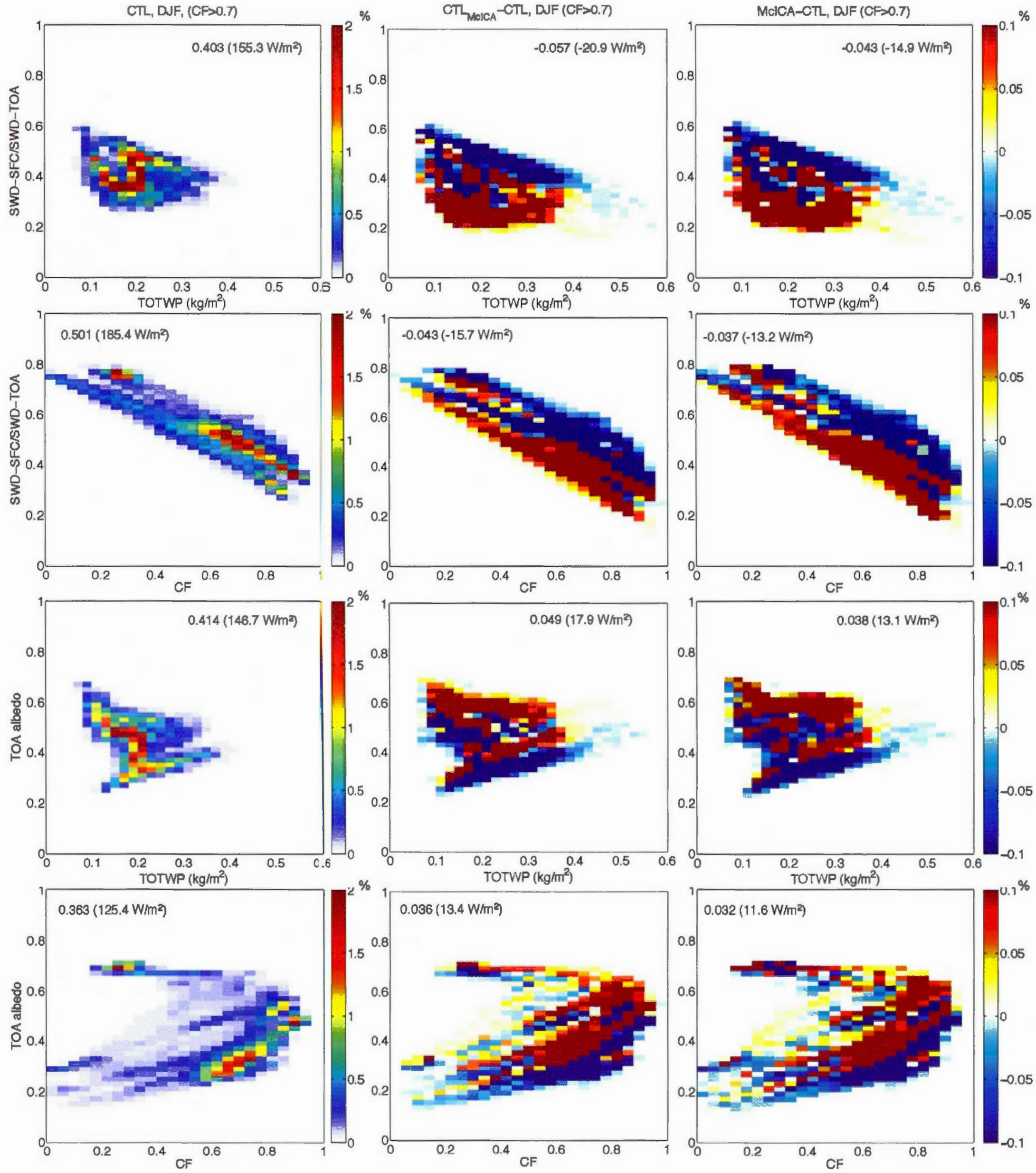

Figure 3.8 SW ratio for the CTL simulation (1^{st} column), SW differences between $\mathrm{CTL_{McICA}}$ - CTL (2^{nd} column) and between McICA - CTL (3^{rd} column) for DJF2007-2009. First and 2^{nd} rows are for SWD ratio at SFC as a function of TOTWP and CF respectively, while 3^{rd} and 4^{th} rows are for TOA albedo. The global mean ratio differences (or the global mean flux differences, i.e. without the normalization by the SWD at TOA) are indicated in each panel.

Table 3.6 Global mean SW ratio and LW flux differences as a function of cloud type for DJF 2007-2009. All conditions is equivalent to co-variability diagrams (as a function of CF) inset information. Values in parenthesis correspond to co-variability diagrams as a function of CWP (for CF>0.7).

cloud type	SWD ratio	TOA albedo	LWD at SFC	LWU at TOA
CTL_{McICA} - CTL				
all	-0.043 (-0.057)	0.036 (0.049)	1.3 (1.7)	-1.6 (-2.0)
liquid	-0.044 (-0.056)	0.040 (0.050)	1.2 (1.5)	-1.6 (-1.8)
ice	-0.040 (-0.050)	0.019 (0.033)	1.7 (2.4)	-1.2 (-2.0)
mixed	-0.049 (-0.056)	0.041 (0.046)	1.7 (1.9)	-1.9 (-2.0)
McICA - CTL				
all	-0.037 (-0.043)	0.032 (0.038)	0.4 (0.3)	-1.7 (-1.8)
liquid	-0.036 (-0.035)	0.033 (0.032)	0.4 (0.3)	-2.2 (-1.7)
ice	-0.035 (-0.042)	0.019 (0.030)	0.5 (0.6)	-1.3 (-1.8)
mixed	-0.039 (-0.044)	0.034 (0.037)	0.4 (0.5)	-1.6 (-1.8)

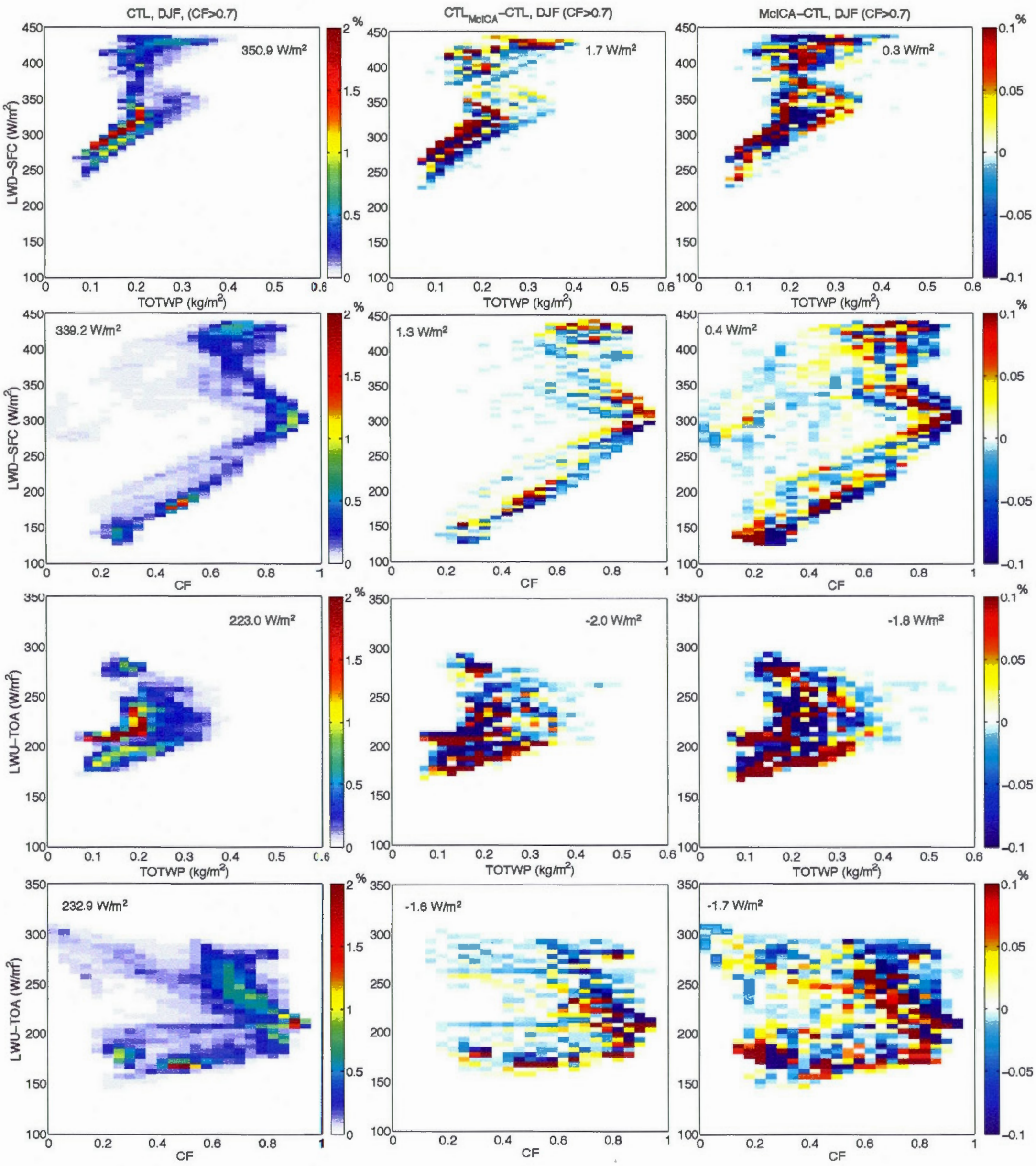

Figure 3.9 LW fluxes for the CTL simulation (1^{st} column), LW flux differences between $\mathrm{CTL_{McICA}}$ - CTL (2^{nd} column) and between McICA - CTL (3^{rd} column) for DJF2007-2009. First and 2^{nd} rows are for LWD at SFC as a function of TOTWP and CF respectively, while 3^{rd} and 4^{th} rows are for LWU differences at TOA. The global mean flux differences are indicated in each panel.

Table 3.7 Global seasonal mean values and differences for DJF and JJA

	CTL DJF/JJA	ΔCTL_{McICA} DJF/JJA	ΔMcICA DJF/JJA
IWV (g/m^2)	23.8 / 26.3	–	-0.2 / -0.3
effective CF (%)	59.3 / 59.9	–	-0.7 / -0.4
true CF (%)	70.9 / 70.1	–	-0.6 / -0.4
LWP (g/m^2)	101.4 / 107.3	–	-2.2 / -2.0
IWP (g/m^2)	38.5 / 39.4	–	0.0 / +0.9
SWD-SFC (W/m^2)	177.8 / 167.1	-15.1 / -14.3	-12.7 / -12.6
SWU-TOA (W/m^2)	120.7 / 109.9	+12.9 / +12.2	+11.2 / +11.5
LWD-SFC (W/m^2)	339.2 / 355.2	+1.3 / +1.3	+0.4 / -0.2
LWU-TOA (W/m^2)	232.8 / 237.8	-1.6 / -1.6	-1.7 / -2.0

3.4 Conclusions

The goal of this chapter was to extricate and explain the McICA contributions at SFC and TOA in the GEMCLIM model. To achieve this, co-variability diagrams were chosen in an attempt to isolate McICA signal tendencies as a function of CWP or CF. The three part analysis (offline instantaneous, offline seasonal mean and online seasonal mean) allowed a step by step analysis of the components that contribute to the seasonal mean signals.

Four main simulations were performed: CTL, HOMOG*, HOMOG and McICA. These simulations allow to assess McICA impacts compared to an homogeneous cloud treatment separately of the overall effect of replacing the SW-ACOD and LW-GD corrections by the McICA methodology.

When using McICA and the SCG, an horizontal inhomogeneity is introduced in

CWP within each model column and the overlap assumption follows an exponential relationship based on decorrelation lengths instead of a MRO. Based on the theory, a decrease in cloud albedo and cloud emissivity is expected with the McICA inhomogeneity treatment, as least for low CWP and particularly for liquid clouds. Inversely, the overlap assumption used in the SCG should lead to a small increase in vertically integrated CF in comparison to the MRO.

Offline results have demonstrated that the dominant McICA effect (compared to an homogeneous cloud treatment) is the horizontal inhomogeneity effect. It effectively produces a decreased cloud albedo and cloud emissivity, which results in an increased SWD at SFC and LWU at TOA and a decreased SWU at TOA and LWD at SFC. One exception is the ice clouds albedo which increases with the horizontal inhomogeneity introduction.

The signal is presented with two components, the global mean signal and the amplitude. Compared to instantaneous results, the maximum amplitude of the signal is reduced for all flux variables on the seasonal scale. However, the global mean signal is increased for the SW on the seasonal scale while remaining the same for the LW. For the SW, the signal is similar between SFC and TOA except for a generalized attenuation of the signal at TOA due to SFC reflection which partly compensates the decreased cloud albedo. For the LW, the SFC signal is more disconnected from the TOA signal with different patterns as a function of CWP and CF.

For the signal tendencies as a function of CWP and CF, the instantaneous time scale results allow to see the decreasing McICA sensitivities with CWP while the increasing effects with CF are visible also on the seasonal time scale.

For the SW, the liquid and mixed clouds are the main contributors to the McICA signals while for the LW, the ice clouds have a more important contribution.

The McICA overlap assumption has smaller and opposite effects compared to horizontal inhomogeneity effects, except for ice clouds where both effects are of the same sign. In general, the overlap assumption decreases the global mean McICA signal.

When replacing the SW-ACOD and LW-GD inhomogeneity corrections of the model by the McICA methodology, the McICA effects are counteracted by the removal of the SW-ACOD and LW-GD corrections. For the GEMCLIM model, this removal has much stronger effects than the McICA introduction which means that the SW-ACOD and LW-GD corrections are stronger (in decreasing the cloud albedo and emissivity) than what McICA produces with the standard SCG parameters. The general results are decreased SWD at SFC and LWU at TOA with increased SWU at TOA and LWD at SFC.

Similarly to the McICA effects, the signal amplitude is reduced on the seasonal scale compared to the instantaneous time scale. However, its global mean signal is also reduced on the seasonal scale. This signal is increasing with CF in all conditions while as a function of CWP, it decreases for the LW at the instantaneous time scale while it increases in all other conditions (at the seasonal scale and for the SW). For all flux variables, liquid and mixed clouds are the principal contributors to this signal.

For all effects, the SW signals are always attenuated at TOA compared to SFC while the LW signals are approximately the same. Moreover, the LW signals are much weaker than the SW signals.

Finally, when looking at the online McICA effects (which include the SW-ACOD and LW-GD removal, the horizontal inhomogeneity introduction and the change of vertical overlap assumption), all global mean signals are reduced except for the LWU at TOA. This suggests some atmospheric adjustments for the McICA simulation. However, the signal tendencies remain the same between offline and online McICA effects.

To conclude, the McICA methodology modifies SW and LW fluxes as expected with a reduced cloud albedo and emissivity (except for the ice cloud albedo) coming from the horizontal inhomogeneity introduction with opposite effects due to the overlap assumptions. A surprise was the intensity of the SW-ACOD and LW-GD inhomogeneity corrections, which, when replaced by the McICA methodology, produces a dominant opposite signal over the whole CWP and CF ranges. The next chapter will explain why this correction, implemented from the literature without any particular tuning, is so strong in the GEMCLIM model.

This chapter has only presented results for the DJF season for practical reasons, but the boreal summer season (JJA) exhibited similar conclusions as presented by table 3.7.

These results are model dependent in a sense that it is a function of: the modeled clouds, which are dependent on the convection and microphysics schemes; the different radiative corrections that are replaced by the McICA methodology; and finally the radiative transfer scheme in itself. However, a clear demonstration was made concerning the greater contribution coming from the horizontal inhomogeneity over the overlap assumptions; how the inhomogeneity impacts wear off rapidly with increasing CWP but increase with CF; how its different impacts are depending on the cloud phase; and on the asymmetry in the McICA radiative impacts between SW and LW fluxes. Particularly, the McICA sensitivity to the CWP and CF that was observed in this study can help understand and anticipate in which cloud regimes it will have more or less radiative impacts. For example, the inhomogeneity introduction will mostly modify cloud albedo for optically thin (liquid) clouds whereas the longwave emissivity will change mostly for ice clouds.

As a last point, it is important to notice that the SCG was used with its basic parameters untouched as this was not a sensitivity study and it may not be the optimal parameter set for this model configuration. This work, an extended parameter sensitivity study, will be presented in the last chapter.

CHAPTER IV

MCICA IN THE GEMCLIM MODEL: COMPARISON WITH GLOBAL OBSERVATIONS

4.1 Introduction

The intention of this chapter is to assess the radiative budget of the GEMCLIM model and its cloud components at TOA and SFC against recent global observation data sets. This will help understand the model biases and how the McICA methodology can change the relationship between cloud and radiative variables. Furthermore, vertical profiles of radiative fluxes are presented and compared between the two model simulations to illustrate the link between SFC and TOA radiative McICA responses.

4.2 Methodology

4.2.1 Model simulations

The two simulations used in this study are the same used in the previous chapter: CTL and McICA. Moreover, CTL_{McICA} offline flux calculations are also presented as a third comparison to help disentangle McICA direct contributions from the model adjustments to the modified fluxes.

As a reminder, the model is run with an horizontal grid mesh of 0.5° and 56 vertical levels, extending up to 10 hPa on a global grid. The model time step is 1200 s whereas the radiative time step is 3600 s. In between the radiative time steps, the LW fluxes and heating rates are constant, whereas the SW fluxes and heating rates are corrected for the change in solar angle. The different simulations are made for the period 2006/11 to 2009/12 both employing observed sea surface temperatures (SSTs) and sea-ice as the lower boundary conditions from the Atmospheric Model Intercomparison Project data set (AMIP, Hurrell *et al.*, 2008). The first month of simulation is excluded from analysis.

4.2.2 Observation data sets and evaluated variables

This study uses 3 years (December 2006-August 2009) of Clouds and the Earth's Radiant Energy System Energy Balanced and Filled (CERES-EBAF) data product for SFC and TOA fluxes and cloud radiative effect (CRE) in 1° zonal bands. CERES-EBAF v2.7 TOA fluxes and CRE are produced with an objective constraint algorithm that adjusts SW and LW TOA fluxes within their range of uncertainty to remove the inconsistency between average global net TOA flux and heat storage in the Earth-atmosphere system (Loeb *et al.*, 2009). It uses instantaneous TOA fluxes from unfiltered radiances (Loeb *et al.*, 2003) for scene types from MODIS (Minnis *et al.*, 2011b).

For surface fluxes and CRE, radiative transfer calculations are performed hourly on the CERES 1° equal-area grid with cloud properties derived from narrowband imagers onboard both EOS Terra and Aqua satellites as well as geostationary satellites. Gridded monthly mean cloud and atmospheric properties are adjusted so that results approach TOA EBAF product and closely match modeled LWD surface fluxes that include active cloud base measurements from CALIPSO and

CloudSat. Uncertainties regarding surface fluxes are below 5 W/m^2 and 3 W/m^2 for the SW and the LW fluxes respectively (Kato *et al.*, 2012), while for TOA fluxes are below 5 W/m^2 (Loeb *et al.*, 2009). The clear-sky TOA fluxes are from cloud free regions both from the CERES footprint and from the MODIS sub-CERES footprint, while at the surface, clear-sky fluxes are adjusted separately to the monthly mean EBAF-TOA clear sky product.

Model clear-sky fluxes are calculated diagnostically at every time step in parallel to the complete radiative transfer calculations. When comparing to observations, one has to be careful since the clear-sky sampling from observations may not come from all atmospheric conditions unlike the model clear-sky fluxes.

For the cloud properties and integrated water vapor (IWV), this study uses two data sets. The first one is MODIS-derived and 3-hourly geostationary satellite cloud properties from the CERES-SYN1deg product available in 1° zonal bands (Minnis *et al.*, 2011a). Whereas the second is the SSM/I (Special Sensor Microwave Imager, F16-v7) available at 0.25° resolution, over ocean only (Wentz, 2013). While SSM/I observations are only available for IWV and LWP, MODIS data set also includes CF and IWP. However, for multi-layered clouds containing ice in the top layers, only an IWP estimate is produced, even if liquid is possibly present in lower cloud layers. Moreover, Minnis *et al.* (2011a) mention that this derived IWP overestimates the total water path (TOTWP), since for a theoretical only ice-cloud, the TOTWP needs to be greater to match the optical depth radiative properties of a cloud containing even only a thin liquid layer. Other issues for the MODIS cloud properties are the great discrepancies seen over ice-covered surfaces against other observations and greater uncertainties for the nighttime derived cloud microphysics properties. Finally, the LWP uncertainties are around $\pm 100 g/m^2$ when compared to AMSR-E (Aqua Advanced Microwave Scanning Radiometer–Earth Observing System) datasets for zonal mean overcast nonprecipitating liquid clouds over ocean (Minnis *et al.*, 2011a), whereas the IWP uncertainties are not available on the global scale.

On the other side, microwave observations have large uncertainties related to the radiative treatment of large precipitating particles and they are only available over ocean. Finally, the better agreements between MODIS and microwaves observations are for warm, non-precipitating, low clouds (Horváth and Davies, 2007). For all these reasons, both data sets are presented for LWP. For IWP, estimations from MODIS are still presented in order to have some insight on the model TOTWP but the absolute biases have to be taken with great caution.

4.3 Results and interpretation

Results are presented in four sections. The first two sections are the comparison between model simulations and observations for the water vapor and cloud variables, followed by the SFC and TOA fluxes. The last two sections present detailed differences between the two simulations, with zonal mean vertical profiles and seasonal mean 2D maps for vertically integrated variables and SFC/TOA fluxes. All results are for three year seasonal means for DJF and JJA.

4.3.1 Modeled cloud variables and water vapor against observations

This section presents cloud variables and integrated water vapor against observations to evaluate the basic atmospheric state of the model that is relevant to radiative fluxes. Only two simulations are compared against observations, CTL and McICA, as the $\mathrm{CTL_{McICA}}$ simulation has, by definition, the same atmospheric state than CTL.

First are presented the cloud fraction (CF), integrated water vapor (IWV), liquid water path (LWP) and ice water path (IWP) in figures 4.1 and 4.2 to assess how the model represents the basic cloud properties. In all figures, the zonal mean is presented for the boreal winter seasonal mean (DJF) for both model and observations as a reference, followed by differences between model and observations for both winter and summer seasonal means (DJF and JJA).

The modeled CF is presented against MODIS observations in figure 4.1 left column. For the model, two variables are presented, the total or "true" cloud fraction (plain lines) as calculated with the maximum-random overlap and the effective cloud fraction (dashed lines) in which the cloud fraction is weighted by the cloud transmittance in the atmospheric window at $\approx 11\ \mu m$ following Ebert and Curry (1992). As seen in the figure, the modeled effective CF is close to observed CF with biases generally below 0.1 for both seasons. One exception is towards the South Pole where the model effective CF underestimates the observed CF but the true CF is closer to it, particularly for DJF. It means that model clouds are too optically thin and that is why it does not show for the effective CF. For both variables, no significant difference appears between the CTL and McICA simulations.

The modeled IWV is presented in figure 4.1 right column against MODIS and SSM/I observation data sets. As the SSM/I is available only over ocean, the modeled IWV has also been filtered over ocean (dashed lines). Model biases are up to 3 g/m^2 at high latitudes but are generally lower than 2 g/m^2 against the two data sets. In this case, the McICA simulation exhibits a significantly different IWV zonal mean compared to CTL, particularly for latitudes north of 30°N for JJA where the values are reduced up to 5%. Note that this signal is not seen in CF even if this diagnostic variable is based on humidity (it will be shown in section 4.3.3 that this IWV decrease is accompanied by a temperature decrease).

Figure 4.2 presents modeled LWP, IWP and TOTWP against MODIS and SSM/I observations. As for the IWV, modeled LWP is filtered over ocean (dashed line, left column) for comparison with SSM/I. Looking at modeled LWP (left column), it is clearly overestimated with respect to either MODIS or SSM/I, except for high latitudes where it is underestimated (approximately south of 50°S for both seasons, north of 45°N for DJF and between 50-70°N for JJA); whereas for modeled IWP (right column) it is a clear underestimate. As the phase separation for MODIS derived LWP and IWP has to be taken with caution, a summation of LWP and IWP from MODIS is also presented (dashed lines, right column) against modeled TOTWP. Compared to this variable, the model overestimate is restricted to latitudes below 30° approximately, with an underestimate over these latitudes. However, as mentioned in section 4.2.2, the TOTWP may be too high in MODIS where ice clouds are occurring. Looking at the three CWP variables together, a conservative conclusion would be that the model has a wrong phase separation (too much liquid and too few ice) with an overall TOTWP overestimate in the Tropics and underestimate over 30°. As seen for CF, no important difference appears between the McICA and CTL simulations for IWP and only small reductions in LWP are visible for McICA, mostly over the Tropics and mid-latitudes.

In conclusion, the model reproduces fairly well the observed CF and IWV but seems to do a poor job at producing the right separation between liquid and ice water content, resulting in a general overestimation of LWP, except polewards, and an underestimation of IWP. The McICA simulation reproduces generally the same cloud properties as CTL.

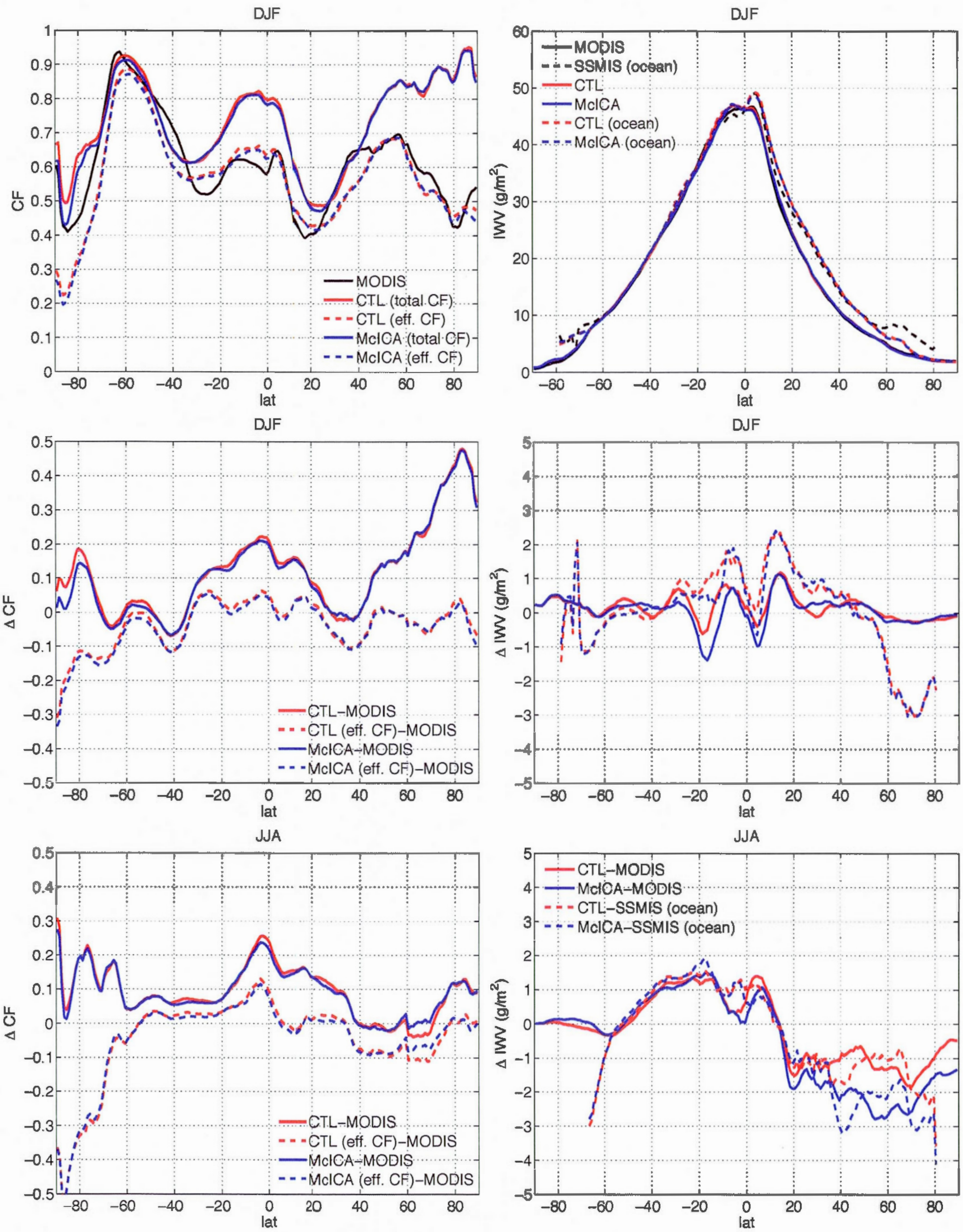

Figure 4.1 Seasonal zonal means for CF (left column) and IWV (right column) for observations (black) and model simulations for DJF (1^{st} row) and differences between model and observations for DJF (2^{nd} row) and JJA (3^{rd} row).

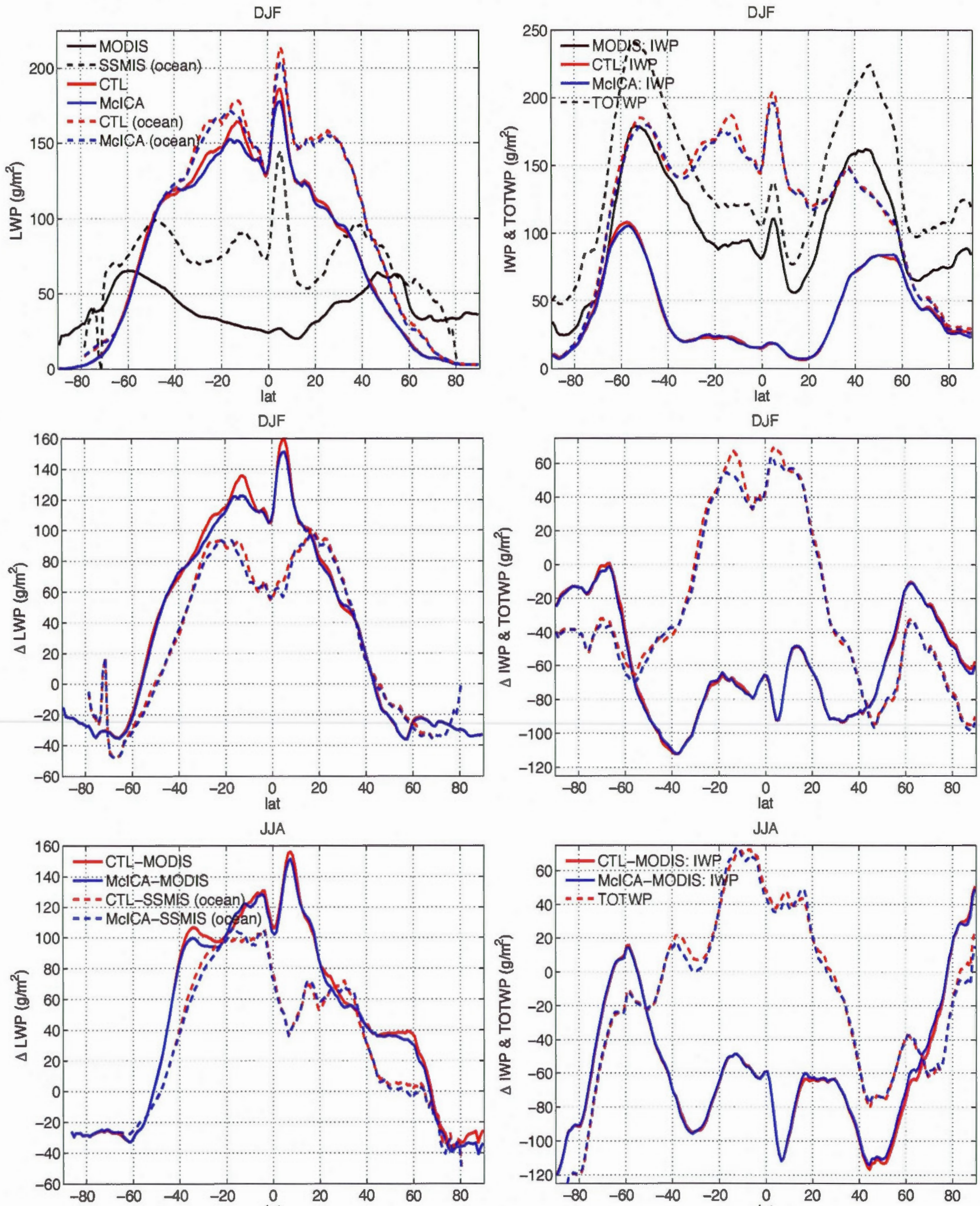

Figure 4.2 As for figure 4.1 but for LWP (left column), IWP (full lines, right column) and TOTWP (dashed lines, right column)

4.3.2 Modeled SFC and TOA fluxes against observations

Looking now at the fluxes for both SFC and TOA, the SW fluxes are first assessed, followed by the LW fluxes and finally the cloud radiative effects (CREs) defined as:

$$CRE = F^{clr} - F^{all} \tag{4.1}$$

following Liou (2002), where F^{clr} is for the clear-sky fluxes and F^{all} is for the all-sky fluxes.

Figure 4.3 presents SWD at SFC and SWU at TOA as well as clear sky fluxes (dashed lines; for SFC fluxes, net clear sky fluxes are presented for technical reasons, with the sign convention SW_{net}=SWD-SWU). Looking at the SWD first (left column), the modeled clear sky net fluxes (the three simulations are collapsing on the same line as expected) are relatively close to observations, except polewards, with better results for DJF compared to JJA. For high latitudes regions, observations are to be taken with caution due to high observational uncertainties over ice-covered surfaces (Minnis *et al.*, 2011a). Looking at differences between the two simulations, the only change between McICA and CTL ($\text{CTL}_{\text{McICA}}$ being exactly the same to CTL, by definition) is for JJA north of 80°N with McICA presenting a very important reduction in net clear sky fluxes. This is mainly coming from the SWU reflected at surface since figure 4.4 shows higher SFC albedo for the McICA simulation.

On the other hand, the modeled all sky SWD are underestimated almost everywhere for both seasons, up to 30 W/m^2 for CTL simulation. This is expected with regards to the overestimate in LWP, but the underestimation does not fade out for high latitudes where LWP becomes underestimated. A significant decrease in biases around 40°S and 40°N is also visible for all simulations and both seasons. This feature could explain why the biases are not fading at higher latitudes with the decreased LWP biases: from these latitudes, the modeled IWP is increasing rapidly towards the poles and could be responsible for the underestimate of SWD at SFC (combined with the clear sky biases for JJA). This could suggest that the IWP biases are not as negative as suggested by MODIS observations and possibly even positive. Another hypothesis would be that ice clouds, even if underestimated in their water content, are wrongly treated in the RT scheme with, for example, wrong effective radius assumption. More specifically, the model has a constant ice effective radius of 15 μm, which could strongly overestimate ice cloud albedo. As a reference, MODIS zonal mean ice effective diameter varies between 42 and 66 μm (not shown).

When looking at $\mathrm{CTL_{McICA}}$ and McICA simulations compared to CTL, the underestimation is even worse (up to $50 W/m^2$) since the SW-ACOD (as explained in section 1.2) is removed and the horizontal inhomogeneity introduction cannot counteract its effects, especially for such large LWP values. Differences between $\mathrm{CTL_{McICA}}$ and McICA simulations are small but fairly constant and could be due to the reduced LWP seen in figure 4.2. It is also coherent with the global mean reduced online McICA signals seen in the previous chapter. These differences are much smaller compared to the McICA and CTL differences, indicating that the atmosphere response to McICA fluxes is not a major contribution in the later. However, for latitudes north of 80°N for JJA, McICA fluxes are higher (presenting lower negative differences against observations) and closer to CTL whereas $\mathrm{CTL_{McICA}}$ fluxes present larger negative biases. A possible cause for this would be that, for thin clouds in that region, the lower McICA LWP values (compared to CTL), seen in figure 4.2, lead to significantly higher McICA SWD fluxes compared to $\mathrm{CTL_{McICA}}$ (which sees the CTL LWP by definition).

For the SWU at TOA (right column), the clear sky SWU are now presented (instead of the net fluxes presented for the SFC). As seen for the SFC fluxes, the modeled clear sky SWU are generally close to observations with few latitudinal band biases reaching 10 W/m^2 except for latitudes over 80°N for JJA where biases are reaching 60 W/m^2 as seen at SFC and linked to SFC albedo overestimate. The all sky modeled SWU biases are generally of similar amplitude as seen for SFC with an important overestimated SWU linked to the overestimated LWP and the increasing IWP towards poles. The main differences between SFC and TOA biases are for latitudes south of 70°S for DJF where the modeled SWU at TOA have almost no bias compared to SWD biases of 20-30 W/m^2, probably due to high reflective SFC reflection compensation. Finally, the difference seen at SFC between McICA and CTL_{McICA} for latitudes north of 80°N in JJA is now reversed for TOA with greater biases seen in McICA than CTL_{McICA} even if the McICA LWP is lower. In this case, the SFC reflexion with the greater clear sky bias (or greater SFC albedo bias) is compensating the lower LWP.

Figure 4.5 presents LW fluxes with the net clear-sky fluxes at SFC presented with reverse sign convention for practical reasons (left column, LW_{net}=LWU-LWD). The net clear-sky LW at SFC are relatively close to observations with larger biases polewards and for JJA. Maximum biases are around 15 W/m^2 for DJF and 25 W/m^2 for JJA. At TOA (right column), clear sky LWU are closer to observations than at SFC with maximum biases around 10 W/m^2. For the LW fluxes, particularly at SFC, the observational sampling for clear-sky fluxes that differs from the model, may have more impacts than for SW, and could be responsible for larger differences seen between model and observations. As for SW fluxes, almost no difference is seen between CTL and McICA at SFC and only small differences are visible at TOA; these differences are coherent with the IWV differences visible in figure 4.1

For the all sky fluxes, LWD at SFC (left column) present smaller biases compared to observations than SW fluxes. However, these biases are still important, reaching

20-30 W/m^2 towards the poles. Biases are generally positive, coherently with the overestimated LWP and the increasing IWP where the LWP biases disappear. On the other hand, regions of negatives biases, like for latitudes south of 70°S and between 30-70°N, for JJA, are coherent with the underestimate of effective CF (in figure 4.1) which means that clouds are optically too thin, also corresponding to regions with higher IWP negative biases. For LWU at TOA (right column), biases are generally negative, again coherently with the overestimated LWP. TOA biases are smaller compared to SFC and, contrarily to SW fluxes, are not as related in their zonal patterns, to SFC biases. One difference is that the LWU biases are minimal in the Tropics and maximal from the mid-latitudes to the poles. This could be supported by the hypothesis that the ice effective radius is too small in the model, which leads to an overestimate of ice cloud optical depth, hence reducing the LWU at TOA.

Comparing the two simulations, differences in LW flux biases are much smaller than for the SW fluxes. As expected from chapter 3, $\mathrm{CTL_{McICA}}$ generally follows CTL biases, with a small constant increase in LWD at SFC and decrease in LWU at TOA, as it has been shown that replacing the LW-GD corrections by McICA produces increased cloud emissivity. For the McICA simulation, LWD at SFC are between the $\mathrm{CTL_{McICA}}$ and CTL fluxes, suggesting some atmospheric adjustments as seen in chapter 3. One exception is visible in the zonal band between 40-70°N for JJA, where the McICA LWD are smaller than CTL, coherently with the IWV differences between CTL and McICA seen in figure 4.1. However, at TOA, McICA follows more the $\mathrm{CTL_{McICA}}$ LWU fluxes and exhibits greater differences in particular regions. North of 40°N in JJA, McICA presents decreased LWU at TOA, oppositely to what is expected with a decreased IWV. It will be shown in section 4.3.3 that it can be related to an important decreased temperature going from the surface up to 250 hPa.

Figure 4.6 presents CREs for SW (left column) and LW (right column) for both SFC (dash lines) and TOA (full lines). The modeled SW CREs are too strong (as expected from the overestimated cloud albedo) for both seasons and biases are generally slightly lower for SFC compared to TOA. McICA have more important biases (up to 20 W/m^2 greater) even for JJA for latitudes north of 80°N where McICA SW CRE biases are becoming positive. This is coherent with the greater McICA net clear sky SW fluxes at SFC compared to CTL combined with the similar all sky SWD fluxes.

On the contrary of SW CREs, LW CREs are very different between SFC and TOA with greater CREs at SFC from mid-latitudes to poles and greater CREs at TOA in the Tropics. The modeled LW CREs have smaller biases compared to modeled SW CREs, particularly for TOA where biases are generally positive and within 10 W/m^2. For SFC, modeled LW CREs have also general positive biases, up to 20 W/m^2 except for JJA between 20-70°N where a negative bias is seen as reported for the LWD at SFC (figure 4.2). The greater LW CREs biases at SFC compared to TOA can be expected, since the dominant model bias is concerning the liquid clouds, which have more impacts on the LW fluxes in the lower atmosphere, in comparison to the ice clouds that have more influence on the LWU at TOA.

This section has shown that the general trends are:

- Clear sky fluxes are relatively close to observations (within 10 W/m^2) for both SW and LW at SFC and TOA, with better results for DJF than JJA and growing biases towards poles. Almost no distinction is seen between CTL and McICA simulations.
- All sky SW fluxes are underestimated at SFC and overestimated at TOA for all seasons due mainly to the large overestimation of modeled LWP. However, for high latitudes where modeled LWP is not overestimated, the SW biases

are still present possibly due to too low ice effective radius. Patterns are very similar between SFC and TOA, as expected.

- The McICA simulation exhibits greater SW biases (up to 20 W/m^2 greater) due to the SW-ACOD correction removal primarily. The differences between $\mathrm{CTL_{McICA}}$ and McICA are small compared to CTL suggesting that the atmosphere modifications are not important contributors to SW flux responses.

- Coherently, the SW CREs are overestimated at SFC and TOA with McICA having bigger biases than CTL.

- All sky LW fluxes are generally overestimated at SFC and underestimated at TOA, coherently with the overestimation of modeled LWP and possibly the too low ice effective radius. Biases are generally smaller than for SW fluxes, smaller for DJF compared to JJA, as well as smaller at TOA compared to SFC. The LW CREs exhibit the same features with general positive biases and smaller biases at TOA compared to SFC.

- Differences between simulations are much smaller than for SW fluxes with McICA LW biases being slightly greater, both at SFC and TOA meaning that cloud emissivity is enhanced with the McICA methodology. However, $\mathrm{CTL_{McICA}}$ and McICA differences are now of the same order of McICA and CTL differences, meaning that the atmospheric modifications in McICA simulations are playing an important role in the modified LW fluxes.

However, some zonal exceptions are also present:

- For clear sky fluxes, an exceptional bias (up to 60 W/m^2) is shown for McICA SW fluxes over 80°N in JJA linked to higher SFC albedo for that simulation.

- Some regions exhibit different SW bias trends between SFC and TOA: south of 70°S for DJF, smaller biases are seen at TOA probably due to SFC reflexion compensation; and between 30-60°N for JJA, the TOA biases are greater than SFC biases, may be linked to the model SFC albedo small overestimation.

- For LW fluxes, a region over 40°N for JJA exhibits decreased LWD for McICA simulation compared to CTL. This could be linked to the decreased IWV in McICA or other variables like temperature that will be presented in the next section.

4.3.3 Differences in modeled zonal vertical profiles

This section presents zonal mean vertical profiles for SW and LW fluxes to help understand the link between the different radiative responses to McICA methodology at SFC and TOA presented in the previous section. Other variables such as CF, total water content (TOTWC), temperature (T) and absolute humidity (HU) are presented to see how the atmosphere vertical structure is modified in response to McICA fluxes over the three year period.

First is presented the vertical structure of CF and TOTWC in figure 4.7 with differences between McICA and CTL. The modified McICA atmosphere exhibits differences up to 0.05 for CF and $7.5*10^{-3}$ g/kg for TOTWC with slightly more negative occurrences for the winter season. At the two poles, both variables are reduced in the McICA simulations for both seasons. The low clouds also exhibit slightly reduced TOTWP and CF, particularly for DJF, that were only slightly visible in their corresponding vertically integrated variables of the previous section (figures 4.1 and 4.2).

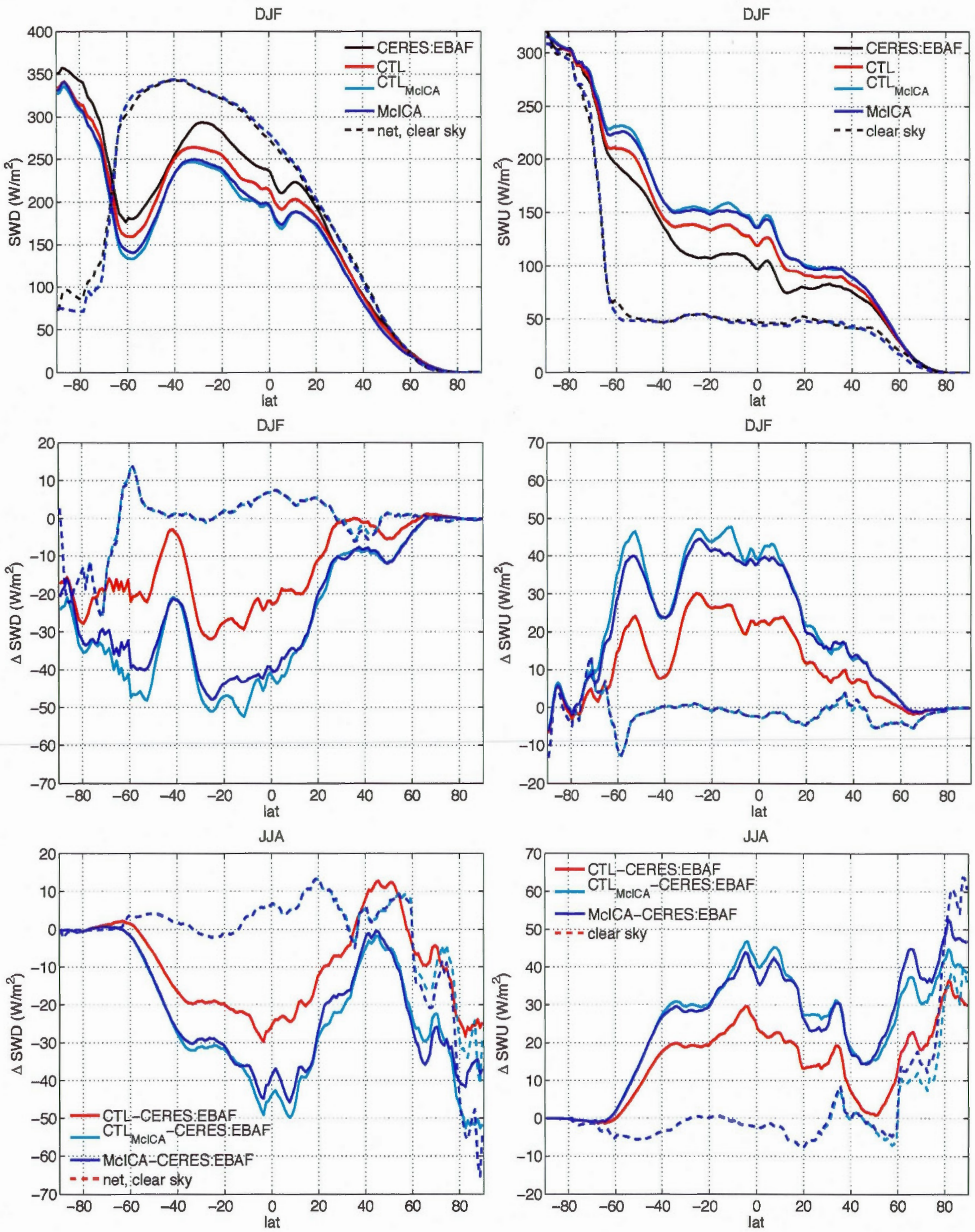

Figure 4.3 Seasonal and zonal mean SWD at SFC (left column) and SWU at TOA (right column) for observations (black) and model simulations for DJF (1^{st} row) and differences between model and observations for DJF (2^{nd} row) and JJA (3^{rd} row).

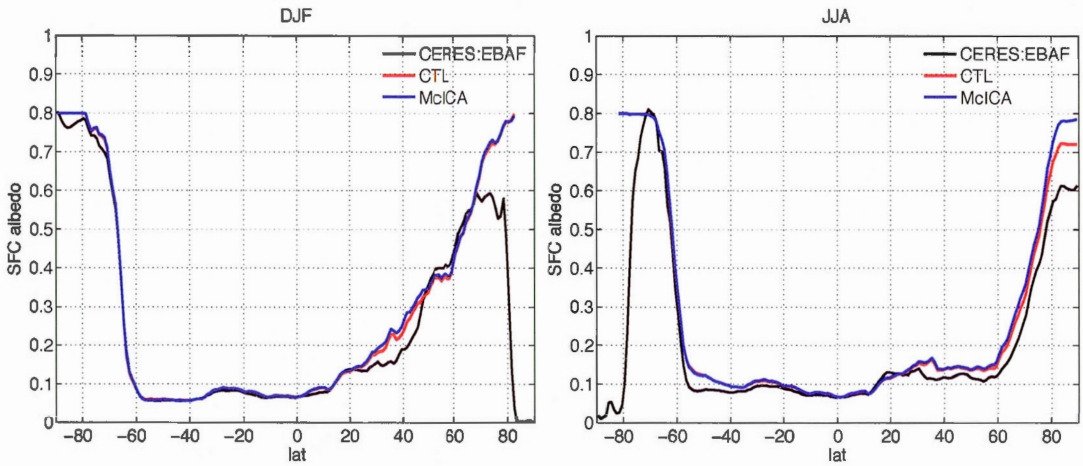

Figure 4.4 Surface albedo for DJF (left) and JJA (right).

Figure 4.8 presents how the SW fluxes are modified with McICA. The CTL_{McICA}-CTL differences (2^{nd} row for DJF and 5^{th} row for JJA) show how the fluxes are modified with the McICA methodology without any changes to the atmospheric conditions. It is clear from the SWD fluxes how the cloud albedo is increased, particularly for low clouds due to the SW-ACOD removal which is proportional to cloud optical depth. The resulting SWU are increased from the low level clouds and up, except for latitudes south of 70°S for DJF. For this region, high ice clouds have little condensate and are probably more scattering than reflecting SWD, and this is reduced with CTL_{McICA}. Moreover, as seen in the top panel for CTL, the SWU are mainly coming from surface reflection, which is reduced by the reduced SWD reaching SFC for CTL_{McICA}.

Looking at McICA-CTL differences, which includes atmospheric interactions with McICA fluxes, the McICA signal is still predominant with fluctuations that slightly reduce the signal for DJF and even increase the signal for SWU for JJA for latitudes north of 45°N. In that later case, both CF and TOTWC are increased for low to mid-level clouds, increasing the reflected SWU, but for high clouds,

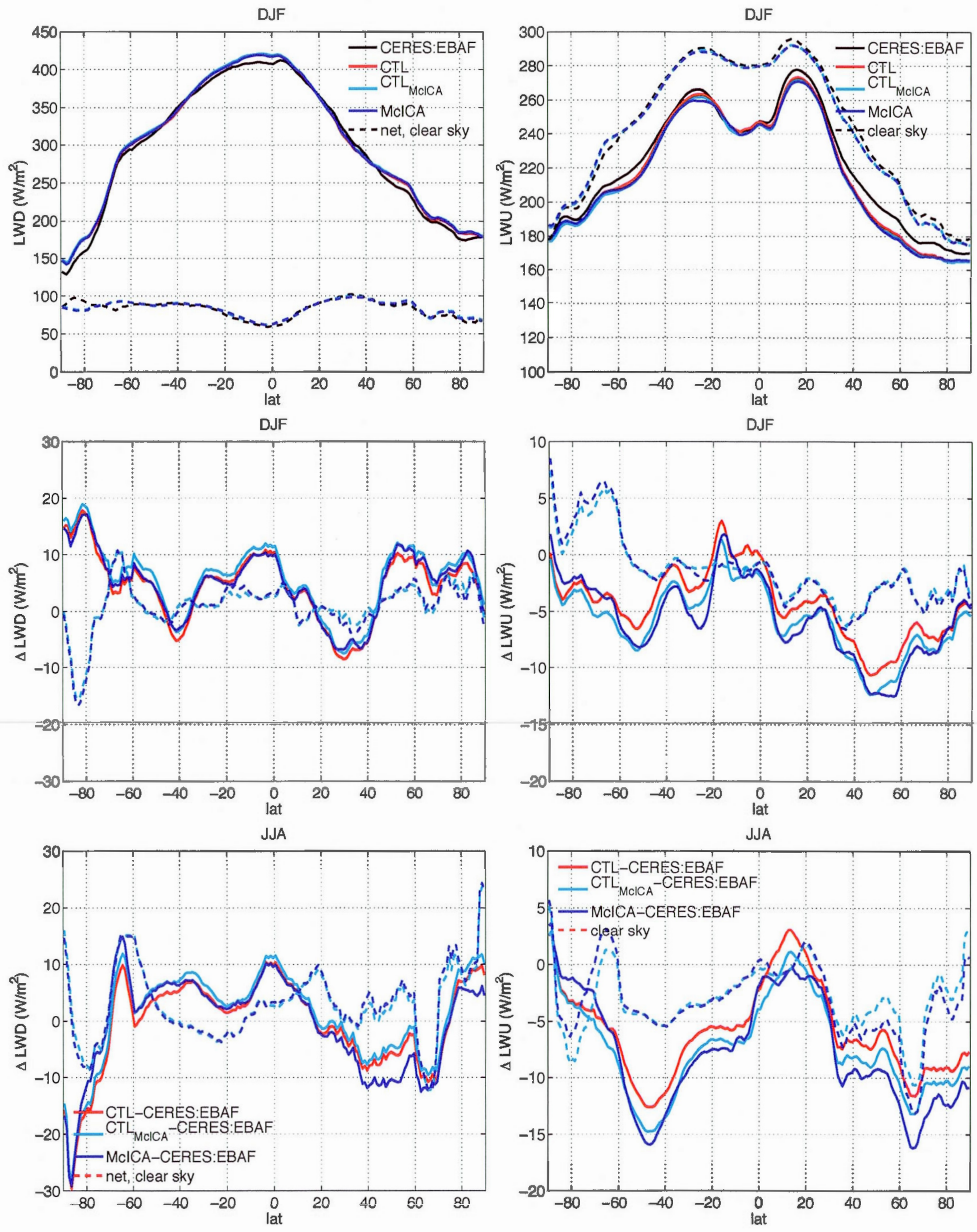

Figure 4.5 As figure 4.3 but for LWD at SFC (left column) and LWU at TOA (right column).

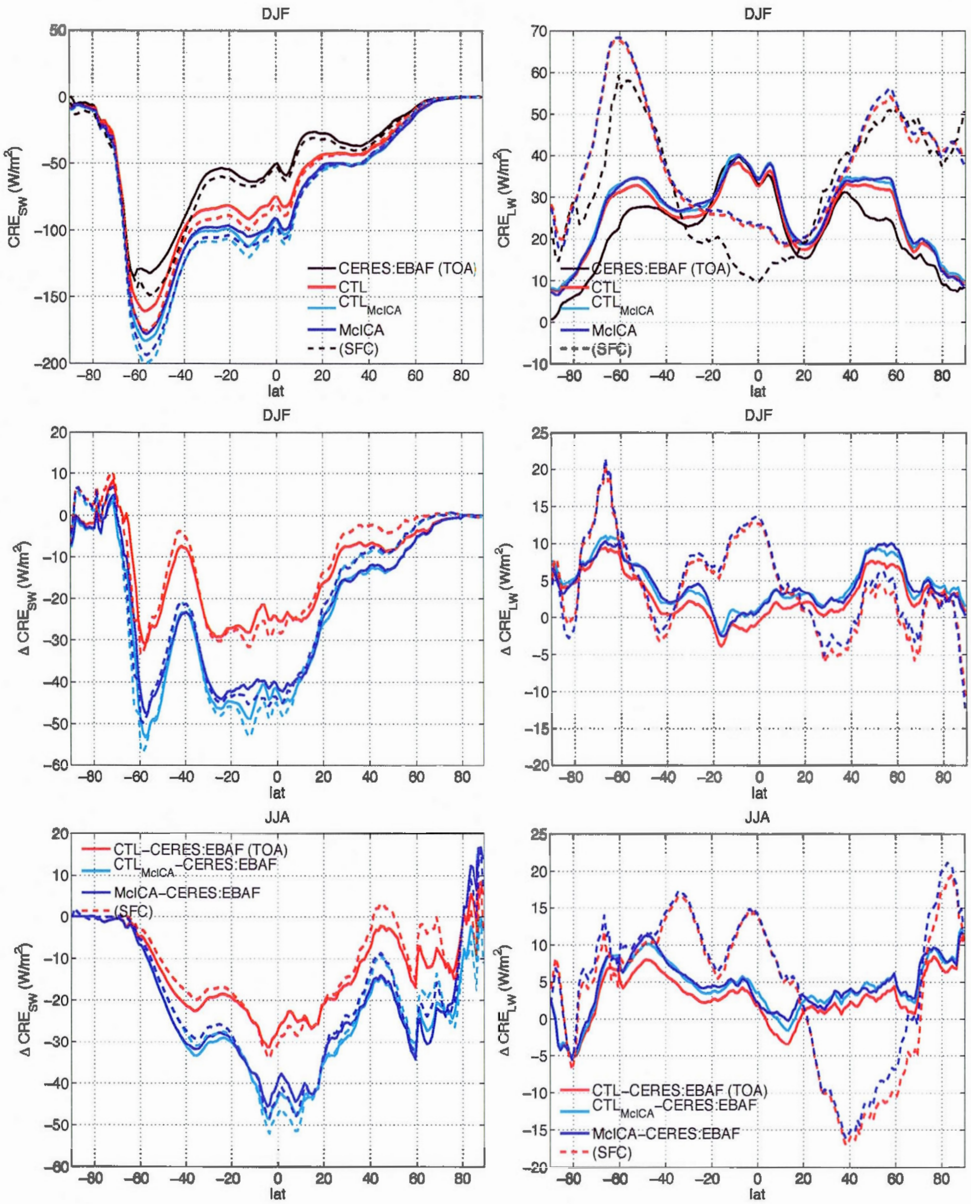

Figure 4.6 Seasonal and zonal mean CRE_{SW} (left) and CRE_{LW} (right) at SFC (dashed lines) and at TOA (full lines) for observations (black) and model simulations for DJF (1^{st} row) and differences between model and observations for DJF (2^{nd} row) and JJA (3^{rd} row). For convenience, the SFC $CRE_{SW/LW}$ sign convention is reversed in this figure.

TOTWC is decreased resulting in a cancellation of the SWD reduction in that region for McICA compared to CTL. This combination leads to the greater TOA biases (compared to SFC) seen in the previous section.

In figure 4.9, temperature (T) and absolute humidity (HU) vertical profiles are presented with their differences as they are key variables, together with CF and TOTWC, for LW fluxes. It is clear that T and HU modification structures are more organized than what was seen for CF and TOTWC (figure 4.7). For DJF, a marked T difference dipole is seen above 250 hPa with a general decrease in both T and HU below 250 hPa except for few zonal bands. For JJA, a heating and moistening is visible for latitudes south of 60°S while the opposite is more striking for latitudes north of 30°N.

Looking now at LW fluxes in figure 4.10, differences between CTL_{McICA} and CTL show how the McICA methodology increases the cloud emissivity or enhanced its greenhouse effects by increasing LWD and decreasing LWU for all seasons and latitudes. However, differences between McICA and CTL exhibit how the LW fluxes are dominated by atmospheric modifications of cloud, water vapor and temperature. For DJF, the general McICA effect of increasing LWD is still visible even with the generally decreased T with small zonal bands of decreasing LWD where the HU, CF and TOTWC are decreasing the most. However, these opposite trends are not visible in the LWU differences. Moreover, bands of no difference or slight increased LWU are more correlated with T differences.

For JJA, differences between McICA and CTL are more homogeneous through latitude bands. Looking at the North Hemisphere, the decreased LWD and LWU fluxes are corresponding to the decreased T and HU for latitudes north of 30°N. Even if CF and TOTWP exhibit patches of increased values, HU differences have more impacts on LW fluxes as contrary of DJF. Around 15°N, both CF and

TOTWC are contributing to the increased LWD and decreased LWU. For the South Hemisphere, the increased LWD seems to come from increased high cloud CF, increased TOTWC for mid-level clouds, with a high altitude increased T, and a strong T increased for the whole atmosphere south of 60°S. Where the increased T is dominating, an increased LWU is also seen, whereas when the increased LWD is more linked to water variables, it results in a decreased LWU.

Finally, the visible and infrared heating rates (VIS-HR and IR-HR) zonal mean vertical profiles are presented in figure 4.11. The $\mathrm{CTL_{McICA}}$ differences show that McICA methodology has the effect of heating more the low cloud layers and high cloud layers through SW fluxes with a reduced heating below these cloud layers. For JJA, the increased heating for low clouds is only visible in the Tropics as there is less CF and TOTWC over the North hemisphere mid-latitudes compared to the South hemisphere. For the IR-HR, $\mathrm{CTL_{McICA}}$ exhibits increased cooling for the low and high clouds. The separation between increased and reduced cooling is located higher in the cloud layers (particularly for low clouds) compared to the VIS-HR. Besides, the IR-HR scale is 2.5 times the VIS-HR scale. The McICA differences are much noisier through the cloud layers and $\mathrm{CTL_{McICA}}$ remaining signals are only visible at SFC and for high clouds.

Looking at the sum of the visible and infrared HR, or the NET-HR, in figure 4.12, it is clear that the IR-HR is dominating with a general cooling except for TOA and SFC in the Tropics where a small heating is visible. For high clouds, the $\mathrm{CTL_{McICA}}$ signal is also dominated by the IR-HR tendencies with more cooling at cloud tops and less below. For low clouds, as the VIS-HR and IR-HR tendencies are partly overlapping, the increased cooling is reduced for cloud tops and the reduced cooling is still present in clouds and below. Looking at the McICA-CTL NET-HR, the low cloud dipoles seen for $\mathrm{CTL_{McICA}}$-CTL lose their clear structures and the signal amplitude is generally reduced. These modifications from offline to online heating rates could explain how the McICA low cloud adjustments are taking place: i.e. a reduced cooling in the lower atmosphere could reduce CF or TOTWP, and in turn, it would modify the online HR.

The goal of this section was to demonstrate how the McICA methodology changes radiative fluxes in the vertical as well as how the atmospheric structure is modified. The general results are:

- For SW fluxes, zonal mean vertical profiles show that McICA effects of increased cloud albedo is dominant for low clouds (as expected since the SW-ACOD removal effects are stronger with greater cloud optical depth);
- The McICA simulation exhibits these McICA effects with small modifications compared to the offline signal (CTL_{McICA}) due to CF and TOTWC modifications;
- For LW fluxes, the offline signal shows how cloud emissivity is increased for all clouds (due to LW-GD correction removal);
- However, as mentioned in the previous section, the online signal is greatly modulated by atmospheric changes in T, HU, CF and TOTWC;
- Differences between CTL and McICA simulations are more striking in the T and HU zonal mean profiles compared to CF and TOTWC: for JJA, a general decrease in T and HU is visible over the North hemisphere while for CF and TOTWC, signals are noisy except for a reduction of both variables over the poles at both seasons;
- LWD seems to be more correlated to changes in cloud and water variables (CF, TOTWC and HU) whereas for LWU, it seems more correlated to T changes;

- Even if SW differences are almost three times the LW differences, IR-HR differences are approximately two times greater than the VIS-HR, resulting in offline McICA NET-HR effects of increased cooling at high and low cloud tops, and reduced cooling at low cloud bases;

- Online McICA NET-HR effects are very noisy (similarly to LW effects) with the increased cooling at high cloud top still visible.

4.3.4 Local differences in modeled SFC and TOA fluxes

This section looks in more detail the different areas that present opposite patterns to the general zonal mean differences between McICA and CTL fluxes at TOA and SFC.

As shown in section 4.3.2 with the zonal means, the main McICA effects are to increase SWU at TOA and LWD at SFC and oppositely, to decrease SWD at SFC and LWU at TOA. Looking at figure 4.13 for DJF seasonal mean, these general tendencies are clear, particularly for SW fluxes, and with more variations for LW fluxes since LW fluxes respond as strongly to McICA modifications as to atmospheric state modifications as shown in section 4.3.3.

For the SW fluxes, only few areas are presenting opposite signals, with an increased SWD at SFC and a reduced SWU at TOA. To try to explain what processes underly these opposite signals, four of these regions are highlighted (with grey rectangles) in figure 4.13 : west of the Baja California coast over the Pacific Ocean, west of the Sahel region over the Atlantic Ocean, south-east of the Brazilian coast over the Atlantic Ocean and north of the Australian coast over the Pacific Ocean. As a reference, three other regions over the Pacific and Atlantic oceans around 60°S and equator are chosen and highlighted by grey ovals. For the LW fluxes, the

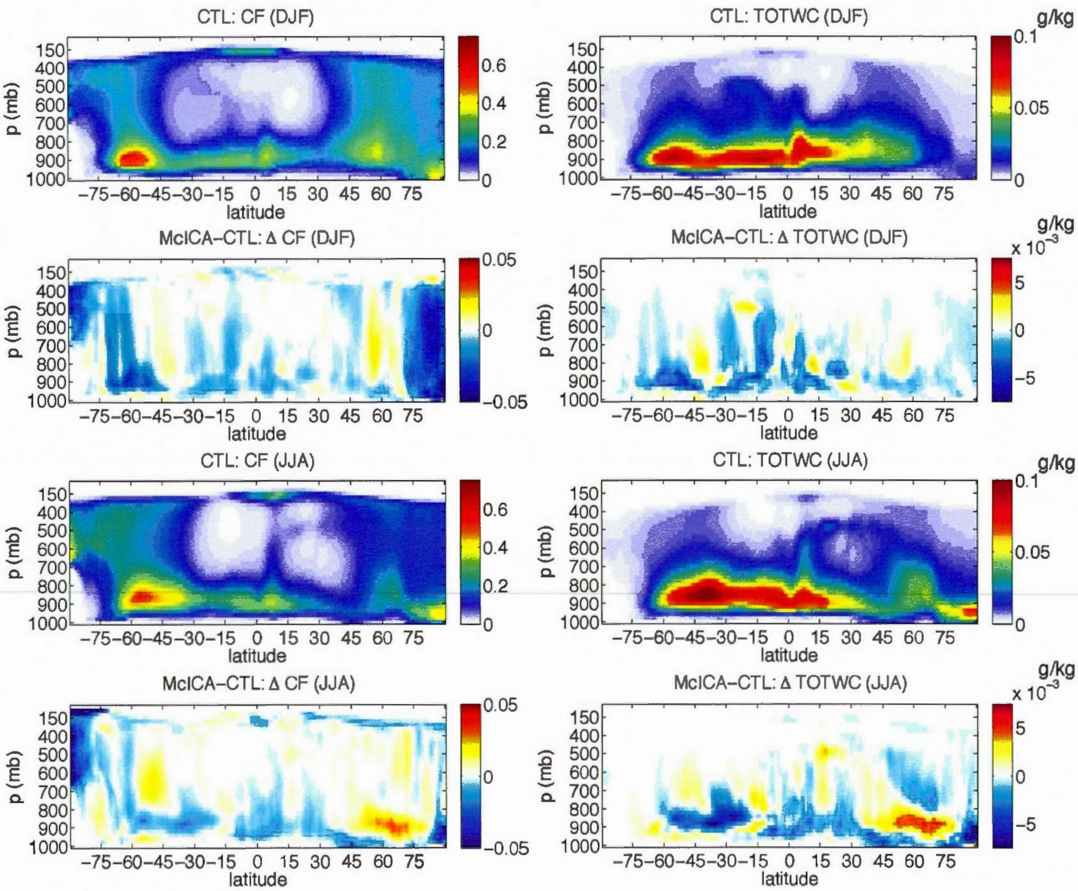

Figure 4.7 Zonal mean vertical profiles for CF (left column) and TOTWC (right column) for CTL and absolute differences for McICA-CTL for DJF (1^{st} and 2^{nd} rows) and JJA (3^{rd} and 4^{th} rows).

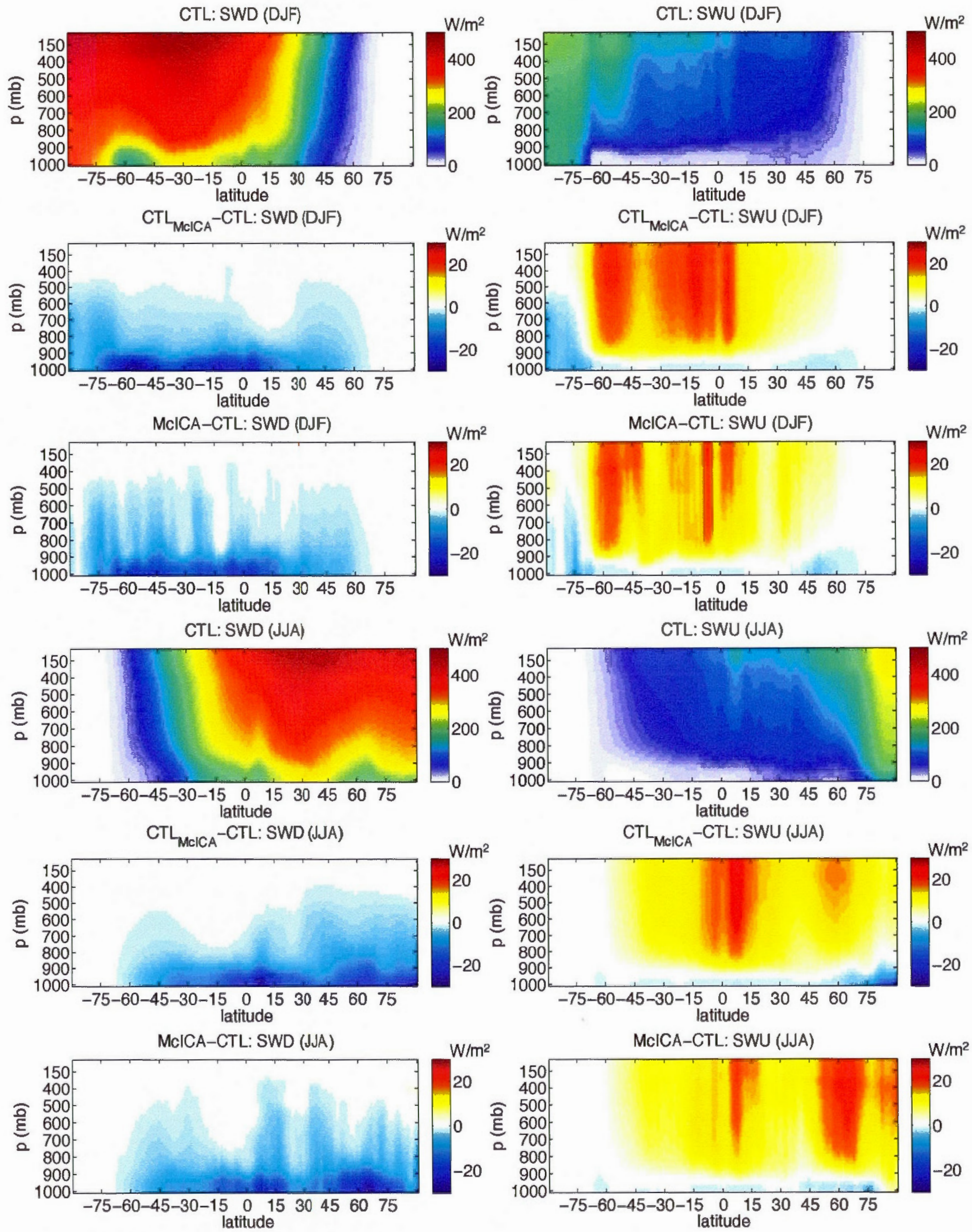

Figure 4.8 Zonal mean vertical profiles for SWD (left column) and SWU (right column) for CTL and differences for $\mathrm{CTL_{McICA}}$-CTL and McICA-CTL for DJF (1^{st} to 3^{rd} row) and JJA (4^{th} to 6^{th} row).

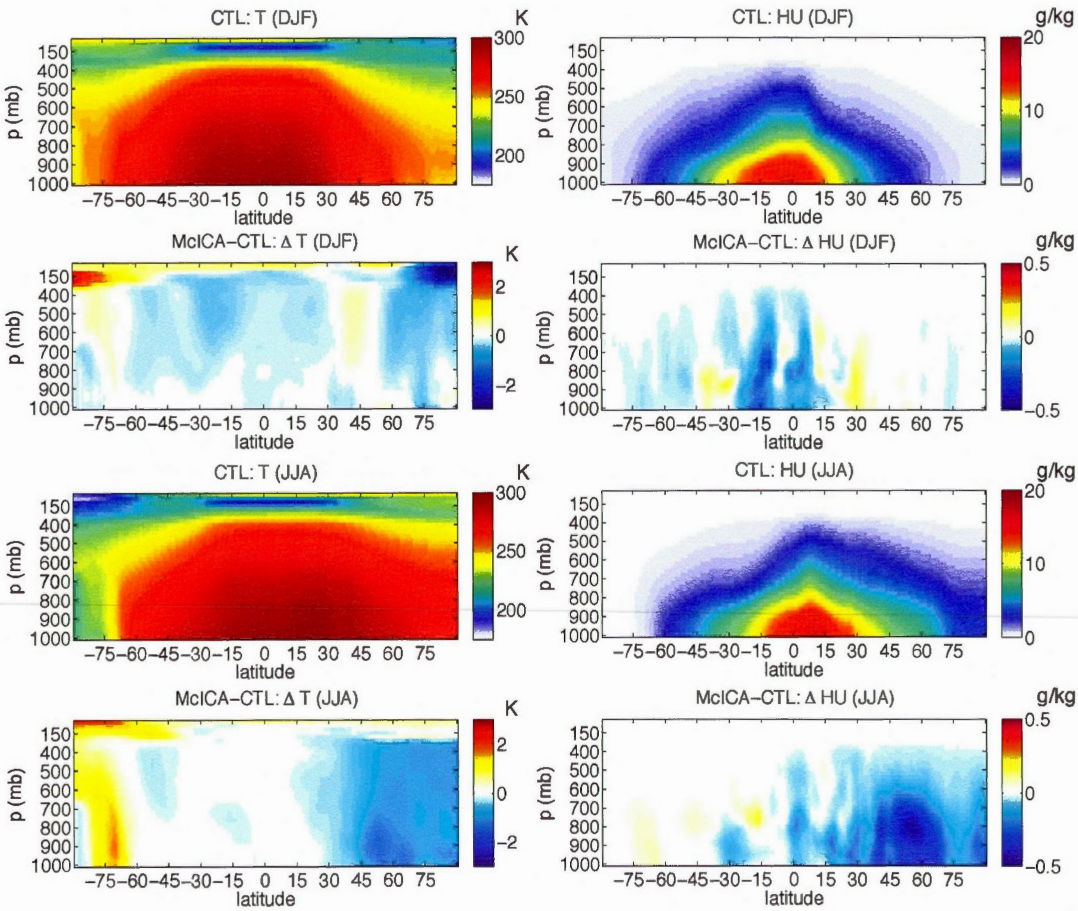

Figure 4.9 Zonal mean vertical profiles for T (left column) and HU (right column) for CTL and differences for McICA-CTL for DJF (1^{st} and 2^{nd} row) and JJA (3^{rd} and 4^{th} row).

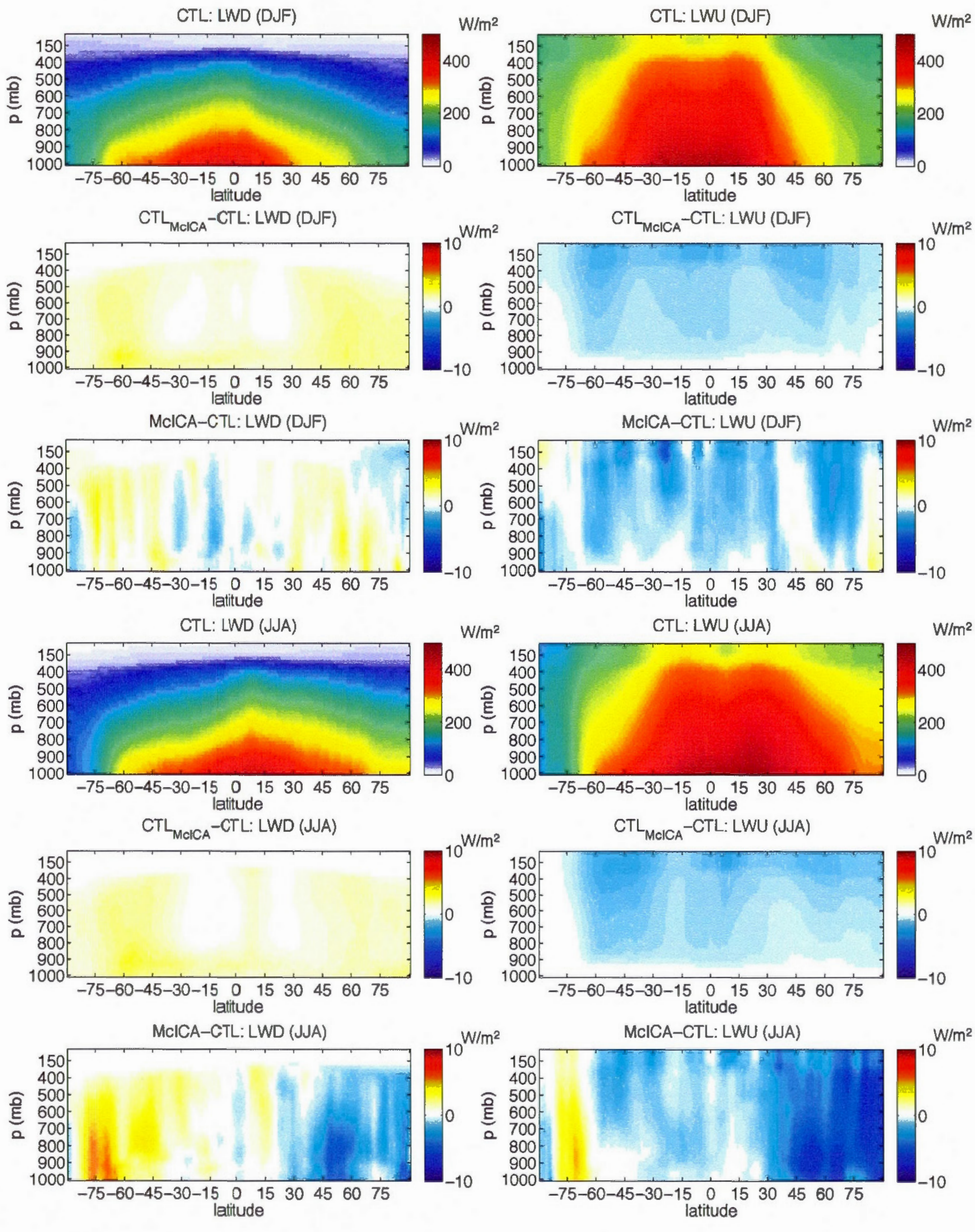

Figure 4.10 As figure 4.7 but for LWD (left column) and LWU (right column).

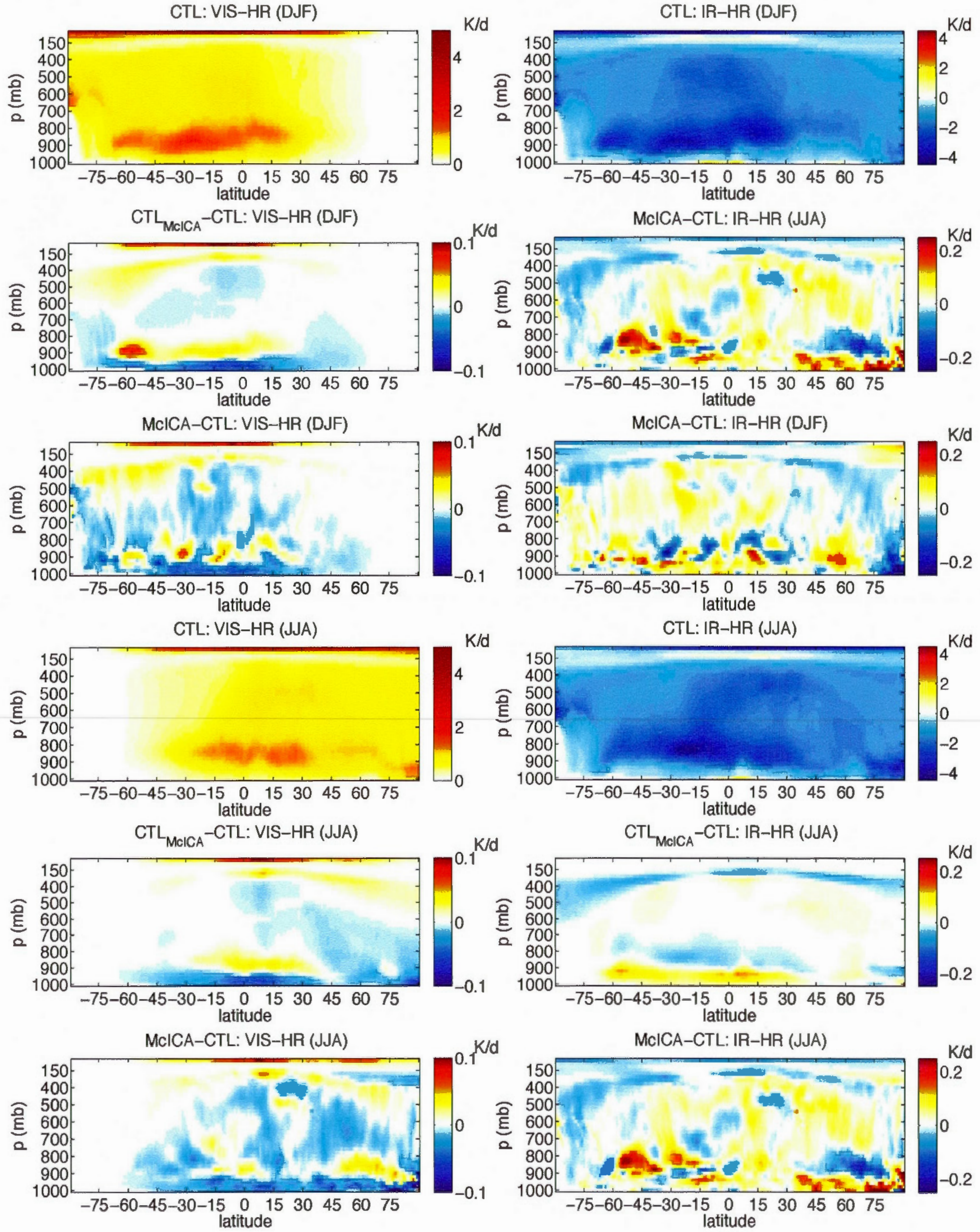

Figure 4.11 As figure 4.7 but for VIS-HR (left column) and IR-HR (right column).

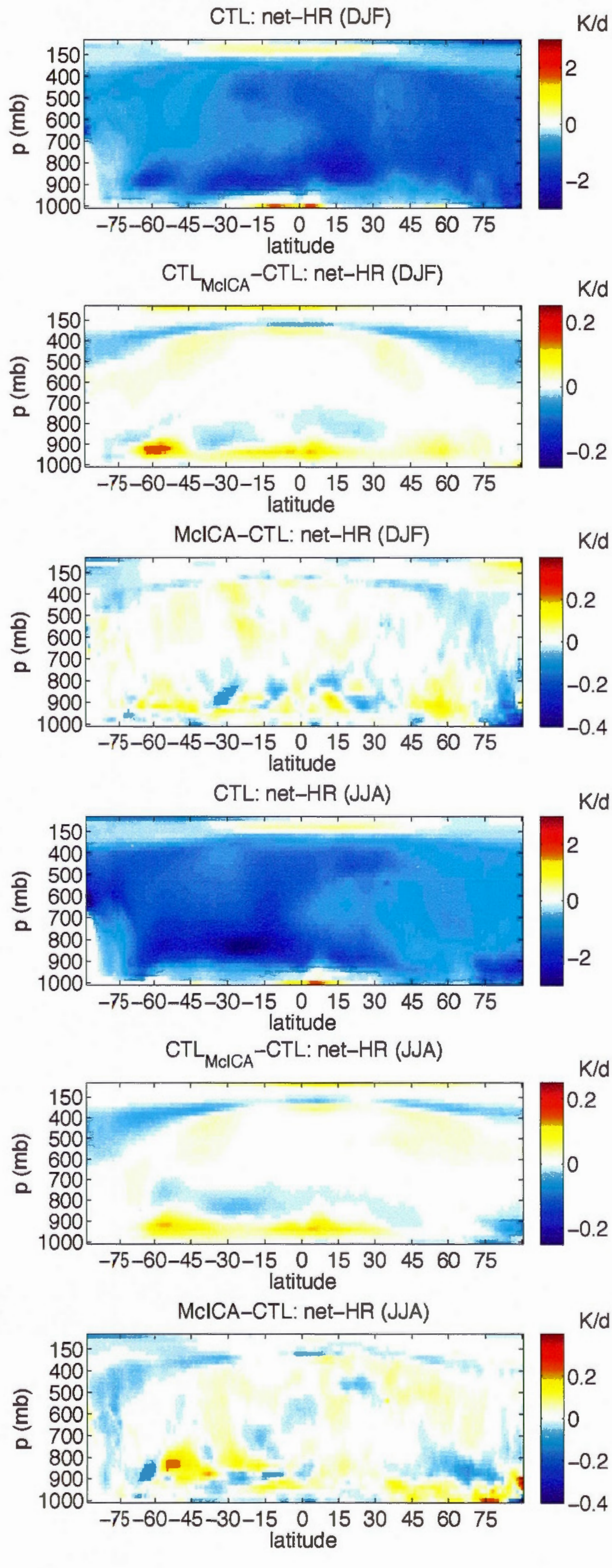

Figure 4.12 As figure 4.11 but for NET-HR.

rectangle regions are also exhibiting opposite signals (decreased LWD at SFC and increased LWU at TOA) compared to the zonal average but it is not restricted to these areas as even the oval reference areas are sometimes exhibiting the same opposite signals.

Looking first at the offline McICA signal ($\mathrm{CTL_{McICA}}$-McICA) in figure 4.14, the rectangle regions are sometimes showing a weaker signal (for SW fluxes west of the Baja California coast and west of the Sahel region) but all regions, rectangles and ovals, are showing the same trends of increased cloud albedo and emissivity under the same atmospheric conditions as CTL.

Figure 4.15 presents differences in IWV, effective CF, LWP and IWP between McICA and CTL. Over the four rectangle regions, all variables are decreasing with different strengths. This could explain a decrease in cloud albedo and emissivity (from less TOTWP) and a decrease in cloud effects (from less CF), hence resulting in an increased SWD at SFC and LWU at TOA, and a decreased SWU at TOA and LWD at SFC, as it is seen in figure 4.13. However, looking at the reference regions in ovals, the same tendencies are visible for all four variables except for IWV over one region. These reductions in IWV, TOTWP and effective CF do not lead to increased SWD at SFC, reduced SWU at TOA, or not always to decreased LWD at SFC and increased LWU at TOA in these regions.

Thus, for all these regions, generally over ocean, modifications to cloud variables and IWV do not seem to be entirely responsible for the opposite differences in radiative fluxes between McICA and CTL. In the rectangle regions, the cloud albedo and emissivity are reduced, as it was seen in chapter 3 when McICA was compared to homogeneous cloud treatment. In other words, when the SW-ACOD and LW-GD correction removal effects (of increasing of cloud albedo and emissivity) are low, the McICA horizontal inhomogeneity introduction effects become visible with reduction of cloud albedo and emissivity. These effects were shown to be visible for specific conditions like low CF or low CWP but generally disappear over seasonal mean. Figure 4.16 shows the same variables as figure 4.15 but for the CTL simulation. The common feature to the rectangle regions is the lower effective CF (generally below 0.6) contrary to the oval regions. In conclusion, the combination of low effective CF and reduced water variables allows the McICA horizontal inhomogeneity introduction effects to counteract the SW-ACOD and LW-GD correction removal effects of increasing cloud albedo and emissivity.

Looking back at figure 4.13, other regions exhibit small but opposite trends in SW fluxes such as over north India and the west Mediterranean basin. These regions exhibit the same decrease in water variables but more importantly, the same lower effective CF. Finally, the LW fluxes are less coherent in their responses to McICA fluxes with much more opposite signals than the four rectangle regions as they are more correlated to IWV and cloud variable modifications.

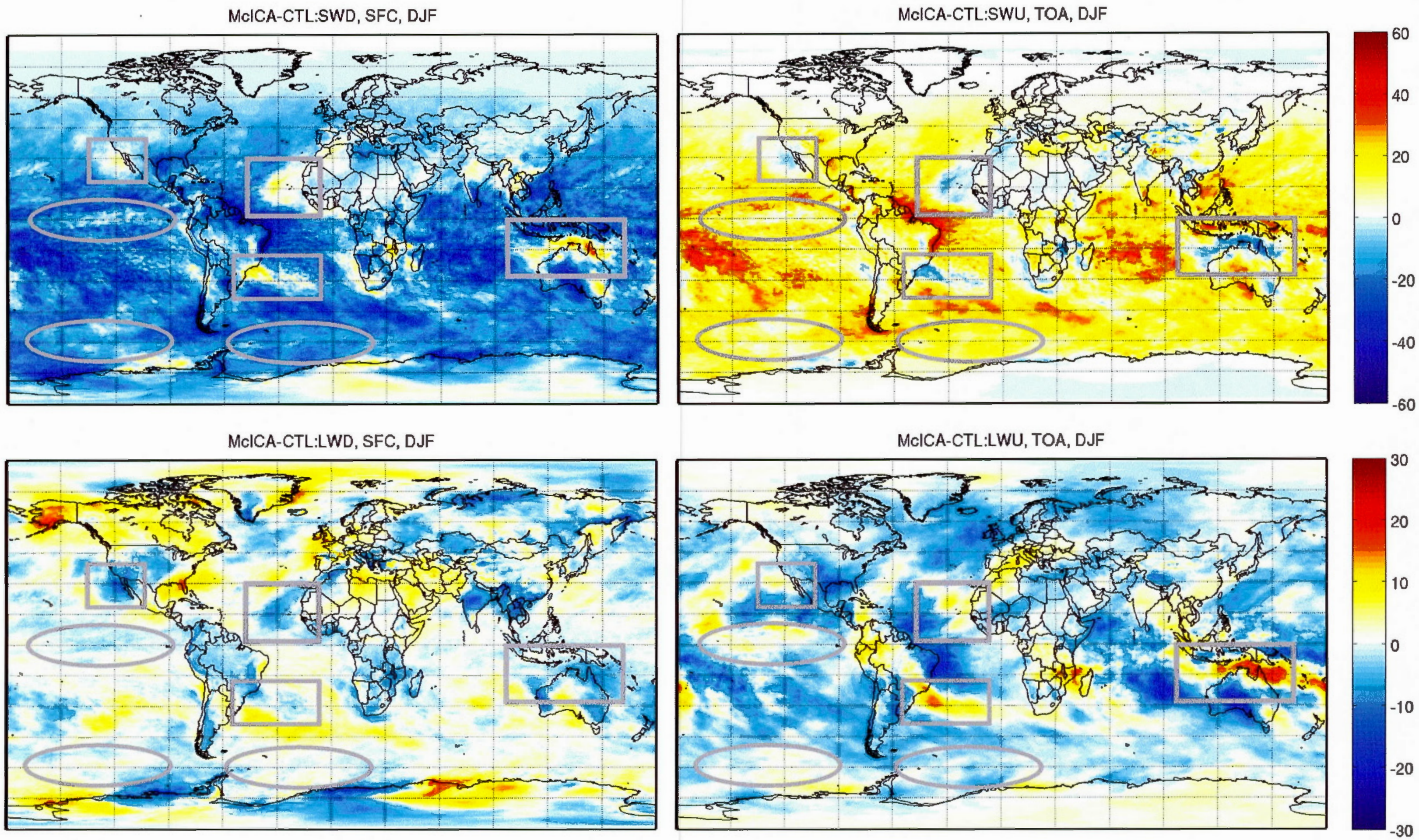

Figure 4.13 Seasonal mean differences between McICA and CTL for DJF for SWD at SFC (top left), SWU at TOA (top right), LWD at SFC (bottom left) and LWU at TOA (bottom right) in W/m^2.

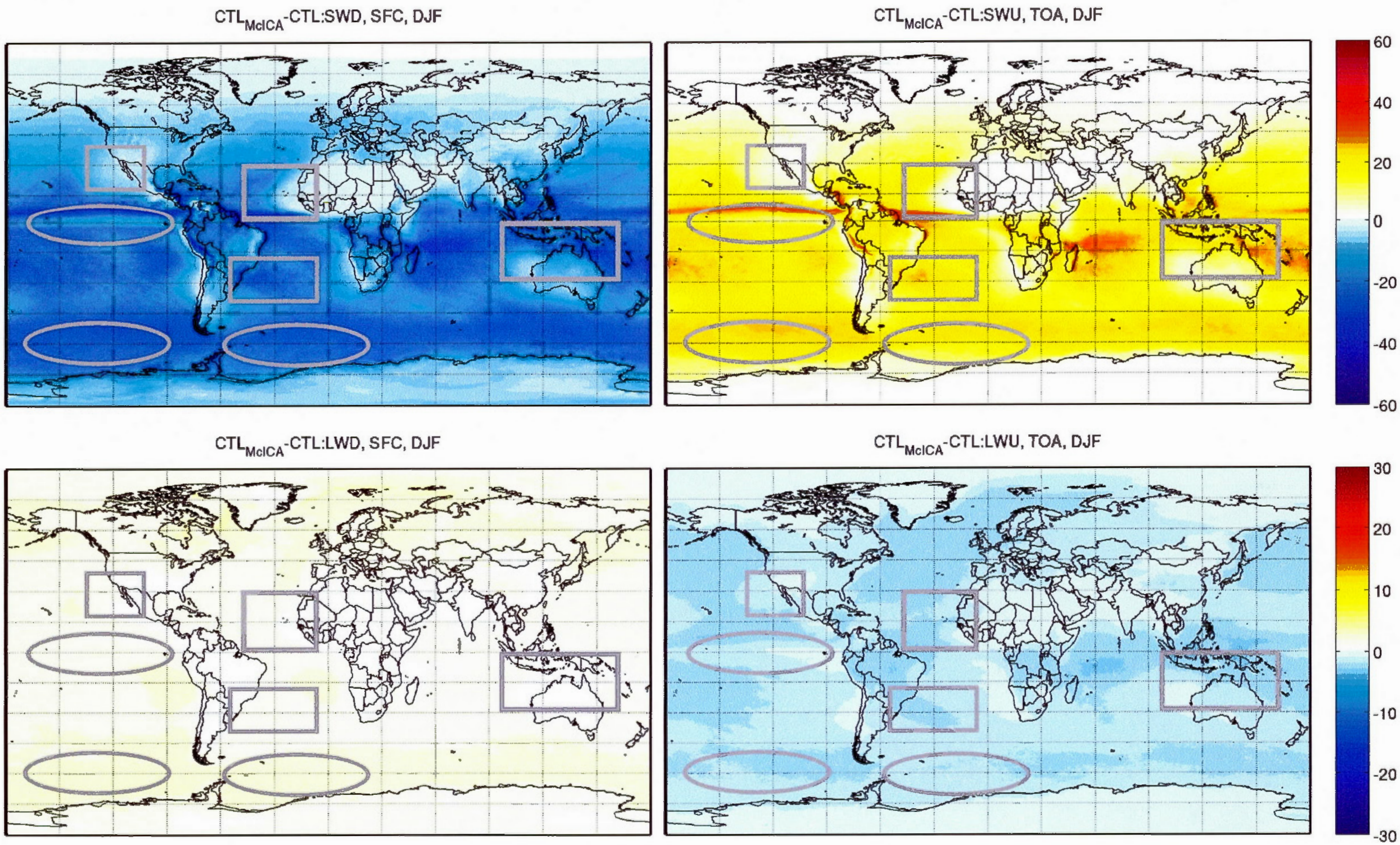

Figure 4.14 As figure 4.13 but for differences between $\mathrm{CTL}_{\mathrm{McICA}}$ and CTL.

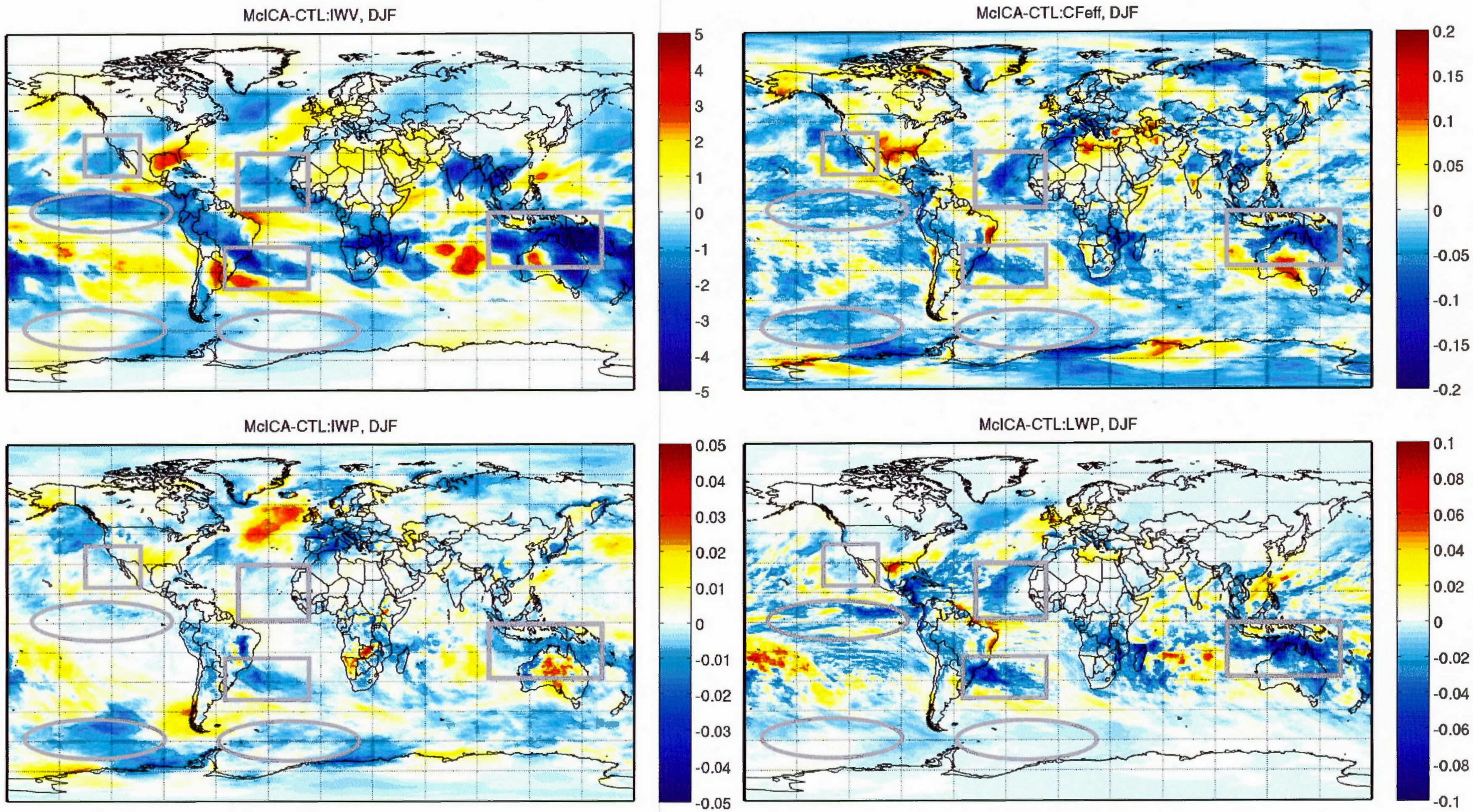

Figure 4.15 Seasonal mean differences between McICA and CTL for DJF for IWV (top left, g/m^2), effective CF (top right), LWP (bottom left, g/m^2) and IWP (bottom right, g/m^2).

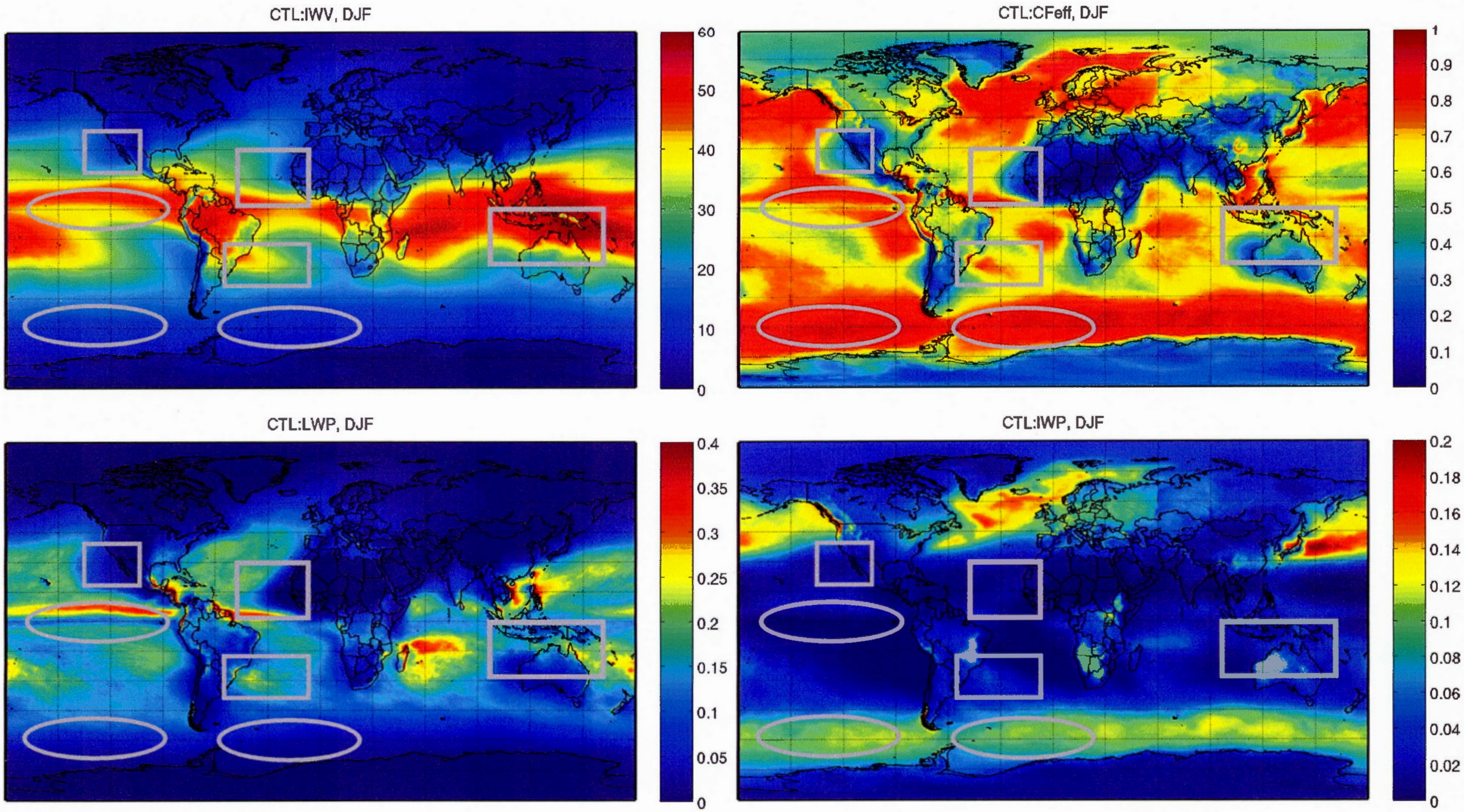

Figure 4.16 Seasonal mean values for CTL for DJF for IWV (top left, g/m^2), effective CF (top right), LWP (bottom left, g/m^2) and IWP (bottom right, g/m^2).

4.4 Conclusions

This chapter has presented, in a first part, the modeled results for two simulations, CTL and McICA in comparison to global satellite observations to validate and explain model results for zonal seasonal means (DJF and JJA) over a three year period. As the seasonal zonal mean results hide many details, both in the time and space averaging as in the integrated vertical variables, two sections were focusing on some of these different aspects. In the second part, zonal mean vertical profiles were presented to explain in more detail the link between SFC and TOA flux modifications when the McICA methodology is applied and the atmosphere structure freely evolves. Finally, maps of SFC and TOA fluxes were presented to illustrate how, in specific conditions, some areas are presenting opposite flux signals when McICA is applied.

For the first section, the model was compared to two data sets for the cloud and water variables: SSM/I and MODIS. The model reproduces fairly well the observed IWV and CF but exhibits large biases when it comes to CWP, with a large overestimation of LWP in the Tropics (compared to both data sets) and an underestimate of IWP or TOTWP elsewhere. These conclusions are to be taken with caution concerning the IWP (and derived TOTWP) as the observational uncertainties can be very large in some conditions. The two simulations, CTL and McICA exhibit only small differences in CF and LWP for the seasonal zonal mean.

With these informations on atmospheric water variables, the second section compared the SFC and TOA modeled fluxes to CERES-EBAF data set. For the clear-sky fluxes, the model results were within 10 W/m^2 to observations, with greater biases for JJA and polewards. As for the water variables, there were almost no difference between the two simulations.

For the all sky SW fluxes, large biases were present (an underestimation for SWD at SFC and an overestimation for SWU at TOA), mainly due to the overestimated LWP. For latitudes over 40°, LWP biases fade out rapidly but the SW biases do not. One hypothesis is that the ice cloud may be too reflective in the model due to too low effective radius, even if MODIS observations suggest that the IWP is underestimated. Further tests on ice effective radius will be presented in the next chapter. As the dominant McICA effect is an increased cloud albedo due to the inhomogeneity correction removal, the SW biases are worse for the McICA simulation. Differences between offline McICA results (CTL_{McICA}) and online McICA results are small compared to differences with the CTL simulation, suggesting that the atmospheric modifications are minor contributors to McICA SW flux differences.

Similarly for the all sky LW fluxes, the model presents a general overestimation for LWD at SFC and underestimation of LWU at TOA coherently to the LWP overestimation and the ice effective radius underestimation. LW biases are smaller than SW biases and smaller for DJF and TOA. Oppositely to SW, differences between CTL_{McICA} and McICA are now of the same order as between McICA and CTL, since the atmospheric modifications in McICA simulations are now playing as much an important role in the modified LW fluxes as the McICA methodology.

The third section focused on zonal mean vertical profiles for the model simulations only, to link the SFC and TOA results. It has shown that for SW fluxes, the biggest McICA differences (both offline and online) are coming from the low clouds, as expected, due to the SW-ACOD correction removal that is proportional to cloud optical depth. Whereas for the LW fluxes, all clouds are responding similarly to McICA modifications for offline fluxes. However, as mentioned before, the LW online fluxes are strongly modulated by differences in T, HU, CF and TOTWC. The NET-HR is dominated by the IR-HR with increased high cloud top cooling and reduced cooling at low cloud bases for the offline McICA signals. This reduced cooling could be responsible for the low cloud reduction in CF and TOTWP. The online signals are more noisy, particularly at low altitude but still show the increased high cloud top cooling.

Finally, the last section has presented maps of seasonal mean flux differences at SFC and TOA to understand some opposite signals, particularly in the SW fluxes. It demonstrates that in a few areas, McICA exhibits decreased SWU at TOA and increased SWD at SFC due to a combination of decreased cloud variables and more importantly, to conditions of low CF. These conditions allow the McICA horizontal inhomogeneity introduction effect to compensate the SW-ACOD and LW-GD correction removal. For the LW fluxes, these regions also present opposite signals compared to the zonal mean trends, but these opposite signals are not restricted to these areas, since LW responds strongly to variations in water variables and temperature.

To conclude, this chapter has shown how the model is biased high for the LWP compared to observations and how it affects its radiative fluxes both at SFC and TOA. As shown in the previous chapter, the model response to McICA methodology is strongly restricted by the SW-ACOD and LW-GD corrections removal, particularly with overestimated LWP since this removal strength is increasing with optical depth, and its McICA counterpart is decreasing with CWP. One could expect that under observed LWP values, McICA would be more equilibrated between the SW-ACOD and LW-GD correction removal and the horizontal inhomogeneity introduction, and that resulting flux signals would be more subtle depending on the atmospheric conditions. In that regard, next chapter will explore McICA sensitivities in lower cloud optical depth regimes.

As a last point, an hypothesis was formulated about the ice effective radius parameterization being too low. Next chapter will present tests, on short time scales, on the different parameterizations available in the SCG as well as on ice effective radius to explore the McICA flux sensitivities and to illustrate its potential.

CHAPTER V

RADIATIVE SENSITIVITIES OF THE MCICA METHODOLOGY AND THE SCG PARAMETERS

5.1 Introduction

Chapter 3, section 3.3.2, shows that the McICA inhomogeneity introduction is more sensitive at low TOTWP or cloud optical depth, meaning that its radiative impacts will be more important at low cloud optical depth. It further shows that the GEMCLIM SW-ACOD and LW-GD corrections have stronger capabilities to reduce cloud albedo and emissivity compared to the McICA inhomogeneity introduction. Replacing the former by the later results in increased cloud albedo and emissivity. In parallel, chapter 4 shows that the GEMCLIM model is highly overestimating LWP, resulting in too high cloud albedo and emissivity, which the present McICA methodology further amplifies.

This overestimation of LWP is problematic for the proper understanding of the McICA methodology impacts. The McICA approach is meant as a method to allow flexible sampling of sub-grid scale variability, not has a method to compensate for biases in the inputs to the RT scheme. As discussed in section 2.2, the SCG creates cloudy subcolumns with a cloud water content varying according to a defined horizontal distribution around the mean, provided by the model. If this mean is systematically too high, and therefore farther in the "saturation" region (i.e. where the cloud albedo or emissivity are less varying as a function of CWP, see section 1.1), then little sensitivity will result, i.e the McICA response will be close to that of the HOMOG simulation, as seen in section 3.3.2.

The first goal of this chapter is to study the McICA sensitivity under reduced cloud optical depth conditions. Two simple techniques will be presented to effectively reduce it: first, by reducing the LWP passed to the radiative transfer scheme, and second, by changing the constant ice effective radius to a function of IWC, with a minimum value that is greater than the previous constant value. The first correction is suggested by the model and observation comparison of section 4.3.1. The second correction is based both on observational results (as mentioned in section 4.3.2) and literature (e.g. Okamoto *et al.*, 2010) that suggests higher values of ice effective radius.

These two approaches are simple since the goal of this chapter is to study the McICA sensitivity under reduced cloud optical depth, to see if it confirms the theoretical behavior explained in section 1.1 and the instantaneous results of section 3.3.2 on a global scale. Furthermore, the radiative sensitivity of these cloud optical scalings is also addressed by comparing how fluxes are modified with the classic RT calculations compared to the McICA methodology.

The second goal of this chapter is to study the sensitivity of the SCG horizontal and vertical parameters, i.e. the horizontal cloud water inhomogeneity and the decorrelation lengths. This part will provide several examples of the flexibility and potential of the McICA approach to better parameterize the effect of cloud subgrid scale variability as diagnosed from observations or from information provided by the model itself. Finally, a few combinations are explored to illustrate the possible non-linearities between all these radiative parameters and to give an example of possible tuning techniques to approach observations.

5.2 Methodology

In this chapter, up to 28 simulations that combine one or many parameters modifications are presented. All results showed are for a one day mean average. The one day mean starts 24h after the beginning of the simulations (i.e. November 2^{nd}, 2006). This time period allows to compare simulations that have not diverged much from the initial conditions while the water variables (e.g. IWV, CWP, CF) spin up is mostly achieved (not shown).

Results are compared to CERES-SYN1deg observation data set since the CERES-EBAF dataset used in the previous chapter is not available for daily mean. The CERES-SYN1deg data set (Doelling *et al.*, 2013) provides temporally interpolated TOA fluxes from 3-hourly radiances and cloud properties from geostationary imagers to model temporal variability between CERES observations on a 1° latitude zonal grid. MODIS derived cloud properties are also included as well as computed surface fluxes from the Langley Fu-Liou radiative transfer model.

The model configuration for all these simulations is the same as in the previous chapters.

5.2.1 Test descriptions

Table 5.1 presents a first group of simulations. The CTL, HOMOG and McICA simulations are the same as presented in chapters 3 and 4. The ICE simulation includes the ice effective radius modification following Lohman and Roeckner (1996) (see equation 5.1) with a range of $[20 : 50]\mu m$. The simulation named McICAice includes both the McICA methodology and the ice effective radius modification.

All those denoted with a "3" (e.g. ICE3, McICAice3) include a scaling factor of 0.3 that multiplies the LWC that is passed to the radiative transfer scheme. This factor is suggested by the overestimation seen in modeled LWP against observations in section 4.3.1. Similarly for the "5", it means a scaling factor of 0.5 to the LWC. For all simulations of table 5.1, the SCG parameters are maintained like the original version: the horizontal inhomogeneity parameter $\nu = [\nu_1; \nu_2; \nu_3] = [1; 2; 4]$ (defined as a function of $CF = [< 0.9; \geq 0.9\& < 1; 1])$ and the decorrelation lengths for CF and water content (WC): L_{cf}=2 km and L_{cw}=1 km.

$$r_{eff,ice} = 83.8 * 10^{-6}(10^3 * IWC)^{0.216} \tag{5.1}$$

As a comparison to the SW-ACOD corrections, the effects of the 0.3*LWC scaling on the cloud optical depth are presented on figure 5.1. The scaling is not as strong on the cloud optical depth as on the LWC, since the cloud optical depth is also a non-linear function of the effective radius, which is in turn function of the LWC (see annex A). In that sense, this scaling is less radiatively effective compared to a direct tuning of 0.3 on the LWP, which would not affect the liquid effective radius and would directly multiply the cloud optical depth by a 0.3 factor.

Table 5.2 presents a second simulation group, which includes the ice effective radius modification but no LWC scaling for all simulations. The first SCG parameter that is tested is the horizontal inhomogeneity which is represented by the ν variable. The first ν modification (denoted simply ν) is to increase the horizontal inhomogeneity when CF <0.9 (with ν_1=0.5) since the McICA horizontal inhomogeneity seems weaker then the SW-ACOD and LW-GW corrections previously implemented in the GEMCLIM model. A more physical way of increasing the inhomogeneity, is to decrease the same ν_1 parameter, but only when shallow or deep convection is triggered, since convective clouds should present more horizontal inhomogeneity than stratiform clouds (Rossow *et al.*, 2002). In this case,

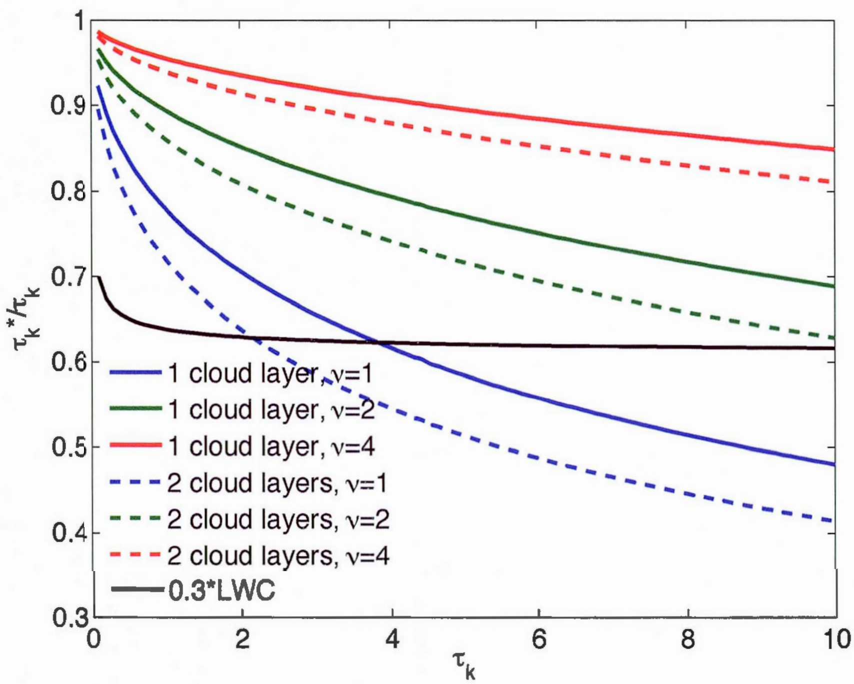

Figure 5.1 Same figure as 1.2 but with the additional example of the 0.3*LWC scaling effects on cloud optical depth.

Table 5.1 Sensitivity tests, part 1

tests	LWC scaling	$r_{eff,ice}$ (μm)	[ν_1;ν_2;ν_3]	L_{cf}; L_{cw} (km)
CTL	1	15	[1; 2; 4]	2; 1
HOMOG	1	15	[1; 2; 4]	2; 1
ICE	1	f(IWC): [20:50]	[1; 2; 4]	2; 1
ICE3	0.3	f(IWC): [20:50]	[1; 2; 4]	2; 1
HOMOGice	1	f(IWC): [20:50]	[1; 2; 4]	2; 1
HOMOGice3	0.3	f(IWC): [20:50]	[1; 2; 4]	2; 1
McICA	1	15	[1; 2; 4]	2; 1
McICAice	1	f(IWC): [20:50]	[1; 2; 4]	2; 1
McICAice3	0.3	f(IWC): [20:50]	[1; 2; 4]	2; 1
McICAice5	0.5	f(IWC): [20:50]	[1; 2; 4]	2; 1

model convective activity serves as a proxy for higher cloud subgrid-scale variability and this test is denoted ν_{conv}. Furthermore, two studies presented in section 2.6, derive ν parameterizations for liquid and ice clouds based on satellite observations as a function of CF and model grid size (Boutle *et al.*, 2013; Hill *et al.*, 2011a, resprectively). Two tests are done based on a approximate mean value of these parameterizations: the ν_{liq} test with only the ν_3 parameter changed to 11 (since ν_1 and ν_2 are close to the suggested parameterization); and the ν_{ice} test with all three ν components changed to 11. Note that these parameterizations decrease the horizontal inhomogeneity.

The other SCG parameters that are tested are the decorrelation lengths (L_{cf} and L_{cw}). Based on the parameterization from Oreopoulos *et al.* (2012a), two simple tests are first performed with the minimum and maximum values used in the article: 1.5 and 0.75 km (for L_{cf} and L_{cw} respectively) and 3.5 and 1.5 km. Since the Oreopoulos *et al.* (2012a) parameterization idea is to set the maximum values at the Intertropical Convergence Zone, a test is done as a function of presence of shallow and deep convection. For both decorrelation lengths, three values are possible, the first one (the minimum value) when only stratiform clouds are present, the second one (the standard value) when shallow convection is triggered and the third one (the maximum value) when deep convection is triggered (with or without shallow convection). This test is denoted L_{conv}. Given that the Oreopoulos *et al.* (2012a) parameterization values are zonal mean values, another test, denoted $L_{convMAX}$, is performed with more extreme values, used in the Zhang *et al.* (2014) study only in presence of convection. Finally, because all tests on decorrelation lengths are using L_{cw} values that are approximately half of the L_{cf} values, a last test, denoted $L_{convMAXw}$, is performed by increasing L_{cw} values to the L_{cf} values.

Finally, table 5.3 presents a last simulation group, which includes the ice effective radius modification and the 0.3 LWC scaling for all simulations. As before, tests were performed with the different ν parameters as well as combinations of decorrelation lengths and horizontal inhomogeneity.

5.3 Results and interpretation

Results are presented with 2° zonal means for a one day mean period. First presented is the offline and online McICA radiative flux sensitivities (SWD and LWD at SFC, SWU and LWU at TOA) under the different cloud optical depth scalings. In parallel, cloud optical depth scaling radiative sensitivities are also presented. Secondly, the SCG parameters sensitivities are presented with different parameterizations, as listed in the previous section, and under different conditions (e.g. with or without the different cloud optical depth scaling or combined with other

Table 5.2 Sensitivity tests, part 2. All tests have $r_{eff,ice}$= f(IWC), [20:50] μm and no LWC scaling.

tests	$[\nu_1;\nu_2;\nu_3]$	L_{cf}; L_{cw} (km)
ICEν	[0.5; 2; 4]	2; 1
HOMOGiceν	[0.5; 2; 4]	2; 1
McICAiceν	[0.5; 2; 4]	2; 1
McICAiceν_{liq}	[1; 2; 11] for liq. clds	2; 1
McICAiceν_{ice}	[11; 11; 11] for ice clds	2; 1
McICAiceν_{conv}	[0.5; 2; 4] for all conv.	2; 1
McICAiceL_{max}	[1; 2; 4]	3.5; 1.5
McICAiceL_{min}	[1; 2; 4]	1.5; 0.75
McICAiceL_{conv}	[1; 2; 4]	L_{cf}=[1.5; 2.0; 3.5]; L_{cw}=[0.75; 1.0; 1.5]
McICAice$L_{convMAX}$	[1; 2; 4]	L_{cf}=[1.0; 5.0; 10]; L_{cw}=[0.5; 2.5; 5.0]
McICAice$L_{convMAXw}$	[1; 2; 4]	L_{cf}=[1.0; 5.0; 10]; L_{cw}=[1.0; 5.0; 10]
McICAice$L_{convMAXw}$, ν	[0.5; 2; 4]	L_{cf}=[1.0; 5.0; 10]; L_{cw}=[1.0; 5.0; 10]

Table 5.3 Sensitivity tests, part 3. All tests have $r_{eff,ice}$= f(IWC), [20:50] μm and a LWC scaling of 0.3.

tests	[ν_1;ν_2;ν_3]	L_{cf}; L_{cw} (km)
McICAice3ν_{liq}	[1; 2; 11] for liq. clds	2; 1
McICAice3ν_{ice}	[11; 11; 11] for ice clds	2; 1
McICAice3ν_{conv}	[0.5; 2; 4] for all conv.	2; 1
McICAice3$L_{convMAX}$, ν	[0.5; 2; 4]	L_{cf}=[1.0; 5.0; 10]; L_{cw}=[0.5; 2.5; 5.0]
McICAice3$L_{convMAX}$, ν_{conv}	[0.5; 2; 4] for all conv.	L_{cf}=[1.0; 5.0; 10]; L_{cw}=[0.5; 2.5; 5.0]
McICAice3$L_{convMAX}$, $\nu_{conv,ice}$	[0.5; 2; 4] for all conv. [11; 11; 11] for ice clds	L_{cf}=[1.0; 5.0; 10]; L_{cw}=[0.5; 2.5; 5.0]

parameterizations). Finally, a combination of different scalings and parameterizations is presented to approach the observational fluxes and illustrate the SCG flexibility. In all figures, global mean values or differences are indicated.

As an introduction to the results, basic features of different simulations using the different cloud optical depth scalings are presented against observations of the one day mean period. Figure 5.2 presents zonal mean differences between different model simulations and CERES-SYN1 observations for effective CF, IWV, LWP and IWP. Similarly to chapter 4, figure 4.1, the modeled effective CF and the IWV are close to observations. For LWP, the ICE3 and McICAice3 simulations illustrate the 0.3*LWC scaling, in order to approach observations between 40°S and 40°N (without completely removing biases). However, LWP becomes underestimated over these latitudes. For these simulations, the global mean LWP bias is reduced to -5 g/m^2. As before, the modeled IWP seems largely underestimated in comparison to values derived from observations, but these derived values include large uncertainties. These conditions for a one day average are representative of the seasonal model biases seen in chapter 4.

Figure 5.3 present flux differences against observations. The ICE simulation (with modified ice effective radius, in red) reduces all flux biases compared to CTL (in black) particularly for latitudes >30°S for SW, and for latitudes >40°S/N for LW. This is expected given that the ice effective radius is bigger, reducing the cloud albedo and emissivity where ice is present, and exhibiting more impacts where the liquid clouds are not radiatively dominant. It confirms the previous chapter hypothesis, that CTL had too low extra-tropical ice effective radii. When McICA is applied with the modified ice effective radius (McICAice, in magenta), SW biases are worse compared to ICE, since the SW-ACOD removal signal dominates but a few zonal regions show improvement with respect to the CTL simulation. For the LW, McICAice is worse than ICE but still reduces the model biases in comparison to CTL.

Since the flux biases are not reduced over the Tropics for the ICE simulation and that the LWP biases are clear for this region, the ICE3 simulation is performed where both the ice effective radius is modified and the LWC is scaled by a 0.3 factor (see table 5.1 for simulation descriptions). In this simulation (blue line), SW flux biases are reduced between 30°S and 30°N but enhanced elsewhere (approximately where the LWP becomes underestimated), whereas LW biases are generally reduced at SFC but increased at TOA. This is also expected since the cloud optical depth is reduced linearly with the reduced LWP, decreasing the cloud albedo and emissivity. Once McICA is applied on ICE3 (McICAice3, in cyan), it increases cloud albedo and emissivity to values between ICE and ICE3 for SW biases and close to ICE for LW biases. This simulation, McICAice3, will be the basic state from which radiative sensitivities are studied in this chapter.

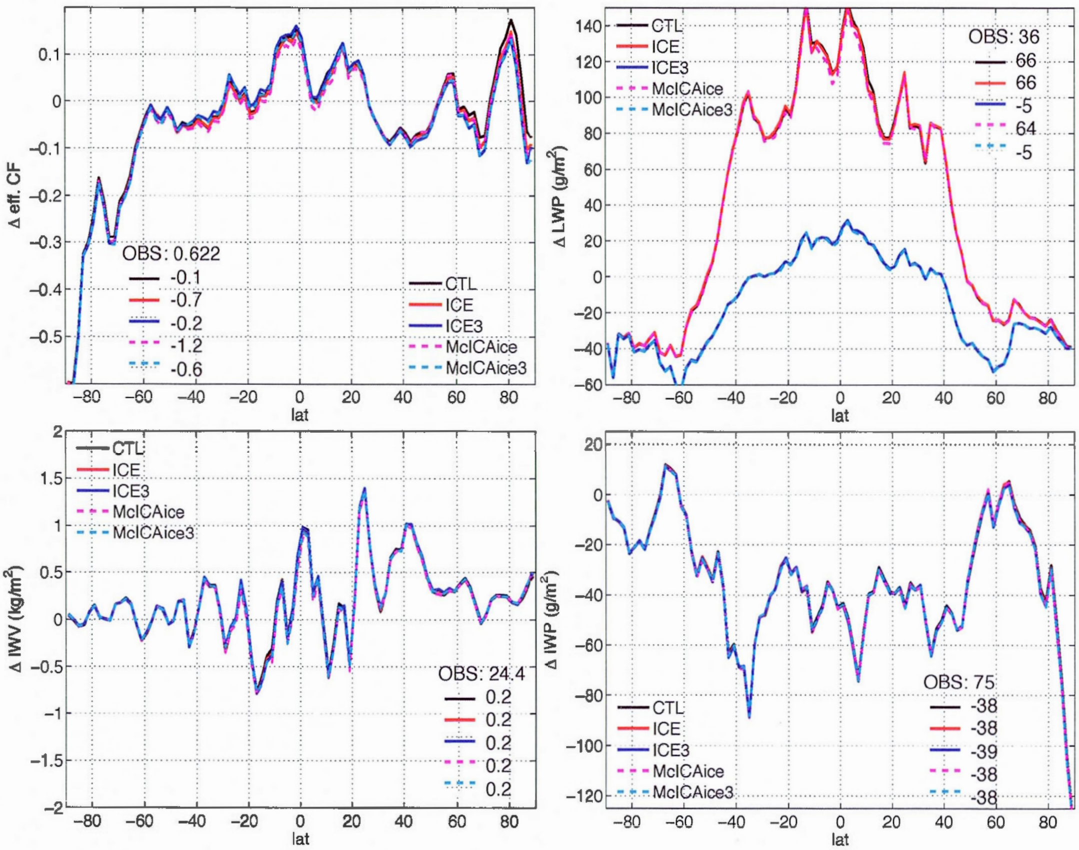

Figure 5.2 Zonal 1 day mean differences between different model simulations (see table 5.1 for simulation descriptions) and observations (CERES-SYN1deg). Global mean observation values or differences against observations are indicated in each panel.

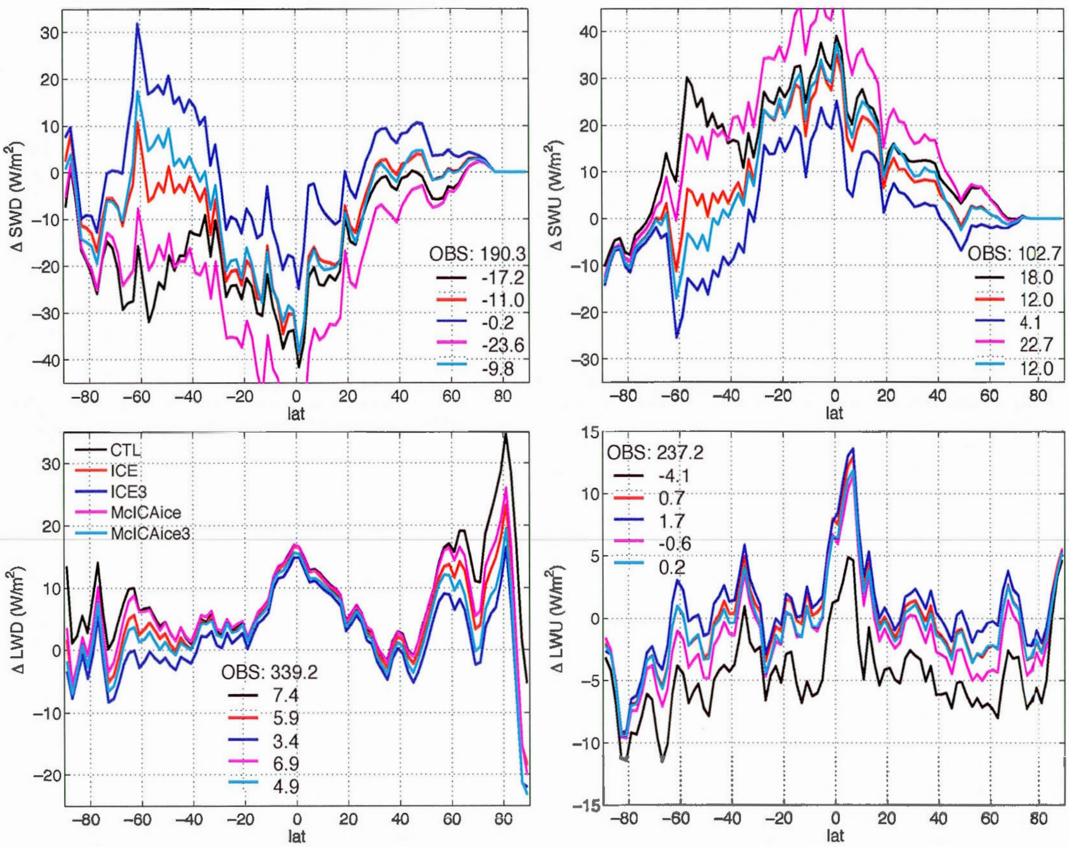

Figure 5.3 As figure 5.2 but for flux differences between different model simulations and observations. See table 5.1 for simulation descriptions.

5.3.1 McICA sensitivities with cloud optical depth scaling

Figure 5.4 presents zonal mean differences between pairs of simulations to illustrate McICA offline (full lines) and online (dashed lines) effects. For all the pairs of simulations, the same inputs are used (i.e. the scaled LWP or the modified ice effective radius) but the RT calculations are different: either the McICA methodology is used or the classic homogeneous RT calculations (HOMOG simulations). Furthermore, for the offline McICA simulations, denoted with subscripts as in the previous chapters, all the atmospheric variables are also identical. Hence the flux differences represent the McICA horizontal inhomogeneity and decorrelation length effects against the homogeneous and MRO cloud treatment.

When compared to the homogeneous cloud treatment, for all pairs of simulations, McICA effects are decreasing cloud albedo (for liquid clouds) and emissivity (as shown in chapter 3), resulting in increased SWD at SFC and LWU at TOA, and decreased SWU at TOA and LWD at SFC. However, for ice clouds, the cloud albedo is increased with McICA (as explained in section 3.3.3) resulting in opposite trends for SW fluxes visible for latitudes south of 65°S.

The red lines represents the offline and online McICA effects for modified (and increased) ice effective radius. Comparing the $\text{HOMOGice}_{\text{McICA}}$-HOMOGice differences to $\text{HOMOG}_{\text{McICA}}$-HOMOG (red lines vs. black lines), almost no difference are visible except for the SWD at latitudes south of 75°S, for the LWD at latitudes greater than 40° and for the LWU over Tropics. This can be understood since the ice cloud SW McICA effects are weak (as seen in chapter 3), and that liquid or mixed clouds are radiatively dominant when averaged with ice cloud effects. For the LW, the reduced cloud emissivity (due to increased ice effective radius) leads to an enhanced McICA effects that is visible in regions where ice clouds can contribute more to the radiative impacts (higher latitudes for LWD, and mid-latitudes and Tropics for LWU).

The cyan lines are for both the modified ice effective radius and the 0.3 LWC scaling simulations. The $\text{HOMOGice3}_{\text{McICA}}$ - HOMOGice3 differences illustrate how the McICA horizontal inhomogeneity effects are increased at lower cloud optical depth values. However, looking at the SW differences, these effects are reduced for latitudes south of 50°S (compared to the $\text{HOMOG}_{\text{McICA}}$-HOMOG differences), since the reduced liquid cloud SW radiative effects leave place to the ice cloud SW radiative effects, which produce the inverse McICA effects. For the LWD at SFC, the increased McICA horizontal inhomogeneity effects are visible for all latitudes except greater than 70°S/N, whereas for the LWU at TOA, no clear tendency is visible. This is understandable since low clouds have more radiative impacts at SFC than TOA for the LW.

Finally, comparing online McICA effects (dashed lines) to offline effects (full lines), the online effects are reduced between 60°S and 40°N particularly for the SW, suggesting some cloud adjustments (as previously seen in section 3.3.4). Figure 5.5 shows McICAice - HOMOGice differences for T, HU and cloud variables (differences between McICA and HOMOG are similar, thus not shown). It shows that low clouds present a small but systematic increase in CF, LWC and IWC. This reduces the McICA effects and, furthermore it directly decreases SWD at SFC and increases SWU at TOA. For the LW, the effects are less clear, particularly for the LWU at TOA (since the high cloud modifications may have more influence). One exception stands out for the LWD at SFC for latitudes north of 60°N, where the CF decreases the most, particularly for the McICA simulation (compared to HOMOG, not shown), thus reducing greatly the LWD at SFC. The McICAice3 simulation differs from the McICA and McICAice simulations since its LWP is already reduced greatly and therefore presents only small cloud adjustments (not shown).

Once the McICA effects are understood for different cloud optical depth scalings in comparison to the radiative homogeneous cloud treatment, another comparison can be made to the CTL simulation, which includes the SW-ACOD and LW-GD corrections to take into account cloud inhomogeneities (as discussed in detail in chapter 3).

Figure 5.6 presents also the McICA offline and online effects as figure 5.4, but in comparison to control simulations that include the SW-ACOD and LW-GD corrections. Therefore, the flux differences for each pair of simulations represent the combined effects of McICA horizontal inhomogeneity and decorrelation lengths, and the SW-ACOD and LW-GD removal. Compared to figure 5.4, the combined McICA effects are reverse since the SW-ACOD and LW-GD removal effects dominate (also shown in chapter 3).

Looking at the red lines for the McICA combined effects for modified ice effective radius (ICE_{McICA}-ICE), more differences are visible compared to the black lines (CTL_{McICA}-CTL). It shows smaller SW combined McICA effects for latitudes south of 40°S while almost no SW effect were visible in figure 5.4. This means that the reduction in cloud optical depth (from the increased ice effective radius) weakens the SW-ACOD removal effects, since the SW-ACOD corrections are proportional to cloud optical depth. For LWU at TOA, a small similar reduction in LW-GD removal effects is also visible over the Tropics. However, opposite effects are clear for LWD at SFC for latitudes greater than 40°S/N. This effect can be understood by looking at the zonal mean vertical LW flux profiles in figure 5.7. The top panel shows that the combined McICA effects are reduced for ICE_{McICA} compared to CTL_{McICA} for the high ice clouds as expected, and then increased lower in the clouds. This is due to the LW-GD correction that varies non-linearly as a function of cloud optical depth, contrarily to the SW-ACOD. This increase in combined McICA effects is maximum for low ice clouds around 60°S/N.

Looking at the ICE3$_{\mathrm{McICA}}$ - ICE3 differences (cyan lines which include both the modified ice effective radius and the 0.3 LWC scaling), it further reduces the SW combined McICA effects compared to ICE$_{\mathrm{McICA}}$ - ICE (red lines), and for all latitudes. At a lower LWP range, the SW-ACOD corrections are weaker and the McICA horizontal inhomogeneity introduction effects are stronger, resulting in more balanced opposite effects, with still the SW-ACOD removal effects dominating. The opposite effects seen for LWD at SFC can be understood by looking at figure 5.7 bottom two panels. It shows how low liquid clouds have an increased emissivity due to LW-GD removal non-linearities when the LWC is scaled by 0.3. These LW effects are again more visible at SFC compared to TOA.

Finally, comparing online combined McICA effects (dashed lines) to offline effects (full lines), the online effects are reduced between 60°S and 60°N for the SW and the LWD at SFC, suggesting some cloud adjustments similarly to figure 5.4. Figure 5.8 shows McICAice - ICE differences for T, HU and cloud variables (differences between McICA and CTL are similar, thus not shown). Even if the vertically integrated values shown in figure 5.2 did not exhibit significant differences between McICAice and ICE, the vertical profiles in figure 5.8 show that low clouds present a small but systematic decrease in CF, LWC and IWC (inversely of figure 5.5 but coherently with section 4.3.3 for seasonal means). These conditions reduce the SW-ACOD and LW-GD removal effects. One exception is the LWU at TOA, which are not very sensitive to this low cloud adjustment, and this can be understood since LWU at TOA are mainly controlled by high cloud radiative properties.

In conclusion, McICA effects are dependent on the cloud optical depth range. Under lower cloud optical depth conditions, McICA horizontal inhomogeneity effects are increased (particularly for liquid clouds), reducing more the cloud albedo and emissivity, confirming the theoretical behavior deduced from section 1.1. Therefore, the combination of McICA horizontal inhomogeneity introduction and SW-ACOD and LW-GD correction removal are more balanced, resulting in smaller effects since the later are still overrunning the former. Moreover, McICA horizontal inhomogeneity effects are inverse for the ice cloud albedo, with an increased cloud albedo compared to the homogeneous treatment.

From another perspective, radiative sensitivities are now presented for the two different cloud optical scaling techniques used: the ice effective radius modification and the LWC scaling. Given that the goal behind these scalings is to modify SFC and TOA fluxes, the idea is to understand how the flux responses will vary with different RT methodologies such as the "classic" RT calculations and the McICA methodology. In other words, how the cloud optical depth scalings are radiatively sensitive to RT methodologies. Figure 5.9 presents the ice effective radius modification radiative effects, while figure 5.10 presents the LWC scaling radiative effects. For both scaling techniques, the cloud albedo and emissivity are reduced, producing increased SWD at SFC and LWU at TOA and decreased SWU at TOA and LWD at SFC.

For the ice effective radius modification in figure 5.9, SW flux differences are increased between the classic RT scheme (in black) and the offline McICA methodology (in red) where the ice cloud radiative effects are dominant (south of 50°S). This is due to McICA being more sensitive than the SW-ACOD corrections to low cloud optical depth values, hence increasing the SW flux differences between lower cloud optical depth values and the original values. For the LW differences, as explained previously, the LW-GD corrections vary non-linearly with cloud optical depth, resulting in this case, with less sensitivity when McICA is applied for LWD at SFC and a similar response for LWU at TOA. When McICA online is applied (in blue), the zonal flux sensitivities to ice effective radius are slightly increased, mostly over Tropics for SW and LWU at TOA. This can be explained by the low cloud adjustment shown in figure 5.8 (and that occurs for both McICAice and McICA simulations), since a reduction in low clouds, that are mostly liquid, will allow the ice clouds above to have a bigger radiative contribution. Hence, the different ice effective radius parameterization shows slightly increased radiative impacts in these conditions. The global mean values put in perspective that global mean differences for LWU at TOA are of the same order of the SW differences, whereas the global mean LWD differences at SFC are smaller.

Looking at figure 5.10, the LWC scaling radiative effects are presented. Similarly to the ice effective radius sensitivities, the offline McICA simulation (in red) is more sensitive in the SW and less in the LW compared to the classic RT scheme (in black). This is for the same reasons of greater SW sensitivities in lower cloud optical depth for McICA and non-linearities in the LW-GD correction responses. However, for the McICA online simulations (in blue), the flux sensitivities are now decreased compared to the offline McICA simulations (in red). Since the low liquid cloud adjustment is taken place, the LWC scaling is applied over lower values, producing slightly lower flux differences. Finally, McICAice5 (in cyan) is presented as an example of the LWC scaling factor being 0.5 instead of 0.3, to illustrate the relative radiative strength of different LWC scalings. As expected, the radiative sensitivities are smaller compared to McICAice3, with global mean values that are approximately half the McICAice3 values. One test was also performed with an increased horizontal inhomogeneity (ICE3ν_{McICA}-ICEν_{McICA}, not shown), and flux sensitivities were similar to ICE3$_{\mathrm{McICA}}$-ICE$_{\mathrm{McICA}}$, suggesting no significant influence from this parameter on the LWC scaling radiative sensitivities.

In conclusion, these results show that these different cloud optical depth scaling techniques are producing greater radiative differences at SFC and TOA with the McICA methodology. These conclusions should hold only for scalings that are reducing cloud optical depth, since McICA is generally more sensitive at lower cloud optical depth values.

5.3.2 SCG horizontal and vertical parameter sensitivities

This section presents SCG parameter radiative sensitivities. First presented are the radiative sensitivities to decorrelation lengths in figure 5.11. The black lines are for the maximum values and minimum values used in Oreopoulos *et al.* (2012a) (see table 5.2 for simulation descriptions). The maximum values (black full line) increase the CF overlap, thus reduce the integrated CF, hence increase the SWD at SFC and LWU at TOA, and decrease the SWU at TOA and LWD at SFC, compared to control values. These effects are maximum in the Tropics for the SW fluxes while generally constant for LW fluxes. The minimum values (black dashed line) exhibit the opposite flux sensitivities with smaller amplitudes since differences to control values are smaller.

When the maximum values (same as L_{max}) are applied for deep convection and the minimum values (same as L_{min}) are applied to the stratiform clouds (keeping the control values when only shallow convection is triggered), the flux sensitivities (L_{conv} in cyan) are oscillating around 0 and approaching the minimum flux sensitivities (black dashed line) at high latitudes (where the stratiform clouds are dominating). This means that the L_{conv} values associated with deep convection activity is not sufficient over zonal mean to recreate the L_{max} radiative effects over the Tropics but rather reproduces the control radiative effects. However, it does not mean that, locally, in presence of deep convection, the change in decorrelation lengths is not significant.

Looking at figure 5.12, similar tests are presented with different values. The blue lines ($L_{convMAX}$) represent values of 10 km for L_{cf} (5 km for L_{cw}) for deep convection, 5 km (2.5 km) for shallow convection and 1 km (0.5 km) for stratiform

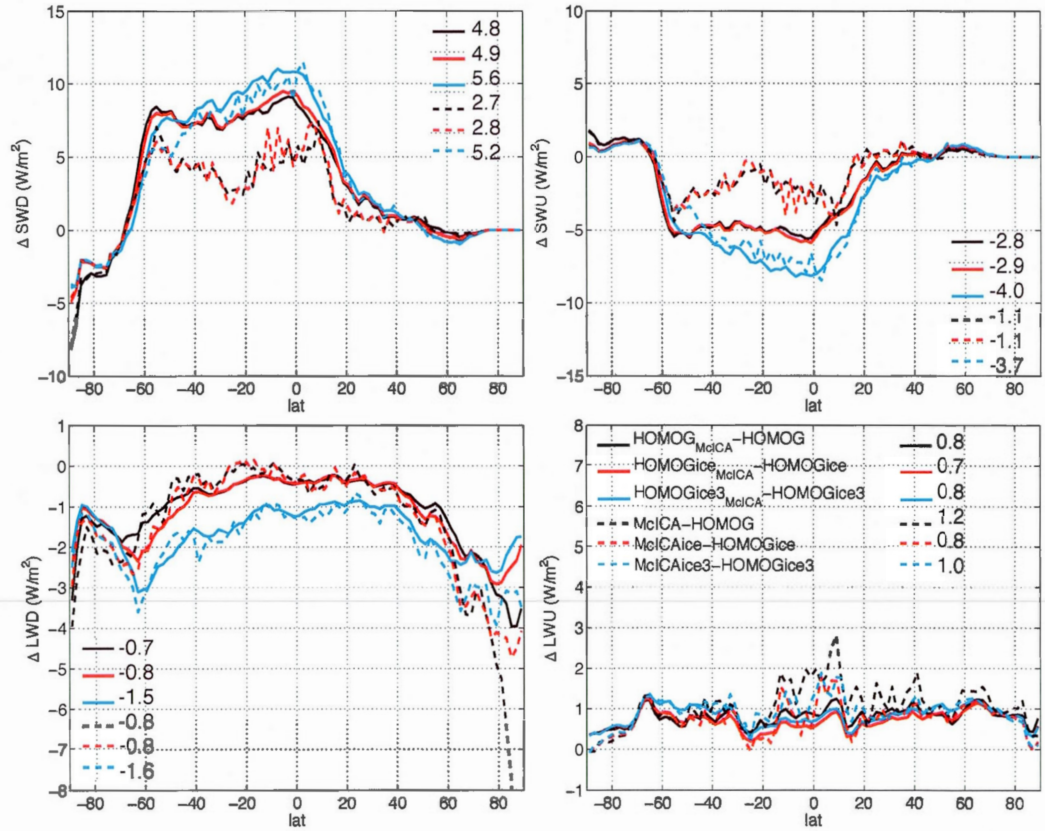

Figure 5.4 Zonal 1 day mean differences between different pairs of simulations (see table 5.1 for simulation descriptions) for SWD at SFC, SWU at TOA, LWD at SFC and LWU at TOA to illustrate McICA offline (full lines) and online (dashed lines) effects. Global mean differences are indicated in each panel.

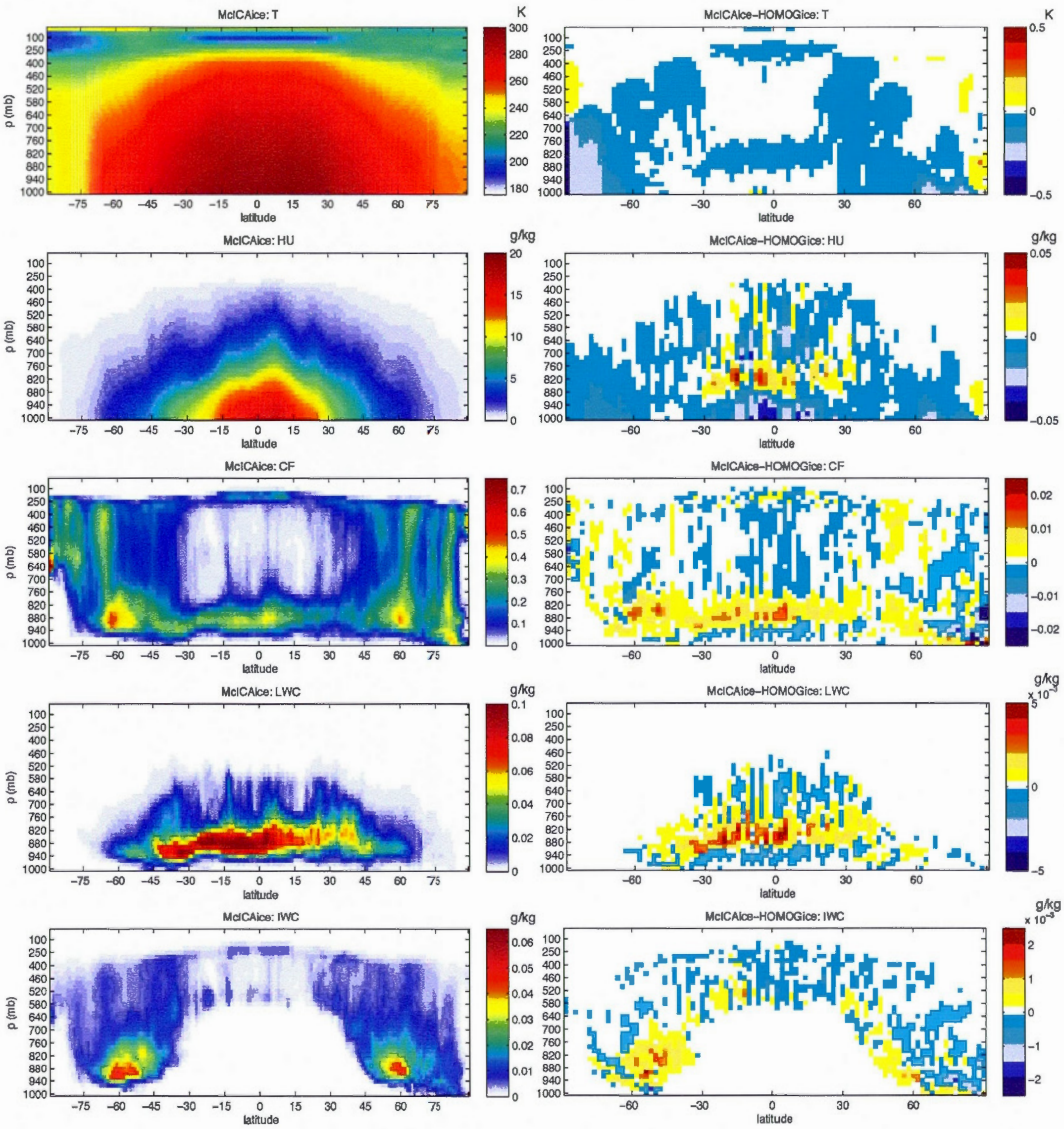

Figure 5.5 Zonal 1 day mean T, HU, CF, LWC and IWC for McICAice (left column) and differences between McICAice and HOMOGice (right column).

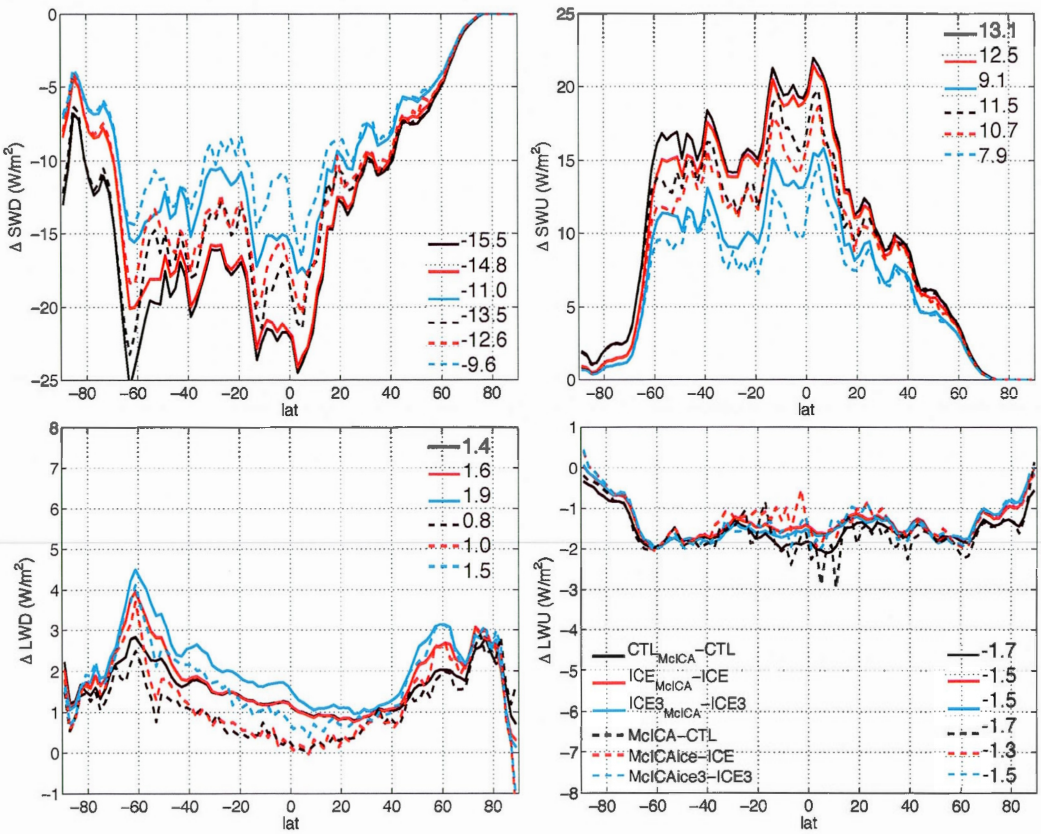

Figure 5.6 As figure 5.4 but for different pairs of simulations. See table 5.1 for simulation descriptions.

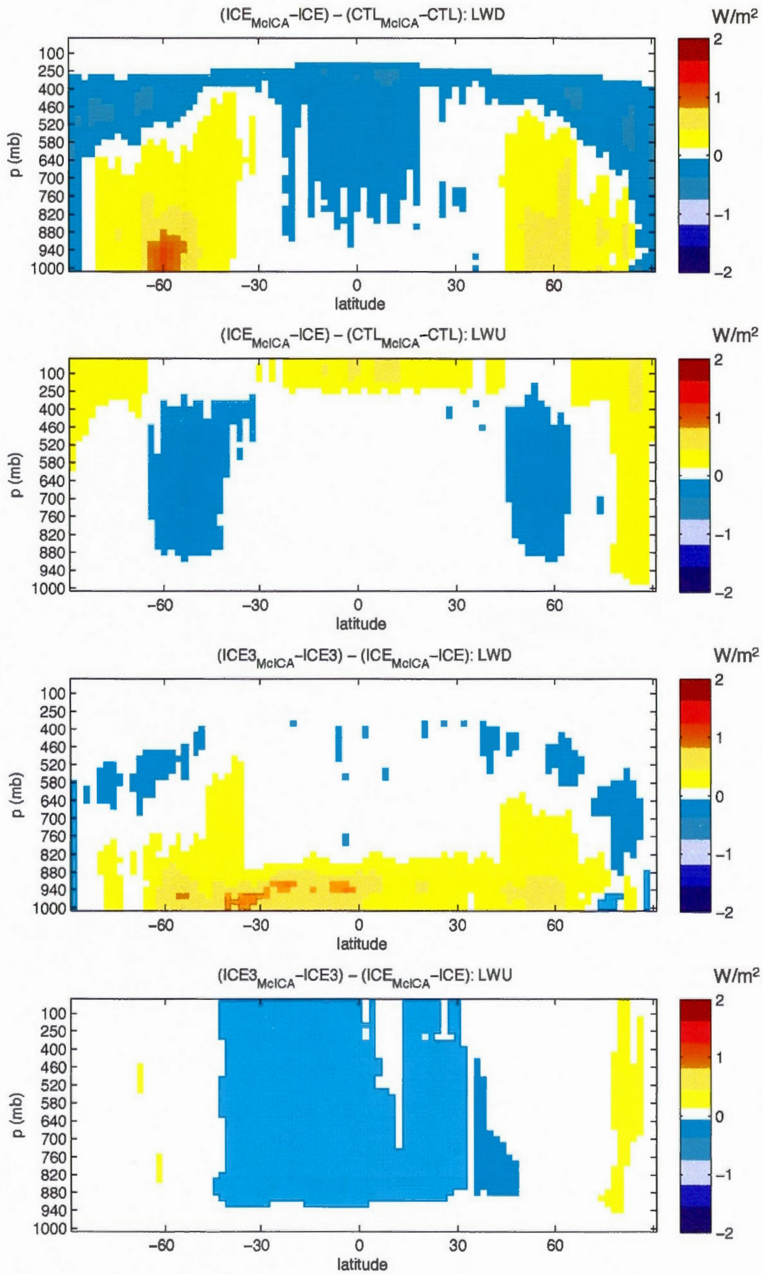

Figure 5.7 Zonal 1 day mean differences for LWD and LWU fluxes between (ICE_{McICA} – ICE) – (CTL_{McICA} – CTL) (top two panels) and (ICE_{McICA} –ICE3) – (ICE_{McICA} – ICE) (bottom two panels).

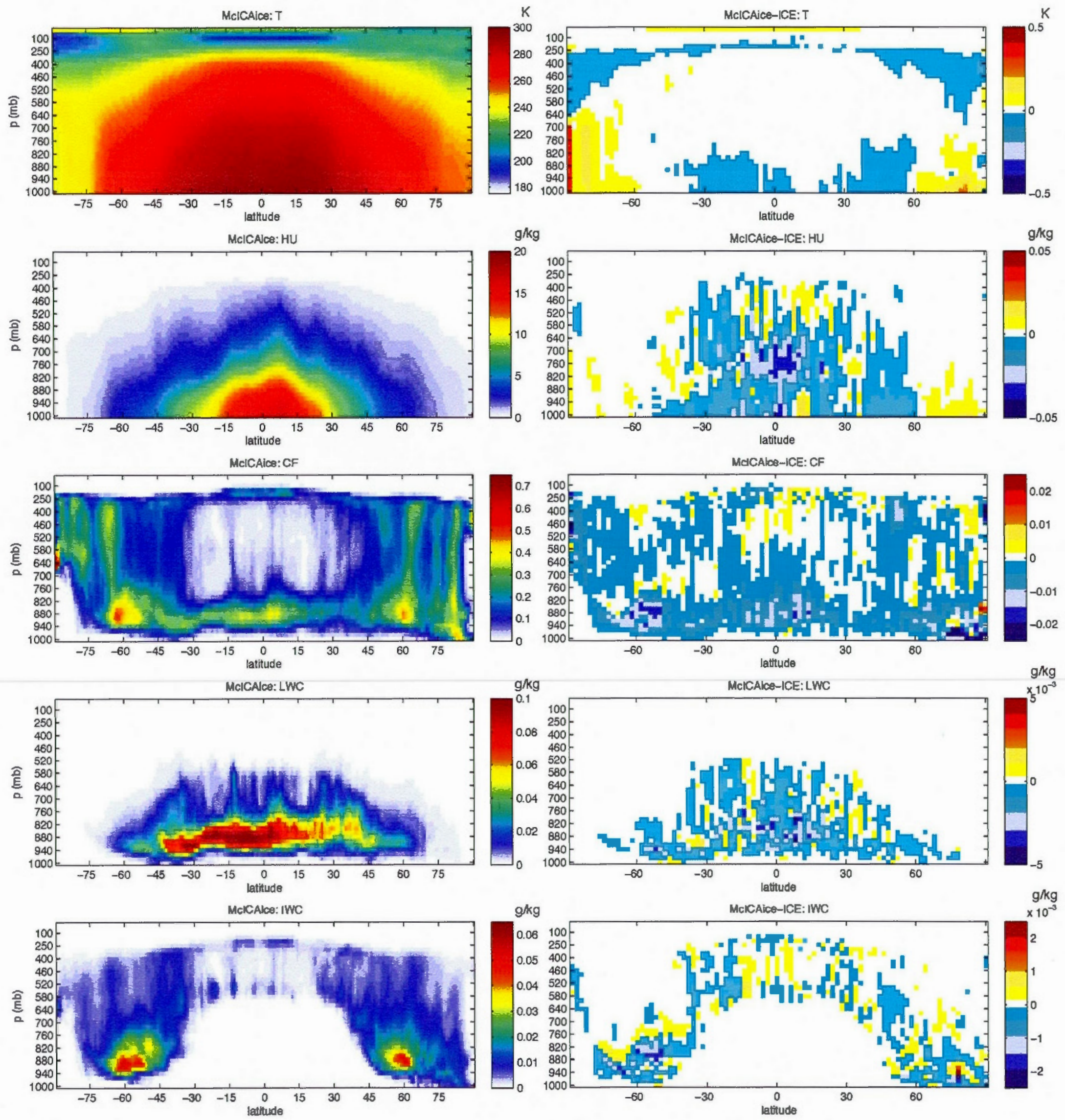

Figure 5.8 As figure 5.5 but for differences between McICAice and ICE (right column).

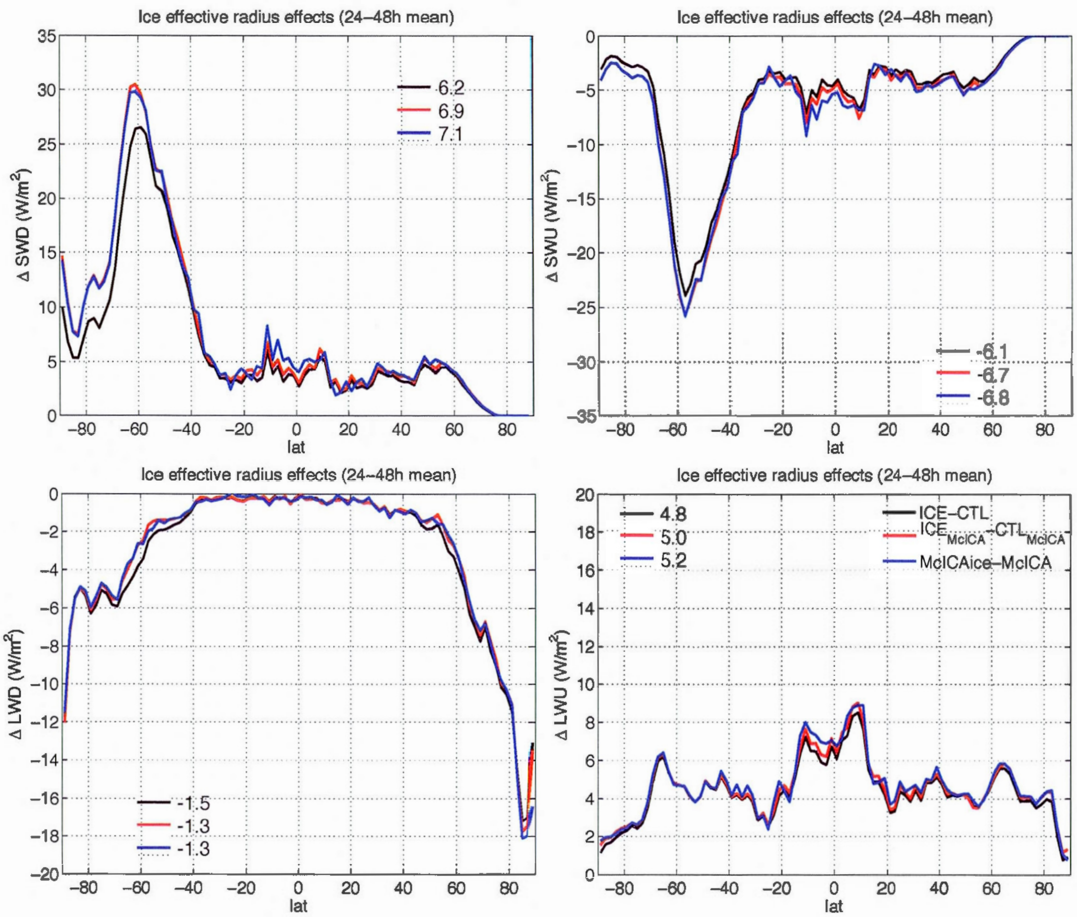

Figure 5.9 As figure 5.4 but for ice effective radius effects. See table 5.1 for simulation descriptions.

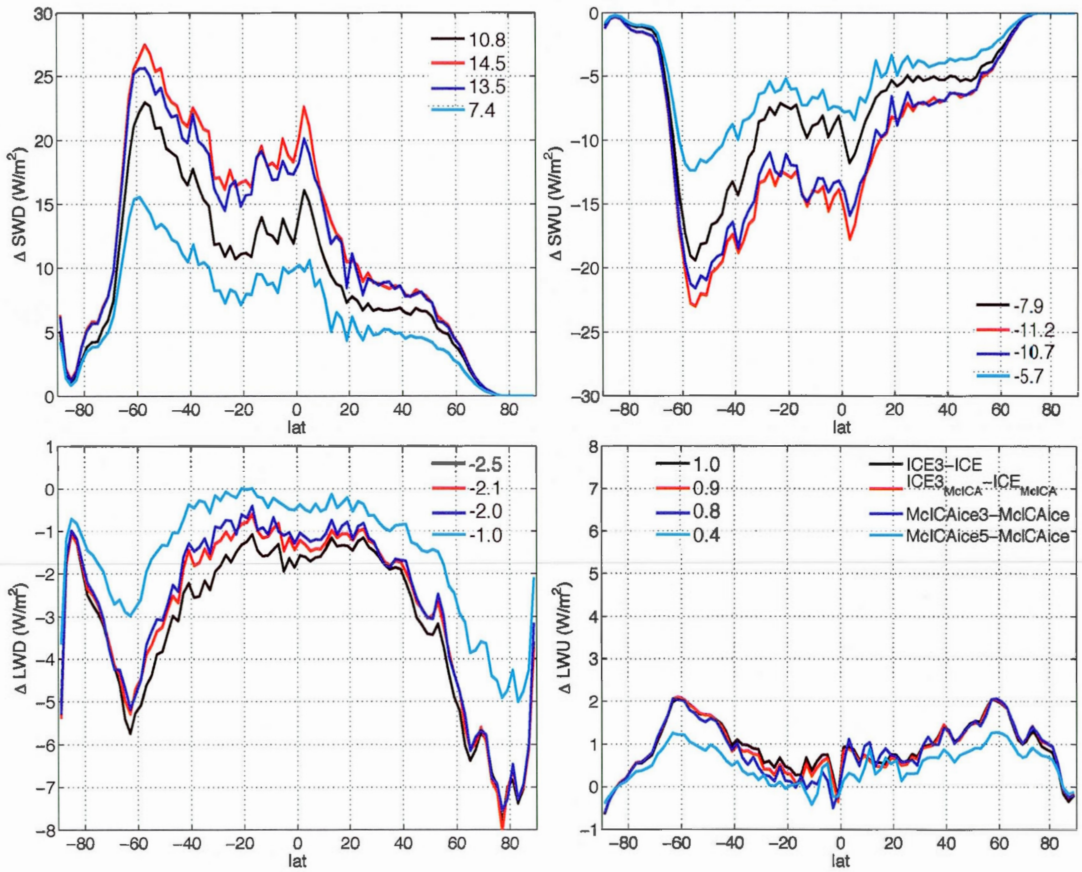

Figure 5.10 As figure 5.9 but for the LWC scaling effects. See table 5.1 for simulation descriptions.

clouds, inspired from Zhang *et al.* (2014). The flux sensitivities (in blue) are reaching the values of the constant maximum value of 3.5 km (L_{max}, black full line in figure 5.11) in the Tropics and are exceeding the values of the constant minimum value of 1.5 km (L_{min}, black dashed line in figure 5.11) over high latitudes. It means that such large decorrelation lengths for deep convection are able to recreate zonal mean flux sensitivities of constant L_{max} values. However, with varying decorrelation lengths as a function of cloud type, this parameterization is more physically sound and weather dependent.

The red lines ($L_{convMAXw}$) represent the test with CWC decorrelation lengths set to the same values as CF. By increasing these decorrelation lengths, the CWC is vertically more overlapping, reducing the integrated cloud albedo and emissivity, and it should increase the SWD at SFC and LWU at TOA, and decrease the SWU at TOA and LWD at SFC, compared to the previous experiment (in blue). These expected effects are only visible at high latitudes and mostly for the LW fluxes, where the integrated cloud albedo and emissivity are lower and fluxes are more sensitive to smaller variations.

Finally, the dashed lines represent the same two previous tests ($L_{convMAX}$ and $L_{convMAXw}$) but with other pairs of simulations (which both include increased horizontal inhomogeneity) to see if the signal is constant within different inhomogeneity regimes. Surprisingly, only the red dashed line exhibits a different signal for the LW fluxes and even becomes of opposite sign for the LWU at TOA (whereas the increased horizontal inhomogeneity produces increased LWU at TOA). This is an example of non-linear interactions between parameters.

Note here that decorrelation length tests were mostly performed and compared to McICAice simulations and not to the LWC scaled version McICAice3. Another test was done with McICAice3 (not shown) and showed the same sensitivities as the one in figure 5.11, suggesting that changing to lower cloud optical depth values does not impact the decorrelation lengths flux sensitivities.

Figure 5.13 presents the horizontal cloud water inhomogeneity (with the variability parameter ν) radiative effects, with two increased inhomogeneity parameterizations (decreased ν) whereas figure 5.14 presents two decreased inhomogeneity parameterizations (increased ν).

In figure 5.13, when the inhomogeneity is increased, the cloud albedo and emissivity are reduced, increasing the SWD at SFC and the LWU at TOA, and decreasing the SWU at TOA and the LWD at SFC. These effects are all seen for the different experiments. Two groups of experiments are shown: the increased inhomogeneity in all cases (denoted ν, blue and cyan lines), and the increased inhomogeneity only when shallow or deep convection is triggered (ν_{conv}, red lines). The effects are similar over the Tropics and mid-latitudes and generally larger over high latitudes for the former, as expected, since no convection is triggered in these regions. However, large differences occurs within the two groups. For example, the differences between the cyan line and the two blue lines are important for the LW fluxes almost everywhere except for the Tropics. Even by taking into account that the blue lines includes thc $L_{convMAX}$ parameterization which, for example, reduces LWD over Tropics and mid-latitudes, and increases LWD over high latitudes, it does not explain directly the discrepancies seen in figure 5.13. However, since a higher L_{cw} value means that the CWC is more overlapping in the vertical, it can reduce inhomogeneities between cloud vertical layers. Hence, it can counteract the increased horizontal inhomogeneity when this effect is integrated over the vertical. In this case, differences are more important at all latitudes for LWU at TOA whereas for LWD at SFC, differences are seen only for latitudes >40°.

Looking at the two decreasing horizontal inhomogeneity parameterizations on figure 5.14, the opposite responses are seen, as expected. The ice parameterization (ν_{ice} with $\nu = [11; 11; 11]$ for IWC, blue and cyan lines) presents more sensitivities, especially over high latitudes for SW fluxes and everywhere for LWU at TOA. This is expected, since for SW fluxes, ice cloud contributions are more important when liquid clouds are minimal, and LWU at TOA are mainly controlled by high (ice) clouds. When the LWC scaling is applied, the ice sensitivity is even higher, as explained in the previous section: with less liquid to interact with radiation, the ice clouds are contributing more to the radiative sensitivities. For the liquid parameterization (ν_{liq} with $\nu = [1; 2; 11]$ for LWC, red and magenta lines), the lower sensitivities can be explained by the fact that only ν_3 is increased (contrarily to the ice parameterization where all three ν components are increased), and that this parameter is used only when CF=1. The differences due to the LWC scaling do not seem to be significant in this case.

Looking at all these tests, the horizontal inhomogeneity parameter has the larger radiative sensitivities, at least for the increased inhomogeneity tests in the GEM-CLIM model. Whereas the decreased inhomogeneity tests are similar in global mean sensitivity to the decorrelation lengths tests. In comparison, Barker and Räisänen (2005) have also found similar global mean sensitivities between horizontal inhomogeneity and CF decorrelation length. While Shonk and Hogan (2010) have found more important radiative sensitivities for horizontal inhomogeneity compared to CF decorrelation lengths. Moreover, Barker and Räisänen (2005) also found similar radiative sensitivities between effective radius and horizontal inhomogeneity, while this chapter results show higher ice effective radius sensitivities. However, the present ice effective radius test is a much more drastic test compared to Barker and Räisänen (2005) test of $\pm 10\%$ variation in effective radius.

In conclusion, this section showed that both horizontal and vertical SCG param-

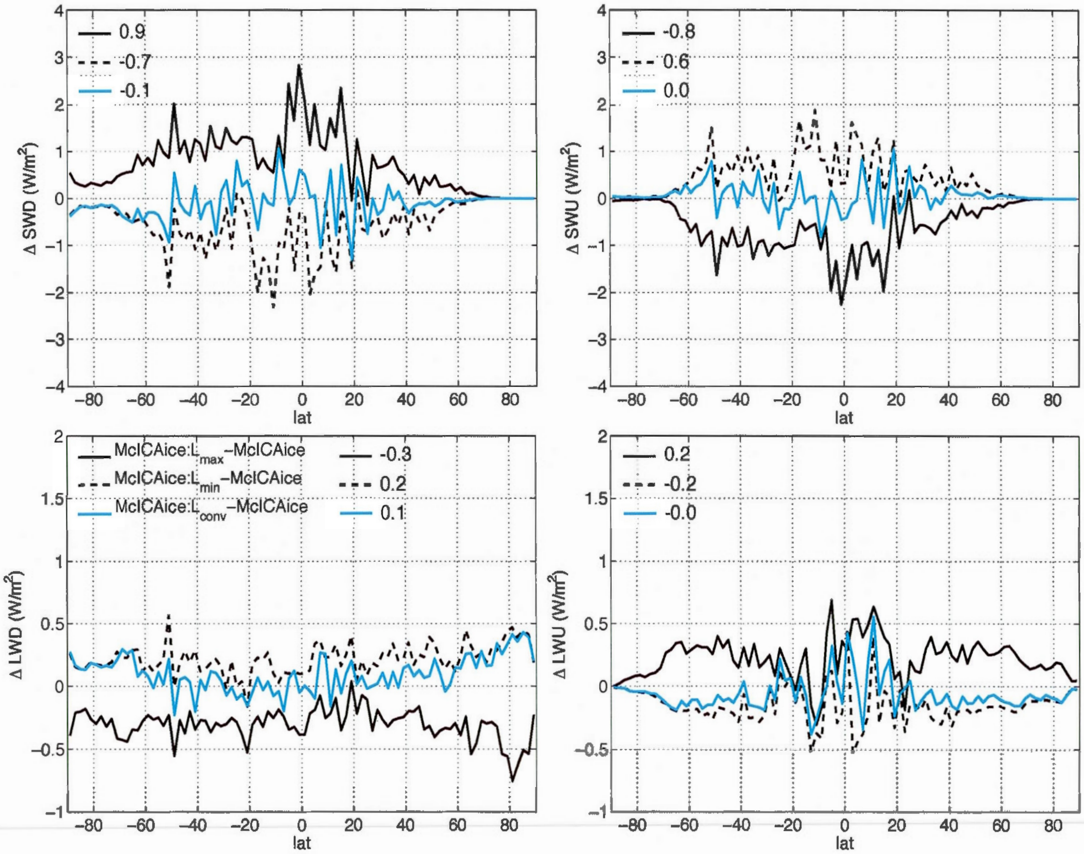

Figure 5.11 As figure 5.4 but for decorrelation length effects. See tables 5.2 for simulation descriptions.

eterizations are generally producing what is expected from their modifications. However, a few examples have shown that non-linear interactions can exist and produce unexpected flux modifications. Besides, it is shown that parameterizations linked to the cloud phases or cloud types can be easily introduced in the SCG and they can produce significant radiative responses compared to constant parameters.

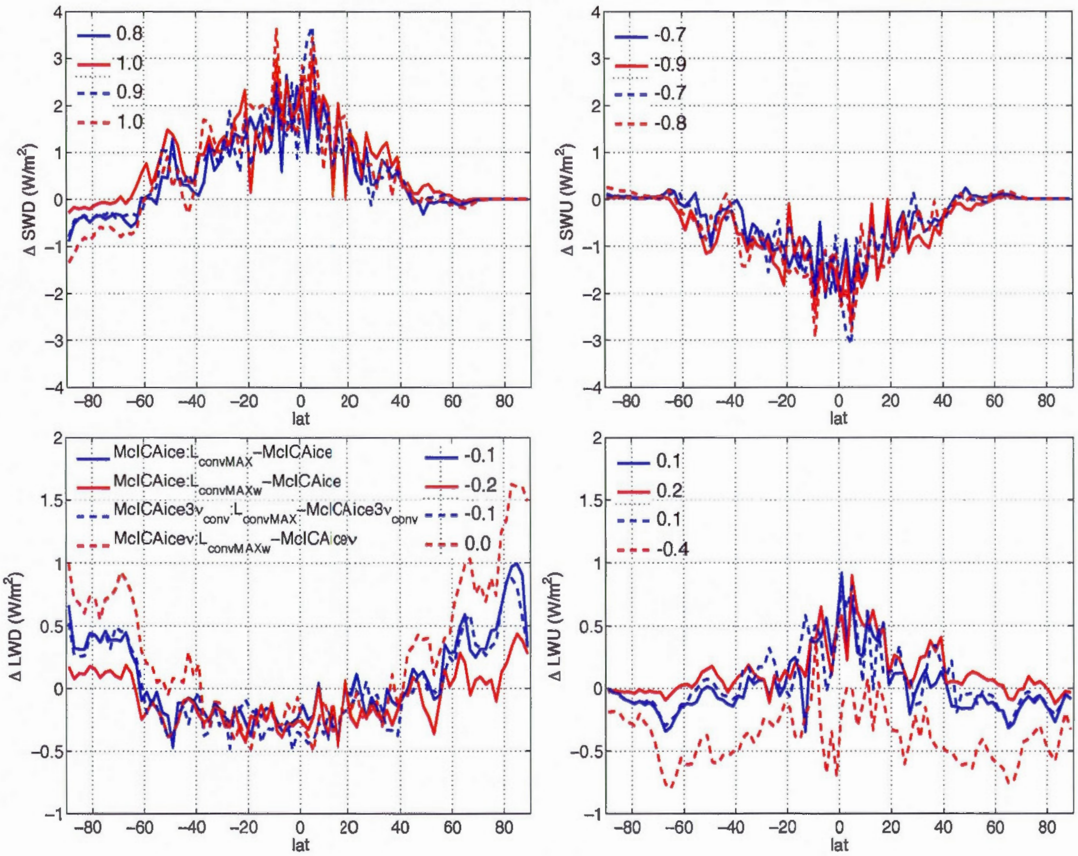

Figure 5.12 As figure 5.11 but for other decorrelation length parameterizations. See tables 5.2 and 5.3 for simulation descriptions.

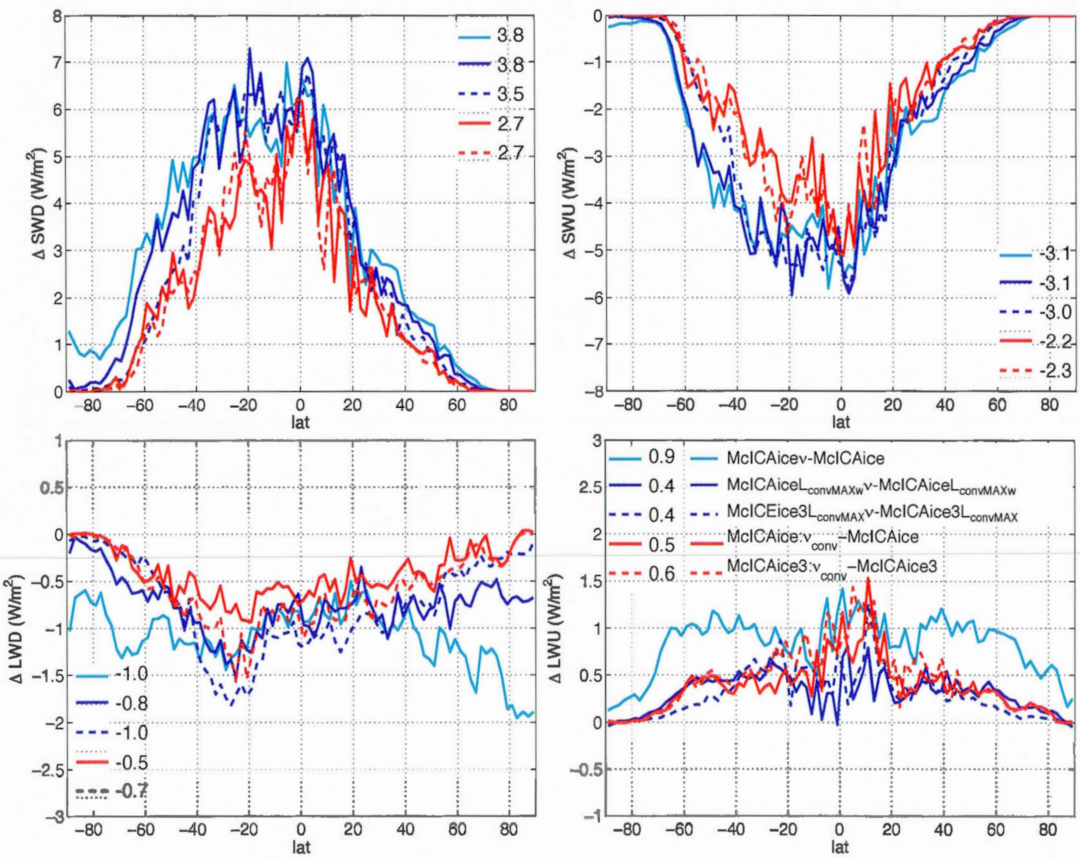

Figure 5.13 As figure 5.11 but for horizontal CWC increased inhomogeneity parameterizations. See tables 5.2 and 5.3 for simulation descriptions.

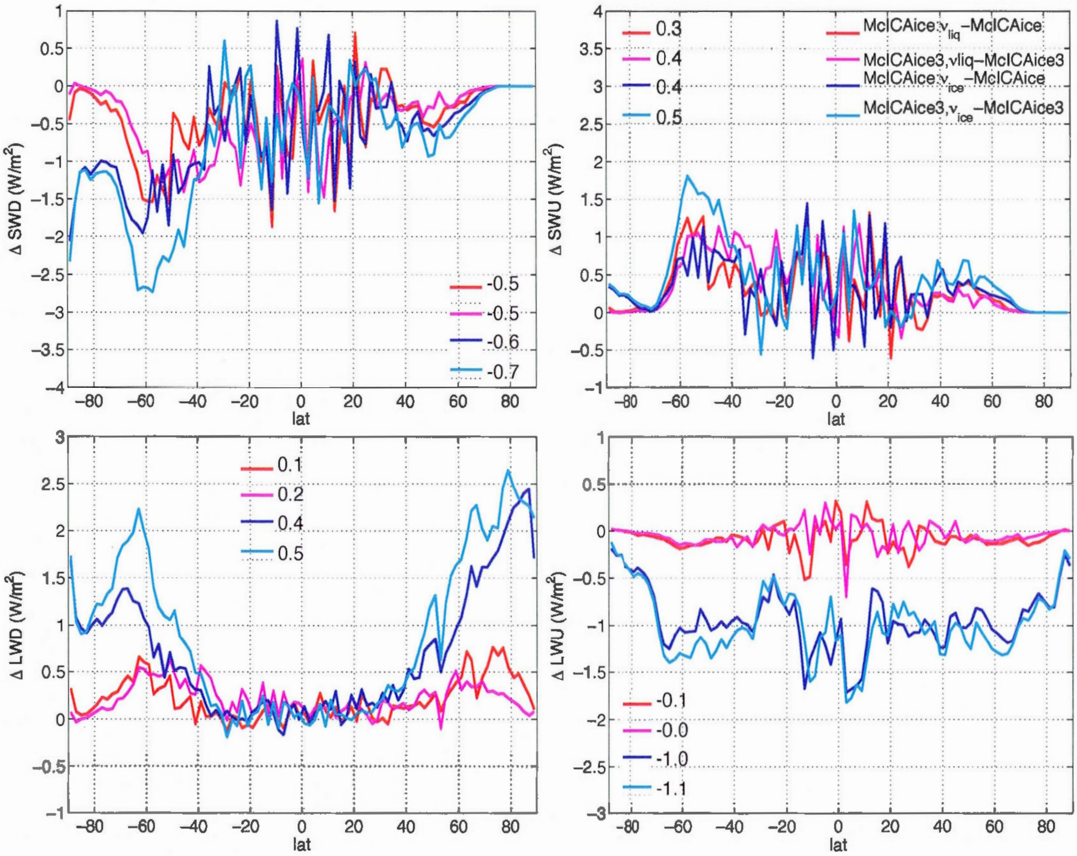

Figure 5.14 As figure 5.13 but for horizontal CWC decreased inhomogeneity parameterizations. See tables 5.2 and 5.3 for simulation descriptions.

5.3.3 Combined parameterizations to approach observations

For this last result section, a combination of different scalings and SCG parameterizations is presented step by step (by modifying one parameter at a time) to illustrate how it can be combined to approach the observations.

Figure 5.15 presents the different flux differences against CERES-SYN1deg observations. The basic state is the McICAice3 simulation (black line) since both the ice effective radius parameterization and the LWC scaling reduce the model radiative biases. To further reduce the SW biases over the Tropics, the horizontal inhomogeneity is increased when the shallow and deep convection is triggered (ν_{conv}, red line). However, this increases the LWU biases over the Tropics and increases the SW biases between 40°S and 60°S. To go one step further, the $L_{convMAX}$ is applied (blue line) which reduces only slightly the SW biases over the Tropics and still increases the LWU biases over the Tropics (but reduces the global mean LWU bias at TOA). Finally, mainly to reduce the LWU biases over the Tropics, the ice horizontal inhomogeneity is decreased (ν_{ice}, cyan line), effectively reducing the LWU biases over the Tropics and the SW biases between 40 and 60°S at the cost of increasing all global mean biases.

These flux modifications can seem insignificant compared to the observation biases but they are an illustration of what can be done with the SCG and the McICA methodology. This is also an example of correcting some zonal biases at the cost of degrading other areas even if parameters are more physically related to the different cloud phases or regimes.

From a global mean perspective, the ICE3 simulation presented in figure 5.3 presents better results compared to observations, whereas in figure 5.15, it is the McICAice3$\nu_{\mathrm{conv}}\mathrm{L}_{\mathrm{convMAX}}$ simulation which performs better. This can lead to the conclusion that McICA does not perform as well as the classic RT calculations in this case, but it can be argued that the model cloud biases are certainly not helping since McICA is not designed to counteract such cloud related biases. This is a conclusion that other authors have reached when comparing basic McICA implementations in their respective models (e.g. Pincus *et al.*, 2006; Räisänen *et al.*, 2005, 2007). Furthermore, it can also be argued that it is more physically sound to clearly identify the modeled cloud biases and try to reduce them instead of mitigating the mean results with radiative compensations. It is reasonable to believe, that once the basic cloud biases are reduced, the different SCG parameterizations proposed here could be used to approach the radiative flux observations with physically based parameterizations.

5.4 Conclusions

This chapter focuses on McICA and SCG parameters radiative sensitivities in different conditions. Many simulations were performed to i) assess the McICA effects under different cloud optical depth scalings, ii) isolate the different parameters effects and iii) illustrate the combined parameter effects.

Since many simulations were required, only short-term simulations were analyzed, over a one day mean period, 24 h after the beginning of the simulations. With regards to the previous chapter results, two cloud optical depth scaling were tested: a reduced LWC passed to the RT scheme and a modified (and increased) ice effective radius parameterization. These two scaling techniques reduce the cloud optical depth and therefore allow to test the theoretical McICA behavior that was demonstrated in section 1.1: the McICA horizontal inhomogeneity effects should be greater at lower cloud optical depth values.

Results were presented in three sections: the McICA sensitivities under different cloud optical depth scalings, the SCG parameters sensitivities, and an example of

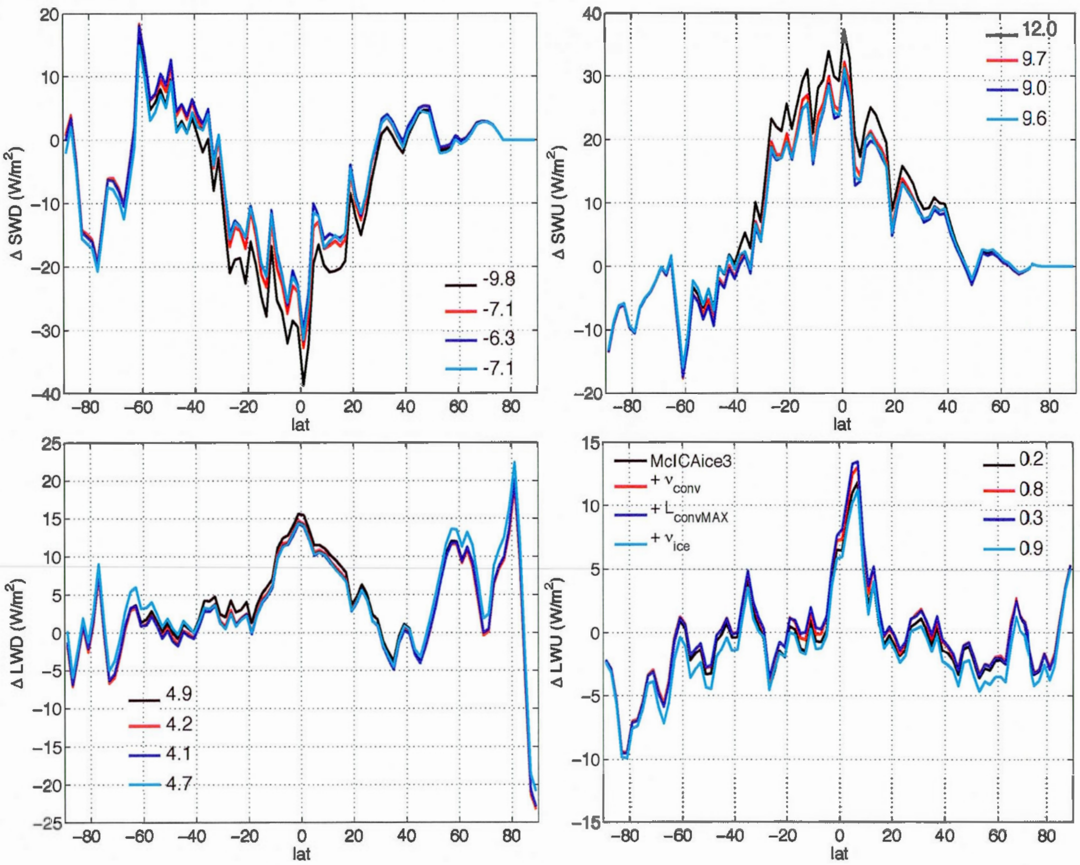

Figure 5.15 Zonal 1 day mean flux differences between different model simulations and observations (CERES-SYN1deg).

combined parameterizations to approach observations.

The first section showed that at lower cloud optical depth values, the McICA horizontal inhomogeneity radiative effects are generally larger, particularly for liquid clouds, when compared to homogeneous cloud treatment. However, when compared to the classic RT calculations, the combined McICA effects (of horizontal inhomogeneity introduction and decorrelation lengths, and the SW-ACOD and LW-GD correction removal) are smaller due to more balanced effects between the horizontal inhomogeneity introduction (that have stronger effects) and the SW-ACOD and LW-GD removal (that have smaller effects). However, for the LWD at SFC, McICA effects are stronger in specific regions to due non-linearities between the LW-GD corrections and cloud optical depth. It is also demonstrated that the McICA horizontal inhomogeneity radiative effects are increasing the ice cloud albedo, oppositely to the liquid clouds, but as expected from theory in section 1.1. Besides, the reducing cloud optical depth scalings have more radiative impacts when the McICA methodology is applied, given that it is more sensitive to lower cloud optical depth values.

The second section showed that the SCG parameters exhibits radiative sensitivities that are expected: increased horizontal inhomogeneity decreases cloud albedo and emissivity, and increased decorrelation lengths decreases integrated CF. However, these sensitivities vary under different conditions or combinations (e.g. the parameterizations regarding ice clouds are more radiatively sensitive when liquid clouds are radiatively reduced) and in few cases, even produce unexpected results when combined. As a further matter, parameterizations that are linked to either the cloud phase or cloud type are producing significant radiative sensitivities (comparable to the constant parameter sensitivities) and with more zonal variability. Finally, under the tested conditions and for the GEMCLIM model, the horizontal inhomogeneity parameter is showing the largest radiative sensitivities.

The last section is an example of combined parameterizations to approach radiative flux observations. It shows how parameterizations that are based on cloud phase or cloud type can modify biases over more specific regions than a constant parameter. However, the parameterizations presented here are still simple, and even if it allows to reduce some zonal biases for one flux component, it generally increases other flux biases at the same time.

It is important to mention that the McICA methodology and its SCG are not conceived to correct or mitigate the cloud intrinsic biases in their CF or CWC. It is rather a flexible tool to integrate one or many parameterizations for the horizontal inhomogeneity and overlap assumption. The parameterizations presented here were mostly to illustrate the possibilities that the SCG offers.

Once the cloud biases are reduced in a model, the SCG offers the flexibility to include parameterizations that are based on observations or directly on the model cloud schemes. It further offers the possibility to link the different cloud schemes through both the subgrid and the resolved scales. An example would be the length of a convective tower calculated by the convective scheme that could be passed as a decorrelation length. Another example would be the distribution form and width for the horizontal water content, as calculated or defined by a second or third moment microphysics scheme.

CONCLUSION

Context

Cloud-radiation interactions are a complex problem to isolate, analyze and improve in today's GCMs because of: the many scales involved, the lack of observation or knowledge about some fundamental cloud processes, and the remaining open question about how to represent subgrid cloud processes in GCMs.

The McICA methodology has been proposed by Barker *et al.* (2002) and Pincus *et al.* (2003) to remove fixed assumptions on unresolved cloud structure from the radiative transfer solution and replace it with a flexible stochastic representation of cloud subgrid-scale variability. Such an approach gives much more flexibility to test observed cloud properties (e.g. vertical overlap, cloud water horizontal distributions) and also allows to potentially use weather dependent parameterizations. However, models are often tuned to have a right mean top of atmosphere radiative budget that hides compensating biases. Correcting a specific bias can degrade the general model performance.

This methodology has been implemented in a number of NWP and climate models but with mitigated results since it can reveal cloud biases that were previously corrected by the radiative transfer scheme fixed corrections. However, it is generally recognized as an improvement since it offers a new flexibility in cloud subgrid-scale parameterization. A few studies have also derived SCG parameterizations based on observations or on model variables.

Scientific questions

Even if the McICA methodology has been introduced more than 10 years ago, many questions remain on different levels.

For a specific model implementation, the basic questions would be: how does McICA perform? How does it compare to existing and already implemented inhomogeneity corrections? How does the model adjust to these flux modifications?

Concerning the general McICA methodology, the more fundamental questions would be: how do the subgrid scale cloud variability radiative effects vary? On what conditions are they dependent?

Finally, cloud subgrid scale variability boils down to two distinct components from the radiative transfer perspective: the horizontal distribution of cloud water content and the vertical overlap or correlation of cloud fraction and cloud water content. Given that, how do these parameter radiative effects compare to each other? How do they compare to other radiative parameters such as effective radii? How do they interact? How can they be connected to model variables or physical processes and is it radiatively significant?

Thesis framework

This thesis is focusing on the implementation of the McICA methodology in the GEMCLIM model and trying to answer the McICA questions that are beyond this specific model.

To achieve these goals, the GEMCLIM model is used in a global uniform mode with an horizontal grid mesh of 0.5° in order to test and evaluate the McICA radiative effects in all conditions: over land and ocean, from Arctic to tropical conditions. The different chapters present simulation results from timescales that spread from 24h after the beginning of simulations to three year seasonal means. This is dictated, on one side, by the great number of simulations (almost 30) that were needed to assess the different parameterizations, and on the other side, by a longer simulation period to assess the model responses and possible adjustments on longer time scales. However, it is clear that this study is not a climatological assessment of the model or the McICA methodology. Moreover, the model possible adjustments were still limited to a few years and to conditions of prescribed SSTs.

Different tools and approaches were used in this thesis to try to illustrate the many components behind the cloud-radiation interactions. As mentioned, different time scales were studied: from the instantaneous results to the seasonal mean results, but also different spatial scales were studied. For the radiative effects at surface and top of atmosphere, global mean signals were used, in parallel to zonal mean, and 0.5° by 0.5° maps. To connect the surface and top of atmosphere signals, zonal mean vertical profiles were also presented. In parallel, co-variability diagrams were used to illustrate the relations between the different flux signals and the cloud fraction or cloud water content. Finally, offline McICA simulations where also presented to put in perspective the direct McICA effects and the possible model adjustments to this new methodology (and to remove natural variability).

Observations used to validate the model simulations were different global satellite data sets: the CERES EBAF and SYN1deg data sets for all the radiative fluxes and for the derived cloud variables, and the SSM/I data set for another source of cloud liquid water path and water vapor. One key variable that was limiting this analysis was the IWP that was available with the different CERES data sets, but that has such a great associated uncertainty that it was impossible to conclude about the model performance concerning this variable.

Results and contributions

Compared to homogeneous cloud treatment and the MRO assumption, the McICA methodology general effect is a reduced cloud albedo and emissivity due the dominant horizontal inhomogeneity introduction. The change from MRO to decorrelation lengths has only small effects and generally slightly attenuates the horizontal inhomogeneity effects (since its effects are reverse to the horizontal inhomogeneity effects).

Given that the comparison with observations showed a major overestimation of LWP on all time scales in the GEMCLIM model, it has been demonstrated that the McICA methodology generally degrades the radiative fluxes at surface and top of atmosphere in comparison to CERES fluxes, both on the one day mean period and the three year seasonal mean. This is explained by the fact that the McICA methodology within its standard implementation (i.e. without any parameterization modification) has much less radiative effects both in SW and LW in comparison to the GEMCLIM existing inhomogeneity cloud corrections. Moreover, the existing SW corrections are increasingly correcting the cloud albedo with increasing cloud optical depth, while the McICA methodology effects of reducing the cloud albedo are oppositely decreasing with cloud optical depth. This later effect is linked to the relationships between cloud albedo (and emissivity) and cloud optical depth: they vary more rapidly at low cloud optical depth values, creating greater differences between homogeneous and inhomogeneous cloud treatment at low optical depth values. Hence, the overestimated LWP enhances the flux discrepancies since the existing corrections are stronger at larger cloud optical depth values and inversely for the McICA methodology.

Once the McICA methodology is implemented, small cloud adjustments are visible on all time scales. These adjustments are visible through a reduction in low cloud

CF and CWP. A probable cause is the modification of heating rates with McICA: with offline McICA fluxes, a reduced cooling in net heating rate is visible in low clouds and below. However, for online McICA fluxes, this signal structure mostly disappears. It can mean that the McICA reduced cooling reduces low clouds in online simulations and, in turn, these modified clouds would alter the online net heating signal. These modifications lead to reductions in McICA zonal and global mean signals for all fluxes except for LWU at TOA, which are less influenced by low clouds.

From a more general perspective, the McICA methodology has been shown to be CWP dependent as suggested by the theoretical behavior of cloud albedo or emissivity as a function of LWP or IWP. It has been shown that under reduced cloud optical depth conditions, McICA horizontal inhomogeneity effects are greater, i.e. it reduces more the cloud albedo and emissivity. However, it has also been shown that ice cloud albedo is increased with McICA, a feature that was also expected from the theory since the curvature of the cloud albedo relationship to IWP is inverse of the one to LWP. Besides, since the emissivity relationship to LWP reaches a saturation point more rapidly (at lower LWP values) compared to the albedo relationship, the McICA LW effects also diminish more rapidly and therefore, are generally much weaker than the McICA SW effects. As an example, results from one winter (DJF) seasonal mean McICA effects against homogeneous cloud treatment show a global mean increase of 4.7 W/m^2 for the SWD at SFC and a decrease of 0.8 W/m^2 for LWD at SFC. Moreover, the McICA SW effects are greater at SFC compared to TOA while the LW effects are of similar amplitude at SFC and TOA, with a decrease of 2.6 W/m^2 for the SWU at TOA and an increase of 0.8 W/m^2 for LWU at TOA. Finally, the McICA effects increase with CF since more clouds can contribute to these flux modifications.

Looking at the SCG parameters, many parameterizations have been tested on short time scales: from global constant values to cloud type or cloud phase dependencies, both for the horizontal inhomogeneity and the decorrelation length parameters. It has been shown that the horizontal inhomogeneity parameter has more potential to modify the radiative fluxes compared to the decorrelation lengths, with global mean signals two to three times bigger for the former. The increased inhomogeneity parameterization as a function of convection produces global mean differences of 2.7 W/m^2 for SWD at SFC and between -0.5 and -0.7 W/m^2 for the LWD at SFC, while the decorrelation length parameterization as a function of convection produces global mean differences of 1.0 W/m^2 for SWD at SFC and between 0 and -0.2 W/m^2 for LWD at SFC. However, these radiative effects are only half the ice effective radius effects tested. The ice effective radius modification tested are producing global mean differences of 7.1 W/m^2 for the SWD at SFC and -1.3 W/m^2 for the LWD at SFC while the zonal mean maxima can reach 30 W/m^2 for the SWD at SFC around 60°S and -18 W/m^2 over the Arctic for the LWD at SFC. In general, these parameterizations produce radiative effects that are expected but a few tests showed unexpected results with non-linear interactions between the two parameters, particularly for the LW fluxes.

Examples with cloud phase or cloud type parameterizations seem promising since they are either based on observations or physical insights and produce radiative effects that are discernible and that vary locally. One example is the decorrelation lengths based on convection occurrences, which can reproduce the global mean radiative effects of the constant decorrelation lengths, while being meteorologically dependent. Furthermore, these parameterizations offer the possibility of easily link the different cloud schemes in a model via both the subgrid and resolved scales. This coherence would enhance the physical representation of clouds and could even help in understanding the cloud biases while comparing to observations since the radiative transfer scheme would reflect more directly the model cloud biases.

Previous articles have shown how the McICA improves or not the respective model performances but few have looked at specific SCG parameterizations. This work innovates by analyzing in detail the different McICA contributions (the horizontal inhomogeneity vs. the vertical overlap, the SW vs. the LW effects, the SFC vs. the TOA effects, the local vs. the global mean effects, the liquid vs. the ice cloud effects, etc.) and putting it in perspective with an already existing cloud inhomogeneity correction. Moreover, a clear demonstration was made about how the horizontal inhomogeneity radiative effects vary as a function of CWP and cloud phase. Furthermore, it demonstrates how the SCG parameters can be easily linked to model variables and observations to be more weather dependent and more physically sound and that such implementations are producing significant radiative responses. By regrouping and comparing many parameterizations, a new step is taken to understand these parameter radiative effects and the possibilities they offer.

Limitations of the project

This project has looked mainly at the SFC and TOA radiative budget, but these components are only a part of a complete model evaluation. Since the McICA methodology changes the radiative fluxes also in their vertical structure, it can affect significantly other variables such as temperature and precipitation. Furthermore, the diurnal cycle may be affected, both from the direct radiative modifications and from indirect feedbacks such as the convection triggering.

The model's significant LWP bias has limited the possibility of comparing the many parameterization tests with observations given that the modeled clouds were far from the observational range, even with the different cloud optical depths scalings used (since zonal biases remain). This problem is not currently seen in limited area studies with the same model, probably due to the lateral boundary constraints. The choice of global grid was made in order to sample all cloud conditions, and therefore all McICA possibilities.

In terms of timescale, many simulations (particularly for the different parameterizations) were performed only over a few days, thus limiting our conclusions with regards to the long terms model responses and adjustments. Moreover, as mentioned before, the model being only an atmospheric model, the adjustments possibilities were more restricted compared to a coupled model. With regards of the previous points, no conclusion is drawn from the different SCG parameterizations in terms of specific model performances.

Remaining questions

For the GEMCLIM model, despite the obvious LWP bias in global mode that has to be addressed, the McICA methodology remains to be tested on climatological time scales and for a more complete set of variables that include at least surface temperature and precipitation, as mentioned in the previous section.

For the SCG parameterizations, development needs to be done to link the different cloud scheme information or the other model variables to the parameters. In parallel, these modifications need to be evaluated with observations, possibly at higher spatiotemporal resolutions with data sets that include more cloud variables. Surface observation sites can provide such observation data sets at the cost of spatial coverage. New satellite observation data sets are also providing more coherent cloud and radiative informations, but again, only at the satellite spatiotemporal scale (generally two times a day for bands of a few kilometers).

Going one step further would be to include a stochastic treatment of subgrid scale variability for different variables that influence clouds and to be coherent between the different schemes. For example, a subgrid scale variability in humidity could be integrated to a double or triple moment microphysics scheme (which include subgrid CF), which could in turn, provide horizontal distribution of cloud water content to the SCG. Convection, which is generally subgrid scale, could also be integrated better into the SCG by keeping the associated cloud tower together in the subgrid columns depending on the wind shear. This suggests that the different schemes in a model would be connected not only via the resolved scales but also via the subgrid scales.

ANNEX A

Other useful equations

From Liou (1992), the cloud optical depth (in the visible) can be approximated as a function of effective liquid radius or effective ice diameter and LWP or IWP as followed:

$$\begin{aligned}\tau_{liq} &\simeq \frac{3LWP}{2\rho_{liq} * r_{eff,liq}} \\ \tau_{ice} &\simeq IWP\left(c + \frac{b}{D_{eff,ice}}\right)\end{aligned} \tag{A.1}$$

However, in the GEMCLIM model formulations, the cloud optical depth is calculated as followed:

$$\begin{aligned}\tau_{liq,SW} &= LWP\left[a_1 + \frac{a_2}{r_{eff,liq}} + \frac{a_3}{r^2_{eff,liq}} + \frac{a_4}{r^3_{eff,liq}}\right] \\ \tau_{ice,SW} &= IWP\left[A_1 + \frac{A_2}{c * r_{eff,ice}}\right] \\ \tau_{liq,LW} &= LWP\left[b_1 + b_2 * r_{eff,liq} + \frac{b_3}{r_{eff,liq}} + \frac{b_4}{r^2_{eff,liq}} + \frac{b_5}{r^3_{eff,liq}}\right] \\ \tau_{ice,LW} &= IWP\left[B_1 + \frac{B_2}{c * r_{eff,ice}} + \frac{B_3}{(c * r_{eff,ice})^2}\right]\end{aligned} \tag{A.2}$$

With these model equations, the relationship for τ is proportional to LWP or IWP and approximately inversely proportional to r_{eff} similarly to equation A.1 except for $\tau_{liq,LW}$ where it can either increase or decrease as a function of $r_{eff,liq}$.

ANNEX B

Co-variability diagrams by cloud phases

This annex presents flux differences similarly to chapter 3 but as a function of cloud phase. For all figures, top row is for all cases (as seen in chapter 3 figures), 2^{nd} row is for liquid clouds only, 3^{rd} row is for ice clouds only and bottom row is for mixed clouds only. Global mean values are indicated in each panel and were included in chapter 3 in tables 3.4, 3.5 and 3.6.

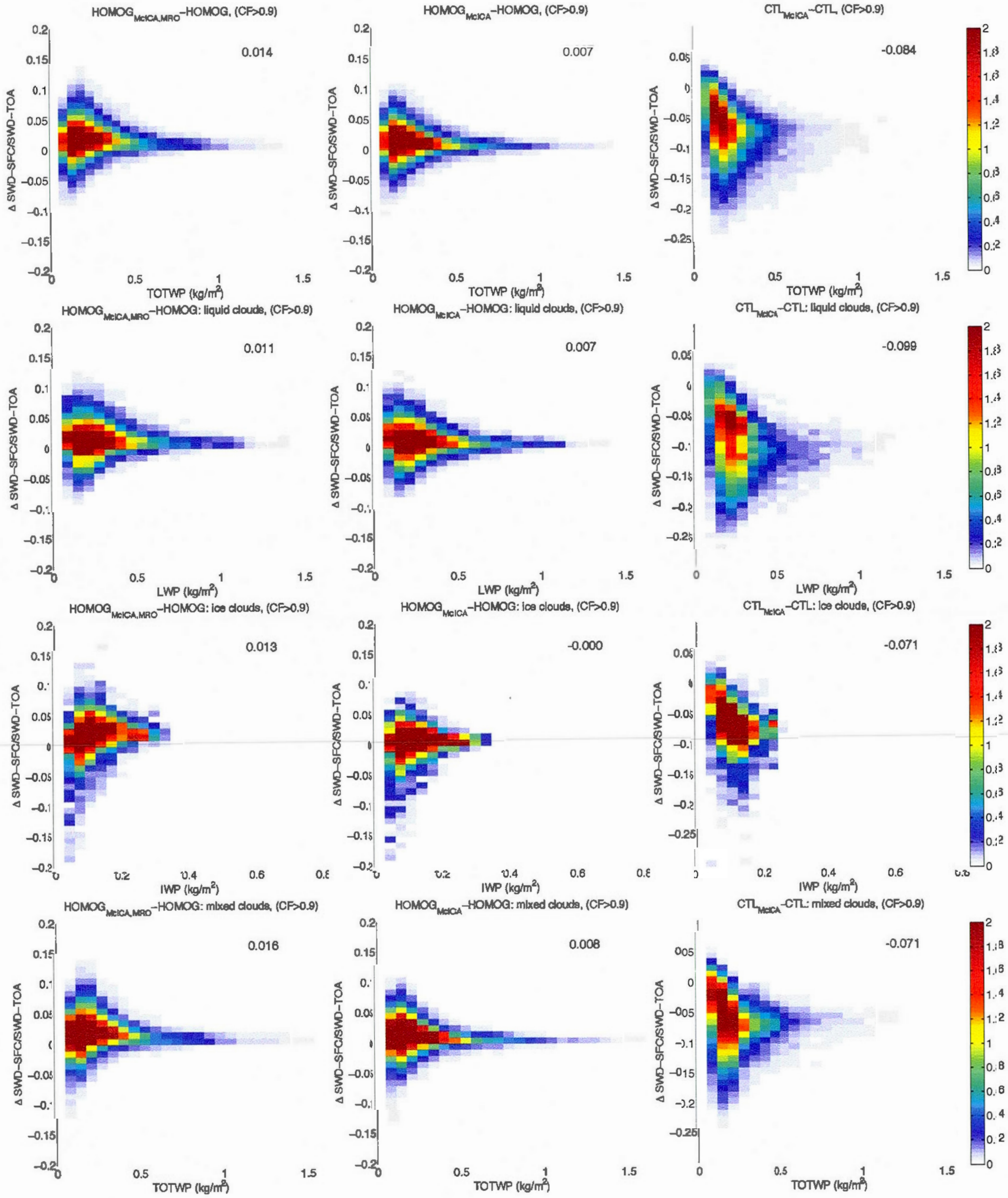

Figure B.1 SW ratio differences at SFC as a function of CWP for January 1^{st} for the HOMOG* (1^{st} column), the HOMOG (2^{nd} column) and the CTL simulations (3^{rd} column). Top row is seen in figure 3.3.

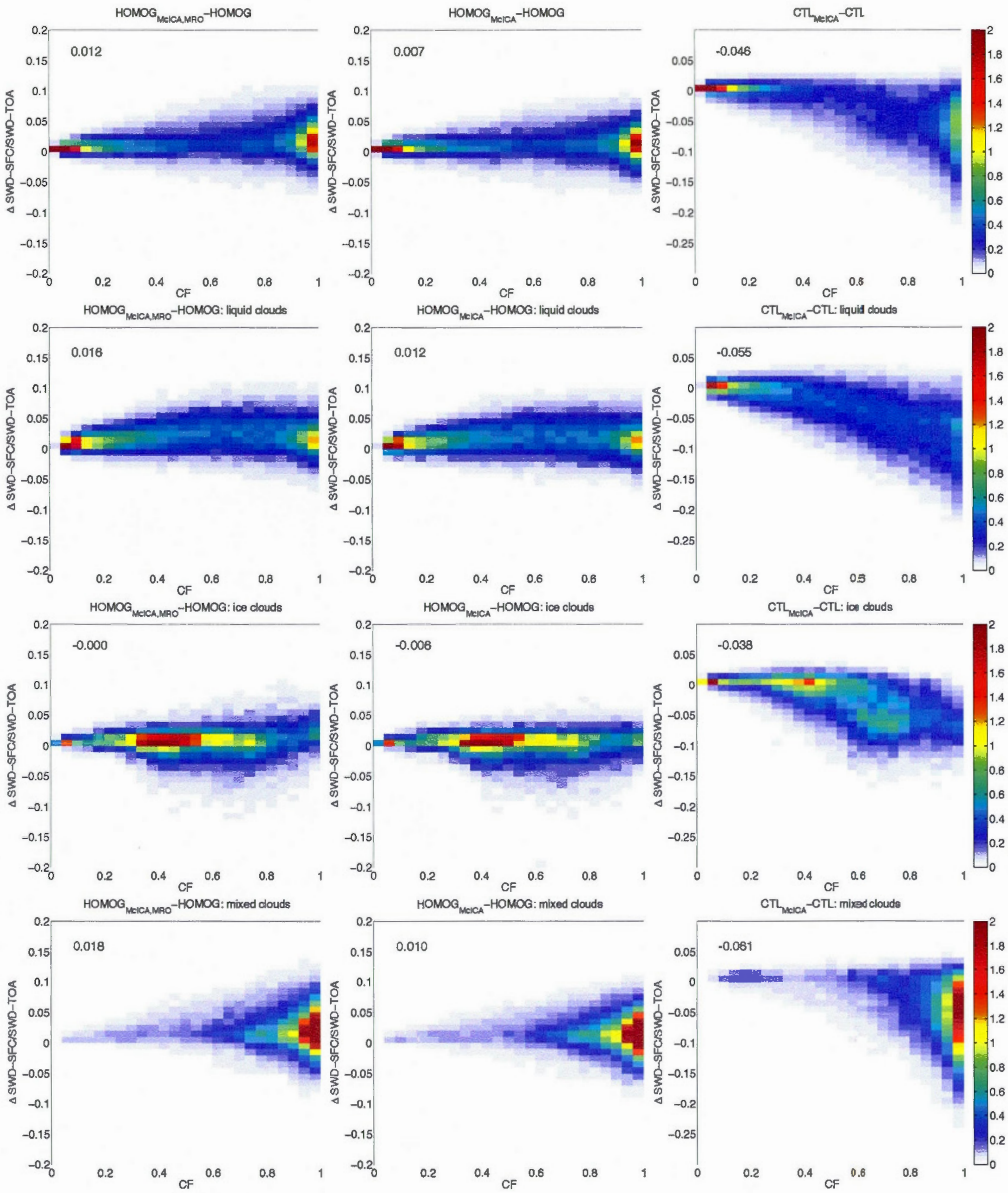

Figure B.2 SW ratio differences at SFC as a function of CF for January 1^{st} for the HOMOG* (1^{st} column), the HOMOG (2^{nd} column) and the CTL simulations (3^{rd} column). Top row is seen in figure 3.3.

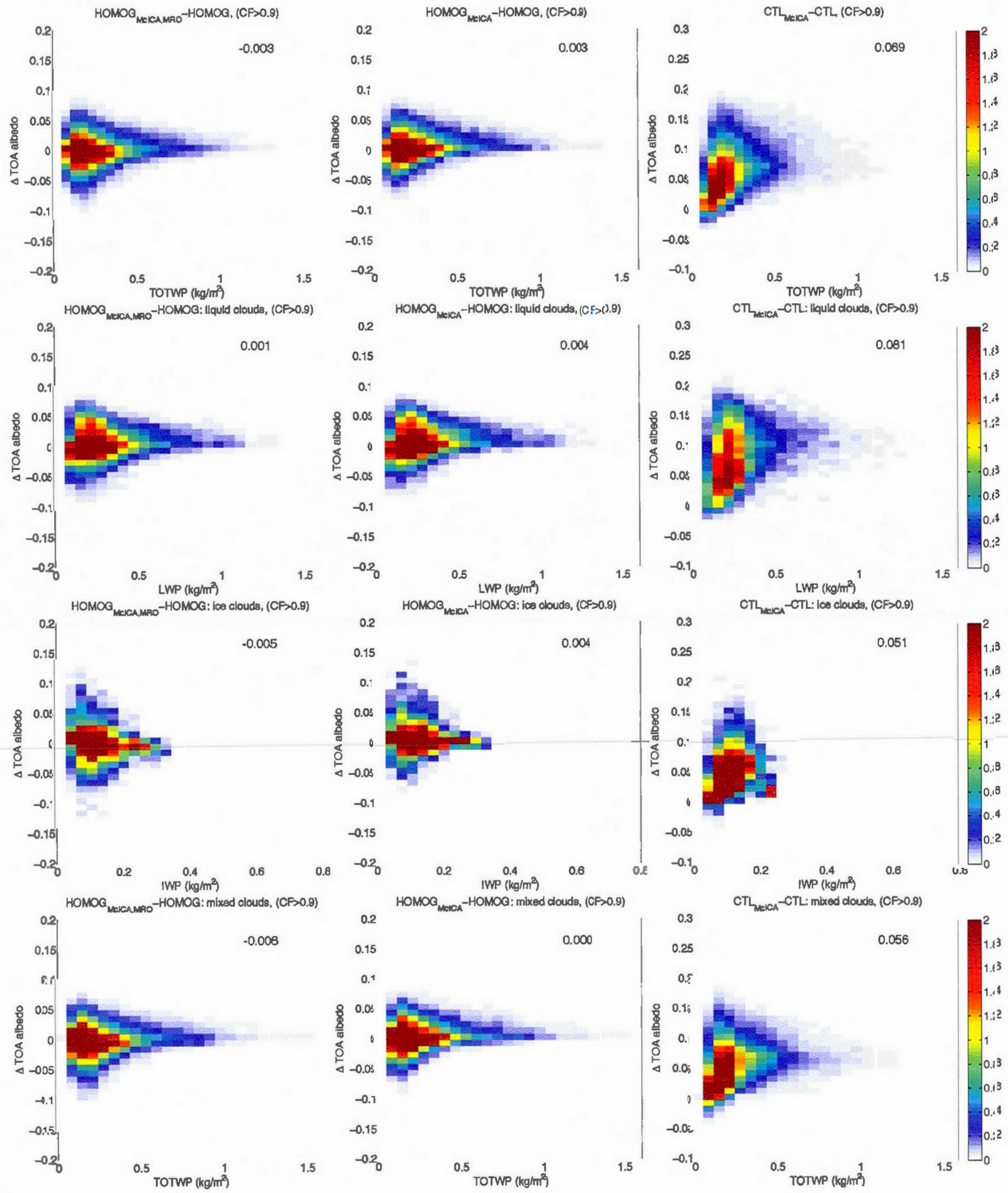

Figure B.3 TOA albedo differences as a function of CWP for January 1^{st} for the HOMOG* (1^{st} column), the HOMOG (2^{nd} column) and the CTL simulations (3^{rd} column). Top row is seen in figure 3.3.

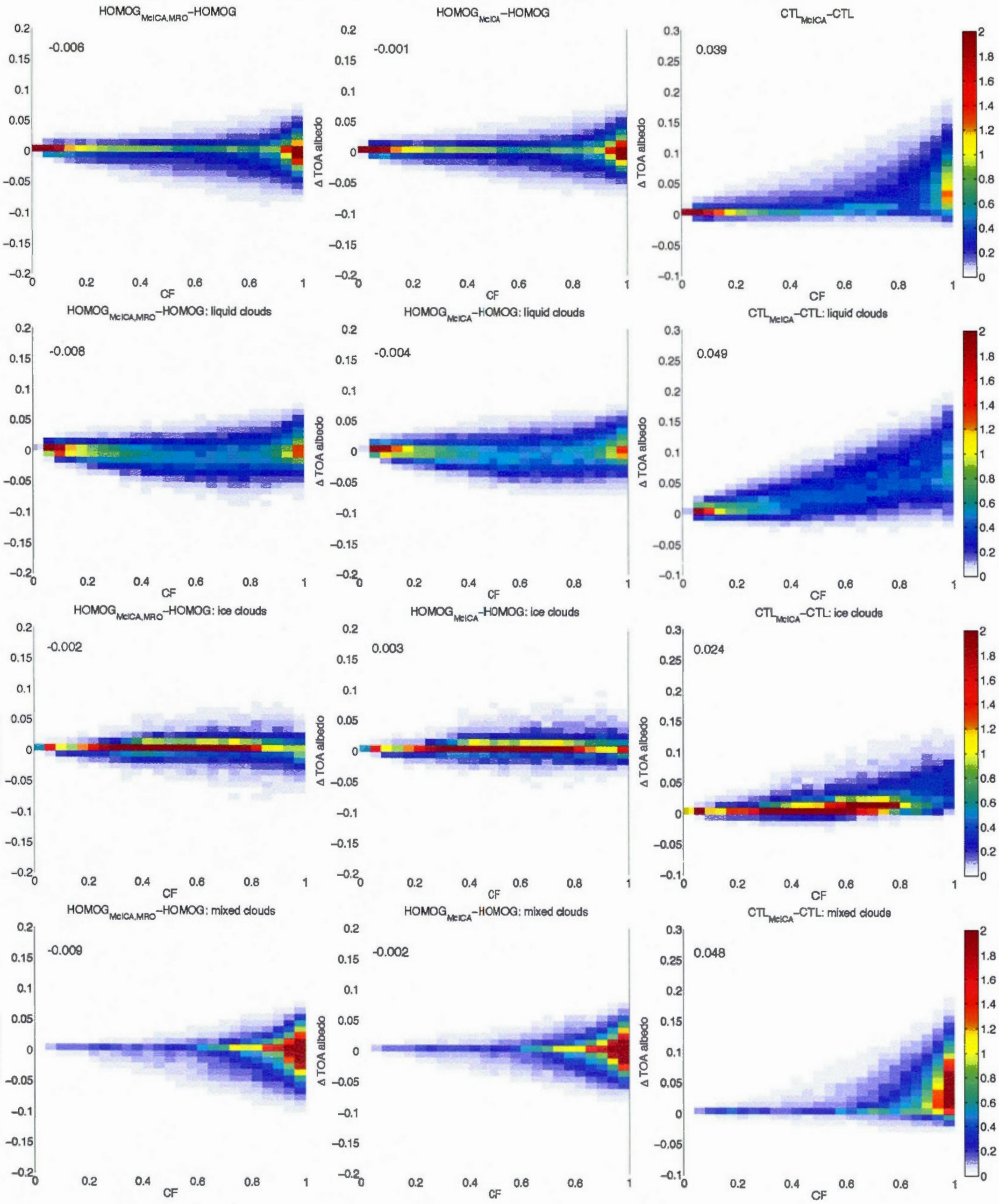

Figure B.4 TOA albedo differences as a function of CF for January 1^{st} for the HOMOG* (1^{st} column), the HOMOG (2^{nd} column) and the CTL simulations (3^{rd} column). Top row is seen in figure 3.3.

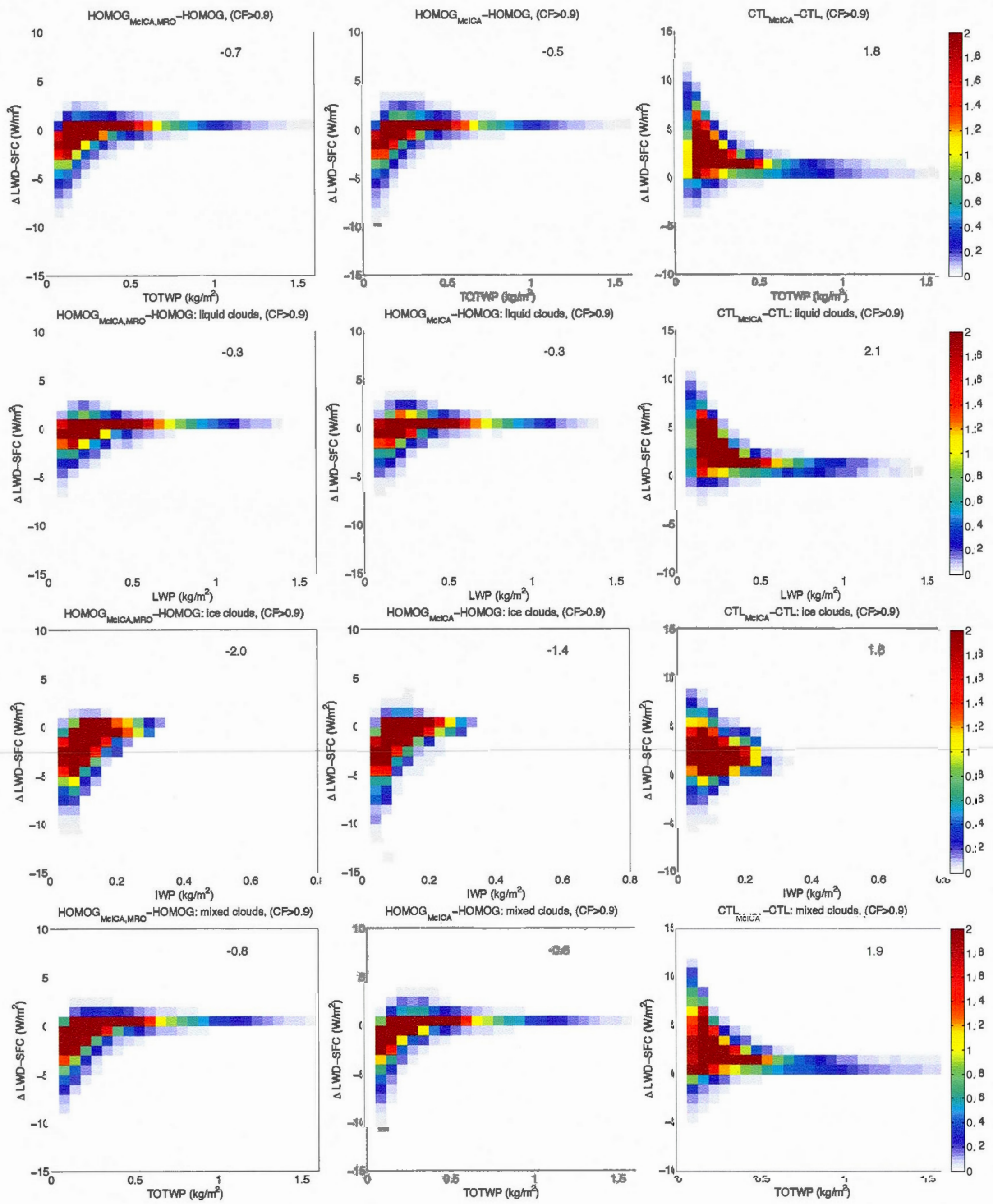

Figure B.5 LWD differences at SFC as a function of CWP for January 1^{st} for the HOMOG* (1^{st} column), the HOMOG (2^{nd} column) and the CTL simulations (3^{rd} column). Top row is seen in figure 3.5.

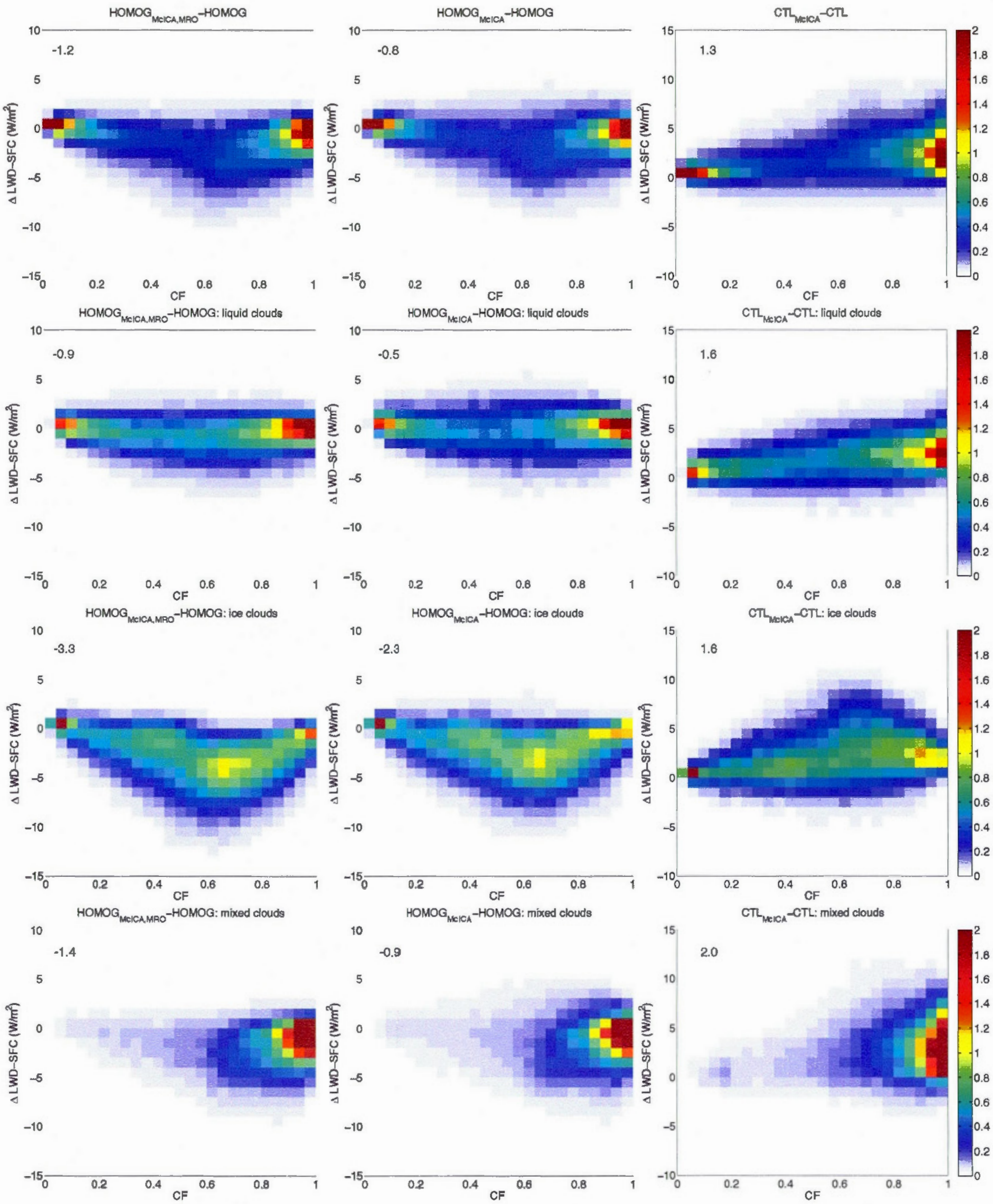

Figure B.6 LWD differences at SFC as a function of CF for January 1st for the HOMOG* (1st column), the HOMOG (2nd column) and the CTL simulations (3rd column). Top row is seen in figure 3.5.

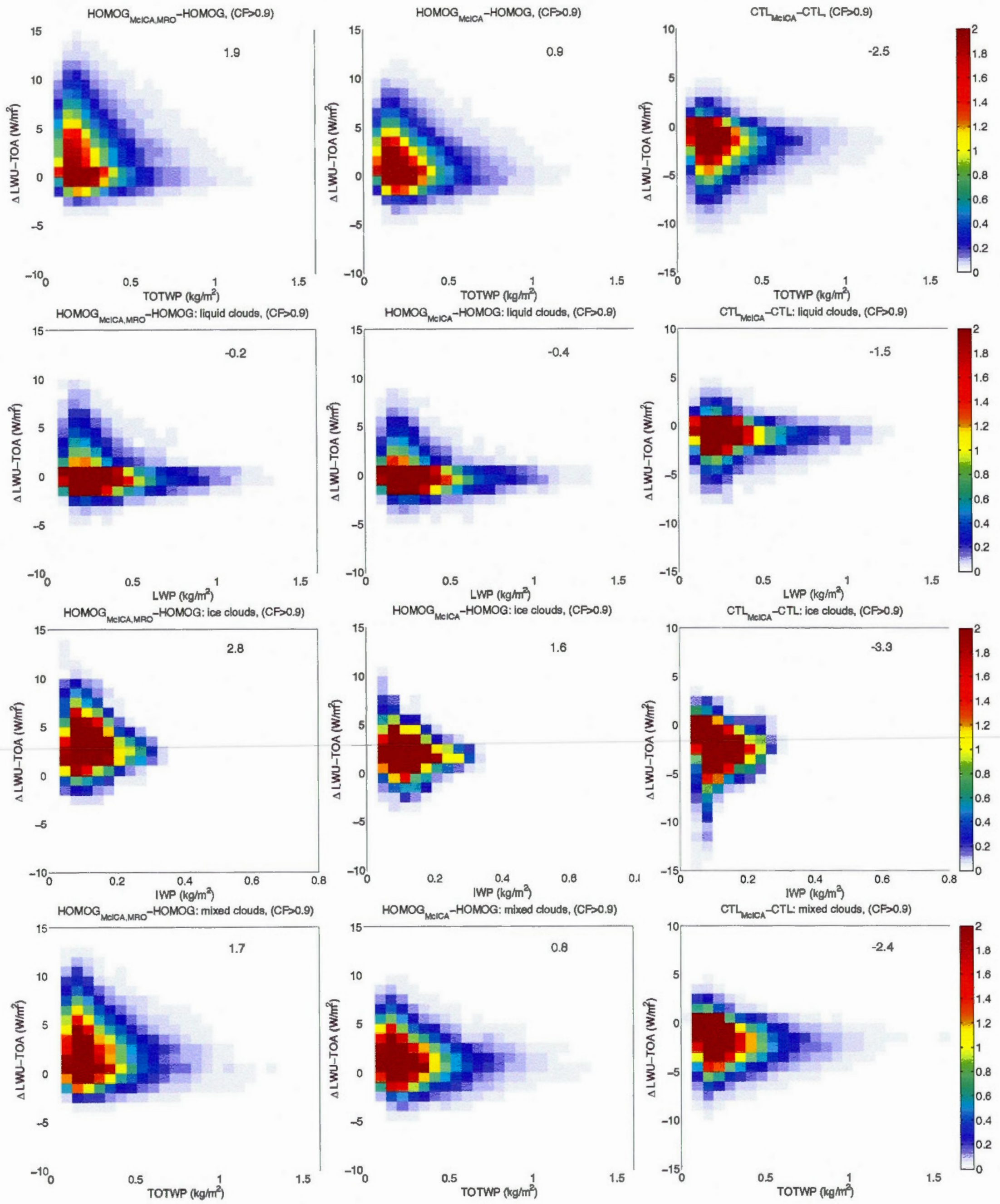

Figure B.7 LWU differences at TOA as a function of CWP for January 1^{st} for the HOMOG* (1^{st} column), the HOMOG (2^{nd} column) and the CTL simulations (3^{rd} column). Top row is seen in figure 3.5.

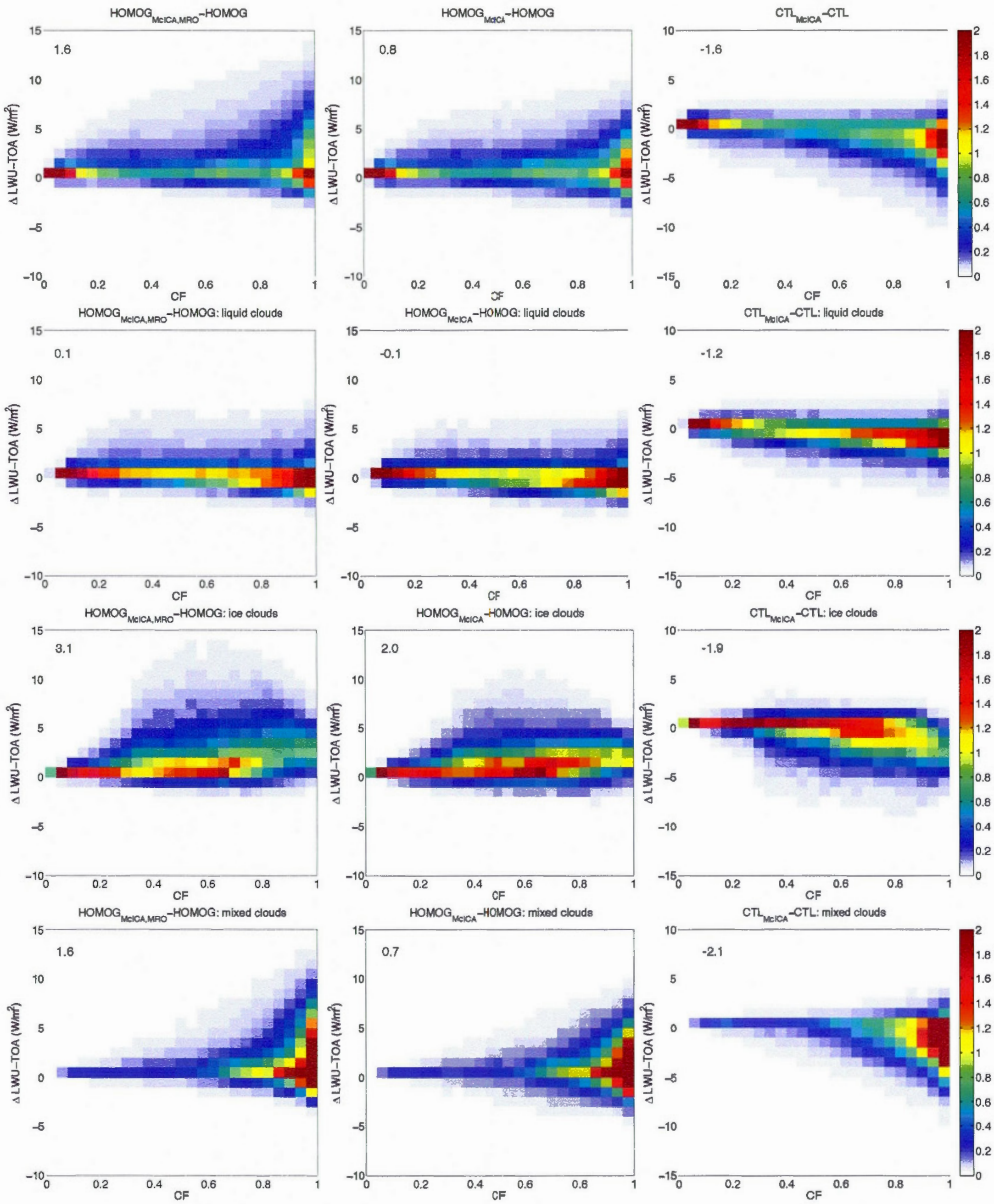

Figure B.8 LWU differences at TOA as a function of CF for January 1^{st} for the HOMOG* (1^{st} column), the HOMOG (2^{nd} column) and the CTL simulations (3^{rd} column). Top row is seen in figure 3.5.

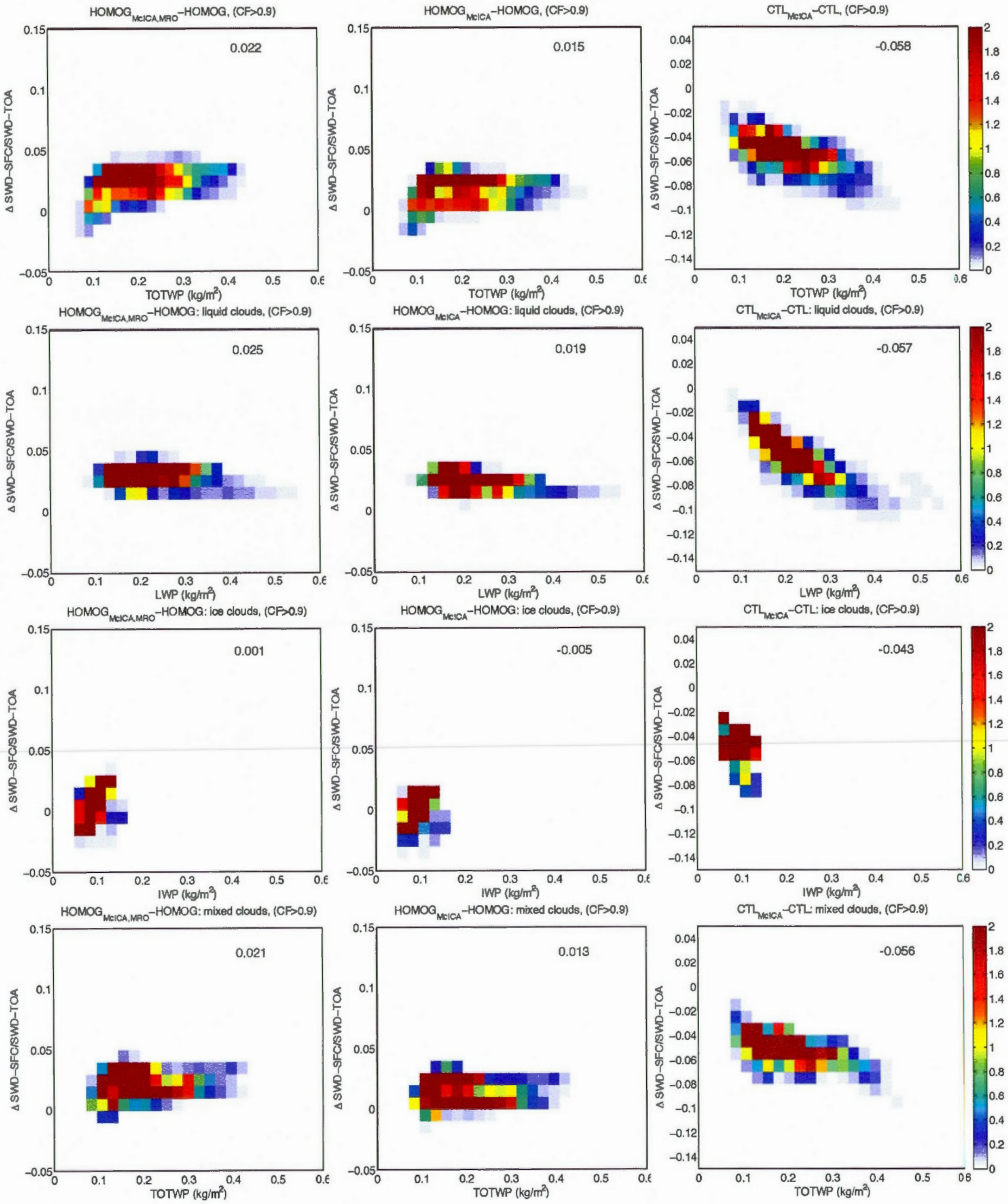

Figure B.9 SW ratio differences at SFC as a function of CWP for DJF 2007 for the HOMOG* (1^{st} column), the HOMOG (2^{nd} column) and the CTL simulations (3^{rd} column). Top row is seen in figure 3.6.

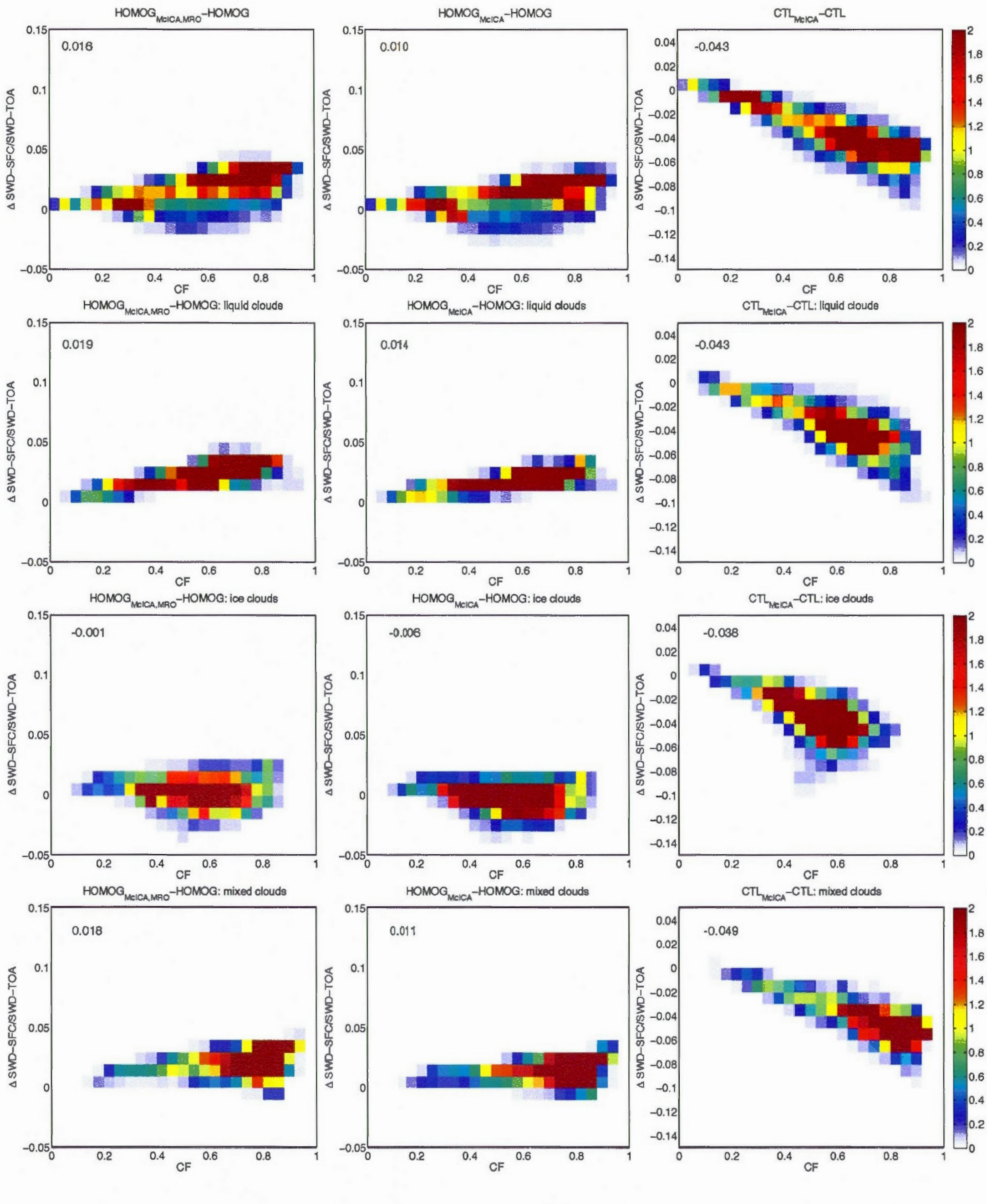

Figure B.10 SW ratio differences at SFC as a function of CF for DJF 2007 for the HOMOG* (1^{st} column), the HOMOG (2^{nd} column) and the CTL simulations (3^{rd} column). Top row is seen in figure 3.6.

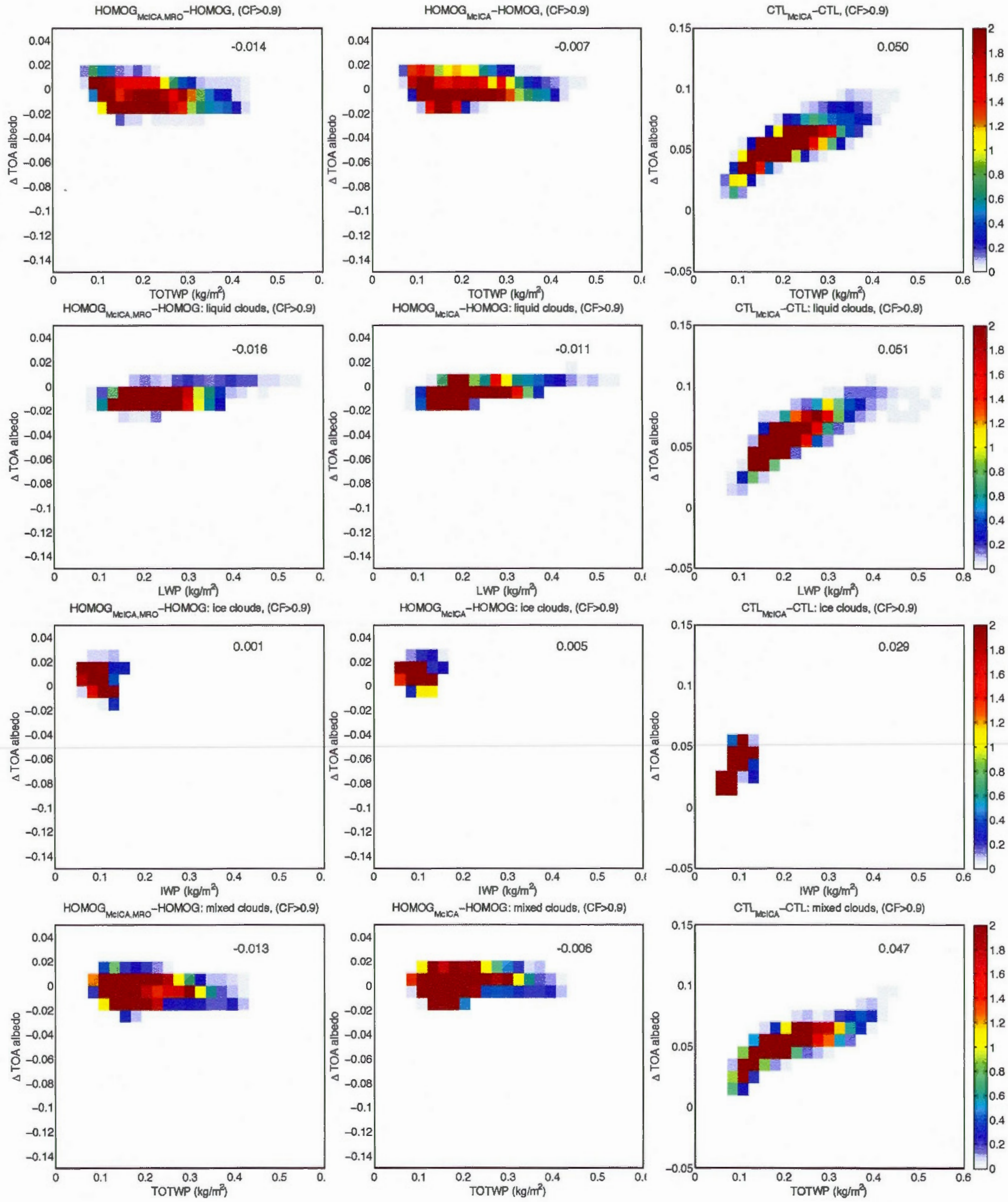

Figure B.11 TOA albedo differences as a function of CWP for DJF 2007 for the HOMOG* (1^{st} column), the HOMOG (2^{nd} column) and the CTL simulations (3^{rd} column). Top row is seen in figure 3.6.

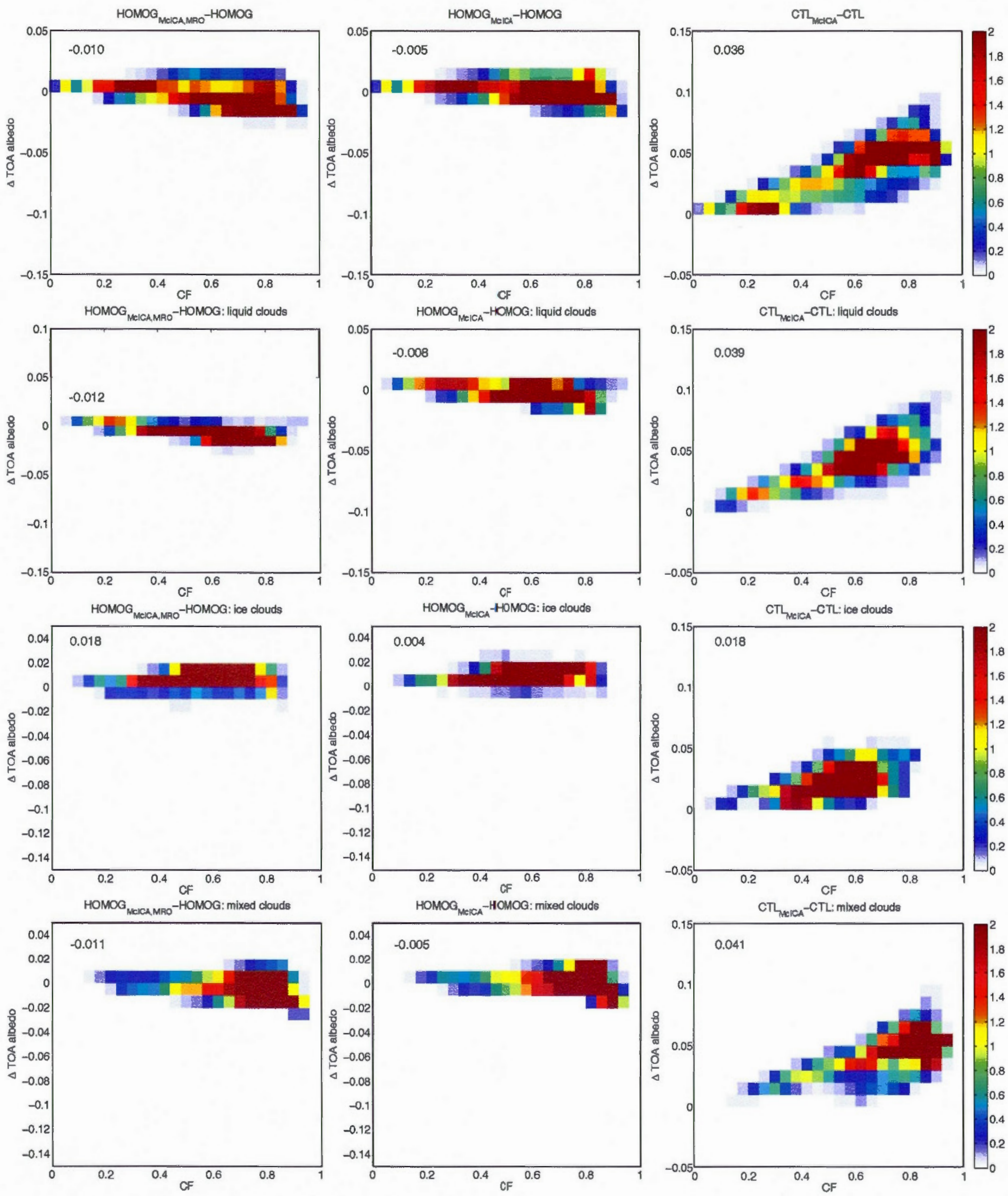

Figure B.12 TOA albedo differences as a function of CF for DJF 2007 for the HOMOG* (1^{st} column), the HOMOG (2^{nd} column) and the CTL simulations (3^{rd} column). Top row is seen in figure 3.6.

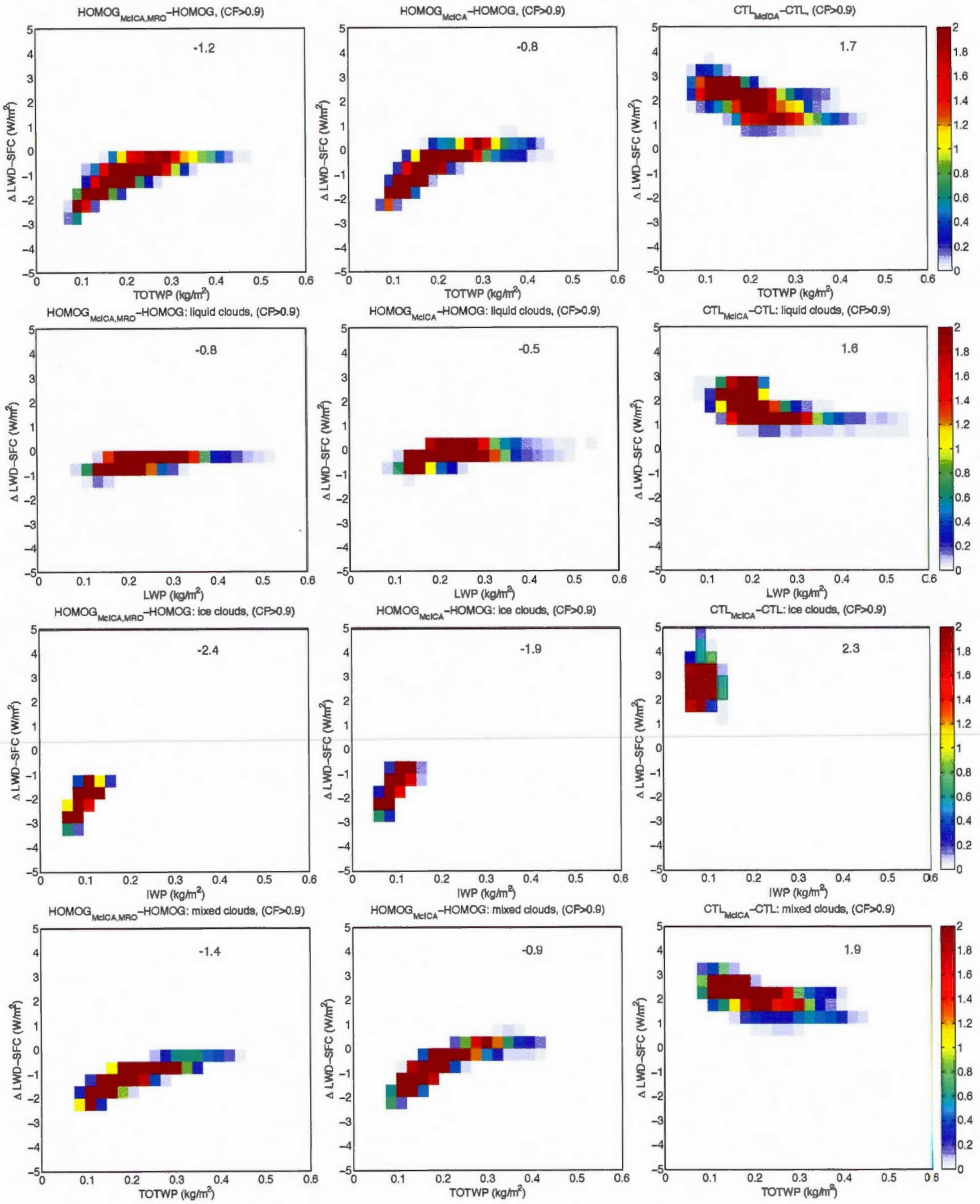

Figure B.13 LWD differences at SFC as a function of CWP for DJF 2007 for the HOMOG* (1^{st} column), the HOMOG (2^{nd} column) and the CTL simulations (3^{rd} column). Top row is seen in figure 3.7.

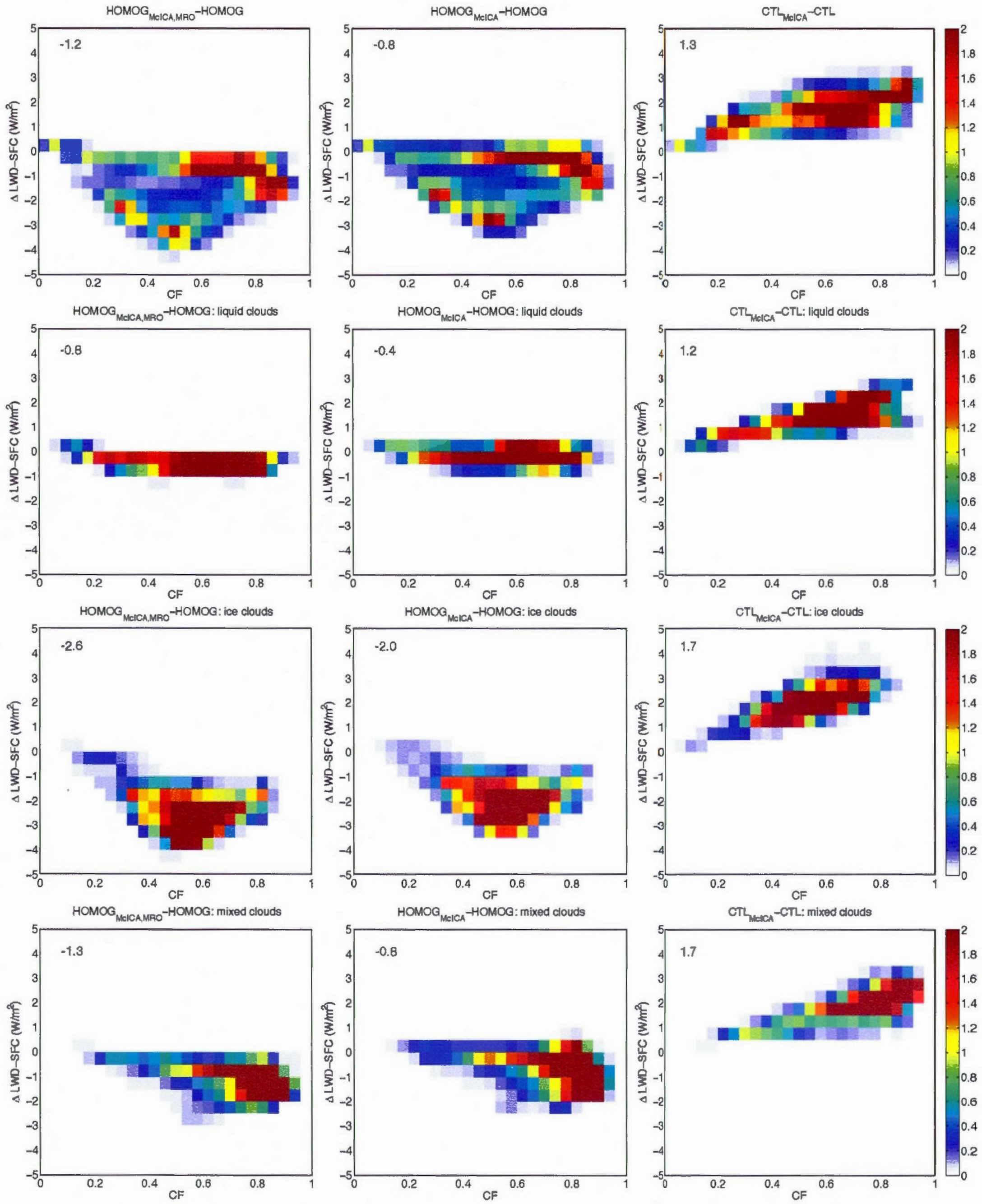

Figure B.14 LWD differences at SFC as a function of CF for DJF 2007 for the HOMOG* (1^{st} column), the HOMOG (2^{nd} column) and the CTL simulations (3^{rd} column). Top row is seen in figure 3.7.

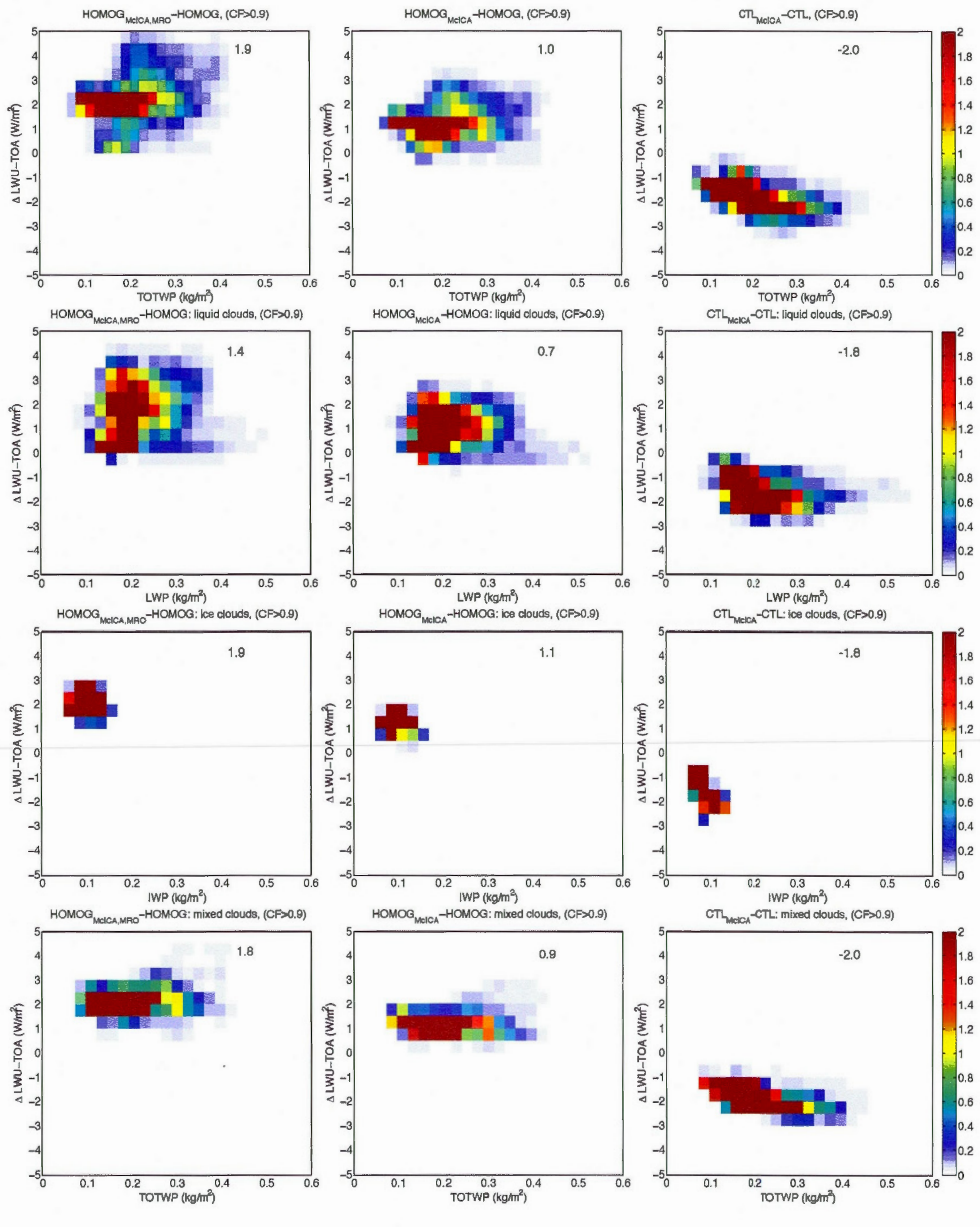

Figure B.15 LWU differences at TOA as a function of CWP for DJF 2007 for the HOMOG* (1^{st} column), the HOMOG (2^{nd} column) and the CTL simulations (3^{rd} column). Top row is seen in figure 3.7.

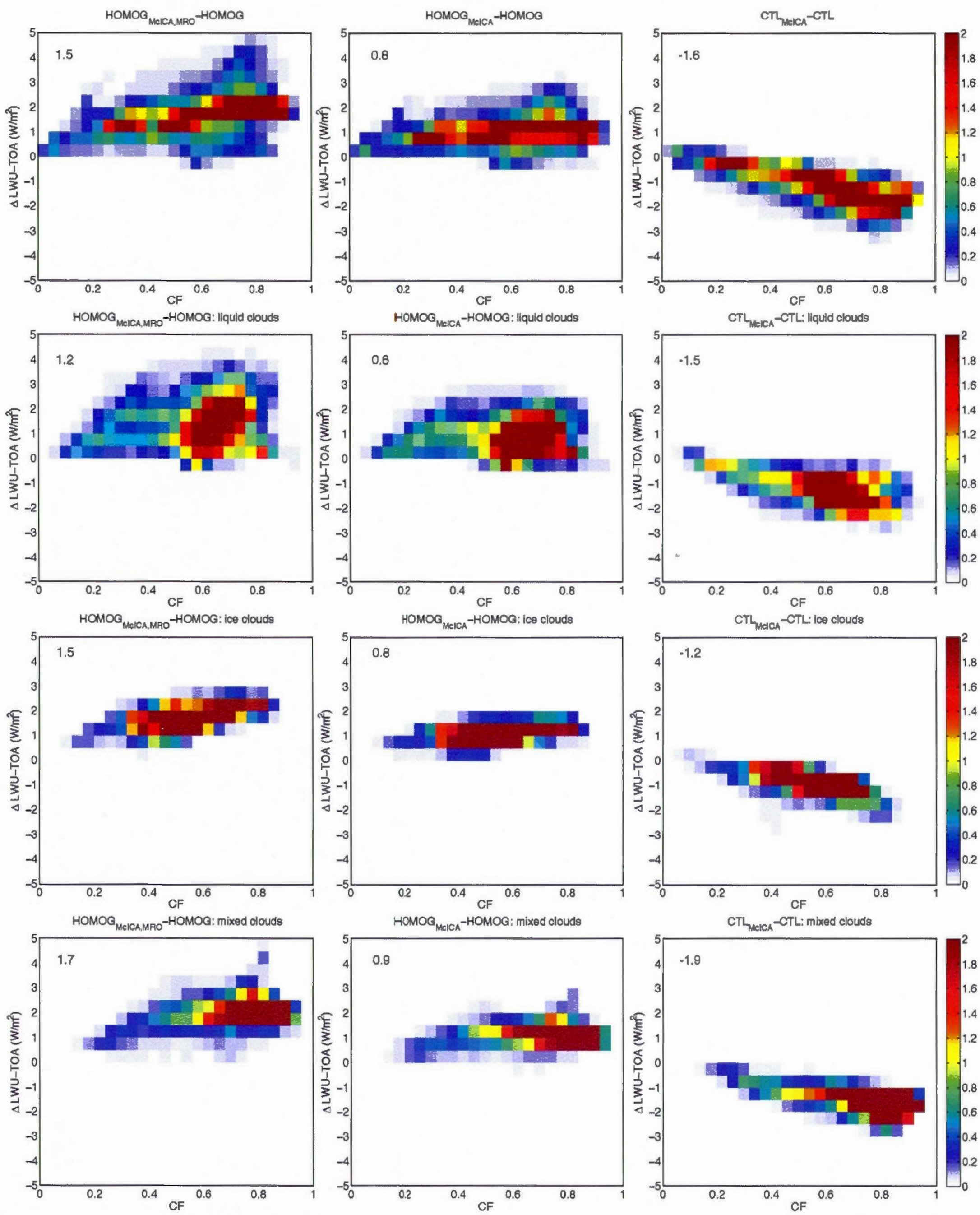

Figure B.16 LWU differences at TOA as a function of CF for DJF 2007 for the HOMOG* (1^{st} column), the HOMOG (2^{nd} column) and the CTL simulations (3^{rd} column). Top row is seen in figure 3.7.

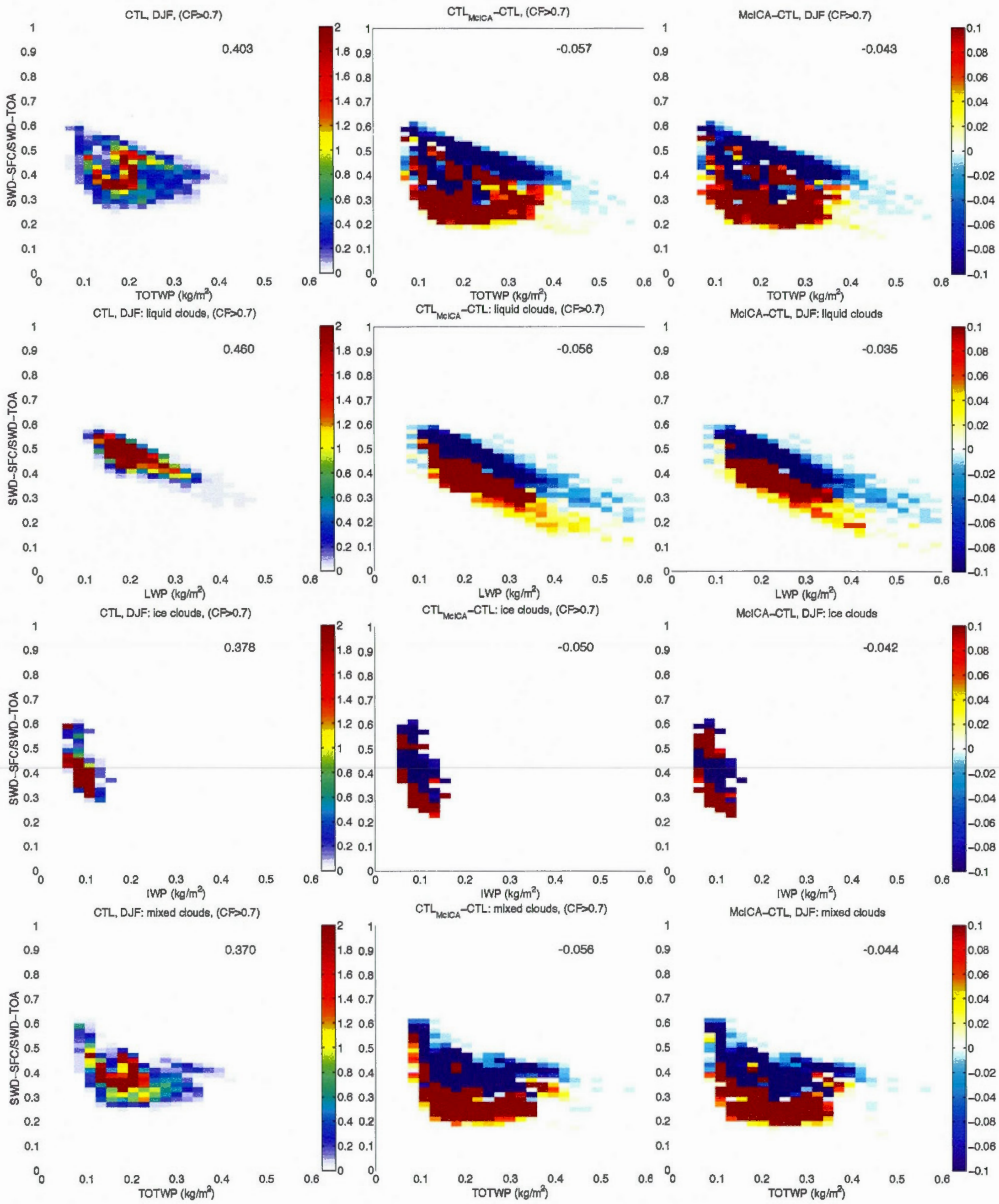

Figure B.17 SW ratio for the CTL simulation (1st column), SW differences for the offline McICA (CTL_{McICA} - CTL, 2nd column) and the online McICA simulation (McICA - CTL, 3rd column) for DJF 2007-2009 as a function of CWP. Top row is seen in figure 3.8.

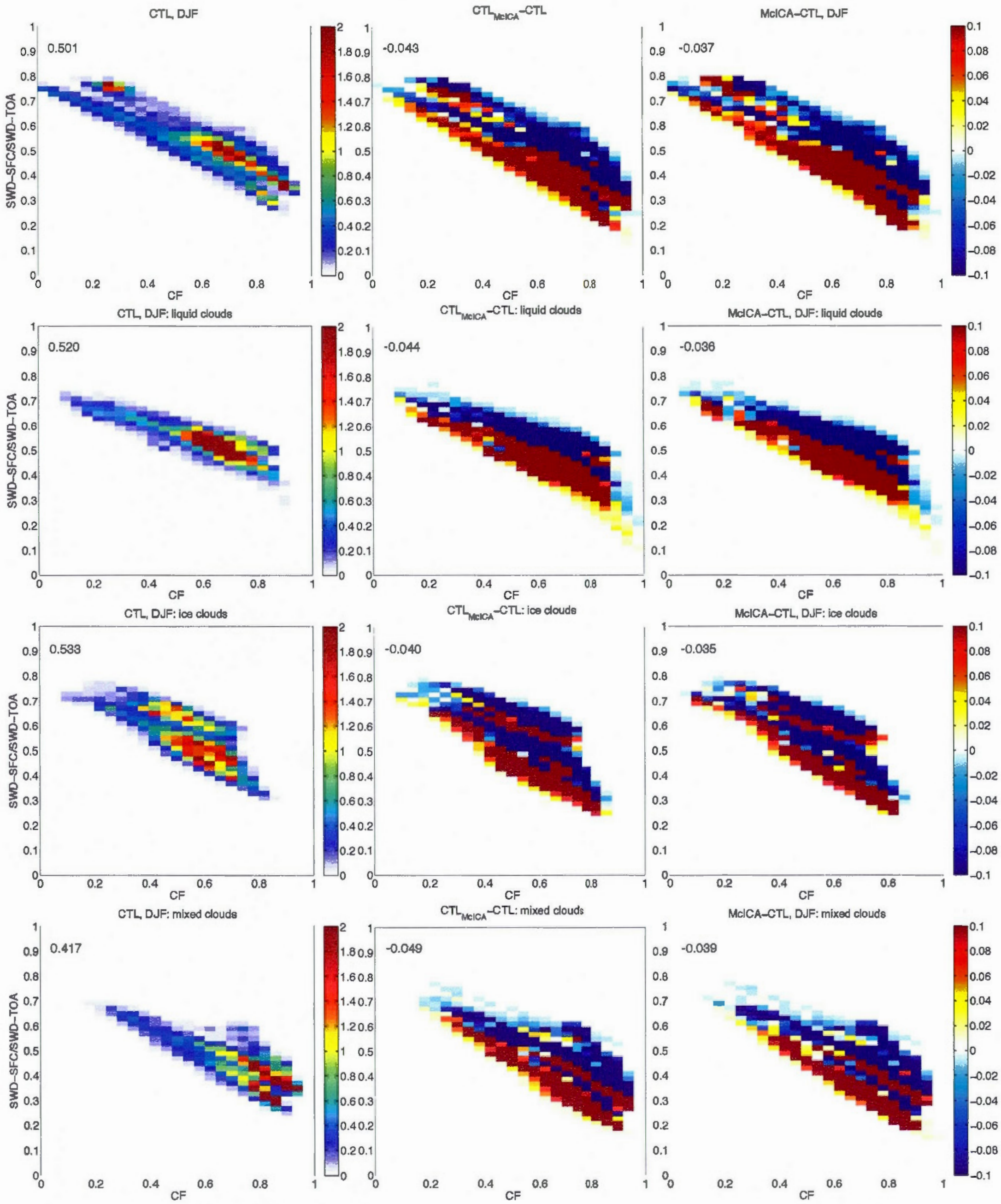

Figure B.18 SW ratio for the CTL simulation (1^{st} column), SW differences for the offline McICA (CTL_{McICA} - CTL, 2^{nd} column) and the online McICA simulation (McICA - CTL, 3^{rd} column) for DJF 2007-2009 as a function of CF. Top row is seen in figure 3.8.

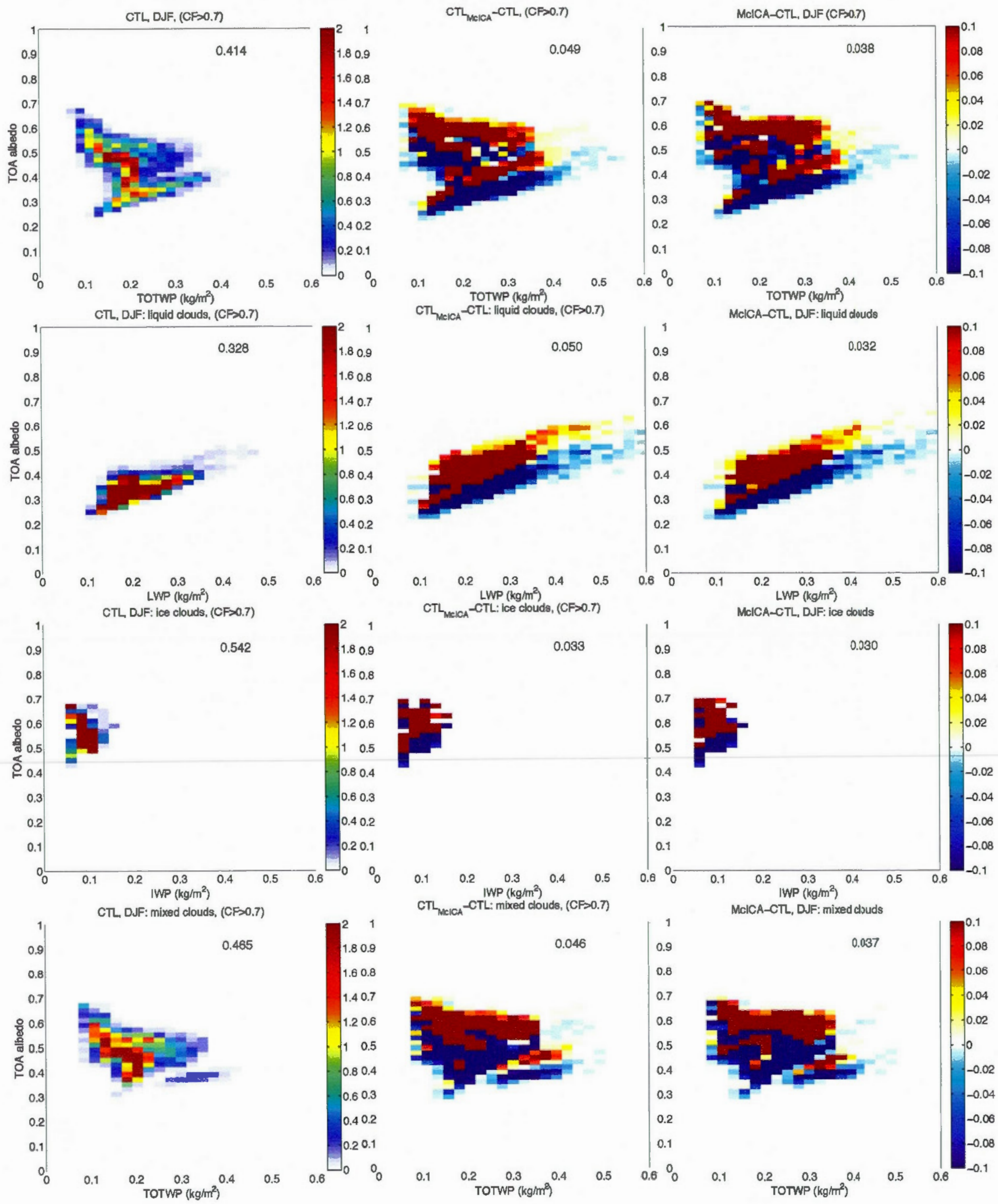

Figure B.19 TOA albedo for the CTL simulation (1st column), TOA albedo differences for the offline McICA (CTL$_{\mathrm{McICA}}$ - CTL, 2nd column) and the online McICA simulation (McICA - CTL, 3rd column) for DJF 2007-2009 as a function of CWP. Top row is seen in figure 3.8.

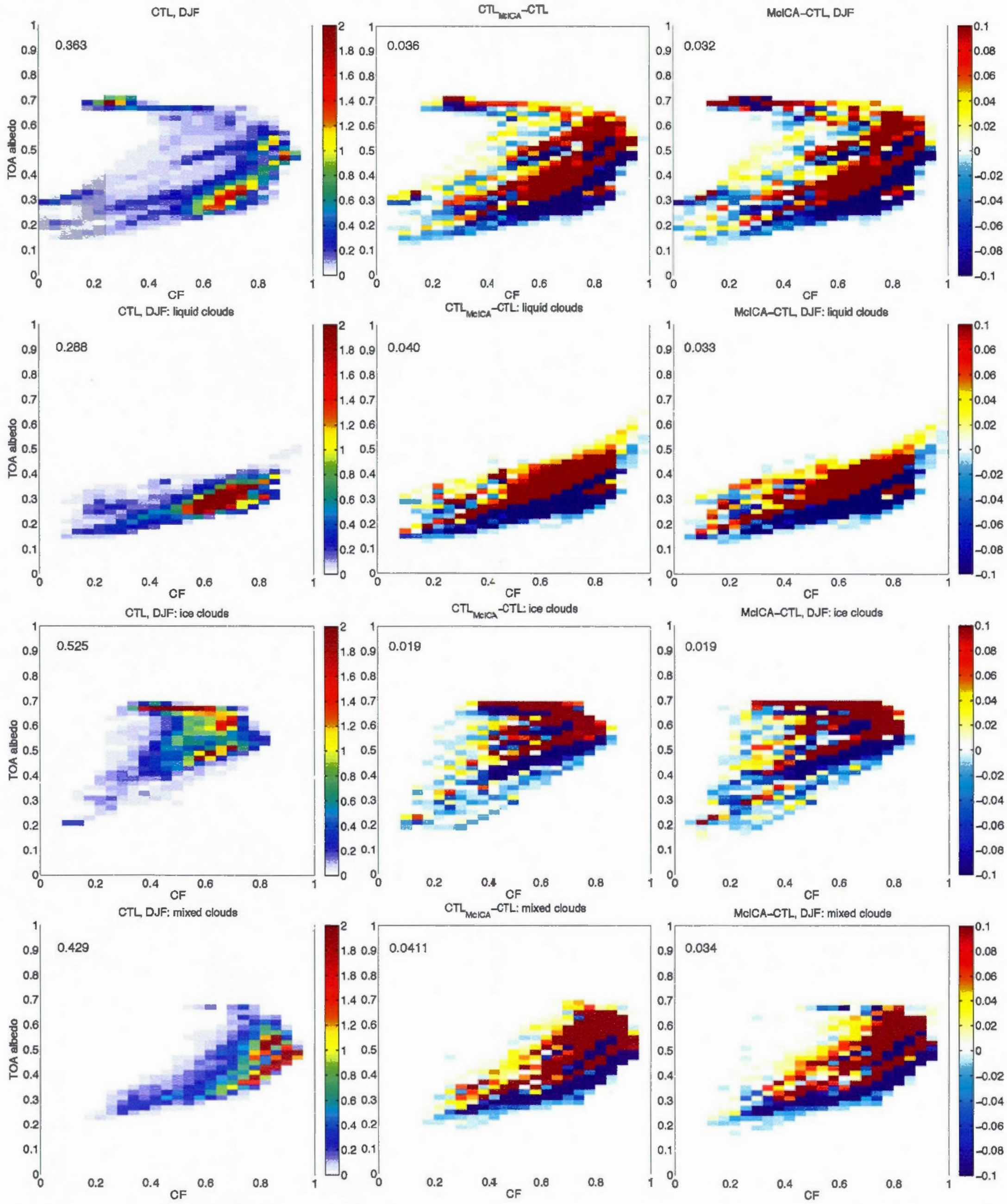

Figure B.20 TOA albedo for the CTL simulation (1^{st} column), TOA albedo differences for the offline McICA (CTL_{McICA} - CTL, 2^{nd} column) and the online McICA simulation (McICA - CTL, 3^{rd} column) for DJF 2007-2009 as a function of CF. Top row is seen in figure 3.8.

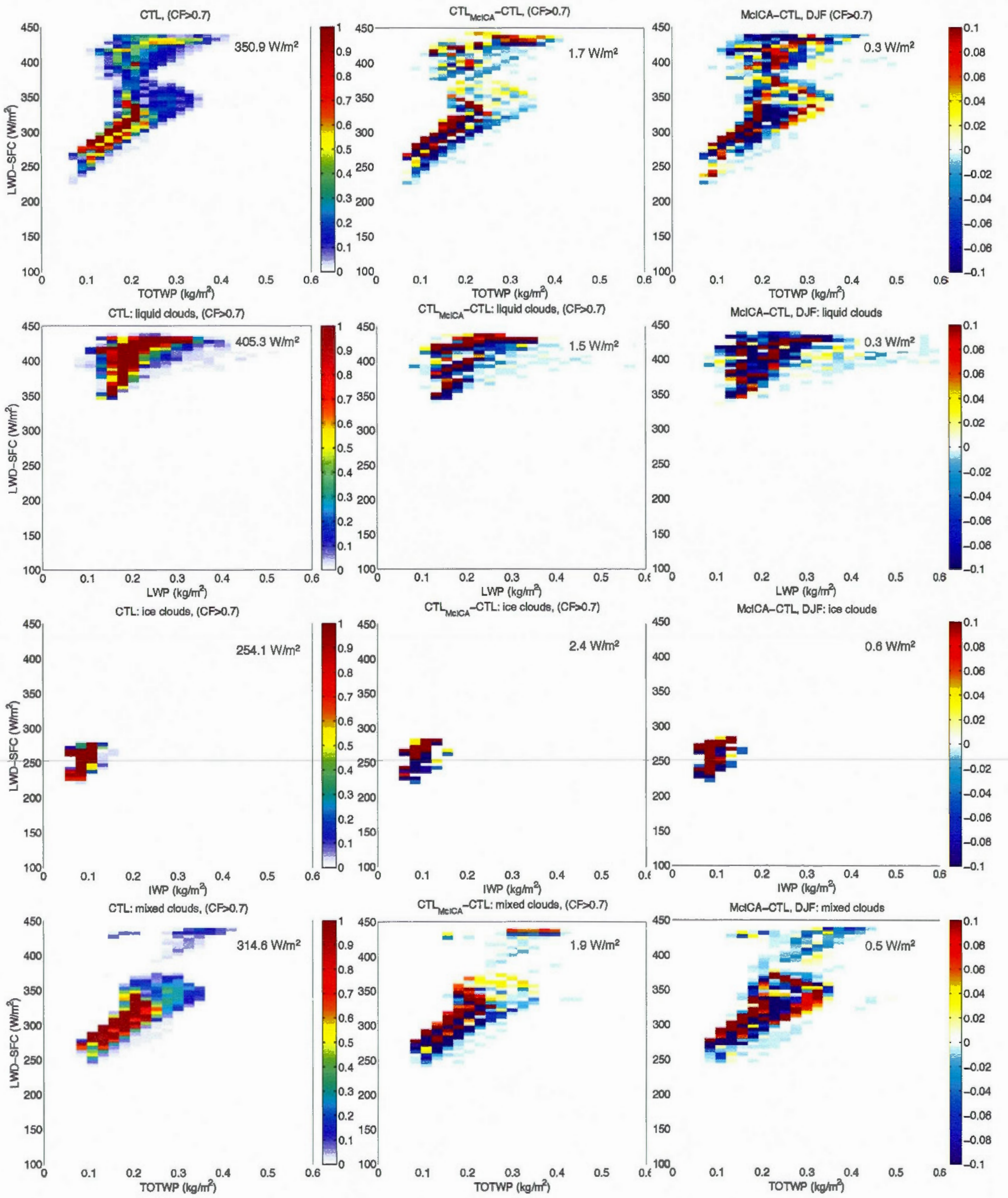

Figure B.21 LWD at SFC for the CTL simulation (1^{st} column), LWD differences at SFC for the offline McICA (CTL_{McICA} - CTL, 2^{nd} column) and the online McICA simulation (McICA - CTL, 3^{rd} column) for DJF 2007-2009 as a function of CWP. Top row is seen in figure 3.9.

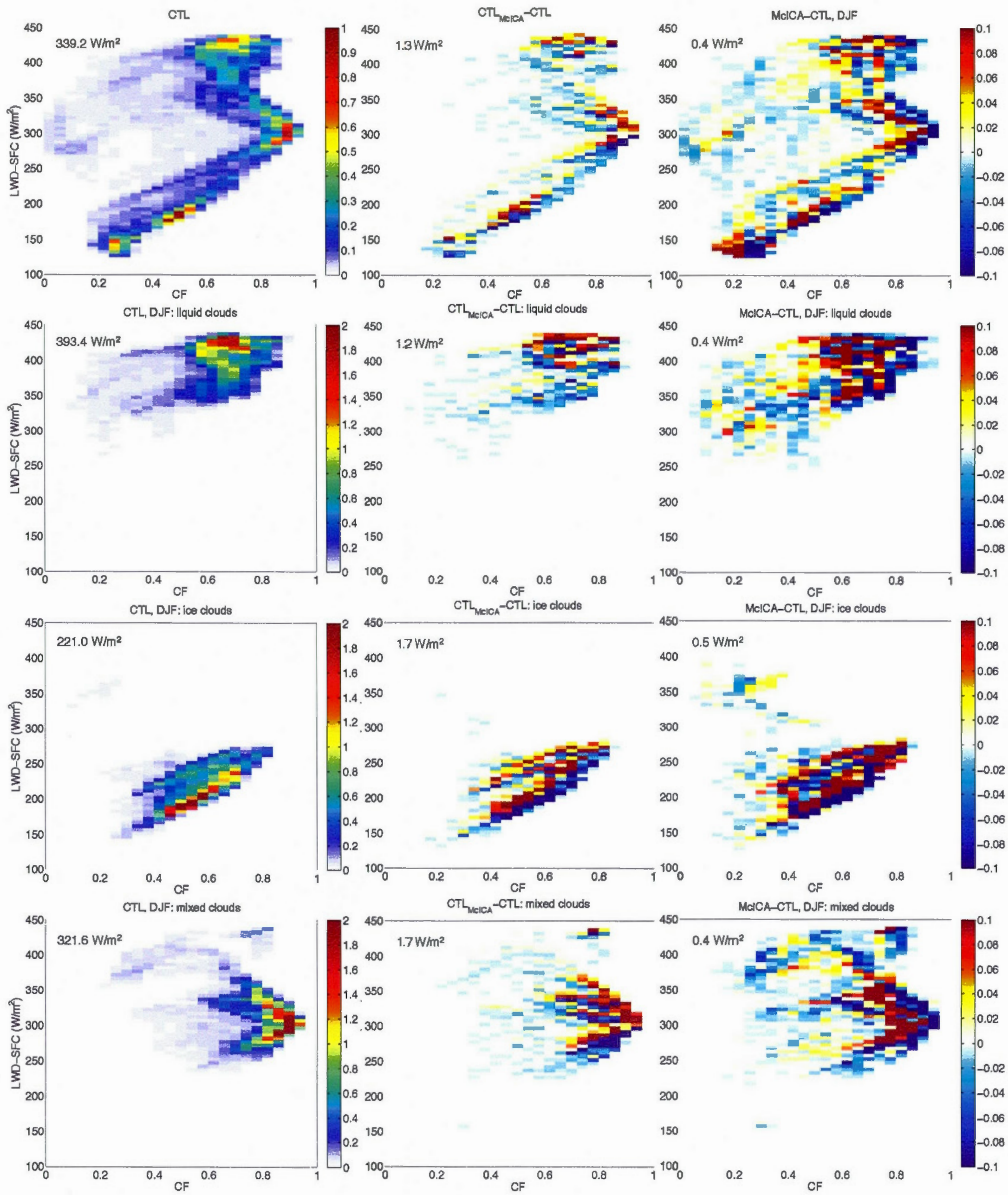

Figure B.22 LWD at SFC for the CTL simulation (1^{st} column), LWD differences at SFC for the offline McICA (CTL_{McICA} - CTL, 2^{nd} column) and the online McICA simulation (McICA - CTL, 3^{rd} column) for DJF 2007-2009 as a function of CF. Top row is seen in figure 3.9.

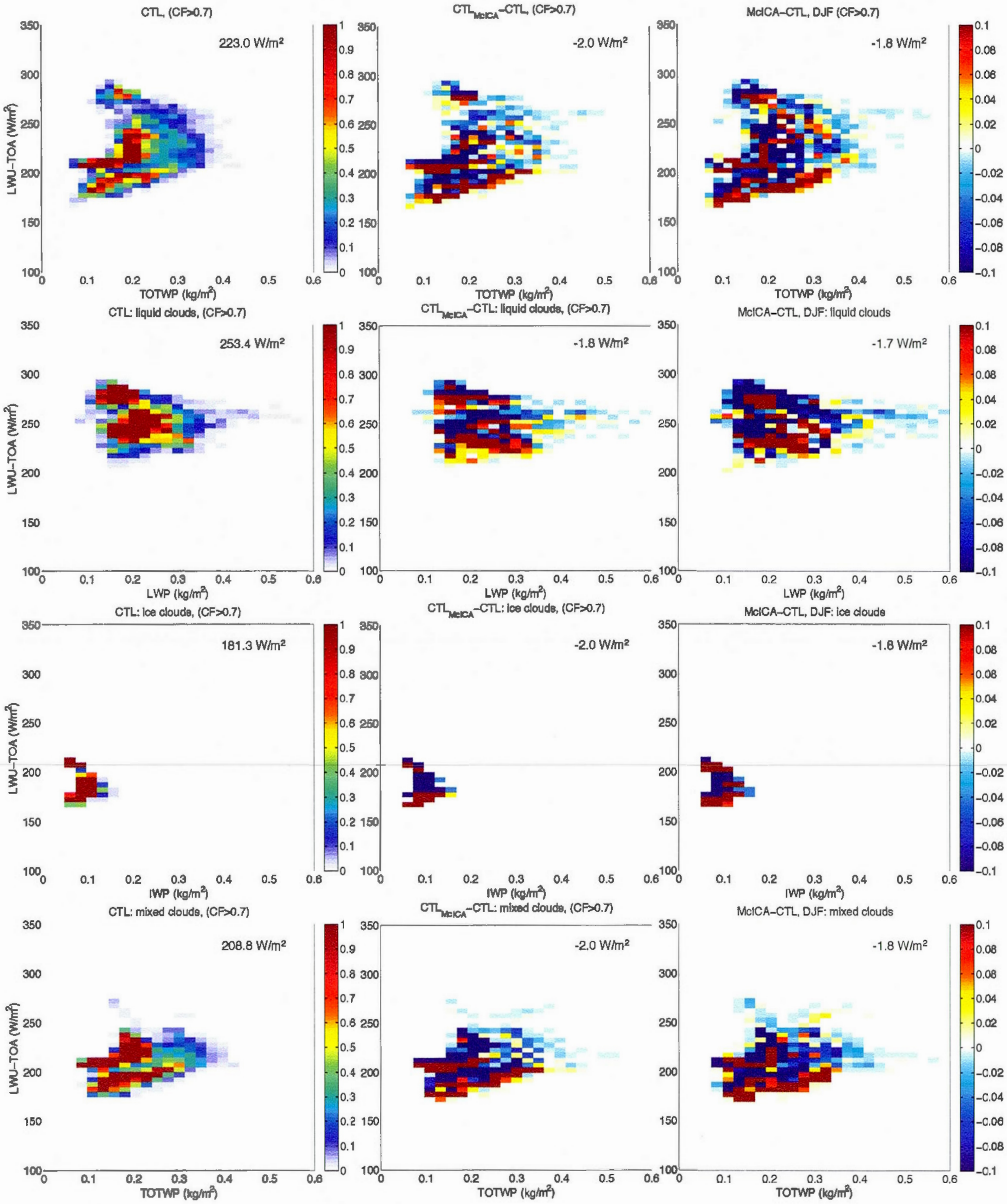

Figure B.23 LWU at TOA for the CTL simulation (1^{st} column), LWU differences at TOA for the offline McICA (CTL_{McICA} - CTL, 2^{nd} column) and the online McICA simulation (McICA - CTL, 3^{rd} column) for DJF 2007-2009 as a function of CWP. Top row is seen in figure 3.9.

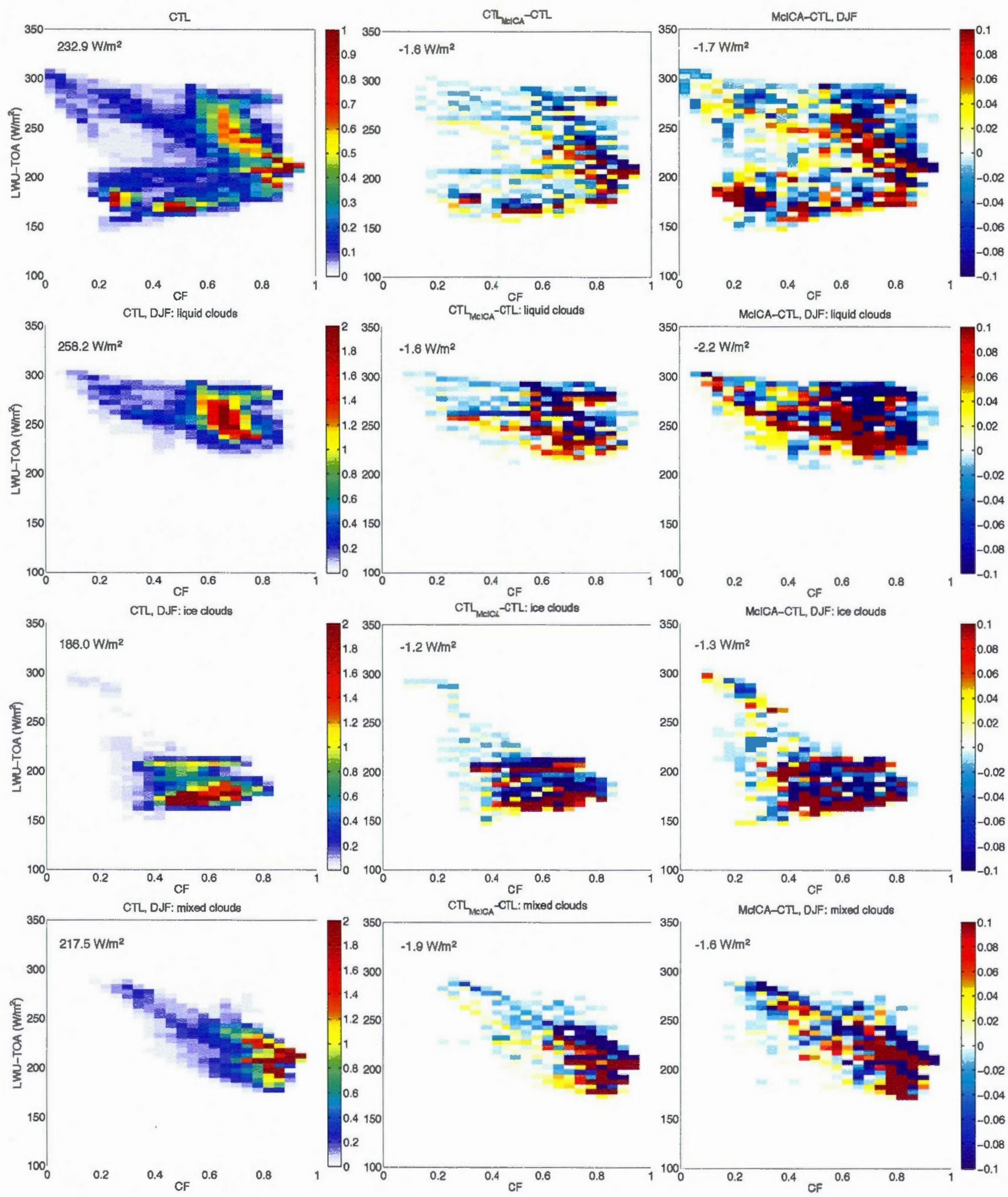

Figure B.24 LWU at TOA for the CTL simulation (1^{st} column), LWU differences at TOA for the offline McICA (CTL_{McICA} - CTL, 2^{nd} column) and the online McICA simulation (McICA - CTL, 3^{rd} column) for DJF 2007-2009 as a function of CF. Top row is seen in figure 3.9.

REFERENCES

Arakawa, A. (1975). Modeling clouds and cloud processes for use in climate models. *The Physical Basis of Climate and Climate Modelling*, *16*, 181–197.

Arakawa, A. (2004). The cumulus parameterization problem: Past, present, and future. *Journal of Climate*, *17*, 2493–2525.

Barker, H. W. (2008a). Overlap of fractional cloud for radiation calculations in GCMs: A global analysis using CloudSat and CALIPSO data. *Journal of Geophysical Research*, *113*, 1–15.

Barker, H. W. (2008b). Representing cloud overlap with an effective decorrelation length: An assessment using CloudSat and CALIPSO data. *Journal of Geophysical Research*, *113*(D24), 1–17.

Barker, H. W., Cole, J. N. S., Morcrette, J. and Pincus, R. (2008). The Monte Carlo Independent Column Approximation : An assessment using several global atmospheric models. *Quarterly Journal of the Royal Meteorological Society*, *1478*, 1463–1478.

Barker, H. W., Morcrette, J.-J. and Alexander, G. D. (1998). Broadband solar fluxes and heating rates for atmospheres with 3D broken clouds. *Quarterly Journal of the Royal Meteorological Society*, *124*(548), 1245–1271.

Barker, H. W., Pincus, R. and Morcrette, J.-J. (2002). The Monte Carlo Independent Column Approximation : Application within Large-Scale Models. In *GCSS-ARM*.

Barker, H. W. and Räisänen, P. (2005). Radiative sensitivities for cloud structural properties that are unresolved by conventional GCMs. *Quarterly Journal of the Royal Meteorological Society*, *131*(612), 3103–3122.

Barker, H. W., Stephens, G. L. and Fu, Q. (1999). The sensitivity of domain-averaged solar fluxes to assumptions about cloud geometry. *Quarterly Journal of the Royal Meteorological Society*, *125*(558), 2127–2152.

Barker, H. W., Stephens, G. L., Partain, P. T., Bergman, J. W., Bonnel, B., Campana, K., Clothiaux, E. E., Clough, S., Cusack, S., Delamere, J., Edwards, J., Evans, K. F., Fouquart, Y., Freidenreich, S., Galin, V., Hou, Y., Kato, S., Li, J., Mlawer, E., Morcrette, J.-J., O'Hirok, W., Räisänen, P., Ramaswamy, V., Ritter, B., Rozanov, E., Schlesinger, M., Shibata, K., Sporyshev, P., Sun, Z., Wendisch, M., Wood, N. and Yang, F. (2003). Assessing 1D Atmospheric Solar Radiative Transfer Models: Interpretation and Handling of Unresolved Clouds. *Journal of Climate*, *16*(16), 2676–2699.

Barker, H. W., Wielicki, B. a. and Parker, L. (1996). a parameterization for computing gris-averaged sloar fluxes for inhomogeneous marine boundary layer clouds. part II: validation using satellite data. *Journal of Atmospheric Aciences*, *53*(16), 2304–2316.

Bélair, S., Brown, R., Mailhot, J., Bilodeau, B. and Crevier, L.-P. (2003a). Operational implementation of the ISBA land surface scheme in the Canadian regional weather forecast model. Part II: Cold season results. *Journal of Hydrometeorology*, *4*, 371–386.

Bélair, S., Crevier, L.-P., Mailhot, J., Bilodeau, B. and Delage, Y. (2003b). Operational implementation of the ISBA land surface scheme in the Canadian regional weather forecast model. Part I: Warm season results. *Journal of Hydrometeorology*, *4*, 352–370.

Bélair, S., Mailhot, J., Girard, C. and Vaillancourt, P. (2005). Boundary layer and shallow cumulus clouds in a medium-range forecast of a large-scale weather system. *Monthly Weather Review*, *133*, 1938–1960.

Bélair, S., Mailhot, J., Strapp, J. W. and MacPherson, J. I. (1999). An examination of local versus nonlocal aspects of a TKE-based boundary layer scheme in clear convective conditions. *Journal of Applied Meteorology*, *38*, 1499–1518.

Bergman, J. W. and Rasch, P. J. (2002). Parameterizing vertically coherent cloud distributions. *Journal of the Atmospheric Sciences*, *59*(14).

Bony, S., Colman, R., Kattsov, V. M., Allan, R. P., Bretherton, C. S., Dufresne, J.-L., Hall, A., Hallegatte, S., Holland, M. M., Ingram, W., Randall, D. a., Soden, B. J., Tselioudis, G. and Webb, M. J. (2006). How Well Do We Understand and Evaluate Climate Change Feedback Processes? *Journal of Climate*, *19*(15), 3445–3482.

Boucher, O., Randall, D., Artaxo, P., Bretherton, C., Feingold, G., Forster, P., Kerminen, V.-M., Kondo, Y., Liao, H., Lohmann, U., Rasch, P., Satheesh, S., Sherwood, S., Stevens, B. and Zhang, X. (2013). *Clouds and Aerosols. In: Climate Change 2013: The Physical Science Basis. Contribution of Working Group I to the Fifth Assessment Report of the Intergovernmental Panel on Climate Change.* Cambridge University Press.

Boudala, F. S., Isaac, G. A., Cober, S. G. and Fu, Q. (2004). Liquid fraction in stratiform mixed-phase clouds from in situ observations. *Quarterly Journal of the Royal Meteorological Society*, *130*(603), 2919–2931.

Bougeault, P. and Lacarrère, P. (1989). Parameterization of orography-induced turbulence in a mesobeta-scale model. *Monthly Weather Review*, *117*, 1872–1890.

Boutle, I. a., Abel, S. J., Hill, P. G. and Morcrette, C. J. (2013). Spatial variability of liquid cloud and rain: observations and microphysical effects. *Quarterly Journal of the Royal Meteorological Society*.

Cess, R. D., Potter, G., Blanchet, J., Boer, G., Ghan, S., Kiehl, J., Le Treut, H., Li, Z.-X., Liang, X.-Z., Mitchell, J. *et al.* (1989). Interpretation of cloud-climate feedback as produced by 14 atmospheric general circulation models. *Science*, *245*(4917), 513–516.

Chambers, L., Wielicki, B. A. and Evans, K. (1997). Independent pixel and two-dimensional estimates of landsat-derived cloud field albedo. *Journal of the Atmospheric Sciences*, *54*(11), 1525–1532.

Charney, J. G., Arakawa, A., Baker, D. J., Bolin, B., Dickinson, R. E., Goody, R. M., Leith, C. E., Stommel, H. M. and Wunsch, C. I. (1979). *Cardon Dioxide and Climate: A Scientific Assessment.* Rapport technique.

Côté, J., Gravel, S., Méhot, A., Patoine, A., Roch, M. and Staniforth, A. (1998). The operational CMC-MRB Global Environmental Multiscale (GEM) Model. Part I: Design considerations and formulation. *Monthly Weather Review*, *126*, 1373–1395.

Doelling, D. R., Loeb, N. G., Keyes, D. F., Nordeen, M. L., Morstad, D., Nguyen, C., Wielicki, B. A., Young, D. F. and Sun, M. (2013). Geostationary enhanced temporal interpolation for ceres flux products. *Journal of Atmospheric and Oceanic Technology*, *30*(6), 1072–1090.

Ebert, E. E. and Curry, J. A. (1992). A parameterization of ice cloud optical properties for climate models. *Journal of Geophysical Research: Atmospheres*, *97*(D4), 3831–3836.

Fouquart, Y. and Bonnell, B. (1980). Computations of solar heating of the earth's atmosphere: A new parameterization. *Contribution in Atmospheric Physics*, *53*, 3542.

Fu, Q., Cribb, M. C., Barker, H. W., Krueger, S. K. and Grossman, a. (2000). Cloud Geometry Effects on Atmospheric Solar Absorption. *Journal of the Atmospheric Sciences*, *57*(8), 1156–1168.

Fu, Q. and Liou, K. N. (1992). On the Correlated k-Distribution Method for Radiative Transfer in Nonhomogeneous Atmospheres. *Journal of the Atmospheric Sciences*, *49*(22), 2139–2156.

Geleyn, J.-F. and Hollingsworth, A. (1979). An economical analytical method for the computation of the interaction between scattering and line absorption of radiation. *Contribution in Atmospheric Physics*, *52*, I–16.

Grabowski, W. W. and Smolarkiewicz, P. K. (1999). Crcp: A cloud resolving convection parameterization for modeling the tropical convecting atmosphere. *Physica D: Nonlinear Phenomena*, *133*(1), 171–178.

Hegerl, G. C., Zwiers, F. W., Braconnot, P., Gillett, N. P., Luo, Y., Orsini, J. A. M., Nicholls, N., Penner, J. E. and Stott, P. A. (2007). *Understanding and Attributing Climate Change. In: Climate Change 2007: The Physical Science Basis. Contribution of Working Group I to the Fourth Assessment Report of the Intergovernmental Panel on Climate Change.* Cambridge University Press.

Hernández-Díaz, L., Laprise, R., Sushama, L., Martynov, A., Winger, K. and Dugas, B. (2013). Climate simulation over CORDEX Africa domain using the fifth-generation canadian regional climate model (CRCM5). *Climate Dynamics*, *40*(5-6), 1415–1433.

Hill, P. G., Hogan, R. J., Manners, J. and Petch, J. C. (2011a). Parametrizing the horizontal inhomogeneity of ice water content using CloudSat data products. *Quarterly Journal of the Royal Meteorological Society*, *10*, 1–10.

Hill, P. G., Manners, J. and Petch, J. C. (2011b). Reducing noise associated with the Monte Carlo Independent Column Approximation for weather forecasting models. *Quarterly Journal of the Royal Meteorological Society*, *137*(654), 219–228.

Hogan, R. J. and Illingworth, A. J. (2000). Deriving cloud overlap statistics from radar. *Quarterly Journal of the Royal Meteorological Society*, *126*(569), 2903–2909.

Horváth, A. and Davies, R. (2007). Comparison of microwave and optical cloud water path estimates from TMI, MODIS, and MISR. *Journal of Geophysical Research*, *112*(D1), D01202.

Hurrell, J. W., Hack, J. J., Shea, D., Caron, J. M. and Rosinski, J. (2008). A new sea surface temperature and sea ice boundary dataset for the Community Atmosphere Model. *Journal of Climate*, *21*, 5145–5153.

Isaac, G. A. and Schmidt, K. S. (2008). *Cloud Properties from In-situ and Remote-sensing Measurements: Capability and Limitations. In Clouds in the Perturbed Climate System.* The MIT Press.

Kain, J. and Fritsch, J. M. (1990). A one-dimensional entraining/detraining plume model and its application in convective parameterization. *Journal of Atmospheric Sciences*, *47*, 2784–2802.

Kain, J. and Fritsch, J. M. (1993). Convective parameterization for mesoscale models: The Kain-Fritsch scheme. *The Representation of Cumulus Convection in Numerical Models, Meteorological Monographs of the American Meteorological Society*, *46*, 165–170.

Kato, S., Loeb, N. G., Rutan, D. a., Rose, F. G., Sun-Mack, S., Miller, W. F. and Chen, Y. (2012). Uncertainty Estimate of Surface Irradiances Computed with MODIS-, CALIPSO-, and CloudSat-Derived Cloud and Aerosol Properties. *Surveys in Geophysics*, *33*, 395–412. `http://dx.doi.org/10.1007/s10712-012-9179-x`

Kuo, H. L. (1965). On formation and intensification of tropical cyclones through latent heat release by cumulus convection. *Journal of Atmospheric Sciences*, *22*, 40–63.

Lacis, A. A. and Oinas, V. (1991). A description of the correlated k distribution method for modeling nongray gaseous absorption, thermal emission, and multiple scattering in vertically inhomogeneous atmospheres. *Journal of Geophysical Research: Atmospheres*, *96*(D5), 9027–9063.

Li, J. and Barker, H. W. (2002). Accounting for unresolved clouds in a 1d infrared radiative transfer model. part ii: Horizontal variability of cloud water path. *Journal of Atmospheric Sciences*, *59*, 3321–3339.

Li, J. and Barker, H. W. (2005). A radiation algorith with correlated-k distribution. Part I: Local thermal equilibrium. *Journal of Atmospheric Sciences*, *62*, 286–309.

Li, J., Dobbie, S., Räisänen, P. and Min, Q. (2005). Accounting for unresolved clouds in a 1d solar radiative-transfer model. *Quarterly Journal of the Royal Meteorological Society*, *131*, 1607–1629.

Liou, K. N. (1992). *Radiation and cloud processes in the atmosphere: theory, observation and modeling.* Oxford University Press.

Liou, K. N. (2002). *An introduction to atmospheric radiation, second edition.* Academic Press.

Loeb, N. G., Manalo-Smith, N., Kato, S., Miller, W. F., Gupta, S. K., Minnis, P. and Wielicki, B. A. (2003). Angular distribution models for top-of-atmosphere radiative flux estimation from the clouds and the earth's radiant energy system instrument on the tropical rainfall measuring mission satellite. part i: Methodology. *Journal of applied meteorology*, *42*(2), 240–265.

Loeb, N. G., Wielicki, B. A., Doelling, D. R., Smith, G. L., Keyes, D. F., Kato, S., Manalo-Smith, N. and Wong, T. (2009). Toward optimal closure of the earth's top-of-atmosphere radiation budget. *Journal of Climate*, *22*, 748–766.

Lohman, U. and Roeckner, E. (1996). Design and performance of a new cloud microphysics scheme developed for the echam general circulation model. *Climate Dynamics*, *12*, 557–572.

Lopez, P. (2006). Cloud and precipitation parameterizations in modeling and variational data assimilation: A review. *Journal of Atmospheric Sciences*, *64*, 3766–3784.

Mace, G. G. and Benson-Troth, S. (2002). Cloud-Layer Overlap Characteristics Derived from Long-Term Cloud Radar Data. *Journal of Climate*, *15*(17), 2505–2515.

Markovic, M., Jones, C. G., Vaillancourt, P. A., Paquin, D., Winger, K. and Paquin-Ricard, D. (2008). An evalution of the surface radiation budget over north america for a suite of regional climate models against surface station observations. *Climate Dynamics*. http://dx.doi.org/10.1007/S00382-008-0378-6

Martynov, A., Laprise, R., Sushama, L., Winger, K., Šeparović, L. and Dugas, B. (2013). Reanalysis-driven climate simulation over CORDEX North America domain using the canadian regional climate model, version 5: model performance evaluation. *Climate Dynamics*, *41*(11-12), 2973–3005.

Meehl, G. A., Stocker, T. F., Collins, W. D., Friedlingstein, P., Gaye, A. T., Gregory, J. M., Kitoh, A., Knutti, R., Murphy, J. M., Noda, A., Raper, S. C., Watterson, I. G., Weaver, A. J. and Zhao, Z.-C. (2007). *Global Climate Projections. In: Climate Change 2007: The Physical Science Basis. Contribution of Working Group I to the Fourth Assessment Report of the Intergovernmental Panel on Climate Change.* Cambridge University Press.

Minnis, P., Sun-Mack, S., Chen, Y., Khaiyer, M. M., Yi, Y., Ayers, J. K., Brown, R. R., Dong, X., Gibson, S. C., Heck, P. W., Lin, B., Nordeen, M. L., Nguyen, L., Palikonda, R., Smith, W. L., Spangenberg, D. a., Trepte, Q. Z. and Xi, B. (2011a). CERES Edition-2 Cloud Property Retrievals Using TRMM VIRS and Terra and Aqua MODIS Data—Part II: Examples of Average Results and Comparisons With Other Data. *IEEE Transactions on Geoscience and Remote Sensing*, *49*(11), 4401–4430.

Minnis, P., Sun-Mack, S., Young, D. F., Heck, P. W., Garber, D. P., Chen, Y., Spangenberg, D. A., Arduini, R. F., Trepte, Q. Z., Jr., W. L. S., Ayers, J. K., Gibson, S. C., Miller, W. F., Hong, G., Chakrapani, V., Takano, Y., Liou, K.-N., Xie, Y. and Yang, P. (2011b). CERES edition-2 cloud property retrievals using TRMM VIRS and terra and aqua MODIS data—part I: Algorithms. *IEEE Trans. on Geoscience and Remote Sensing*, *49*(11), 4374–4400.

Morcrette, J.-J., Barker, H. W., Cole, J. N. S., Iacono, M. J. and Pincus, R. (2008). Impact of a New Radiation Package, McRad, in the ECMWF Integrated Forecasting System. *Monthly Weather Review*, *136*(12), 4773–4798.

Morcrette, J.-J. and Fouquart, Y. (1986). The overlapping of cloud layers in shortwave radiation parameterizations. *Journal of Atmospheric Sciences*, *43*, 321–328.

Nam, C., Bony, S., Dufresne, J.-L. and Chepfer, H. (2012). The 'too few, too bright' tropical low-cloud problem in CMIP5 models. *Geophysical Research Letters*, *39*, L21801.

Okamoto, H., Sato, K. and Hagihara, Y. (2010). Global analysis of ice microphysics from CloudSat and CALIPSO: Incorporation of specular reflection in lidar signals. *Journal of Geophysical Research*, *115*(D22), 1–20. Récupéré de `http://www.agu.org/pubs/crossref/2010/2009JD013383.shtml`

Oreopoulos, L. and Barker, H. W. (1999). Accounting for subgrid-scale cloud variability in a multi-layer 1d solar radiative transfer algorithm. *Quarterly Journal of the Royal Meteorological Society*, *125*(553), 301–330.

Oreopoulos, L., Lee, D., Sud, Y. C. and Suarez, M. J. (2012a). Radiative impacts of cloud heterogeneity and overlap in an atmospheric General Circulation Model. *Atmospheric Chemistry and Physics Discussions*, *12*(5), 12287–12329.

Oreopoulos, L., Mlawer, E., Delamere, J., Shippert, T., Cole, J., Fomin, B., Iacono, M., Jin, Z., Li, J., Manners, J., Räisänen, P., Rose, F., Zhang, Y., Wilson, M. J. and Rossow, W. B. (2012b). The Continual Intercomparison of Radiation Codes: Results from Phase I. *Journal of Geophysical Research*, *117*(D6), D06118. `http://dx.doi.org/10.1029/2011JD016821`

O'Hirok, W. and Gautier, C. (2005). The Impact of Model Resolution on Differences between Independent Column Approximation and Monte Carlo Estimates of Shortwave Surface Irradiance and Atmospheric Heating Rate. *Journal of the Atmospheric Sciences, 62*(8), 2939–2951.

Pincus, R., Barker, H. W. and Morcrette, J.-J. (2003). A fast, flexible, approximate technique for computing radiative transfer in inhomogeneous cloud fields. *Journal of Geophysical Research, 108*(D13), 1–5.

Pincus, R., Batstone, C. P., Hofmann, R. J. P., Taylor, K. E. and Glecker, P. J. (2008). Evaluating the present-day simulation of clouds, precipitation, and radiation in climate models. *Journal of Geophysical Research, 113*(D14), 1–10.

Pincus, R., Hemler, R. and Klein, S. a. (2006). Using Stochastically Generated Subcolumns to Represent Cloud Structure in a Large-Scale Model. *Monthly Weather Review, 134*(12), 3644–3656.

Räisänen, P. and Barker, H. W. (2004). Evaluation and optimization of sampling errors for the Monte Carlo Independent Column Approximation. *Quarterly Journal of the Royal Meteorological Society, 130*(601), 2069–2085.

Räisänen, P., Barker, H. W. and Cole, J. N. S. (2005). The Monte Carlo Independent Column Approximation's Conditional Random Noise: Impact on Simulated Climate. *Journal of Climate, 18*(22), 4715–4730.

Räisänen, P., Järvenoja, S. and Järvinen, H. (2008). Noise due to the Monte Carlo independent-column approximation : short-term and long-term impacts in ECHAM5. *Quarterly Journal of the Royal Meteorological Society, 134*, 481–495.

Räisänen, P., Järvenoja, S., Järvinen, H., Giorgetta, M., Roeckner, E., Jylhä, K. and Ruosteenoja, K. (2007). Tests of Monte Carlo Independent Column Approximation in the ECHAM5 Atmospheric GCM. *Journal of Climate, 20*(19), 4995–5011.

Räisänen, P. and Järvinen, H. (2010). Impact of cloud and radiation scheme modifications on climate simulated by the ECHAM5 atmospheric GCM. *Quarterly Journal of the Royal Meteorological Society, 136*(652), 1733–1752.

Randall, D., Khairoutdinov, M., Arakawa, A. and Grabowski, W. (2003). Breaking the Cloud Parameterization Deadlock. *Bulletin of the American Meteorological Society, 84*(11), 1547–1564. `http://dx.doi.org/10.1175/BAMS-84-11-1547`

Randall, D. A., Wood, R. A., Bony, S., Colman, R., Fichefet, T., Fyfe, J., Kattsov, V., Pitman, A., Shukla, J., Srinivasan, J., Stouffer, R. J., Sumi, A. and Taylor, K. E. (2007). *Climate Models and Their Evaluation. In: Climate Change*

2007: The Physical Science Basis. Contribution of Working Group I to the Fourth Assessment Report of the Intergovernmental Panel on Climate Change. Cambridge University Press.

Rossow, W. B., Delo, C. and Cairns, B. (2002). Implications of the Observed Mesoscale Variations of Clouds for the Earth ' s Radiation Budget. *Journal of Climate, 15*(6), 557–585.

Shonk, J. K. P. and Hogan, R. J. (2008). Tripleclouds: An Efficient Method for Representing Horizontal Cloud Inhomogeneity in 1D Radiation Schemes by Using Three Regions at Each Height. *Journal of Climate, 21*(11), 2352–2370.

Shonk, J. K. P. and Hogan, R. J. (2010). Effect of improving representation of horizontal and vertical cloud structure on the Earth's global radiation budget. Part II: The global effects. *Quarterly Journal of the Royal Meteorological Society,* (July), 1191–1204.

Shonk, J. K. P., Hogan, R. J., Edwards, J. M. and Mace, G. G. (2010). Effect of improving representation of horizontal and vertical cloud structure on the Earth's global radiation budget. Part I: review and parametrization. *Quarterly Journal of the Royal Meteorological Society, 136*(July), 1191–n/a.

Siebesma, A. P., Brengiuer, J.-L., Bretherton, C. S., Grabowski, W. W., Heintzenberg, J., Kärcher, B., Lehmann, K., Petch, J. C., Spichtinger, P., Stevens, B. and Stratmenn, F. (2008). *Cloud-controlling Factors in Clouds in the Perturbed Climate System.* The MIT Press.

Stephens, G. L. (1984). The parameterization of radiation for numerical weather prediction and climate models. *Monthly Weather Review, 112*, 826–867.

Stephens, G. L., Gabriel, P. M. and Tsay, S.-C. (1991). Statistical Radiative Transport in One-Dimensional Media and Its Application to The Terrestrial Atmosphere. *Transport Theory and Statistical Physics, 20*, 139–175.

Stephens, G. L., Vane, D. G., Boain, R. J., Mace, G. G., Sassen, K., Wang, Z., Illingworth, A. J., O'Connor, E. J., Rossow, W. B., Durden, S. L. *et al.* (2002). The cloudsat mission and the a-train. *Bulletin of the American Meteorological Society, 83*(12).

Stephens, G. L. and Webster, P. J. (1981). Clouds and climate: Sensitivity of simple systems. *Journal of Atmospheric Sciences, 38*, 235–247.

Sundqvist, H. (1988). Parameterization of condensation and associated clouds in models for weather prediction and general circulation simulation. *Physically-Based Modelling and Simulation of Climate and Climatic Change - Part 1, NATO-ASI Series, Series C: Math. and Phys. Sciences, 243*, 433–461.

Tiedtke, M. (1996). An extension of cloud-radiation parameterization in the ecmwf model: The representation of subgrid-scale variations of optical depth. *Monthly Weather Review, 124*, 745–750.

Tjernström, M., Sedlar, J. and Shupe, M. D. (2008). How well do regional climate models reproduce radiation and clous in the Arctic? An evaluation of ARCMIP simulations. *Journal of Climate Applied Meteorology.* `http://dx.doi.org/10.1175/2008JAMC1845.1`

Toon, O. B. and Pollack, J. B. (1976). A global average model of atmospheric aerosols for radiative transfer calculations. *Journal of Applied Meteorology, 15*, 225–246.

Wentz, F. J. (2013). Ssm/i version-7 calibration report. In *Remote Sensing Systems.* Santa Rosa, CA.

Winker, D. M., Pelon, J. R. and McCormick, M. P. (2003). The calipso mission: Spaceborne lidar for observation of aerosols and clouds. In *Third International Asia-Pacific Environmental Remote Sensing Remote Sensing of the Atmosphere, Ocean, Environment, and Space*, 1–11. International Society for Optics and Photonics.

Zadra, A., Caya, D., Côté, J., Dugas, B., Jones, C., Laprise, R., Winger, K. and Caron, L.-P. (2008). The next Canadian regional climate model. *Physics in Canada, 64*.

Zhang, F., Liang, X.-Z., Li, J. and Zeng, Q. (2013). Dominant roles of subgrid-scale cloud structures in model diversity of cloud radiative effects. *Journal of Geophysical Research: Atmospheres, 118*(14), 7733–7749.

Zhang, H., Jing, X. and Li, J. (2014). Application and evaluation of a new radiation code under McICA scheme in BCC_AGCM2.0.1. *Geoscientific Model Development, 7*(3), 737–754.